



— Project Review —

**Consortium Project on
Seismic Inverse Methods for Complex Structures**

May 22, 1989

prepared by

**Norman Bleistein, Jack K. Cohen, Wenjie Dong,
Jeff Emanuel, Sebastien Geoltrain
and Christopher Liner**



SPONSORS MAILING LIST: TECHNICAL CONTACTS

The Center for Wave Phenomena gratefully acknowledges the support of the companies listed here. We provide this list as a convenience to the sponsors.

Amerada Hess Corporation
Dr. J. Bee Bednar
P.O. Box 2040
Tulsa, Oklahoma 74102

Amoco Production Company
Dr. Samuel H. Gray
Research Center
P.O. Box 3385
Tulsa, OK 74102

ARCO Oil and Gas Company
Dr. Arthur Weglein
Research and Technical Services
2300 West Plano Parkway
Plano, TX 75075

Chevron Oil Field Research Company
Dr. Leroy C. Pusey
P.O. Box 446
La Habra, CA 90633

Conoco, Inc.
Dr. Roger Parsons
P.O. Box 1267
Ponca City, OK 74601

GECO
Dr. Lars Sønneland
Bjergstedv. 1 - P.O. Box 330
N-4001 Stavanger
NORWAY

Marathon Oil Company
Dr. S. D. Peterson
P.O. Box 269
Littleton, CO 80160

Mobil Research and Develop. Corp.
Dr. Stanley J. Laster
P.O. Box 819047
Dallas, TX 75381

Phillips Petroleum Company
Dr. David H. von Seggern
500A Plaza Office Building
Bartlesville, OK 74004

Shell Development Company
Dr. Jon Sheiman
Bellaire Research Center
P. O. Box 481
Houston, TX 77001

Statoil
Dr. Eivind Berg
P. O. Box 7004
Trondheim, NORWAY
011 47 7 58 40 11

Sun Exploration and Production Company
Dr. Joong H. Chun
P. O. Box 830936
Richardson, TX 75083-0936

Texaco, USA
Dr. Eike Rietsch
Exploration Research
P.O. Box 770070
Houston, TX 77215-0070

UNOCAL
Dr. Robert D. Mager
376 S. Valencia Avenue
Brea, CA 92621

Western Geophysical
Dr. Wendell Wiggins
P.O. Box 2469
Houston, TX 77252



TABLE OF CONTENTS

INTRODUCTION

SELECTED RESEARCH AND PROGRESS REPORTS

Excerpts from Mapping Reflection Seismic Data to Zero Offset
(Doctoral Thesis)

Christopher Liner

Excerpts from Asymptotic Solutions to Direct and Inverse Scattering
in Anisotropic Elastic Media (Doctoral Thesis)

Sebastien Geoltrain

Excerpts from Common Shot, Prestack Inversion of Physical Model
Seismic Data (Master's Thesis)

Jeff Emanuel

Excerpts from Finite Difference Ray Tracing and Common Shot Inversion
(Master's Thesis)

Wenjie Dong

Diffraction Tomography and Inversion Aperture Preliminary Report

Norman Bleistein and Jack K. Cohen



INTRODUCTION

This is the annual consortium project review on the current status of the research program of the Center for Wave Phenomena at the Colorado School of Mines as of April 7, 1989.

We are delighted to welcome a new sponsor, Chevron. We are gratified by the continued support we are receiving in these difficult times for our industry. We know we have survived contractions in university support and in-house support throughout the industry.

We continue to make substantial progress on developing seismic inverse methods for complex structures. Our methods provide a reflector map and estimates of variations in earth parameters across reflectors for progressively more complex (and more realistic) models of the seismic experiment. A natural adjunct of this inversion research is the development of forward modeling capability for problems of the same complexity as are addressed by our inversion research.

We started five years ago with a formalism that seems primitive when compared to our present capabilities. We were able to invert zero-offset acoustic data in a depth-dependent background medium. We now have capability to model and invert elastic data in both isotropic and anisotropic media. We have also revisited dip moveout and transformation to zero-offset and analyzed it with an eye towards true amplitude analysis. We are beginning studies of well-to-well and VSP inversion and the problem of resolution, as constrained by source/receiver configuration, which becomes more severe in these kinds of surveys than in surface surveys.

Our solutions of the inverse problem take the form of spatially weighted Kirchhoff migrations of frequency filtered traces. The amplitude of the output provides a means of estimating the earth parameter variations (sound speed, density, Lamé parameters) across each reflector.

Our forward modeling capability exploits ray theory and/or Kirchhoff-approximate Kirchhoff integral methods. The combination of the two methods allows for Kirchhoff modeling in inhomogeneous media.

Our two-dimensional modeling and inversion both account for out-of-plane geometrical spreading. We refer to this hybrid of three-dimensional propagation in a medium with two-dimensional variation as *two-and-one-half dimensional*, (2.5D). We originally adopted that designation from Gerry Hohmann, who uses it in electromagnetic modeling and inversion. It seems as if that designation is now catching on in the seismic literature, as well.

The People

The consortium project is led by Norm Bleistein and Jack Cohen. Students currently supported by this project during the past year, in whole or in part, are Phil Anno, Kidane Araya, Craig Artley, Sebastien Geoltrain, and Chris Liner. Other supported students working with us are Wenjie Dong and Jeff Emanuel.

Administrative matters are handled by Jo Ann Fink and our technical typist is Barbara McLenon. In addition, John Stockwell has taken on the role of "resident scholar."

Presentations at the November '88 SEG Meeting

- [1] Geoltrain, S., and N. Bleistein, 1988, Aspects of anisotropic wave propagation: Extended Abstracts, 1988 International Meeting of the Society of Exploration Geophysicists, Anaheim, 1151-1155.
- [2] Liner, C. L., and J. K. Cohen, 1988, An amplitude-preserving inverse of Hale's DMO: Extended Abstracts, 1988 International Meeting of the Society of Exploration Geophysicists, Anaheim, 1117-1123.
- [3] Liner, C. L., and N. Bleistein, 1988, Comparative anatomy of common offset dip moveout: Extended Abstracts, 1988 International Meeting of the Society of Exploration Geophysicists, Anaheim, 1101-1105.
- [4] Sumner, B., and N. Bleistein, 1988, Prestack elastic Kirchhoff migration and parameter estimation: Extended Abstracts, 1988 International Meeting of the Society of Exploration Geophysicists, Anaheim, 963-965.

Status of Recent Papers

- [5] CWP-063R: Large Wave Number Aperture Limited Fourier Inversion and Inverse Scattering with Appendices, by Norman Bleistein. Invited paper, Wave Motion, Special Issue on Inverse Problems, March 1989.
- [6] CWP-073P: General Theory and Comparative Anatomy of Dip Moveout, by Christopher Liner. September, 1988. Submitted to Geophysics. Distributed to sponsors as 073R.
- [7] CWP-074R: Propagation of Elastic Waves in Transversely Isotropic Media, by Sebastien Geoltrain. September, 1988. Distributed to sponsors.
- [8] CWP-079: Aperture for Kirchhoff Inversion, Jack K. Cohen. Draft sent to sponsors, January, 1989.
- [9] CWP-080: Stacking of Narrow Aperture Common Shot Inversions, Norman Bleistein and Jack K. Cohen. To be submitted to Wave Motion.
- [10] CWP-081: Mapping Reflection Seismic Data to Zero Offset, Christopher L. Liner. Doctoral thesis. Excerpts in this project review. Full thesis to be distributed to sponsors.
- [11] CWP-082: Asymptotic Solutions to Direct and Inverse Scattering in Anisotropic Elastic Media, by Sebastien Geoltrain. Doctoral Thesis. Excerpts in this project review. Full thesis to be distributed to sponsors.
- [12] CWP-083: Master's Thesis. Jeff Emanuel. (In progress.) Excerpts in this project review.

- [13] CWP-084: Finite Difference Ray Tracing and Common Shot Inversion, by Wenjie Dong. Master's Thesis. Excerpts in this project review. Full thesis to be distributed to sponsors.
- [14] CWP-085: Diffraction and Tomography and Inversion Aperture Preliminary Report, by N. Bleistein and J.K. Cohen. In this project review. (In progress.)
- [15] CWP-087: Seismic Inverse Methods for Complex Structures, Status Report, February, 1989, by Norman Bleistein and Jack K. Cohen. To appear in Internat'l Jour. of Imaging Systems & Technology, June, 1989, ed. Enders Robinson.
- [16] CWP-090: Ray Theoretical Modeling for Seismic Surveys along a Common Trend (Strike) in Layered Acoustic Media, by Kidane Araya. (In progress.)

COMPUTER PROGRAM DOCUMENTATION:

(Proprietary to CWP Consortium Members)

- [17] U09: Docherty, P., CXZ: Fortran program for laterally varying velocity inversion, 1988. Distributed: 7/27/88.
- [18] U10: Sumner, B., Computer programs for modeling and inversion in isotropic elastic media, 1988. Distributed: 9/21/88.
- [19] U11: Geoltrain, S., TRISO: Fortran Ray Tracing Program for Horizontally Layered Transversely Isotropic Media, 1988. Preliminary version available on request. Documented version to be distributed, Summer, 1989.





Excerpts from
**Mapping Reflection Seismic Data
to Zero Offset**

by

Christopher L. Liner

**Partially supported by the Consortium Project
on Seismic Inverse Methods for Complex Structures
at the Center for Wave Phenomena**

**Center for Wave Phenomena
Department of Mathematics
Colorado School of Mines
Golden, Colorado 80401
Phone (303) 273-3557**



ABSTRACT

An important trend in modern seismic data processing is toward the development of amplitude preserving algorithms.

Toward that goal, a Born theory of DMO (BDMO) is developed directly from the wave equation. This follows the work of Jorden (1987), but considerable progress is made toward a more straightforward derivation, simplified amplitude terms and analytical verification. In synthetic tests, common shot BDMO yields a very clean image and successfully preserves the angular reflection coefficient. Finally, Kinematic DMO and BDMO are tested on physical model data. Relative to conventional results, the BDMO algorithm yields greater reflector continuity, as well as meaningful amplitudes.

GLOSSARY OF NOTATION

Symbol	Introduced	Definition
A_i	(2.9)	Born prestack inversion amplitude
A_{COS}	(2.79)	BDMO common offset amp term
A_{shot}	(2.51)	BDMO common shot amp term
A_o	(2.4)	Born zero-offset modeling amplitude
A_1	(1.17)	Hale's A term; common offset without log-stretch
A_2	(1.24)	Log-stretch common offset term
A_3	(1.25)	Notfors Log-stretch common offset term
A_4	(1.26)	Shot profile term
2α	(2.49)	Opening angle between r_s and r_g (α = incident angle)
$\alpha(x)$	(2.1)	Velocity perturbation
$\alpha_a(x)$	(2.9)	" with angular refl. coeff.s
$\alpha_o(x)$	(2.4)	" with normal refl. coeff.s
B	(1.8a)	General inverse DMO amplitude factor
β	(1.58c)	$(y - y')/h$ or y/h
β_g	(2.26)	$x_g - x_o$
β_s	(1.86)	y_s/h
β_s	(2.25)	$x_s - x_o$
C, C'	(A2, A8)	General DMO amplitude factors
Δ	(1.76b)	$\log_e(1 - \beta^2)/2$
Δ_s	(1.86)	$\log_e(1 - \beta_s^2)/2$
$\Delta t_o, \Delta x_o$	(2.81)	Time and space sample rates
f	(1.26)	Full offset
$F(), G()$	(A2, A7)	General functions
ϕ_1, ϕ'_1	(A3, A9)	Temporal phase factors
ϕ_2, ϕ'_2	(A4, A10)	Spatial phase factors
ϕ_o	(2.4)	Zero-offset modeling phase
ϕ_i	(2.9)	Born prestack inversion phase

Symbol	Introduced	Definition
Φ	(2.60, A4)	General phase function
h	(1.12)	Half-offset
$H()$	(A18, A19)	Beylkin determinant
$H_{shot}()$	(2.48)	Common shot Beylkin determinant
$H_{COS}()$	(2.78)	Common offset Beylkin determinant
I	(A4)	Generic integral for stationary phase
$IR_{Fulllog}$	(1.72)	Full Log DMO impulse response
IR_{Hale}	(1.65)	Hale DMO impulse response
$IR_{Notfors}$	(1.68)	Notfors Log DMO impulse response
J	(1.4)	Jacobian for change of variables in an integral
k_f	(1.27)	Offset wavenumber
k_y	(1.11)	Horizontal (midpoint) wavenumber
k_{y_s}	(1.56)	k_y stationary point
k_o	(1.20)	Generic zero offset wavenumber
ω_o	(1.2)	Frequency variable for t_o
ω_i	(2.9)	Frequency variable for t_i
Ω_o	(1.21)	Frequency variable for τ_o
$P_o(t_o, x_o)$	(1.1)	Zero offset data
$\hat{P}_o(\omega_o, x_o)$	(1.58b)	$P_o(\omega_o, x_o) / \sqrt{i\omega_o}$
$\hat{P}_o(\Omega_o, x_o)$	(1.67b)	$P_o(\Omega_o, x_o) / \sqrt{i\Omega_o}$
$P_n(t_n, x_n)$	(1.1)	NMO'd offset data
Q	(1.71)	Simplifying expression
r_o	(2.5)	Distance from subsurface point to x_o
r_g	(2.10)	Distance from subsurface point to x_g
r_s	(2.10)	Distance from subsurface point to x_s
$R(\alpha)$	(2.53)	Non-linear, angular reflection coeff.
t, t_i	(1.12, 2.44)	Recorded reflection time
t_n	(1.1)	NMO'd reflection time
t_o	(1.1)	Zero offset reflection time
t_{oc}	(2.72)	t_o critical point
t_c	(1.18a,b)	Minimum cut-off time for log-stretch
τ_o	(1.18a)	Log-stretch of zero offset time
τ_n	(1.18b)	Log-stretch of NMO time
τ_c	(1.18a,b)	Minimum cut-off for τ

Symbol	Introduced	Definition
θ	(1.9)	Physical dip of reflector
v	(1.9)	Constant wave speed
v_i	(2.10)	Prestack inversion velocity
v_o	(2.5)	Zero-offset modeling velocity
$V(x)$	(2.2)	Velocity field
x, z	(2.4)	Subsurface coordinates
x_c	(2.28)	x stationary point
x_{gc}	(2.62)	x_g stationary point
x_n	(1.1)	General nonzero offset coordinate
x_s, x_g	(2.14, 2.15)	Source and receiver coordinates
x_o	(1.1)	General zero offset coordinate
ξ	(A4)	General variable
ξ_s	(A4)	Stationary point
y, y'	(1.9, 1.58)	Midpoint coordinates
y_i	(1.9)	Surface intercept of dipping bed in midpoint coordinates
y_s	(1.85)	y stationary point
z_c	(2.21)	z critical point

Inversion Theory Approach

Deregowski and Rocca (1981) considered a hypothetical experiment where prestack migration is followed by zero-offset forward modeling. The impulse response for this cascaded process is an operator which maps prestack data to zero-offset: the DMO impulse response. Their analysis was only aimed at finding the *geometry* of the DMO operator. That is, they were concerned only with the kinematics of the cascaded process.

We might imagine extending this idea and cascading a PSFM operator, based on the DSR equation, with zero-offset modeling. Each would be an integral operator and we might hope to simplify the result analytically. But to what end? Any such derived amplitude term is still based on the unknown amplitude behavior of the prestack migration.

However, if we were to use a prestack migration operator whose amplitude characteristics were completely known, then this cascaded approach would take on new meaning. Luckily, such a class of migration operators has recently become available (Bleistein, 1987; Beylkin, 1985). To distinguish these amplitude-preserving operators from those of classical migration, they have generally come to be termed *inversion operators*. The name derives from their origin in mathematical inverse theory.

Pursuing the cascaded operator approach an inversion theory transformation to zero-offset was developed by Jorden (1987; Jorden and Bleistein, 1987). A prestack inversion operator was combined with a zero-offset modeling integral. Both operators were theoretically based on the Born asymptotic solution to the point source, scalar wave equation. This approach combines the elegance of Deregowski and Rocca's original idea with the amplitude-conscious rigor of mathematical inverse theory. Unfortunately, owing to the difficulty and subtlety of the derivation, mathematical errors crept into the analysis of Jorden (1987).

In this Chapter, a correct and simplified derivation will be given. The resulting algorithm will be verified analytically then numerically tested on synthetic and field data. Wherever possible, correct results due to Jorden will be referenced and not re-derived.

2.2 The Wave Equation Basis

In what follows, we will be deriving a direct mapping of offset seismic data to zero-offset. This process will be termed Born theory Dip-Moveout (BDMO). Along the way there will be several caveats which itemize limitations of this method.

With kinematic DMO we identified the NMO equation as the underlying foundation, and the resulting process, regardless of details, contained no more physics than the NMO equation itself. For BDMO, the governing equation is the constant background, point source, scalar wave equation

$$\left[\nabla^2 - \left\{ \frac{1 + \alpha(\mathbf{x})}{v^2} \right\} \frac{\partial^2}{\partial t^2} \right] P(t, \mathbf{x}) = -\delta(t) \delta(\mathbf{x}) , \quad (2.1)$$

where $P(t, \mathbf{x})$ is the wavefield, and \mathbf{x} is a position three-vector. The velocity term is an expansion of the true velocity field, $V(\mathbf{x})$, with respect to a constant background velocity, v ,

$$\frac{1}{V^2(\mathbf{x})} \approx \frac{1 + \alpha(\mathbf{x})}{v^2} . \quad (2.2)$$

The quantity $\alpha(\mathbf{x})$ is termed the *velocity perturbation*, and we will be discussing solutions to the wave equation in a perturbative sense. That is, in the limit as

$$\alpha(\mathbf{x}) \ll 1 . \quad (2.3)$$

We can view (2.1) in two fundamentally different ways. If the velocity terms, v and $\alpha(\mathbf{x})$, are known then solving (2.1) for the data, $P(t, \mathbf{x})$, will be a *forward modeling* process. Conversely, if the data and background velocity are known then solving (2.1) for $\alpha(\mathbf{x})$ is an *inverse problem*.

Of course, this discussion of the wave equation is oversimplified. It is only meant to orient the reader to quantities arising in the inversion and modeling integrals and how they relate back to the wave equation.

To be consistent with Jorden (1987), we will be carrying two background velocities through the analysis. One, v_o , is a *modeling velocity* and the other, v_i , is a *inversion velocity*. The numerical examples below are concerned with Amplitude Versus Offset (AVO), and the two background velocities will be taken as equal. However, discriminating v_o from v_i may be useful in velocity analysis (Jorden, 1987).

Before proceeding we should recognize that whatever results are derived below can have no more physical meaning than the wave equation itself. This equation is highly idealized. Wavefronts are exactly spherical and propagate without distortion with the constant background velocity. There is no allowance for free surface, radiation patterns or attenuation. Even with these limitations, a Dip-Moveout process whose amplitudes are based on (2.1) is a great improvement over one based solely on the NMO equation.

2.3 Born Modeling and Inversion in 2.5-D

The 3-D wavefield, $P(t, \mathbf{x})$, in (2.1) exists at every point in three dimensional space. Consider a backscatter experiment where the source and receiver are coincident. Since we are taking the background velocity, v , as constant the only reflections

2. BORN THEORY OF DIP-MOVEOUT

2.1 Introduction

In Chapter One many forms of kinematic Dip-Moveout were presented. For all their differences these still share a common origin. They were based ultimately and completely on the NMO equation. However, this may not be obvious in some cases. For example, the "Exact Log" algorithm seems to be ultimately based on an analytical expression for the DMO impulse response. But that impulse response was derived from a stationary phase calculation on Hale's DMO integral, which is based in turn on the NMO equation.

Kinematic DMO, by definition, addresses only the issue of travel times. In this Chapter, detailed attention will be given to the problem of DMO amplitudes.

We should be concerned with DMO amplitudes because in practice data amplitudes *are* interpreted after DMO. This interpretation can be prestack Amplitude-Versus-Offset (AVO) analysis or even post-stack, post-migration as in bright spot work. If the entire processing stream, including DMO, is not carefully designed with amplitude preservation in mind, then amplitude interpretation becomes a precarious business.

How can the DMO amplitude problem be approached? DMO was originally developed from the following conceptual model: DMO is defined as whatever must be done to NMO'd data so that poststack migration yields the same result as Prestack Full Migration (PSFM). Whether or not this goal has been attained by kinematic DMO depends on how the DMO definition is interpreted. If we are only concerned with getting the same reflector location as PSFM, then kinematic DMO is just the ticket (until velocity variations become too strong). However, if we want to match amplitudes with the PSFM result, things become more difficult. First, what are correct PSFM amplitudes? Secondly, if we are *stacking* the DMO result before migration, then the amplitude comparison should be with summed prestack migrations, not individual prestack migrations. All of this implies subtle pitfalls for the unwary when considering DMO amplitude.

It was shown in Chapter One that a typical kinematic DMO processing stream decouples into independent processes: Geometric Spreading correction (GS), NMO, and DMO. As the theory of DMO amplitude preservation progresses, we can expect to see (at least) two camps arise. One will attempt to maintain the decoupled processing stream, and place an obligation on DMO to perform whatever amplitude modification is required. Another approach, a more rigorous one, will not insist on a decoupled processing stream. The sequence: GS+NMO+DMO, will give way to a single process that directly maps raw data to zero-offset. This direct mapping approach will be developed here by drawing on the work of Jorden (1987).

Previous Investigations

Every DMO process, kinematic or otherwise, has some kind of amplitude behavior. Some writers explicitly address this issue while others, more interested in the imaging aspects, do not. Since the term DMO applies to many different types of processes, we cannot expect a unique statement of what DMO *should* do to amplitudes. However, we would like to require that DMO, in whatever form, honor the wave equation in an amplitude sense.

As alluded to above, kinematic DMO (Hale, 1984; Berg, 1985) makes no pretense of honoring wave equation amplitudes.

Beginning with Yilmaz and Claerbout (1979) there have been several careful derivations of DMO from Prestack Full Migration (PSFM). We might term this approach *operator decomposition*. The idea is to manipulate the PSFM operator so that something between NMO and post-stack migration is isolated, and call this DMO. Of course many PSFM operators are known. But, the one universally used in this approach to DMO is based on the Double Square Root (DSR) equation (see Claerbout, 1984). A particularly elegant exposition is given by Hale (1983). Recently Black and Egan (1988) revised this approach by proposing a new *imaging condition*.

DMO amplitudes derived by this approach, will be compatible with those of PSFM based on the DSR equation. Unfortunately, this method of prestack migration is, itself, not rigorous with respect to amplitudes. Specifically, we have no theoretical justification for relating the migration result to subsurface reflection coefficients.

Another approach to the DMO amplitude problem has also appeared, which we might term *locally rigorous*. By this we mean a basically intuitive approach of accounting for specific amplitude factors in a rigorous, but isolated, manner. Deregowski and Rocca (1981), while deriving the DMO impulse response from kinematics, propose an amplitude which is empirically related to the impulse response curvature. They mention that a more rigorous amplitude treatment is possible using ray theory. Following up on this, Deregowski (1985) used ray theory and some *a priori* conditions, such as operator taper, to find an amplitude term. This analysis presupposes that various processes such as geometric spreading correction have already been performed on the data. A combination of theoretical derivation and *a priori* assumptions also appears in the amplitude work of Beasley et al. (1988). Finally, Gardener and Forel (1988) argue for an amplitude term based on linearized scattering coefficients, operator curvature, spreading and midpoint sampling. This paper is a follow-up of their work proposing an inherently 3D DMO process which is applied before NMO (Forel and Gardner, 1988).

The difficulty with the locally rigorous approach is its heavy reliance on the individual author's intuition. Also, there is the very real possibility of overlooking a needed term, or confusing amplitude effects of different order.

observed will be due to perturbation, $\alpha(x)$. Within the context of zero-offset modeling $\alpha(x)$ is proportional to the normal incidence reflection coefficient multiplied by a Heaviside step function. The step function gives the location of the velocity discontinuity, and from $\alpha(x)$ its magnitude is known. This interpretation of alpha holds only for zero-offset modeling, and for this special case we will term the perturbation $\alpha_o(x)$.

If the background v and $\alpha_o(x)$ are known, then an approximate 3-D solution to (2.1) can be derived from the Born theory (Cohen, Hagin and Bleistein, 1986). We will be interested here in processing a 2-D line of data, while still allowing for 3-D spreading effects. This is termed 2.5-D theory, and is discussed at length by Bleistein (1986). Modeling and inversion formulas for 2.5-D are derived from their 3-D counterparts by a stationary phase calculation which eliminates the out-of-plane variables.

Let the recorded line of zero-offset data be represented by $P_o(\omega_o, x_o)$, where ω_o is the zero-offset frequency and x_o is the zero-offset source/receiver location. The 2.5-D Born modeling formula is

$$P_o(\omega_o, x_o) \sim (-i\omega_o)^{3/2} \int \int dx dz A_o e^{i\omega_o \phi_o} \alpha_o(x, z), \quad (2.4)$$

where (x, z) is a two-vector spanning the subsurface. The amplitude and phase terms are given by

$$A_o = \frac{1}{16 \pi^{3/2} (v_o r_o)^{3/2}}. \quad (2.5)$$

$$\phi_o = \frac{2r_o}{v_o} \quad (2.6)$$

To avoid ambiguity we will keep careful track of how the frequency multipliers are defined, beginning with

$$(-i\omega_o)^{3/2} \equiv |\omega_o|^{3/2} e^{-i3\pi \text{sgn}(\omega_o)/4}, \quad (2.7)$$

where the goal is to retain analyticity in the upper half of the complex plane. This will assure a causal time function. The relationship defining the zero-offset distance r_o is

$$r_o = \sqrt{(x - x_o)^2 + z^2}, \quad (2.8)$$

which is shown geometrically in Figure 2.1.

Starting with the Born forward modeling integral (2.4), it is possible to derive an *inversion formula* which will recover $\alpha_o(x, z)$ when $P_o(\omega_o, x_o)$ and v are known. Of course this would be a zero-offset inversion formula. In Born DMO we envision a process of transforming a shot profile or a common offset section to zero-offset, not a zero-offset section to zero-offset.

The inversion formula we need is for offset seismic data. Such a formula is given for 3-D and general velocity variation by Cohen et al. (1986). Let the recorded offset seismic data be given by $P_i(\omega_i, x_i)$ where ω_i is the frequency corresponding to reflection time and x_i is the spatial coordinate parameterizing the input data. The beauty of the inversion formula is its generality. We need not specify at this point whether we are inverting a shot profile or common offset section. It is assumed that the input data has not been gained.

The inversion of, say, a shot profile will yield an approximate quantitative image of the perturbation. But, the original shot profile contained angular reflection coefficients. If the inversion background velocity, v , were variable, we would need to trace rays to construct the inversion operator. To be consistent with the Born theory, linearized reflection/transmission would need to be used. However, with a constant background velocity, we have not introduced any reflection or transmission effects. We are *passing* any angular reflection coefficient information present in the input through to the output. To recognize this, we will denote the inverted perturbation as $\alpha_a(x, z)$.

In these notations, the 2.5-D, constant velocity inversion formula is

$$\alpha_a(x, z) \sim \int \int dx_i d\omega_i A_i e^{-i\omega_i \phi_i} \frac{P_i(\omega_i, x_i)}{\sqrt{i\omega_i}}, \quad (2.9)$$

where the amplitude and phase terms are given by

$$A_i = \frac{2^{3/2} v_i^{5/2} (r_s r_g)^{3/2} H}{\pi^{1/2} (r_s + r_g)^{1/2}} \quad (2.10)$$

$$\phi_i = \frac{r_s + r_g}{v_i}. \quad (2.11)$$

As mentioned above, this inversion operator is general with respect to the sorting of the input data. The input data acquisition geometry (common shot, common offset, etc.) is specified by the *Beylkin determinant* (Beylkin, 1985),

$$H = H(x, z, x_i). \quad (2.12)$$

Specific formulas for H will be discussed below.

The frequency term in (2.9) is defined by

$$\sqrt{i\omega_i} \equiv |\omega_i|^{1/2} e^{i\pi \text{sgn}(\omega_i)/4} . \quad (2.13)$$

The length factors r_s and r_g are defined in terms of generic source and receiver locations, x_s and x_g , which are in turn functions of the general coordinate x_i . From the geometry of Figure 2.2, it follows that

$$r_s = \sqrt{(x - x_s)^2 + z^2} \quad ; \quad x_s = x_s(x_i) \quad (2.14)$$

$$r_g = \sqrt{(x - x_g)^2 + z^2} \quad ; \quad x_g = x_g(x_i) \quad (2.15)$$

It is important to note that the inversion operator (2.9), unlike the Double-Square-Root prestack migration operator, cannot be split into separate processes (NMO, DMO, etc.). Although the phase function does allow this decoupling, the wave-equation-based amplitude term (2.10) does not.

2.4 Derivation of 2.5-D Born DMO

At this point we have introduced 2.5-D Born integral operators for inversion of offset seismic data, (2.9), and forward modeling of zero-offset data, (2.4). Following Jorden(1987), we propose a *Born DMO* which can be represented by the cascaded process

$$\text{Born DMO} \equiv \text{Z.O.Modeling} \left[\text{Inversion} \left[\text{Data} \right] \right] ,$$

where *Z.O.* stands for *Zero Offset*.

It should be noted that Jorden began by cascading full 3-D operators. These were then analytically reduced within the DMO derivation to 2.5-D. The 3-D operator approach will not be developed here, but is interesting because it opens the possibility of quantifying the out-of-plane component of 3-D DMO (Jorden, 1987).

The cascaded process defining Born DMO will involve substituting $\alpha_a(x, z)$ for $\alpha_o(x, z)$. This means that we will be designing a process to pass angular reflection coefficients from the input data through to the zero-offset result. The angular information would then be available for further analysis.

Substituting the inversion (2.9) for $\alpha_o(x, z)$ in (2.4), we can write

$$P_o(\omega_o, x_o) \sim (-i\omega_o)^{3/2} \int \int \int \int dx dz dx_i d\omega_i A_1 e^{i(\omega_o \phi_o - \omega_i \phi_i)} \frac{P_i(\omega_i, x_i)}{\sqrt{i\omega_i}}, \quad (2.16)$$

where all of the symbols are as defined above, and the composite amplitude term is

$$A_1 = A_i A_o = \frac{v_i^{5/2} (r_s r_g)^{3/2} H}{2^{1/2} (2\pi)^2 (v_o r_o)^{3/2} (r_s + r_g)^{1/2}}. \quad (2.17)$$

The formula as given in (2.16) is not viable. The subsurface variables (x, z) are not present in either the input data $P_i(\omega_i, x_i)$ or the output $P_o(\omega_o, x_o)$. These were fundamental quantities for the individual modeling and inversion formulas, but for the cascaded operation (2.16) they are dummy variables. In what follows our goal is to analytically eliminate (x, z) . The major events of the derivation follow Jorden (1987), but there are differences in detail.

The first step is to inverse Fourier transform (2.16) with respect to ω_o . The fractional frequency term will transform according to

$$(-i\omega_o)^{3/2} \longrightarrow \partial_{t_o}^{3/2}, \quad (2.18)$$

so that (2.16) can be written as

$$P_o(t_o, x_o) \sim \partial_{t_o}^{3/2} \int \int \int \int dx dz dx_i d\omega_i A_1 \delta(t_o - \phi_o) e^{-i\omega_i \phi_i} \frac{P_i(\omega_i, x_i)}{\sqrt{i\omega_i}}, \quad (2.19)$$

where offsetting factors of 2π have been canceled.

The delta function argument is a function of z through (2.6) and (2.8). By setting the argument to zero a *critical point*, z_c , will be defined. This is given by

$$z_c \equiv \sqrt{r_o^2 - (x - x_o)^2} \quad ; \quad r_o = \frac{v_o t_o}{2}, \quad (2.20)$$

where the second equality follows directly from $t_o = \phi_o$. From a standard δ -function property (Bleistein, 1984, p.48), it follows that

$$\delta(t_o - \phi_o) \equiv \frac{\delta(z - z_c)}{\left| \frac{\partial \phi_o}{\partial z} \right|_{z=z_c}} = \frac{v_o r_o}{2z_c} \delta(z - z_c) . \quad (2.21)$$

Substituting (2.21) into (2.19), the z integration can be done by the sifting property of the delta function to yield

$$P_o(t_o, x_o) \sim \partial_{t_o}^{3/2} \int \int \int dx \, dx_i \, d\omega_i \, A_2 \, e^{-i\omega_i \phi_i} \frac{P_i(\omega_i, x_i)}{\sqrt{i\omega_i}} , \quad (2.22)$$

where the amplitude term is now given by

$$A_2 = A_1 \frac{v_o r_o}{2z_c} = \frac{v_i^{5/2} (r_s r_g)^{3/2} H}{2^{3/2} (2\pi)^2 (v_o r_o)^{1/2} (r_s + r_g)^{1/2} z_c} . \quad (2.23)$$

Note the z integration has been done exactly, no new approximation has been introduced. However, integrating out this variable has had the effect of coupling the other variables. Specifically, by (2.20) r_s and r_g are now functions of t_o .

Isolating the x -dependence, we can write (2.22) as

$$P_o(t_o, x_o) \sim \partial_{t_o}^{3/2} \int \int dx_i \, d\omega_i \frac{P_i(\omega_i, x_i)}{\sqrt{i\omega_i}} \int dx \, A_2 \, e^{-i\omega_i \phi_i} . \quad (2.24)$$

The x integral will be evaluated by the method of stationary phase. The stationary phase condition and its consequence are

$$\frac{\partial \phi_i}{\partial x} = 0 \quad \Rightarrow \quad \beta_s r_g = -\beta_g r_s , \quad (2.25)$$

where

$$\beta_s \equiv x_s - x_o \quad , \quad \beta_g \equiv x_g - x_o . \quad (2.26)$$

The equality on the right of (2.25) is the *stationary phase condition*. Figure 2.3 shows the geometry of this condition. The line r_o bisects the angle between r_s and r_g . This means that the input phase $t_i = \phi_i$ corresponds to a specular reflection, and the output phase $t_o = \phi_o$ is the normal incidence reflection time from that specular point.

This conclusion is in agreement with Jorden (1987).

One consequence of (2.25) is found by multiplying both sides by β_g/r_s ,

$$\beta_s \beta_g = - \frac{\beta_s^2 r_g}{r_s} \leq 0, \quad (2.27)$$

which proves useful in later analysis.

Solving (2.25) for x , will yield a critical point, x_c , given by

$$x_c \equiv x_o + \frac{r_o^2 (\beta_s + \beta_g)}{2 \beta_s \beta_g}. \quad (2.28)$$

The critical point x_c will not be defined if $\beta_s = 0$ or $\beta_g = 0$. We conclude that x_o must lie between the source and receiver (i.e., $|x_s| < |x_o| < |x_g|$).

Applying the stationary phase formula (Bleistein, 1984), gives the result

$$\int dx A_2 e^{-i\omega_i \phi_i} \sim \left[\frac{2\pi v_i r_s^3 r_g}{\beta_s^2 (r_s + r_g)} \right]^{1/2} \frac{e^{-i\omega_i \phi_i}}{\sqrt{i\omega_i}}. \quad (2.29)$$

Using the stationary phase evaluation, (2.29), we can write (2.24) as

$$P_o(t_o, x_o) \sim \partial_{t_o}^{3/2} \int \int dx_i d\omega_i A_3 e^{-i\omega_i \phi_i} \frac{P_i(\omega_i, x_i)}{i\omega_i}, \quad (2.30)$$

where the amplitude term is given by

$$A_3 = A_2 \left[\frac{2\pi v_i r_s^3 r_g}{\beta_s^2 (r_s + r_g)} \right]^{1/2} = \frac{v_i^3 r_s^3 r_g^2 H}{(4\pi)^{3/2} (v_o r_o)^{1/2} (r_s + r_g) |\beta_s| z_c} \quad (2.31)$$

A consequence of the stationary phase calculation is a further coupling of the remaining variables. Specifically, we now have the following relationships

$$t_o = \frac{2}{v_o} \left\{ \beta_s \beta_g \left[1 - (v_i t_i / f)^2 \right] \right\}^{1/2}, \quad (2.32)$$

$$r_s = |\beta_s| \left\{ 1 - \frac{r_o^2}{\beta_s \beta_g} \right\}^{1/2} = |\beta_s| v_i t_i / f, \quad (2.33)$$

$$r_g = |\beta_g| \left\{ 1 - \frac{r_o^2}{\beta_s \beta_g} \right\}^{1/2} = |\beta_g| v_i t_i / f, \quad (2.34)$$

$$\phi_i = \frac{r_s + r_g}{v_i} = \frac{f}{v_i} \left\{ 1 - \frac{r_o^2}{\beta_s \beta_g} \right\}^{1/2}, \quad (2.35)$$

where r_o is given by (2.20) and the full offset, f , is defined by

$$f \equiv |\beta_s| + |\beta_g| = |x_s - x_g|. \quad (2.36)$$

As a time-domain algorithm, we would not know how to implement the $\partial_{t_o}^{3/2}$ operator in (2.30). This calculation will be done analytically. First rearrange (2.30) as

$$P_o(t_o, x_o) \sim \int \int dx_i d\omega_i \frac{P_i(\omega_i, x_i)}{i\omega_i} \partial_{t_o}^{3/2} \left[A_3 e^{-i\omega_i \phi_i} \right], \quad (2.37)$$

which isolates the t_o -dependence of the integrand. To be consistent with previous "leading order" approximations, we can use the asymptotic equality

$$\partial_{t_o}^{3/2} \left[A_3 e^{-i\omega_i \phi_i} \right] \sim A_3 (-i\omega_i)^{3/2} \left[\frac{\partial \phi_i}{\partial t_o} \right]^{3/2} e^{-i\omega_i \phi_i}. \quad (2.38)$$

Differentiating (2.35), and using (2.20), (2.33) and (2.34), we find

$$\frac{\partial \phi_i}{\partial t_o} = \frac{v_o r_o f}{2 v_i r_g |\beta_s|}. \quad (2.39)$$

From the complex square root definitions implied by (2.7) and (2.13) we have

$$\frac{(-i\omega_i)^{3/2}}{i\omega_i} = \sqrt{i\omega_i}. \quad (2.40)$$

Using (2.38)-(2.40), we can write (2.37) as

$$P_o(t_o, x_o) \sim \int \int dx_i d\omega_i A_4 e^{-i\omega_i \phi_i} \hat{P}_i(\omega_i, x_i), \quad (2.41)$$

where the amplitude is given by

$$A_4 = A_3 \left[\frac{v_o r_o f}{2v_i r_g |\beta_s|} \right]^{3/2} = \frac{v_i^{3/2} v_o r_o f^{3/2} r_s^3 r_g^{1/2} H}{8 (2\pi)^{3/2} (r_s + r_g) |\beta_s|^{5/2} z_c}, \quad (2.42)$$

and where we have defined a new symbol for the pre-processed input data

$$\hat{P}_i(\omega_i, x_i) \equiv \sqrt{i\omega_i} P_i(\omega_i, x_i). \quad (2.43)$$

The final step in the general 2.5-D derivation is to perform the ω_i integration. If 2π is scaled out of the amplitude, this is an exact inverse Fourier Transform. The result is

$$P_o(t_o, x_o) \sim \int dx_i A_5 \hat{P}_i(t_i = \phi_i, x_i), \quad (2.44)$$

where the amplitude term is now

$$A_5 = 2\pi A_4 = \frac{v_i^{3/2} v_o r_o f^{3/2} r_s^3 r_g^{1/2} H}{8 (2\pi)^{1/2} (r_s + r_g) |\beta_s|^{5/2} z_c}. \quad (2.45)$$

Finally, from the sifting property of the delta function we can write (2.45) as

$$P_o(t_o, x_o) \sim \int \int dx_i dt_i A_5 \delta(t_i - \phi_i) \hat{P}_i(t_i, x_i). \quad (2.46)$$

which is the final form of the general 2.5-D Born DMO. Below we specialize to two standard input data configurations.

2.5 Common Shot Formula

Consider the input data, $\hat{P}_i(t_i, x_i)$, to be a shot profile. Let x_s be the constant source position, and x_g be variable geophone coordinate. Then we have

$$x_i = x_g, \quad x_s = \text{constant}. \quad (2.47)$$

For this input data geometry, the Beylkin determinant, H , is given by (Jorden, 1987)

$$H_{shot} = \frac{z_c (r_s + r_g) (1 + \cos 2\alpha)}{v_i^3 r_g^3 r_s}. \quad (2.48)$$

The angle 2α is the angle between the vectors r_s and r_g , as shown in Figure 2.1. The cosine term is calculated from

$$1 + \cos 2\alpha \equiv 1 + \nabla r_s \cdot \nabla r_g = 1 + \left[\frac{(x - x_s)(x - x_g) + z^2}{r_s r_g} \right] \Big|_{z=z_c; z=z_c} \quad (2.49)$$

or, after some algebra,

$$1 + \cos 2\alpha = 1 + \frac{1}{r_s r_g} \left[\beta_s \beta_g - \frac{r_o^2 (\beta_s^2 + \beta_g^2)}{\beta_s \beta_g} \right]. \quad (2.50)$$

Combine (2.45) with (2.48), and use the right side of (2.25) to considerably simplify the expression. The result is

$$A_{shot} = A_5(H_{shot}) = \frac{v_o r_o f^{3/2} (1 + \cos 2\alpha)}{8 (2\pi)^{1/2} v_i^{3/2} r_s^{1/2} |\beta_g|^{5/2}}. \quad (2.51)$$

We will find in the next section that this amplitude term must be modified slightly to yield a correct analytic result.

Finally, specializing (2.46) we get the common shot processing formula for Born DMO

$$P_o(t_o, x_o) \sim \int \int dx_g dt_i A_{shot} \delta(t_i - \phi_i) \hat{P}_i(t_i, x_g) . \quad (2.52)$$

The amplitude term (2.51) is singular for zero-offset, $f=0$, because in this limit $\beta_g=0$. This limitation has been present since the stationary phase calculation in x_g , specifically in (2.28). The algorithm as developed is capable of processing finite-offset data, and the incorrect results near zero-offset is easily identified on numerical output.

2.6 Analytic Verification

With (2.52) and (2.51) we have a process which claims to directly map shot profile data to zero-offset. Further it is claimed that any angular reflectivity present in the shot profile will be present in the zero-offset output. In this section we will investigate these claims by applying the processing algorithm to analytic data for a horizontal plane.

Figure 2.4 shows geometry for scattering from a general horizontal plane. The source, x_s , is fixed and there are assumed to be several receivers, x_g . The depth to the reflector is H , and the velocity down to that level is a constant v . In this calculation we will not distinguish v_i and v_o . To leading order, the data received at the geophones will have the form (Bleistein, 1984)

$$P_i(\omega_i, x_g) \sim \frac{R(\alpha) e^{2i\omega_i r/v}}{8\pi r} , \quad (2.53)$$

where

$$r = \frac{1}{2} \sqrt{x_g^2 + 4H^2} . \quad (2.54)$$

The expression (2.53) will be our *test data* for the horizontal plane. The function $R(\alpha)$ is the full non-linear angular reflectivity.

Before using the test data in (2.52), we must multiply by $\sqrt{i\omega_i}$, and go to the time domain via inverse Fourier transform. Now the test data takes the form

$$\hat{P}_i(t_i, x_g) = \frac{R(\alpha)}{16\pi^2 r} \int d\omega_i \sqrt{i\omega_i} e^{-i\omega_i(t_i - 2r/v)} . \quad (2.55)$$

Substituting the test data, (2.55), into the processing formula, (2.52), yields

$$P_o(t_o, x_o) \sim \int \int \int dx_g d\omega_i dt_i B_1 \delta(t_i - \phi_i) \sqrt{i\omega_i} e^{-i\omega_i(t_i - 2r/v)} , \quad (2.56)$$

where the amplitude term is

$$B_1 = \frac{R(\alpha)}{16\pi^2 r} A_{shot} . \quad (2.57)$$

As the analysis progresses the amplitude term will evolve. To simplify notation we will explicitly introduce the A_{shot} function (2.51) only at the end.

We begin the analysis by using the δ -function to perform the t_i integration in (2.56). From this we get

$$P_o(t_o, x_o) \sim \int d\omega_i \sqrt{i\omega_i} \int dx_g B_1 e^{-i\omega_i(\phi_i - 2r/v)} , \quad (2.58)$$

where the x_g -dependence has been isolated.

Without loss of generality, the algebra can be simplified by placing the source at the origin, $x_o=0$, and all geophones to the right, $x_g>0$. It follows from (2.26) that $\beta_s = -x_o$, and from (2.35) the specific form of ϕ_i is

$$\phi_i = \frac{r_s + r_g}{v} = \frac{x_g}{v} \left\{ 1 + \frac{r_o^2}{x_o(x_g - x_o)} \right\}^{1/2} , \quad (2.59)$$

Using (2.59), the phase of (2.58) is given explicitly by

$$\begin{aligned} \Phi &= -\omega_i \left[\phi_i - \frac{2r}{v} \right] . \\ &= \frac{-\omega_i}{v} \left[x_g \left\{ 1 + \frac{r_o^2}{x_o(x_g - x_o)} \right\}^{1/2} - \left\{ x_g^2 + 4H^2 \right\}^{1/2} \right] . \end{aligned} \quad (2.60)$$

We now proceed to asymptotically evaluate the x_g integral in (2.58) by the method of stationary phase. Differentiating (2.60) with respect to x_g yields

$$\frac{\partial \Phi}{\partial x_g} = \frac{-\omega_i}{v} \left[\frac{1 + \frac{r_o^2 (x_g - 2x_o)}{2x_o (x_g - x_o)^2}}{\left\{ 1 + \frac{r_o^2}{x_o (x_g - x_o)} \right\}^{1/2}} - \frac{x_g}{\left\{ x_g^2 + 4H^2 \right\}^{1/2}} \right]. \quad (2.61)$$

Setting (2.61) equal to zero results in an intractable quartic equation for the critical value x_{gc} . However, from the geometry of the problem we suspect that the critical point is

$$x_{gc} = 2x_o. \quad (2.62)$$

Substituting this value for x_g into (2.61) and simplifying gives the result

$$\frac{\partial \Phi}{\partial x_g} = \frac{-\omega_i}{v} \left[\frac{x_o}{(x_o^2 + r_o^2)^{1/2}} - \frac{x_o}{(x_o^2 + H^2)^{1/2}} \right] = 0. \quad (2.63)$$

This condition will be satisfied if $r_o = H$. From Figure 2.4, this is seen to be true.

The second derivative of the phase, evaluated at the stationary point, is

$$\frac{\partial^2 \Phi}{\partial x_g^2} = \frac{-\omega_i H^2}{2v x_o^2 (x_o^2 + H^2)^{1/2}}, \quad (2.64)$$

and the sign of the second derivative is $-\text{sgn}(\omega_i)$.

Using (2.64) the asymptotic evaluation of the x_g integral in (2.58) is

$$\int dx_g B_1 e^{-i\omega_i(\phi_i - 2r/v)} \sim \frac{2\sqrt{\pi v} x_o (x_o^2 + H^2)^{1/4}}{\sqrt{i\omega_i} H} B_1 e^{-i\omega_i(\phi_i - 2r/v)}, \quad (2.65)$$

where B_1 and the phase are evaluated at the stationary point. Substituting this result into (2.58), and canceling the common factor of $\sqrt{i\omega_i}$, we find

$$P_o(t_o, x_o) \sim \int d\omega_i B_2 e^{-i\omega_i(\phi_i - 2r/v)}, \quad (2.66)$$

where

$$\begin{aligned}
B_2 &= \frac{2\sqrt{\pi v} x_o (x_o^2 + H^2)^{1/4}}{H} \frac{R(\alpha)}{16\pi^2 r} A_{shot} \\
&= \frac{R(\alpha) v^{1/2} x_o (x_o^2 + H^2)^{1/4}}{8\pi^{3/2} H r} A_{shot} .
\end{aligned} \tag{2.67}$$

Since B_2 does not depend on ω_i , the ω_i integration in (2.66) can be done explicitly. The result is 2π times a delta function, so (2.66) becomes

$$P_o(t_o, x_o) \sim B_3 \delta(\phi_i - 2r/v) , \tag{2.68}$$

where

$$B_3 = 2\pi B_2 = \frac{R(\alpha) v^{1/2} x_o (x_o^2 + H^2)^{1/4}}{4\pi^{1/2} H r} A_{shot} . \tag{2.69}$$

It is now convenient to explicitly introduce A_{shot} . Rather than use the general form (2.51), we use (2.62) and $r_o = H$ to simplify A_{shot} as

$$A_{shot} = \frac{H(1 + \cos 2\alpha)}{4\pi^{1/2} v^{1/2} x_o (x_o^2 + H^2)^{1/4}} , \tag{2.70}$$

so that B_3 becomes

$$B_3 = \frac{R(\alpha)(1 + \cos 2\alpha)}{16\pi (x_o^2 + H^2)^{1/2}} . \tag{2.71}$$

Because the argument is evaluated at the stationary point, x_{gc} , the δ -function in (2.68) has support at the zero-offset reflector location. Specifically, setting the argument to zero and solving for the critical point t_{oc} we get

$$t_{oc} = \frac{2H}{v} \tag{2.72}$$

in agreement with the geometry of Figure 2.4.

The last step in this analysis is to recast the δ -function in (2.68) as

$$\delta(\phi_i - 2r/v) = \frac{(x_o^2 + H^2)^{1/2}}{H} \delta(t_o - 2H/v) . \quad (2.73)$$

To get this result, we have used the δ -function property illustrated in (2.21) and the fact that $2r/v$ is independent of t_o .

Combining (2.68), (2.71) and (2.73) we can write the final result as

$$P_o(t_o, x_o) \sim \frac{R(\alpha) \delta(t_o - 2H/v)}{8 \pi H} \frac{(1 + \cos 2\alpha)}{2} . \quad (2.74)$$

We have now shown that, when applied to analytic test data for a horizontal plane, the BDMO process yields a reflector in the zero-offset position. Further, the peak amplitude of the reflector is proportional to the angular reflection coefficient. We will take this as a general result.

Of course, in *true* zero-offset data the angle α is zero because the vectors r_i and r_g are colinear. The reflection coefficient is the normal incident one, $R(0)$, and the cosine term in (2.74) goes to unity. In our data *processed* to zero-offset we have two angular terms, $R(\alpha)$ and $(1 + \cos 2\alpha)/2$.

We use (2.74) in the following way. The goal in processing a general shot profile is to create zero-offset output data of the form

$$P_o(t_o, x_o) \sim \frac{R(\alpha) \delta(t_o - 2r_o/v)}{8 \pi r_o} . \quad (2.75)$$

We see from (2.74) that the processing algorithm (2.52) yields the desired output *multiplied by* an additional term $(1 + \cos 2\alpha)/2$. Therefore, the algorithm amplitude factor (2.51) should be divided by $(1 + \cos 2\alpha)/2$, and the correct amplitude to be used in (2.52) is

$$A_{shot} = \frac{v_o r_o f^{3/2}}{4 (2\pi)^{1/2} v_i^{3/2} r_s^{1/2} |\beta_g|^{5/2}} . \quad (2.76)$$

In addition to correcting the processing amplitude term, we could use (2.74) in another way. Imagine processing a shot profile twice, once using the (2.51) amplitude term and again using (2.76). The second processing would be almost free if carried out simultaneously with the first. The ratio of the two outputs, (2.74) divided by (2.75), will be an estimate of $(1 + \cos 2\alpha)/2$. From this number, the incident angle α could be calculated. This estimate of α would have meaning *only* at reflector peak amplitude locations. Following this approach one could hope to extract estimates of both $R(\alpha)$

and α from the data. For a discussion of this topic as it applies to prestack Kirchhoff Inversion, see Bleistein (1987).

Finally, note that for reflection from a horizontal plane the spreading term $8\pi r_o$ is constant. For a dipping plane or curved surface this will not be constant, and may mask variations in $R(\alpha)$. From the result (2.75) it follows that we can process for $R(\alpha)$ directly if the amplitude term (2.76) is multiplied by $8\pi r_o$.

2.7 Common Offset Formula

Briefly, for processing common offset data the spatial coordinate of the input will be midpoint, y . The general spatial variables thus specialize to

$$x_i = y \quad , \quad x_s = y - f/2 \quad , \quad x_g = y + f/2 \quad . \quad (2.77)$$

The Beylkin determinant for 2.5-D common offset is (Jorden, 1987)

$$H_{COS} = \frac{z_c (r_s + r_g) (r_s^2 + r_g^2) (1 + \cos 2\alpha)}{(v_i r_g r_s)^3} \quad . \quad (2.78)$$

As with the common shot amplitude term, we compensate for an extra $(1 + \cos 2\alpha)/2$ and arrive at

$$A_{COS} = A_5(H_{COS}) = \frac{v_o r_o f^{3/2} (r_s^2 + r_g^2)}{4(2\pi)^{1/2} v_i r_s^{5/2} |\beta_g|^{5/2}} \quad . \quad (2.79)$$

Finally, the processing formula for common offset will have the form

$$P_o(t_o, x_o) \sim \int \int dy dt_i A_{COS} \delta(t_i - \phi_i) \hat{P}_i(t_i, y) \quad , \quad (2.80)$$

where the various terms are defined above in terms of the x 's in (2.77).

2.8 Computer Implementation

In the preceding sections a theory for mapping raw, offset seismic data to zero-offset was derived and mathematically verified. This follows and draws heavily on Jorden (1987), but we have made considerable progress toward a more straightforward derivation, simplified amplitude terms and analytical verification.

Here we consider some computational aspects of the problem. To be explicit, the common shot algorithm will be discussed.

Recapping, the equations for common shot Born DMO are

$$P_o(t_o, x_o) \sim \int \int dx_g dt_i A_{shot} \delta(t_i - \phi_i) \hat{P}_i(t_i, x_g), \quad (2.52\text{again})$$

where the amplitude is given by

$$A_{shot} = \frac{v_o r_o f^{3/2}}{4 (2\pi)^{1/2} v_i^{3/2} r_s^{1/2} |\beta_g|^{5/2}}, \quad (2.76\text{again})$$

the phase is

$$\phi_i = \frac{r_s + r_g}{v_i} = \frac{f}{v_i} \left\{ 1 - \frac{r_o^2}{\beta_s \beta_g} \right\}^{1/2}, \quad (2.35\text{again})$$

and

$$\hat{P}_i(\omega_i, x_i) \equiv \sqrt{i\omega_i} P_i(\omega_i, x_i). \quad (2.43\text{again})$$

To calculate the various factors appearing in the amplitude and phase, we refer to the following list. The variable to be calculated is on the left and the pertinent equation number is on the right.

$$t_o \rightarrow (2.32),$$

$$r_o \rightarrow (2.20),$$

$$r_s \rightarrow (2.33),$$

$$r_g \rightarrow (2.34),$$

$$\beta_s \rightarrow (2.26) ,$$

$$\beta_g \rightarrow (2.26) ,$$

$$f \rightarrow (2.36) .$$

The form of (2.52) is that of a (t,x) -domain DMO process. Taken literally, (2.52) says that we should read a shot profile into the computer then do a weighted integration through the profile to generate each output point. The dominant contribution from this integral will be a stationary point corresponding to specular reflection. If the range of integration is too narrow (i.e., too few input traces) then endpoint contributions will dominate the output. We can expect to have confidence in the output amplitudes only when we are well away from the endpoint effects. If we were to process a single trace, the output would be nothing but endpoint effects. It follows that the impulse response, which was the canonical experiment for Kinematic DMO, is inappropriate for evaluating Born DMO. The canonical problem for DMO amplitude, as with migration amplitude, is the plane reflector.

Rather than implement (2.52) literally, we choose an alternative where the input data is read in one trace at a time and each input amplitude is *sprayed* along an ellipse in the output data panel. This allows trace sequential processing, and the input data need not be sorted by offset. The spraying operation is equivalent to performing the integration in (2.52) because integration is a linear process.

In the theoretical development constant velocity has been assumed. Recall that Born DMO simultaneously does spreading correction, NMO and DMO. While a constant velocity DMO might be acceptable, constant velocity NMO is not. As is done with standard NMO, we will use the constant velocity Born DMO theory, but actually allow a variable *rms* velocity field. In this way we are treating the velocity field *consistently* for spreading correction, NMO and DMO.

By treating the velocity field in an *rms* fashion we can expect good results until the true raypaths are significantly curved. In this limit the *rms* treatment will yield incorrect travel times and amplitudes. In general, by using the *rms* velocity field we can expect to be accurate to leading order in offset-squared.

The spraying operation is accomplished as follows. An input trace is read in. The trace is FFT'd, preprocessed in the frequency domain, and inverse FFT'd. For each time, t_i , on the input data we loop over output trace locations, x_o , between the source and receiver. With the output location fixed, compute the output time, t_o , and the amplitude term. Next, multiply the input data value by the amplitude term and the geophone differential. Finally, add this value into the output data panel, and repeat for all x_o , all t_i and all input traces.

The algorithm is summarized by the following program sketch. Here *FFT* and *IFFT* mean Fourier transform and inverse Fourier transform, respectively.

```

input data traces and rms velocity model

initialize output traces to zero

for all input traces {
    read trace( $t_i$ ) and get  $x_s, x_g$ 
    FFT trace( $t_i$ ) {
        multiply by  $\sqrt{i\omega_i}$ 
    } IFFT trace( $t_i$ )
    for all  $t_i$  {
        for all  $x_o$  between  $x_s$  and  $x_g$  {
            compute  $\beta_s, \beta_g$ 
            compute  $t_o$ 
            compute  $r_o, r_s$  and  $r_g$ 
            compute amplitude term  $A$ 
            add trace( $t_i$ )  $\cdot A \cdot dx_g$  into output
        }
    }
}

```

As mentioned in Chapter One, operator aliasing can be a significant problem in (t, x) -domain DMO algorithms. Born DMO is no exception. In fact, spatial aliasing tends to degrade amplitudes before it affects imaging or reflector continuity. In practice, operator aliasing occurs when the ellipse along which energy is being sprayed has a local slope of more than one time sample per trace. The absolute value of the local slope of the operator is found by differentiating (2.32) with respect to x_o . The result is

$$\frac{dt_o}{dx_o} = \frac{|\beta_s + \beta_g|}{v_o} \left[\frac{1 - (v_i t_i / f)^2}{\beta_s \beta_g} \right]^{1/2}. \quad (2.81)$$

This very strict aliasing criteria seems to be necessary for amplitude preservation. However, some dips which are technically aliased according to (2.28) may be desired (e.g., diffractions in stacked output). The aliasing criteria can be relaxed in this situation so that all dips are processed.

Let Δt_o and Δx_o be the time and space sample rates, respectively, on the output data. Then using (2.81) we have the following condition to avoid operator aliasing,

$$\frac{|\beta_s + \beta_g|}{v_o} \left[\frac{1 - (v_i t_i / f)^2}{\beta_s \beta_g} \right]^{1/2} \leq \frac{\Delta t_o}{\Delta x_o} . \quad (2.81)$$

Jorden (1987) has shown that if θ is the maximum anticipated reflector dip then t_o should be limited according to

$$t_o \leq \frac{-4 \beta_s \beta_g \sin \theta}{v_o (\beta_s + \beta_g)} . \quad (2.82)$$

Finally, can we make use of the log-stretch methods of Chapter One for Born DMO? The travel time relationship in (2.52) *could* be decomposed into NMO + DMO, and the DMO part would become time-invariant under the log-stretch transformation. However, the amplitude term is complicated and does not become time-invariant. Thus, the log-stretch trick cannot be used to build a faster algorithm for BDMO.

2.9 Synthetic Examples

In this section the common shot algorithm will be tested on a few synthetic data sets.

Figure 2.5 is a model for a horizontal plane at depth $r_o = 1000 \text{ meters}$, buried in a medium of constant velocity, $v_i = v_o = 3000 \text{ m/s}$. The near offset is 100 m , and there are 100 receivers spaced 10 m apart for a far offset of 1100 m . Let $R(\alpha) = 1$. This model is highly idealized, but will allow us to check the numerical accuracy of the algorithm. Figure 2.6 is the shot profile data for the model in Figure 2.5, and Figure 2.7 is the Born DMO result. The output reflector is properly located at the zero-offset time, $2r_o/v = .667 \text{ secs}$. Since $R(\alpha)$ is unit, the output amplitude should be flat away from the endpoints and have amplitude $(8\pi r_o)^{-1} = 3.98 \cdot 10^{-5}$. The maximum values away from endpoint contributions are within $\pm 10\%$ of the theoretical value. This result is consistent with the theory, allowing for interpolation and other numerical errors.

As a second test, take the model to be as in Figure 2.5 except that a velocity of 7000 m/s exists below the interface. Forward model data was created using Docherty's (1987) *Cshot* computer program. This is a ray tracing algorithm which incorporates the geometrical optics reflection coefficient, $R(\alpha)$. The synthetic shot profile data for the horizontal plane is shown in Figure 2.8. There are two competing amplitude effects on this data. One is an increase of $R(\alpha)$ with offset, and the other is a decrease of amplitude with offset due to geometric spreading. Figure 2.9 is the result of applying BDMO to the shot profile data. Since the reflector is horizontal, the zero-offset BDMO data has a constant spreading factor. The BDMO amplitude variations show $R(\alpha)$. If the *Cshot* data for this case were processed directly for $R(\alpha)$ only the absolute scale of

amplitudes would change.

We next consider a single dipping plane. Figure 2.10 is a ray trace diagram for the model. The velocity increases from 3000 m/s to 7000 m/s across the interface. The near offset is 200 m , the receiver interval is 20 m and there are 100 receivers. At its deepest point the reflector is 1500 m deep and the dip is 24° .

Shot profile data for the dipping plane is shown in Figure 2.11. BDMO of this data to zero-offset gives Figure 2.12. The image is very clean and the amplitude clearly indicates increasing AVO. Recall that the amplitude is composed of two factors; $R(\alpha)$ and zero-offset spreading. Since the dip is not severe the combined effect is a slight boosting of the shallow amplitudes. Apart from this caveat, the BDMO result has been successful in passing $R(\alpha)$ to the output image.

As a final synthetic example, we will process data gathered over a curved surface. A ray trace plot is shown in Figure 2.13. The near offset is 200 m and reflector depth varies from 1200 to 1500 m . Shot profile data for the is model is seen in Figure 2.14. Note the characteristic "bowtie" indicating a geometrical caustic, or buried focus, in the model. Applying BDMO, the zero-offset data of Figure 2.15 is created.

The caustic seen in the shot profile is still present in the zero-offset result. It has not been *unfolded* by the DMO process.

We can imagine that there are two types of geometrical caustics: caustics due to offset, and zero-offset caustics. The model in Figure 2.13 has a zero-offset caustic. This means that we cannot hope to process the data to zero-offset and get valid estimates for $R(\alpha)$ near the caustic. However, if the geometry of the model were such that only a caustic due to offset were present, then the BDMO output would not have a caustic and could yield an estimate for $R(\alpha)$ as in the previous examples.

In general, we can conclude that if a geometrical caustic exists in the zero-offset wavefield, then DMO of any kind is an inappropriate tool for AVO analysis. In such a case, only true amplitude prestack migration will suffice.

2.10 Physical Model Data Test

From the synthetic data tests of the previous section, we know that the BDMO mapping to zero-offset preserves angular reflection information. Using physical model data, we will now compare BDMO with conventional NMO+DMO processing. The physical model data was acquired at the University of Houston, and is supplied courtesy of Marathon Oil Company.

A single shot profile from this data set is shown in Figure 2.16. The direct arrival has been muted, but no gain has been applied. In scaled units, the time sample rate is $.004\text{ sec}$, and the receiver interval is 24 m . The near offset is 244 m and there are 48 traces per shot. Three distinct events are seen on the data. Reckoning from the upper surface the four velocities are 3580 , 4800 , 6830 , and 4800 m/s .

The line graph in Figure 2.16 shows a decrease of amplitude with offset for the first reflection event. Geometric spreading can account for some of this amplitude decay. The velocity contrast is +25% (3580 to 4800 m/s), so we expect a reflection coefficient which increases gradually with offset until the critical angle is reached (about 60°). The depth to this reflector in this part of the model is about 880 m, so the maximum incident angle is $\tan^{-1}(1390/880) = 57^\circ$. The fact that we do not see an amplitude increase at the far offsets implies a non-uniform source radiation pattern. There may also be an attenuation effect at work. These additional amplitude factors will be passed as a modified $R(\alpha)$ through the BDMO process.

Using a stratified *rms* velocity model, the shot profile was processed to zero-offset using BDMO, Figure 2.17, and conventional NMO+DMO, Figure 2.18. These are shown as perspective plots in Figure 2.19. The BDMO result has better reflector continuity, particularly at far offsets and for the deeper events. There is also a striking difference in amplitude behavior with offset, as evidenced by the amplitude line graph. On the basis of enhanced continuity and amplitude preservation, it is fair to conclude that BDMO has given a result superior to NMO+DMO.

A trace sequential DMO algorithm, whether Born theory or conventional, will yield a *DMO stack* when applied to several shot profiles. Any offset information for $R(\alpha)$ which is present in processing of a single shot will be lost as several shot results are summed to form the stack. The net result is like an integral of $R(\alpha)$ over α .

Using fifty shot profiles from the physical model data set, a stacked section was created using BDMO, Figure 2.20, and conventional NMO+DMO, Figure 2.21. These results are shown as perspective plots in Figures 2.22 and 2.23. An identical long-window AGC was applied as display gain. The computer processing time was approximately 50% greater for BDMO than NMO+DMO.

As we would hope, the stacked outputs are very similar. The location and geometry of the major events are in agreement. Relative reflector strength for the well-isolated events cannot be judged due to the application of AGC. However, reflector continuity seems improved on the BDMO data. This is best seen on the deepest reflector between 0.8 and 1.0 sec.

A steeply dipping event which is easily seen on the NMO+DMO stack is present, but weaker, on the BDMO stack. Physically, this is an edge diffraction from the side of the physical model. It seems that BDMO has boosted the continuous reflectors at the expense of this diffracted arrival. One might suspect that the strict aliasing criteria of (2.81) may have eliminated this severe dip. However, this event remains attenuated even when the aliasing restraint is relaxed to process all dips up to 90°. Furthermore, when the data is stacked with the BDMO phase but using the Kinematic DMO amplitude (1.65), this event is still attenuated. The author feels that a more sophisticated approach to operator aliasing would solve this problem (see Beasley, et al., 1988, and Hale, 1988).

The tests given here by no means constitute a comprehensive evaluation of Born DMO. They are meant only to show that the process is computationally feasible and

may have advantages over conventional DMO processing when amplitudes are of concern.

CONCLUSIONS

A general theory of Kinematic DMO and its inverse has been developed. It has been shown that published formulas for common offset and common shot DMO are special cases of the general equations.

An amplitude preserving inverse for Hale's DMO was given and numerically tested against the inversion formula of Ronen (1987b). It was shown that only the new inverse preserves amplitude information.

The log-stretch formulations of Bale and Jakubowicz (1987), herein called Full Log DMO, and Notfors and Godfrey (1987), herein called Notfors Log DMO, were derived in a common notation using the general theory. Because time-independence of the log-stretch frequency was *assumed*, the impulse responses for both of these algorithms depart from the desired "DMO ellipse" geometry. The Full Log algorithm has an impulse response in the form of an "inverted Gaussian". The Notfors Log DMO impulse response is a fairly close match to the DMO ellipse, but is too wide at the top. These departures from the Hale ellipse mean that some range of dips will be improperly handled by the algorithm.

Shot profile DMO was derived, reproducing the formula of Biondi and Ronen (1987).

Utilizing the method of stationary phase for the asymptotic evaluation of Fourier integrals, Kirchhoff algorithms were derived for Hale DMO – reproducing the result of Berg (1985) – and the log-stretch versions of common offset DMO. Analytic impulse responses were derived in all of these cases; these quantified the geometrical differences implied by the earlier numerical results. Also, the impulse response formulas show that, like Hale DMO, the log-stretch formulations have time variant amplitude.

Following a suggestion by Ronen (1987b), a log-stretch formulation of common offset DMO was derived, herein called Exact Log DMO, which preserves the DMO ellipse. The algorithm is *exact* with respect to impulse response geometry, but, again, time variant amplitudes have been sacrificed. The form of this algorithm, like other log-stretch formulas, is simply multiplication by a certain factor in the (k, ω) -domain.

To test the practical aspects of the four common offset DMO algorithms – Hale, Full Log, Notfors Log and Exact Log – each was run on a common offset field data example. Steeply dipping events, particularly shallow ones, were severely degraded by the Full Log algorithm. Notfors Log DMO was a vast improvement, but steep events were still significantly mishandled. The Exact Log DMO algorithm was able to correctly deal with all dips, in agreement with Hale DMO result. We conclude that with Exact Log DMO, we have created a Hale-quality image at FFT speeds.

In the field of DMO amplitude, a Born theory of Dip-Moveout (BDMO) was developed. The method is based on the general theory of inversion due to Beylkin (1985) and Cohen, Hagin and Bleistein (1986). Development of the theory followed the work of Jorden (1987), but differed in the starting point of the derivation and many of the details.



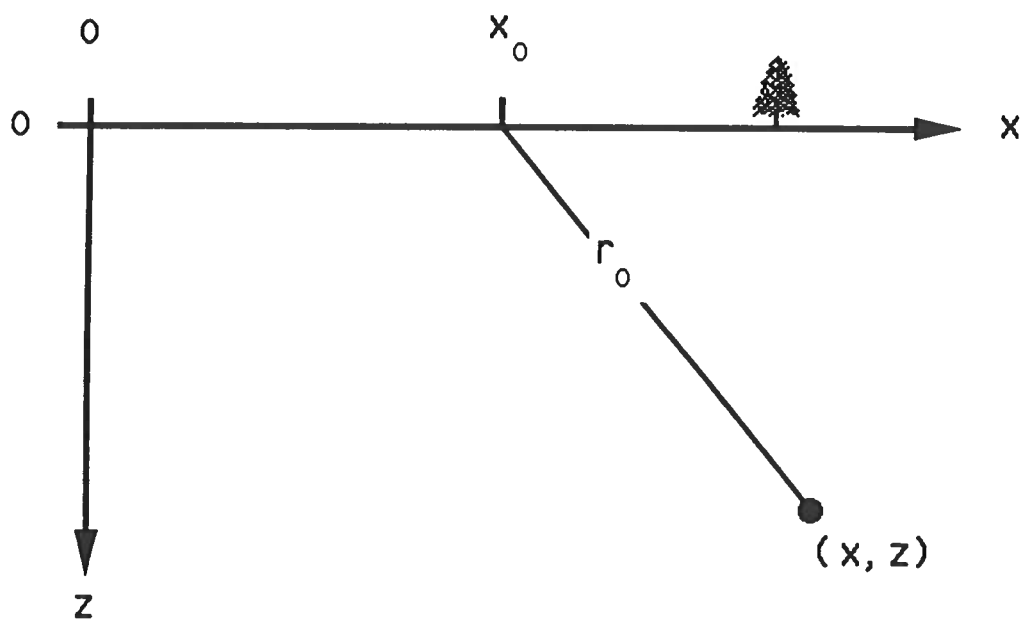


Figure 2.1: Geometry of 2.5-D zero offset Born modeling.



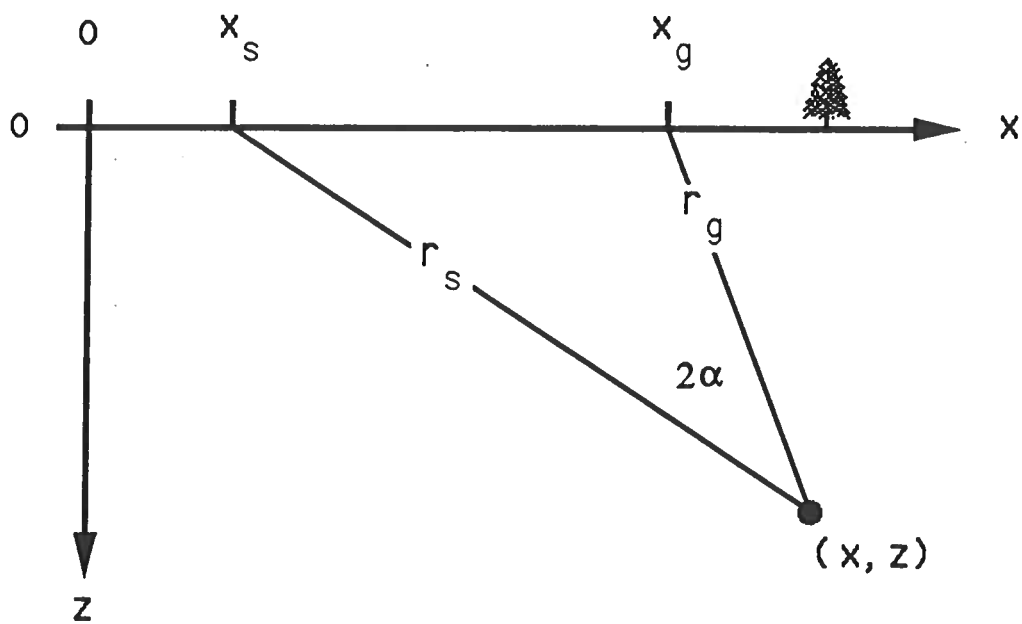


Figure 2.2: Geometry of 2.5-D Born inversion.



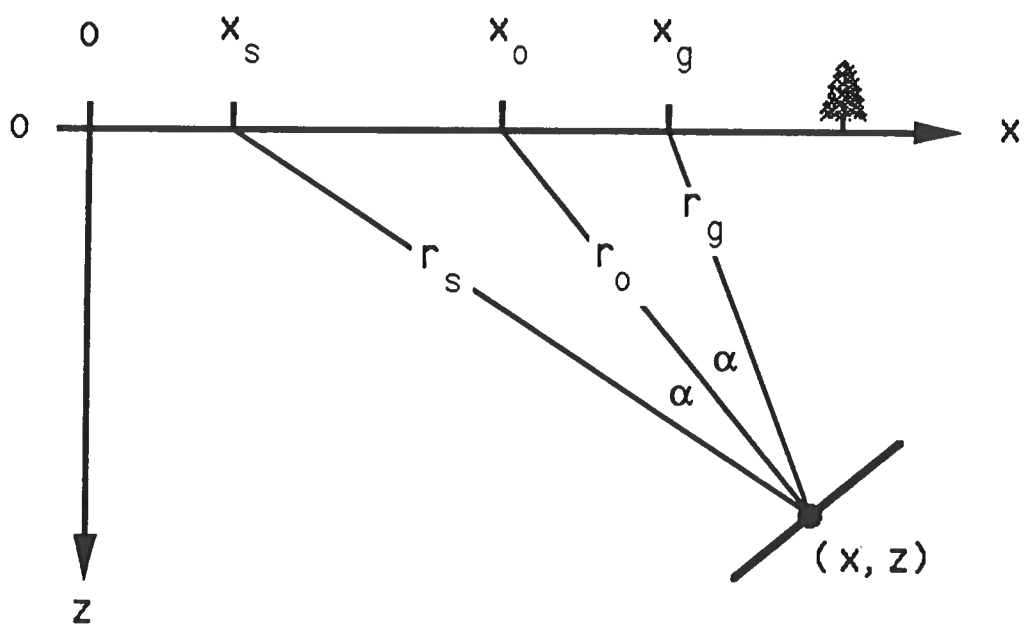


Figure 2.3: Geometry of 2.5-D Born Dip-Moveout (BDMO).



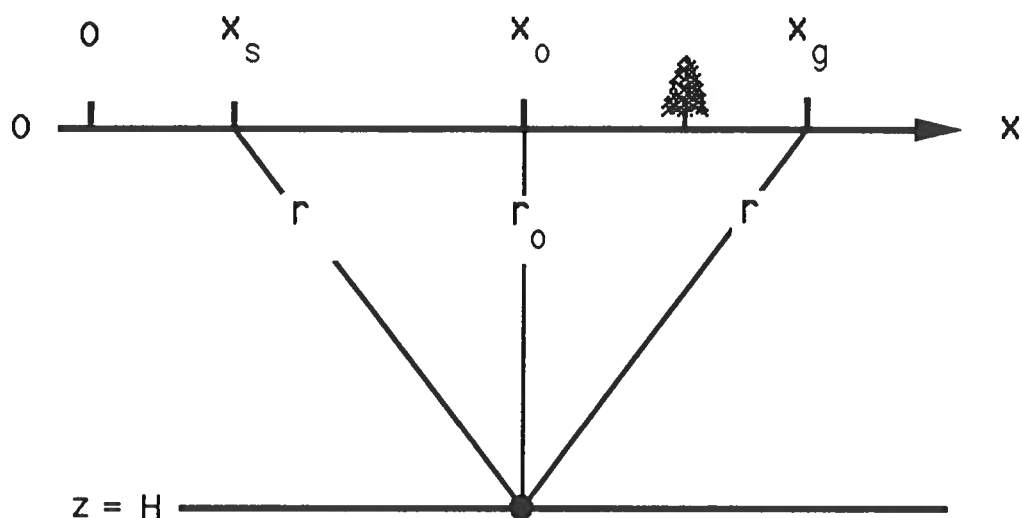


Figure 2.4: Model for general scattering from a horizontal plane.



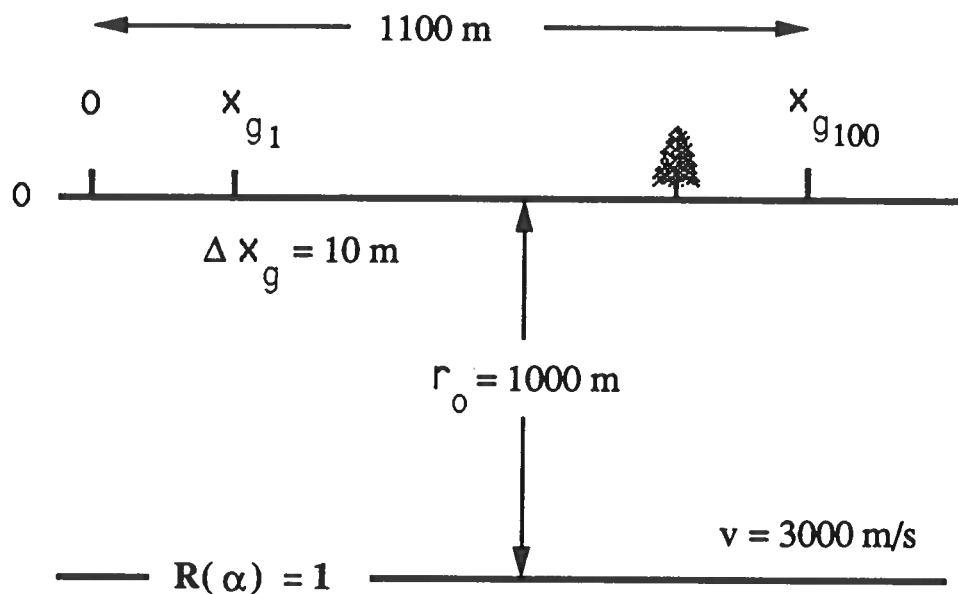


Figure 2.5: Specific horizontal plane model, with $R(\alpha) = 1$



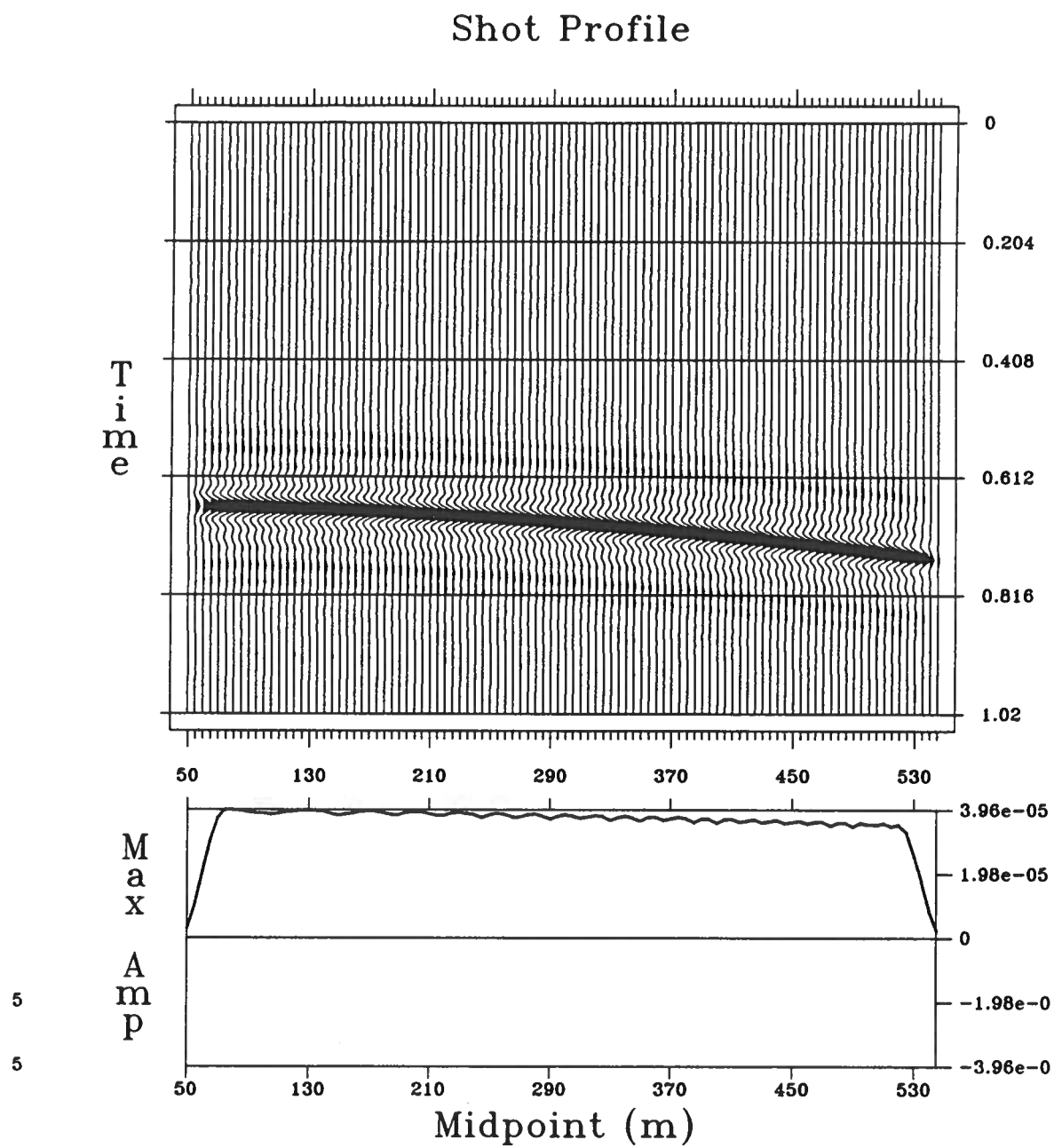


Figure 2.6: Shot profile data for the model in Figure 2.5.



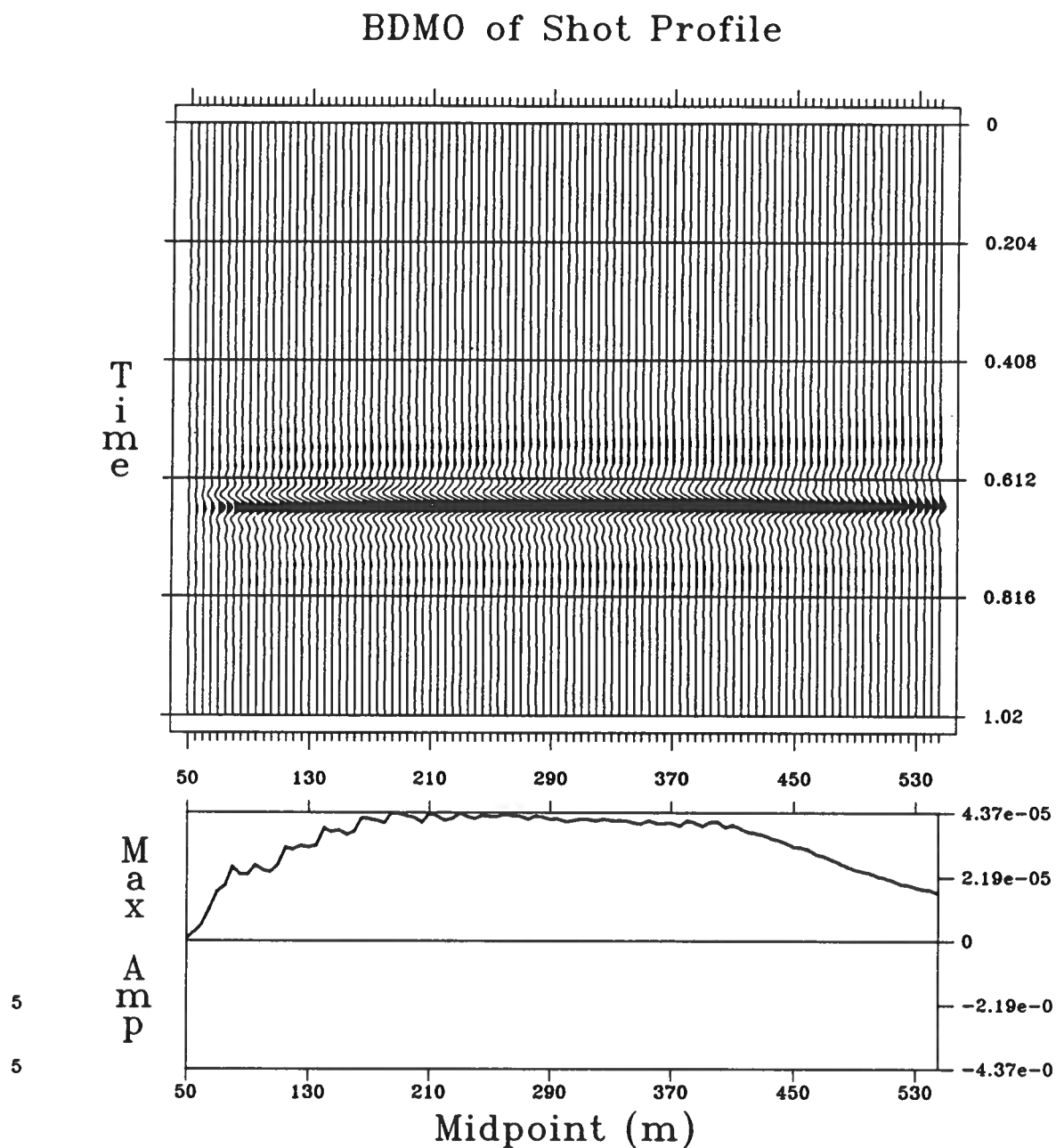


Figure 2.7: Result of processing the data in Figure 2.6 to zero offset using the BDMO common shot algorithm. Away from endpoints, amplitude is constant.



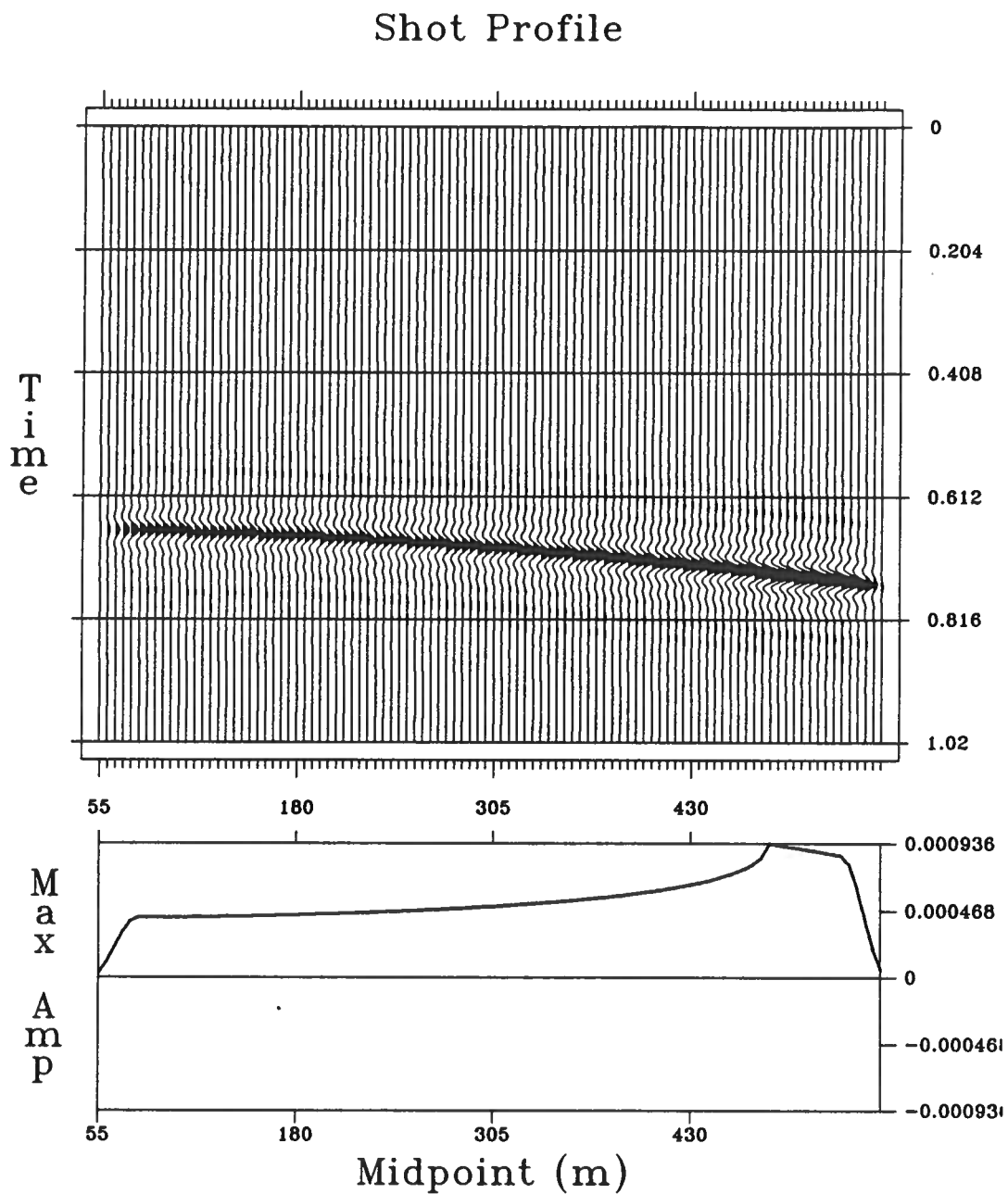


Figure 2.8: Ray theory shot profile for a horizontal plane. The model is that of Figure 2.5 with $v = 7000 \text{ m/s}$ below the interface.



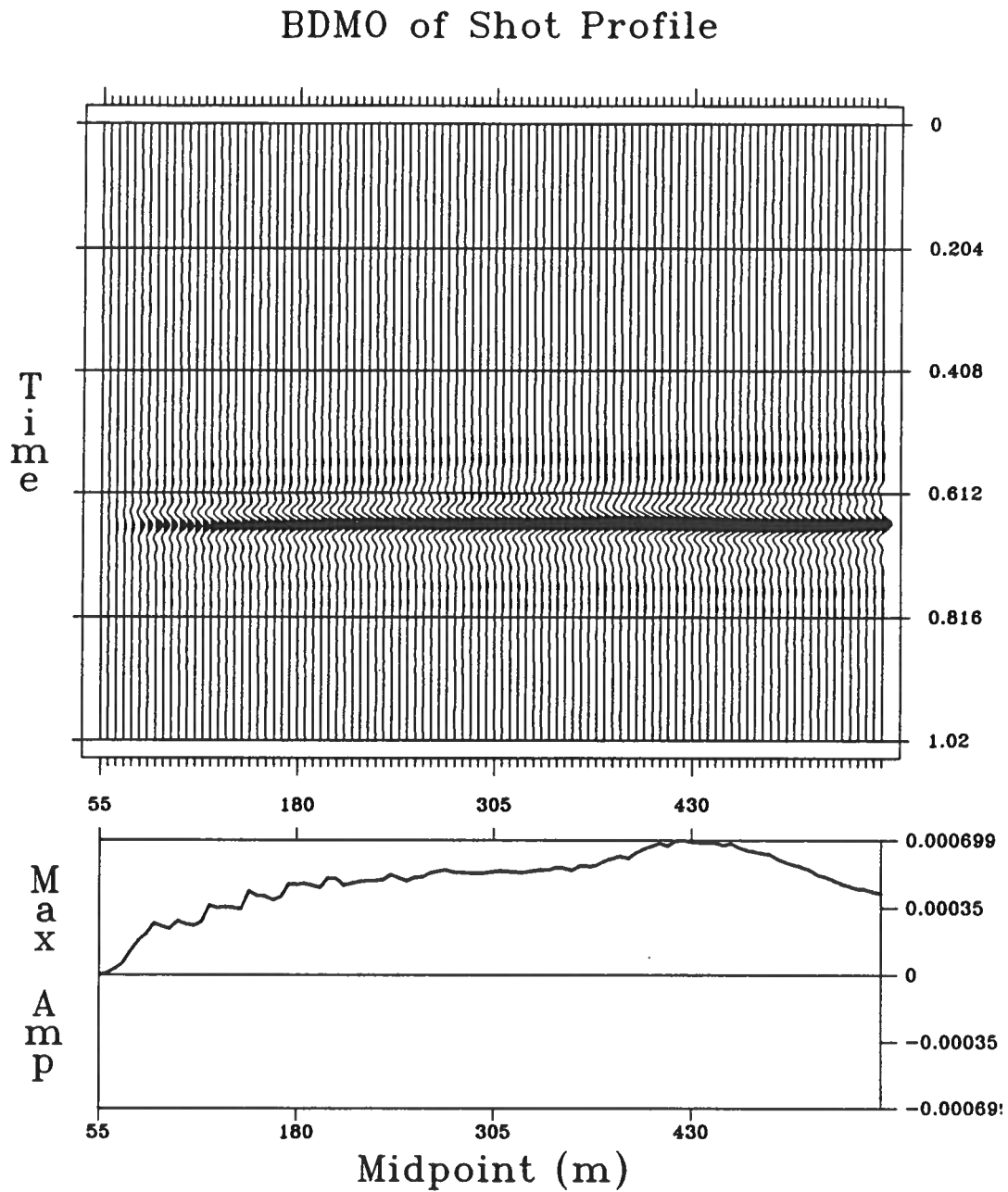


Figure 2.9: BDMO of shot profile data in Figure 2.8. Amplitude Versus Offset (AVO) behavior, due to Angular reflection coefficient $R(\alpha)$, has been preserved.



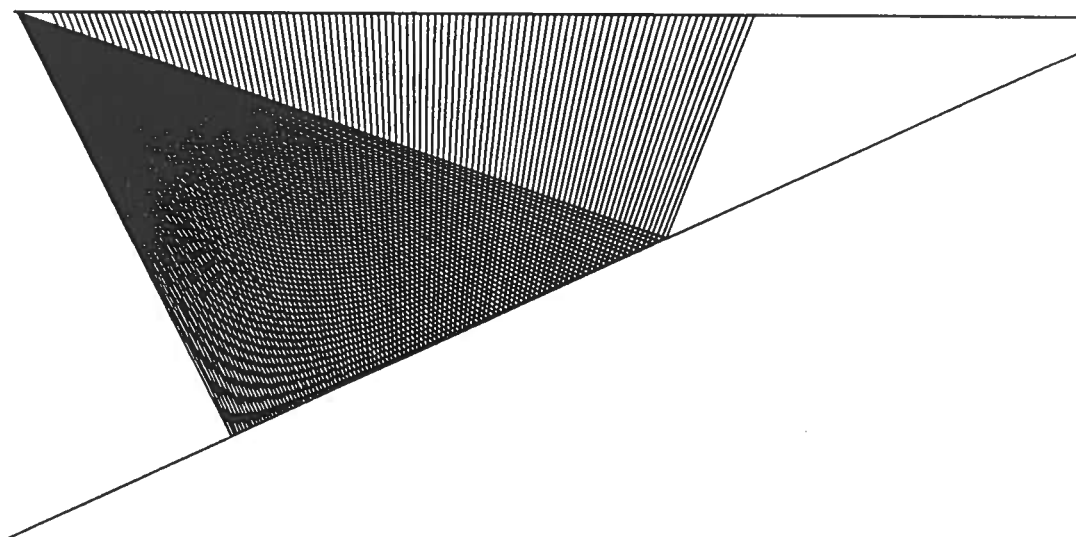


Figure 2.10: Raytrace diagram for dipping plane model.



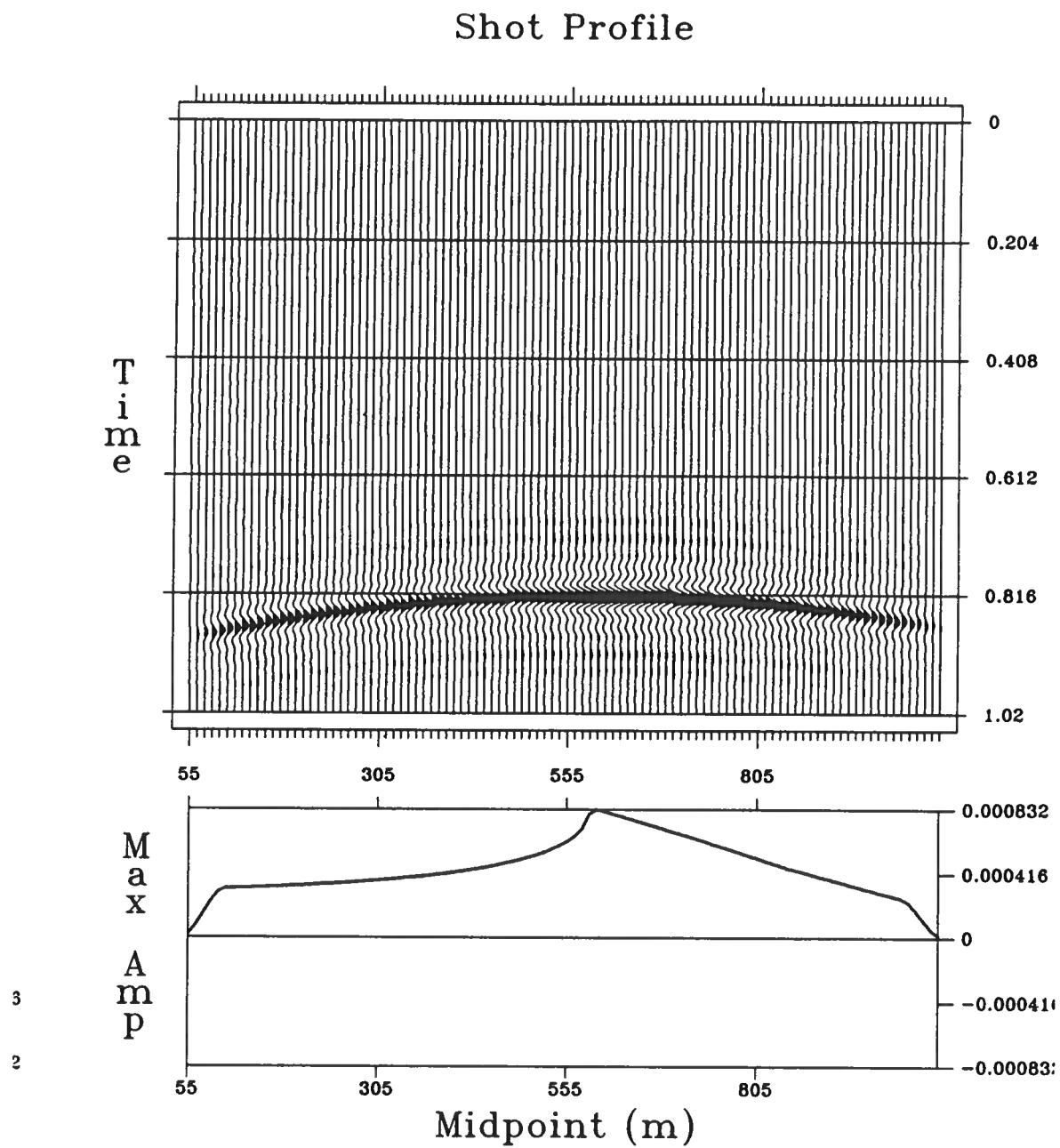


Figure 2.11: Ray theory shot profile data for the dipping plane.



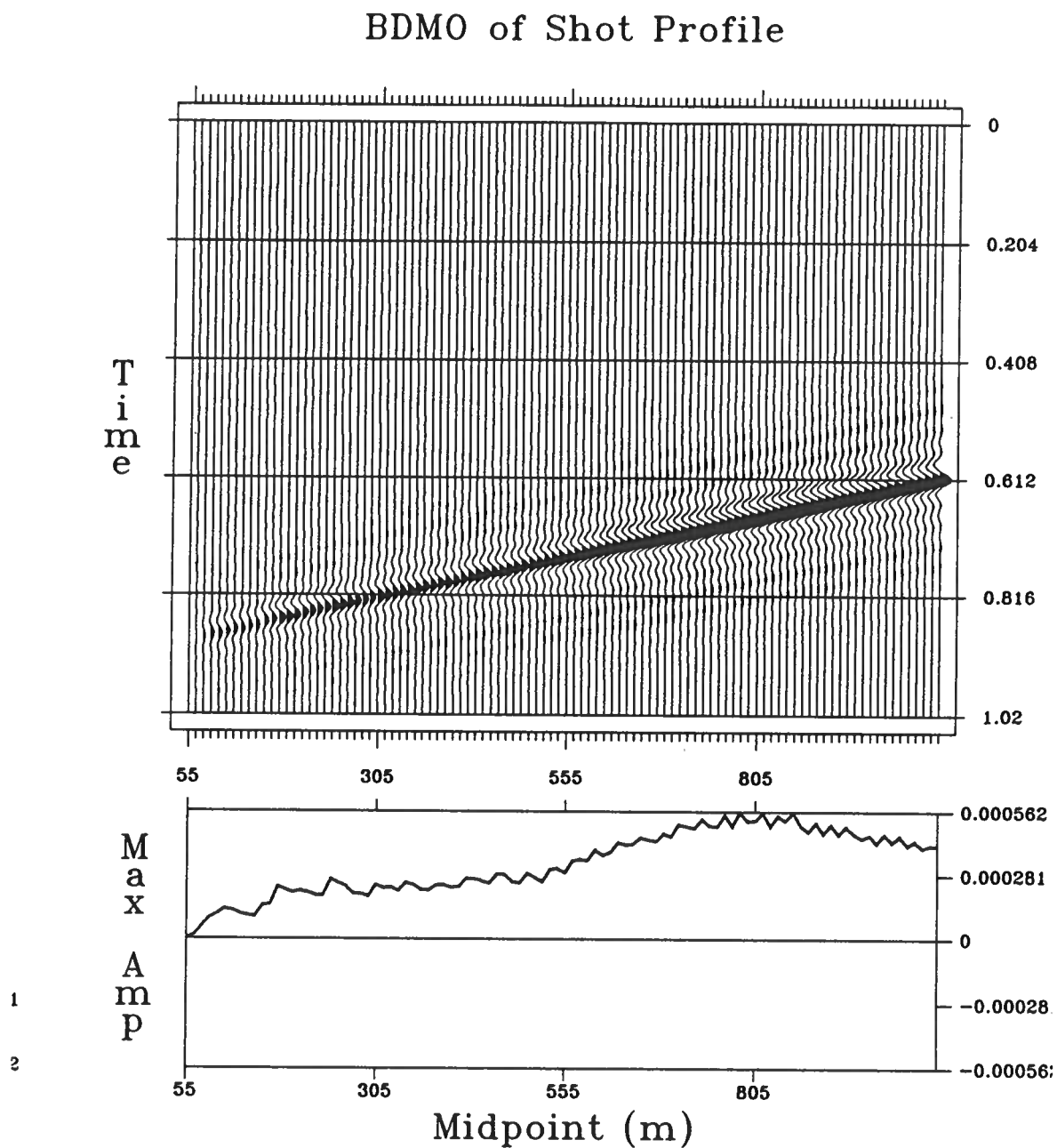


Figure 2.12: BDMO of the dipping plane data in Figure 2.10. This output contains $R(\alpha)$ and zero offset spreading.



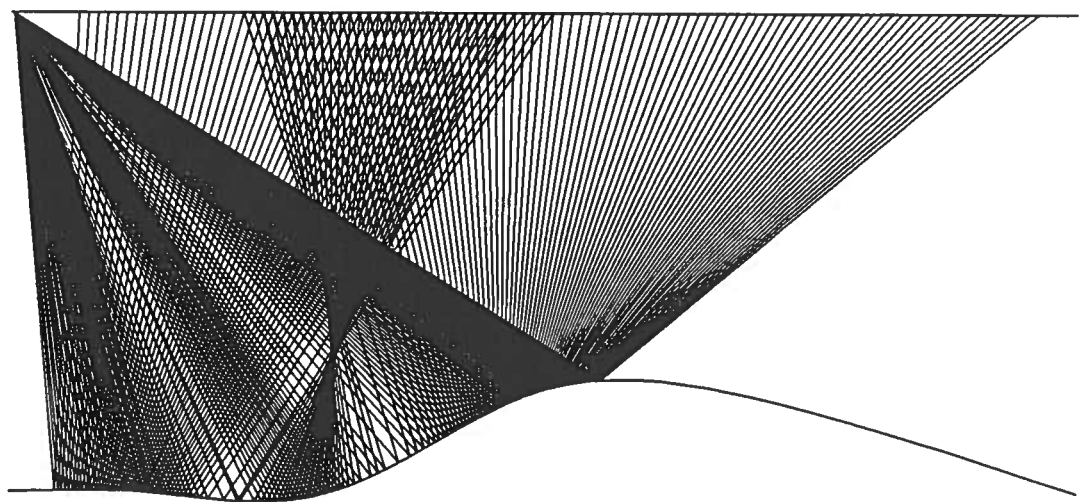


Figure 2.13: Raytrace diagram for curved interface model.



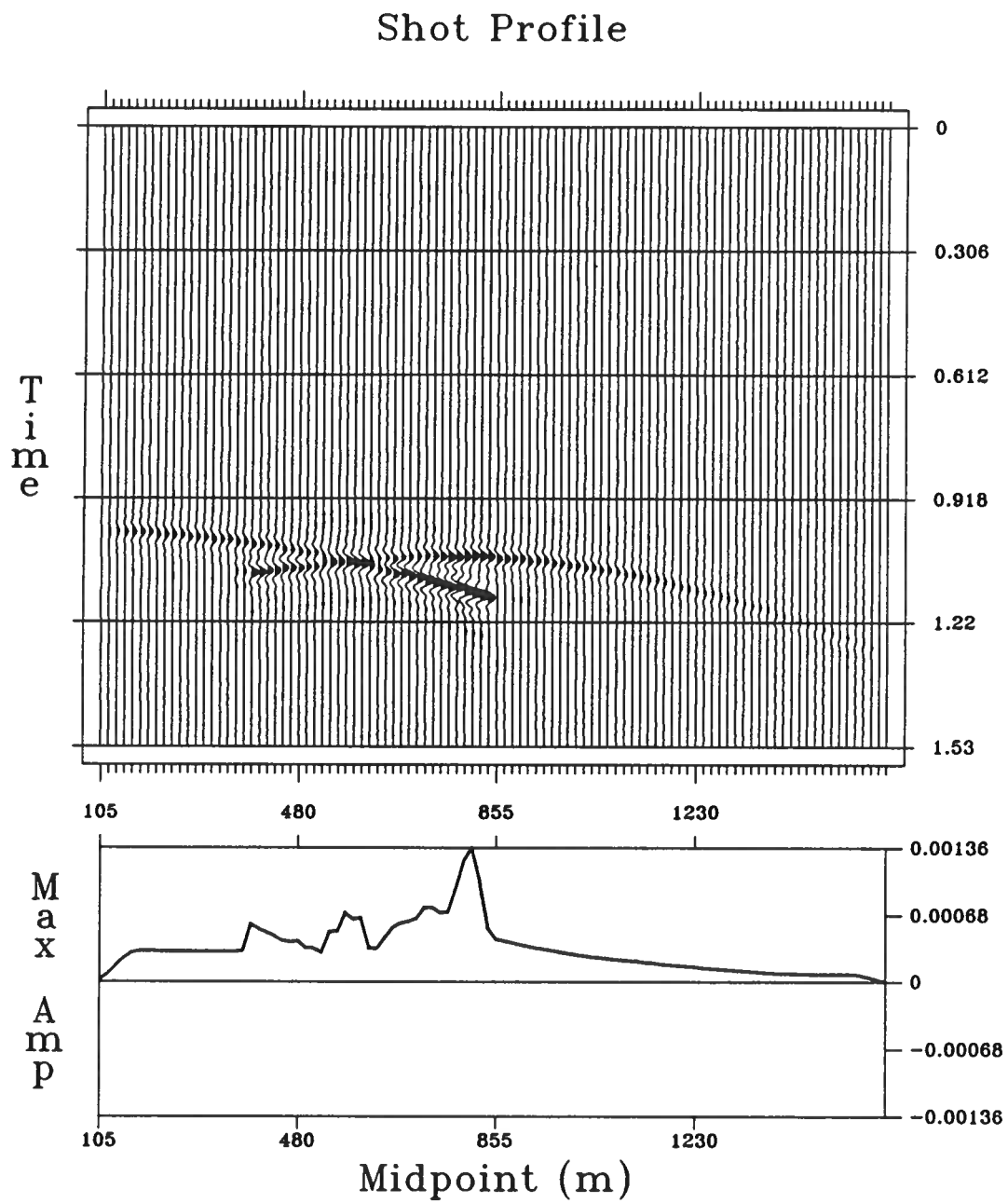


Figure 2.14: Ray theory shot profile data for the curved interface model.



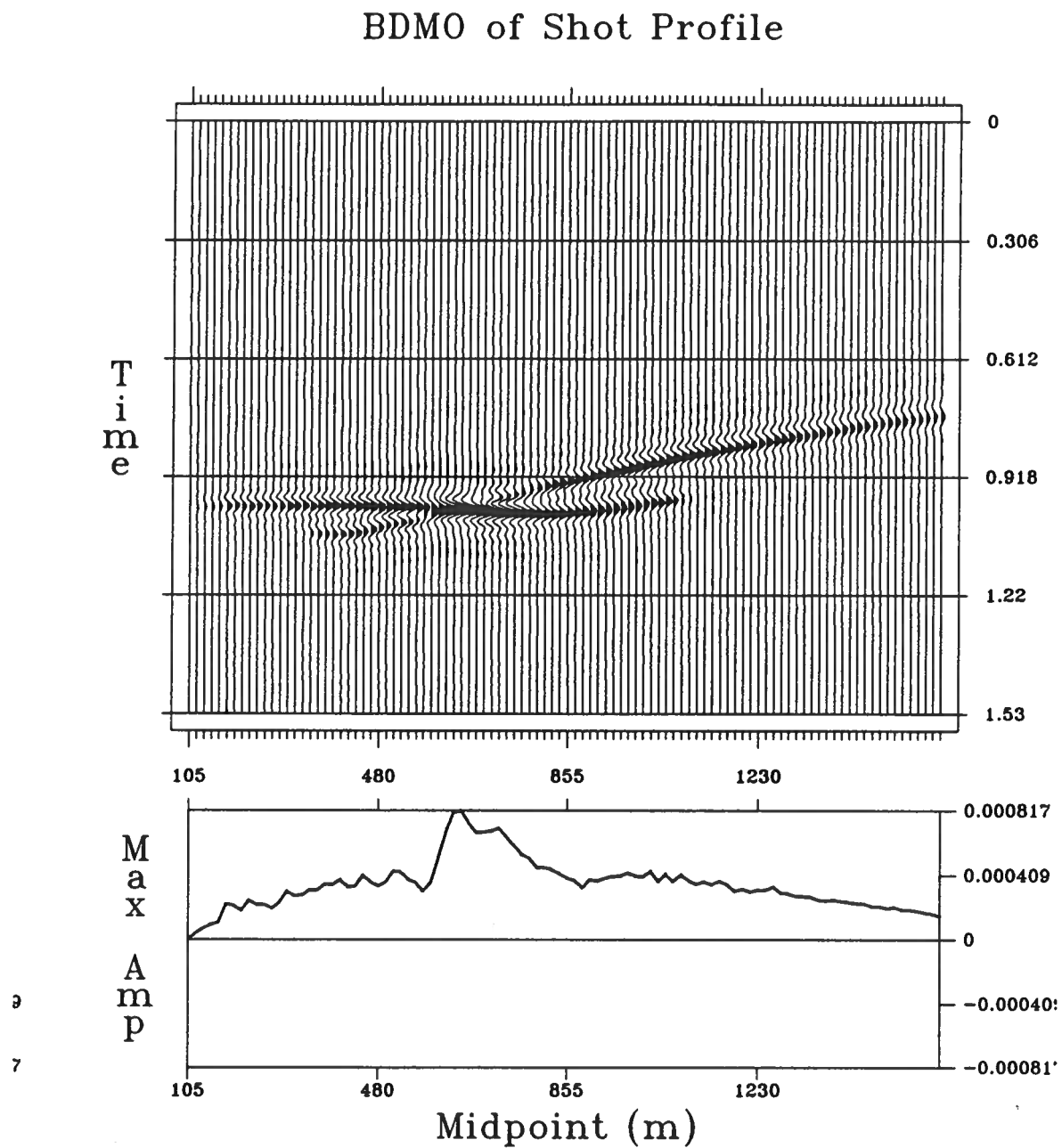


Figure 2.15: BDMO of the curved interface model data in Figure 2.14. Amplitudes are confused by the presence of a zero offset geometrical caustic.



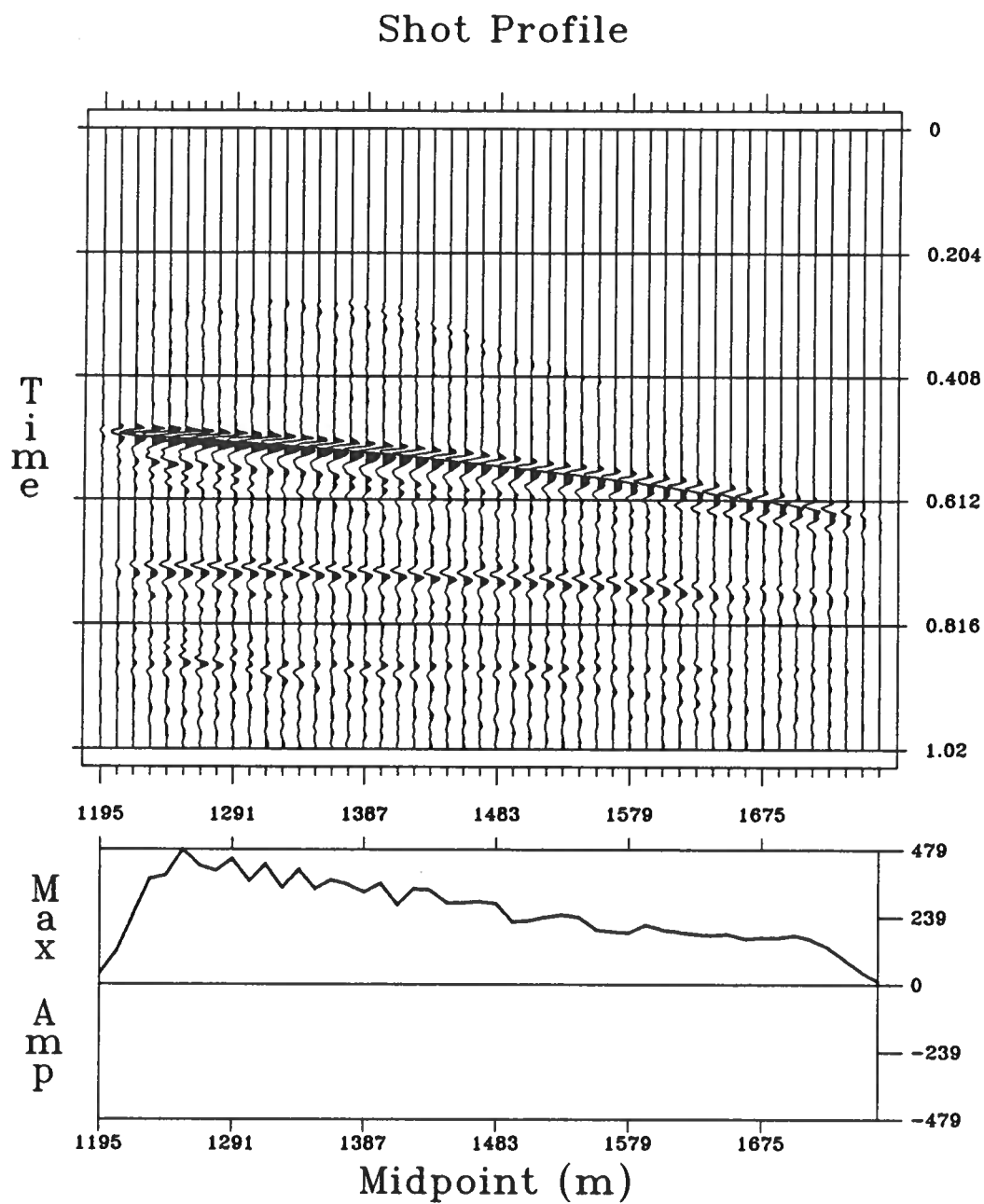


Figure 2.16: One shot profile from physical model experiment. The direct arrival has been muted, but no gain has been applied. Data courtesy of Marathon Oil Company.



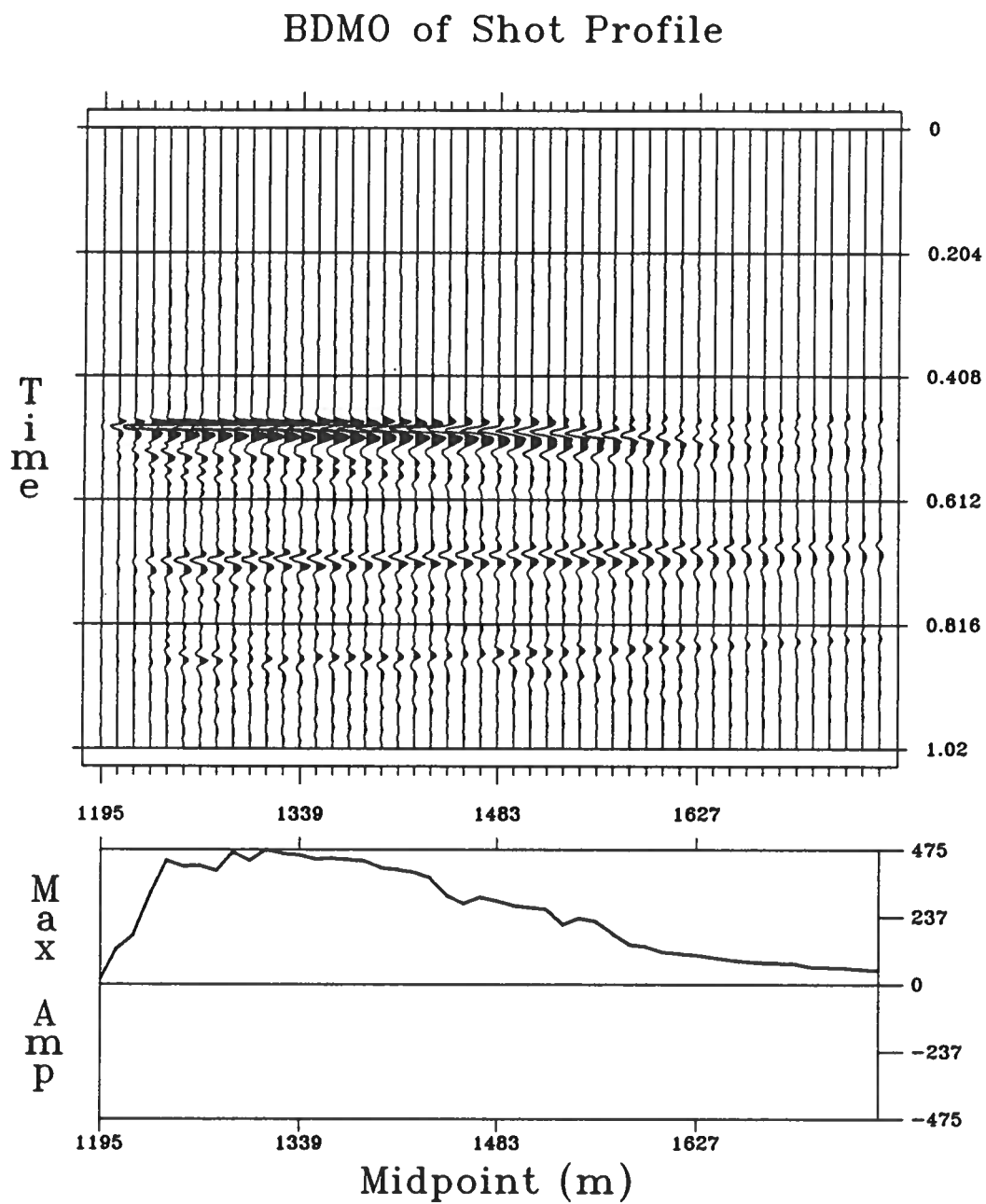


Figure 2.17: Common shot BDMO of the physical model data in Figure 2.16. Zero offset spreading has not been removed. Compare Figure 2.18.



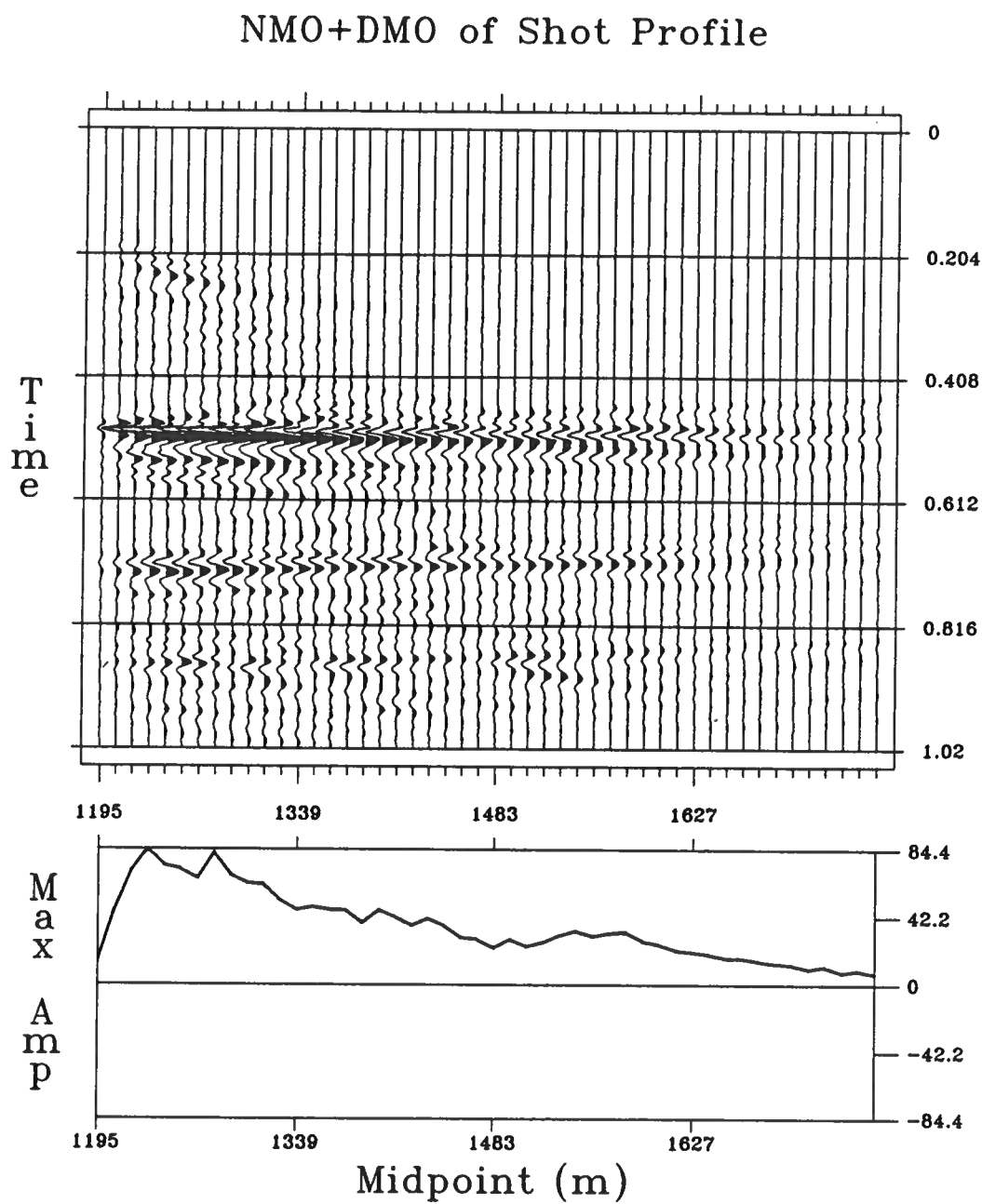


Figure 2.18: Conventional NMO+DMO of the physical model data in Figure 2.16.



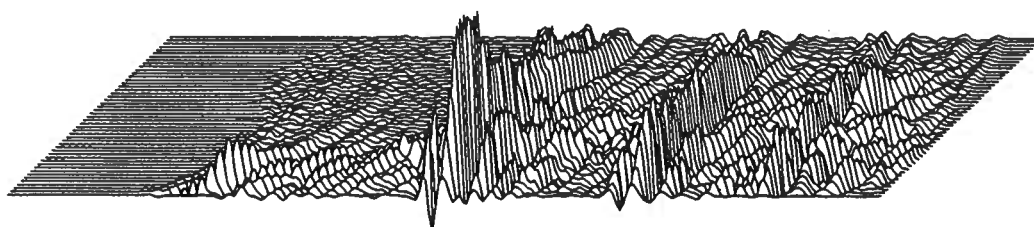
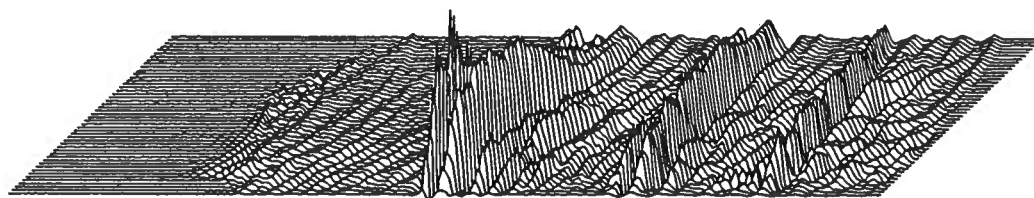


Figure 2.19: Perspective plots of the BDMO result (above) and the conventional NMO+DMO result (below).



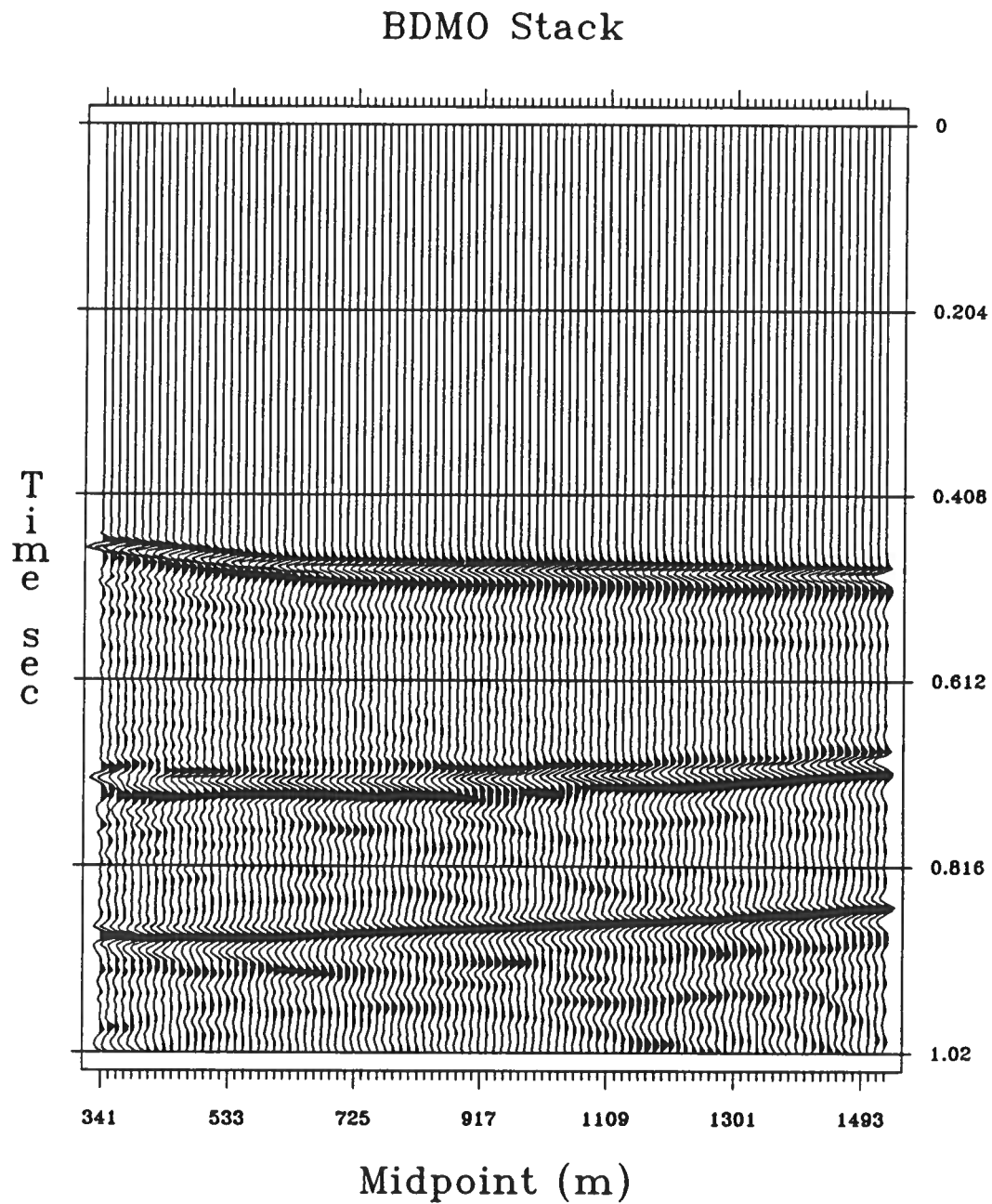


Figure 2.20: BDMO stack of fifty shot profiles from the physical model data set. Long-window ACG has been applied as display gain. Compare Figure 2.21.



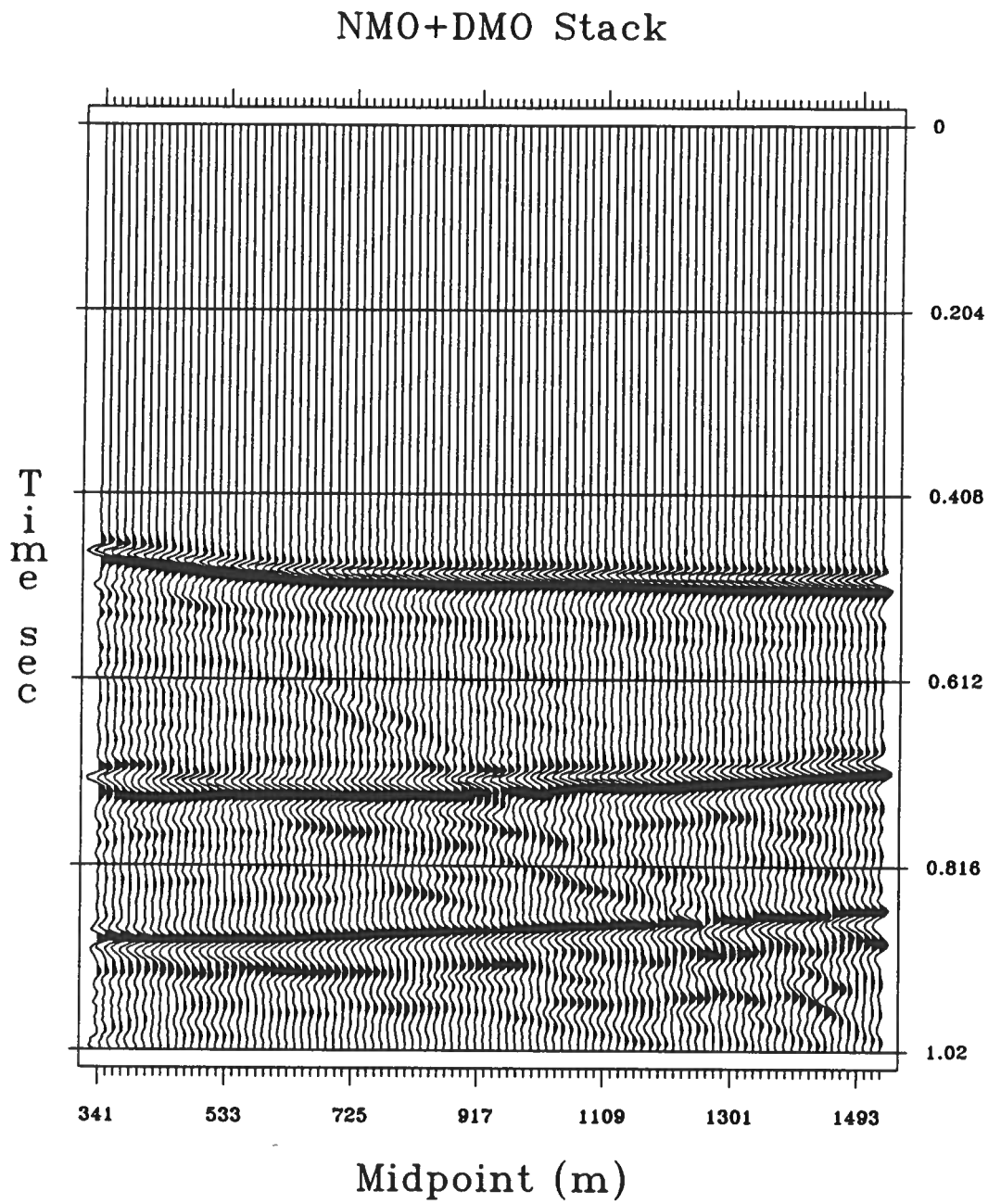


Figure 2.21: Conventional NMO+DMO stack of fifty shot profiles from the physical model data set. Long-window ACG has been applied as display gain.

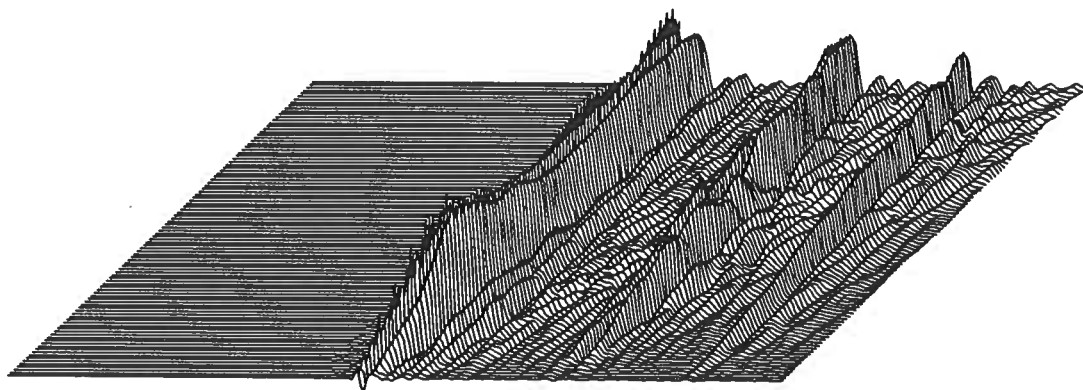


Figure 2.22: Perspective plot of the BDMO stack shown in Figure 2.20.

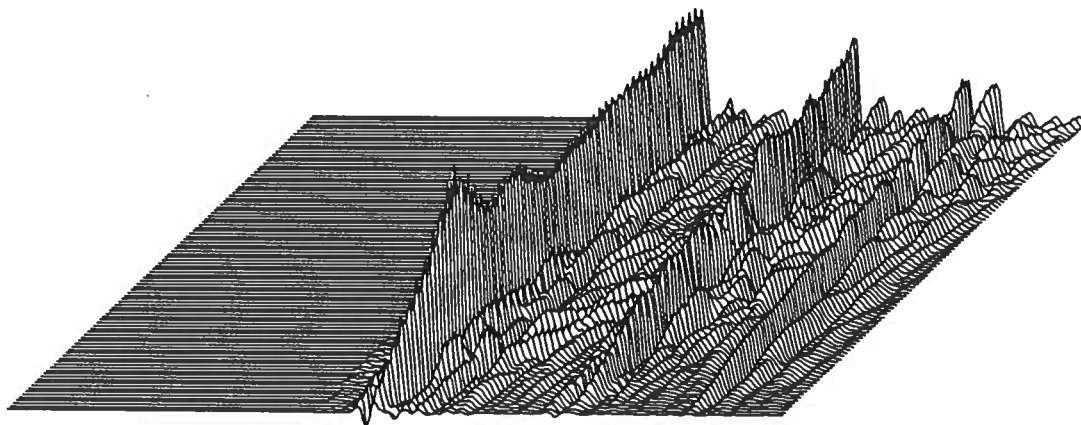


Figure 2.23: Perspective plot of the conventional NMO+DMO stack shown in Figure 2.21.





Excerpts from

**Asymptotic Solutions to
Direct and Inverse Scattering in
Anisotropic Elastic Media**

by

Sebastien Geoltrain

**Partially supported by the Consortium Project
on Seismic Inverse Methods for Complex Structures
at the Center for Wave Phenomena**

**Center for Wave Phenomena
Department of Mathematics
Colorado School of Mines
Golden, Colorado 80401
Phone (303) 273-3557**



III. 2.5D SHOT PROFILE INVERSION

III-1. Inversion of Dip Lines over Cylindrical Models

III-1.1 Introduction

Seismic data is in the majority of cases recorded along lines, that is, a source mechanism (vibrator, explosive, air gun, ...) is activated and the seismic field recorded along a line of receivers, usually aligned with the source. We showed earlier that to image a piece of reflector, one needs to integrate observations collected over a two-dimensional acquisition surface. Therefore it is not surprising if the data gathered by a single receiver line can only reconstruct a curvilinear segment of reflector. However, seismic methods have long been successful in imaging the subsurface from line data. This is probably because sediments often exhibit cylindrical structures, which are completely characterized by their cross-section. Prior knowledge of the structural trend of an area usually allows to position seismic surveys perpendicularly to the structural direction (strike). Processing the data yields a cross-sectional image of the cylindrical reflectors that can be extrapolated by invariance in the strike direction, at least over some distance.

Line recording has obvious economical advantages, on land as well as at sea. On land, a real 3-D survey would for instance involve setting a receiver line, and moving the source perpendicularly to the line, rather than a simple trailing of the receiver line behind the source on a preset and surveyed path. At sea, recording from a large number of parallel streamers would be ideal, but is practically extremely difficult. This is why the cylindrical model is always implicitly used in processing conventional seismic surveys to make for the lack of subsurface coverage inherent to line recording. Moreover, processing under this model is far less costly than full 3-D processing, both computationally and in terms of memory requirements. In inverting for a line of data in the strike direction, it is usually possible to fully account for three-dimensional propagation in the treatment of amplitudes. That treatment is the only one that is truly consistent with the cylindrical model, and is referred to as 2.5-D inversion (Bleistein 1987, Docherty 1987). The images obtained are cross sections of the reflectors in the vertical plane containing the recording line. This, of course, fails to be true if the subsurface geology is not cylindrical or if the line is not perpendicular to the strike.

III-1.2 Inversion Formula

We now assume that the cylindrical model is valid and that a seismic line is recorded perpendicular to the strike of an anisotropic structure (Figure (3.1)). We show that in contrast to the isotropic case, processing with the cylindrical assumption does not in general reduce to a two-dimensional problem, that is, the output (image) is not

located in the vertical plane of the data line. This stems from the peculiar properties of energy propagation in anisotropic media.

We choose the x_2 direction to be along the strike, and parametrize the recording line with the variable ξ_1 , that is:

$$\begin{aligned} \mathbf{x}^s &= (x_1^s, 0, x_3^s) \quad , \\ \mathbf{x}^r &= (x_1^r(\xi_1), 0, x_3^r(\xi_1)) \quad , \end{aligned}$$

where x_1 is the horizontal coordinate along the receiver line and the 2-direction is along strike. We seek an inversion formula in the same form as (2.13), except that the integration over the acquisition surface becomes a simple integral along the receiver line:

$$\beta_2^{NQ}(\mathbf{x}') = \int d\omega \int d\xi_1 \left\{ u_m(\mathbf{x}^r, \mathbf{x}^s, \omega) I_m^{NQ}(\mathbf{x}', \mathbf{x}^r, \mathbf{x}^s) A_2^{NQ}(\mathbf{x}', \mathbf{x}^r, \mathbf{x}^s, \omega) \right\} e^{-i\omega [\tau_N(\mathbf{x}', \mathbf{x}^s) + \tau_Q(\mathbf{x}', \mathbf{x}^r)]} \quad , \quad (3.1)$$

where A_2^{NQ} is the 2.5-D amplitude coefficient that must make the peak value of β_2^{NQ} equal to the specular reflection coefficient times the area under the source spectrum. Proceeding as in (2.15), we substitute the matching mode of the Kirchhoff representation into (3.1) to get:

$$\begin{aligned} \beta_2^{NQ}(\mathbf{x}') &= \int d\omega i\omega S(\omega) \int d\xi_1 \int d\eta_1 dx_2 \left\{ \sqrt{|g_\eta|} u^N(\mathbf{x}, \mathbf{x}^s) R_{NQ}(\mathbf{x}, \mathbf{x}^s) \right. \\ &\quad \left. I_m^{NQ}(\mathbf{x}, \mathbf{x}^r, \mathbf{x}^s) I_m^{NQ}(\mathbf{x}', \mathbf{x}^r, \mathbf{x}^s) A_2^{NQ}(\mathbf{x}', \mathbf{x}^r, \mathbf{x}^s, \omega) \right\} e^{i\omega \Phi_{NQ}(\mathbf{x}, \mathbf{x}', \mathbf{x}^r, \mathbf{x}^s)} \quad , \quad (3.2) \end{aligned}$$

where

$$\begin{aligned} \Phi_{NQ}(\mathbf{x}, \mathbf{x}', \mathbf{x}^r, \mathbf{x}^s) &= \tau^N(\mathbf{x}, \mathbf{x}^s) + \tau^N(\mathbf{x}, \mathbf{x}^r) - \tau^Q(\mathbf{x}', \mathbf{x}^s) - \tau^Q(\mathbf{x}', \mathbf{x}^r) \quad , \\ \mathbf{x} &= (x_1(\eta_1), x_2, x_3(\eta_1)) \quad , \end{aligned}$$

$$\sqrt{|g_\eta|} = \left| \frac{\partial x}{\partial \eta_1} \right| .$$

Note that the cylindrical reflector is parametrized by η_1 and the *strike variable* x_2 . As before, we evaluate (3.2) by the method of stationary phase; the stationarity conditions are the same as (2.19) and (2.20), and can be specialized to our particular case to yield:

$$p_2^N(x, x^s) + p_2^Q(x, x^r) = 0 \quad , \quad (3.3)$$

$$\left[p^N(x, x^s) + p^Q(x, x^r) \right] \cdot \frac{\partial x}{\partial \eta_1} = 0 \quad , \quad (3.4)$$

and

$$\left[p^N(x, x^r) - p^N(x', x^r) \right] \cdot \frac{\partial x^r}{\partial \xi_1} = 0 \quad . \quad (3.5)$$

Once again, the stationary points are specular points on the reflector and (3.2) asymptotically reduces to:

$$\beta_2^{NQ}(x') \sim (2\pi)^{3/2} \int d\omega i\omega S(\omega) \left| \frac{\partial x}{\partial \eta_1} \right| \left\{ \frac{u^N(x, x^s) R_{NQ}^{spec}(x, x^s) I_m^{NQ}(x, x^r, x^s)}{|\omega|^{3/2}} \right. \\ \left. \frac{I_m^{NQ}(x', x^r, x^s) A_2^{NQ}(x', x^r, x^s, \omega)}{\sqrt{|H_{NQ}(x, x', x^r, x^s)|}} \right\} e^{i\omega\Phi(x, x', x^r, x^s) + i\frac{\pi}{4} \text{sgn}(\omega) \text{sig} H_{NQ}} ,$$

where H_{NQ} is now the 3×3 Hessian of the phase:

$$H_{NQ}(x, x', x^r, x^s) = \begin{bmatrix} \frac{\partial^2 \Phi^{NQ}}{\partial \xi_1^2} & \frac{\partial^2 \Phi^{NQ}}{\partial \eta_1 \partial \xi_1} & \frac{\partial^2 \Phi^{NQ}}{\partial x_2 \partial \xi_1} \\ \frac{\partial^2 \Phi^{NQ}}{\partial \xi_1 \partial \eta_1} & \frac{\partial^2 \Phi^{NQ}}{\partial^2 \eta_1} & \frac{\partial^2 \Phi^{NQ}}{\partial x_2 \partial \eta_1} \\ \frac{\partial^2 \Phi^{NQ}}{\partial \xi_1 \partial x_2} & \frac{\partial^2 \Phi^{NQ}}{\partial \eta_1 \partial x_2} & \frac{\partial^2 \Phi^{NQ}}{\partial^2 x_2} \end{bmatrix} .$$

In this form, H_{NQ} is not easily computable; however, using the stationarity conditions, and after some algebra, we can rewrite its determinant as follows,

$$|H_{NQ}(\mathbf{x}, \mathbf{x}', \mathbf{x}^r, \mathbf{x}^s)| = \left| \frac{\partial \mathbf{x}}{\partial \eta_1} \right|^2 |D_{NQ}(\mathbf{x}, \mathbf{x}', \mathbf{x}^r, \mathbf{x}^s)| \quad ,$$

where

$$|D_{NQ}(\mathbf{x}, \mathbf{x}', \mathbf{x}^r, \mathbf{x}^s)| = \begin{vmatrix} 0 & \frac{\partial P^{NQ}}{\partial \xi_1} \cdot t_1 & \frac{\partial P^{NQ}}{\partial \xi_1} \cdot t_2 \\ \frac{\partial P^{NQ}}{\partial \xi_1} \cdot t_1 & \left[\nabla_z P^{NQ} \cdot t_1 \right] \cdot t_1 & \left[\nabla_z P^{NQ} \cdot t_2 \right] \cdot t_1 \\ \frac{\partial P^{NQ}}{\partial \xi_1} \cdot t_2 & \left[\nabla_z P^{NQ} \cdot t_2 \right] \cdot t_1 & \left[\nabla_z P^{NQ} \cdot t_2 \right] \cdot t_2 \end{vmatrix} \quad , \quad (3.6)$$

$$P^{NQ}(\mathbf{x}, \mathbf{x}', \mathbf{x}^s) = p^N(\mathbf{x}, \mathbf{x}^s) + p^Q(\mathbf{x}, \mathbf{x}') \quad ,$$

$$t_1 = \frac{(P_3^{NQ}, 0, -P_1^{NQ})}{|P^{NQ}|} \quad ,$$

and

$$t_2 = (0, 1, 0) \quad .$$

On the other hand, the signature of the Hessian can only assume the following values:

$$\text{sig} H_{NQ} = \pm 1, \pm 3 \quad ,$$

Consequently, within a constant, we can determine A_2^{NQ} in the same way as before:

$$A_2^{NQ}(\mathbf{x}', \mathbf{x}^r, \mathbf{x}^s) = \frac{\sqrt{i\omega} \sqrt{|D_{NQ}(\mathbf{x}', \mathbf{x}', \mathbf{x}^r, \mathbf{x}^s)|}}{(2\pi)^{5/2} \left[I^{NQ}(\mathbf{x}', \mathbf{x}^r, \mathbf{x}^s) \right]^2 u^N(\mathbf{x}', \mathbf{x}^s)} \quad ,$$

so that the output becomes:

$$\beta_2^{NQ}(\mathbf{x}') = \frac{1}{2\pi} \int d\omega S(\omega) R_{NQ}^{spec}(\mathbf{x}, \mathbf{x}^s) e^{i\omega \Phi^{NQ}(\mathbf{x}, \mathbf{x}', \mathbf{x}^r, \mathbf{x}^s)} \quad ,$$

and its peak value, reached at $\mathbf{x}' = \mathbf{x}$, is:

$$\left[\beta_2^{NQ}(\mathbf{x}') \right]^{peak} = R_{NQ}^{spec} \cdot \frac{\int d\omega S(\omega)}{2\pi}$$

Substituting for A_2^{NQ} into (3.1), we finally obtain the 2.5-D common-shot inversion formula:

$$\beta_2^{NQ}(\mathbf{x}') = \frac{1}{(2\pi)^{5/2}} \int d\omega \sqrt{i\omega} \int d\xi_1 \left\{ u_m(\mathbf{x}^r, \mathbf{x}^s, \omega) I_m^{NQ}(\mathbf{x}', \mathbf{x}^r, \mathbf{x}^s) \right. \\ \left. \frac{\sqrt{|D_{NQ}(\mathbf{x}, \mathbf{x}', \mathbf{x}^r, \mathbf{x}^s)|}}{\left[I^{NQ}(\mathbf{x}', \mathbf{x}^r, \mathbf{x}^s) \right]^2 u^N(\mathbf{x}', \mathbf{x}^s)} \right\} e^{-i\omega [\tau_N(\mathbf{x}', \mathbf{x}^s) + \tau_Q(\mathbf{x}', \mathbf{x}^r)]}.$$

III-1.3 Discussion

As in the 3-D case, it is still possible to rewrite the inversion operator in the time domain. However, this requires a preprocessing of the data that is not as simple as a time derivative anymore. Instead, one has to take a *half derivative* of the signal, that is, multiply the data by $\sqrt{i\omega}$ in the frequency domain. This operation is a separate processing step to be applied to the data before the inversion itself. The expression for the preprocessed input $\hat{U}_m(\mathbf{x}^r, \mathbf{x}^s, t)$ is as follows

$$\hat{U}_m(\mathbf{x}^r, \mathbf{x}^s, t) = \frac{1}{2\pi} \int d\omega \sqrt{i\omega} e^{-i\omega t} \int dt' U_m(\mathbf{x}^r, \mathbf{x}^s, t') e^{i\omega t'},$$

where U_m is, once again, the raw data. With this definition, the time domain inversion operator is

$$\beta_2^{NQ}(\mathbf{x}') = \frac{1}{(2\pi)^{3/2}} \int d\xi_1 \left\{ \hat{U}_m \left[\mathbf{x}^r, \mathbf{x}^s, \tau_N(\mathbf{x}', \mathbf{x}^s) + \tau_Q(\mathbf{x}', \mathbf{x}^r) \right] I_m^{NQ}(\mathbf{x}', \mathbf{x}^r, \mathbf{x}^s) \right. \\ \left. \frac{\sqrt{|D_{NQ}(\mathbf{x}, \mathbf{x}', \mathbf{x}^r, \mathbf{x}^s)|}}{\left[I^{NQ}(\mathbf{x}', \mathbf{x}^r, \mathbf{x}^s) \right]^2 u^N(\mathbf{x}', \mathbf{x}^s)} \right\}.$$

This expression does not significantly differ from the full 3-D formula, and indeed except for the absence of the ξ_2 integral, this inversion usually requires three-dimensional ray tracing. This is because the stationary points for a common shot experiment perpendicular to the strike are usually not located in the *dip plane* (i.e. the vertical plane containing the receiver line). This is well illustrated by the example raypath perspective plot of Figure (1.17). As a consequence, the output β_2^{NQ} must be computed on a complete 3-D mesh. The determinant $|D_{NQ}|$ now involves derivatives of the slowness vector P^{NQ} both with respect to the receiver location and the output point.

This complication occurs whenever the symmetry of the anisotropy does not match that of the cylindrical model. In those cases, the cost of inversion is in many respects comparable to that of a 3-D inversion; the 3-D segment of reflector imaged in this manner can be projected on the $x'_2 = 0$ plane to get the desired cross-sectional image of the reflector, and parameter estimation can be carried out as previously described.

However, for isotropic media or anisotropic media that possess the cylindrical symmetry of the model, energy propagation remains within the dip plane and inversion reduces to a much simpler two-dimensional process. This is described in Docherty 1987 for the acoustic case, and Sumner 1988 for the isotropic elastic case. Next we extend their approach to the case of transversely isotropic media with a symmetry axis in the dip plane.

III-2. 2.5-D fractured media

III-2.1 Introduction

The two-and-one-half dimensional fractured model is designed to represent cylindrical media that are fractured along the strike direction. Considering that the regional stresses are usually aligned along the axis of existing geological structures, this model is probably representative of many real situations. On the other hand, this model can be rightfully used whenever a single line of multi-component data is acquired and that a polarization analysis of the shear waves reveals that the recording line is along a principal axis of anisotropy. For our purpose, the 2.5-D fractured medium is a superposition of cylindrical transversely isotropic layers with their anisotropy axis within the dip plane. This means in practice that the various layers may be fractured in different directions, insofar as the fracture planes always contain the strike axis.

In that case, the propagation of energy remains in the dip plane, although ray direction (i.e. that of group velocity) and slowness direction (i.e. that of phase velocity) remain distinct. This is easily verified by studying the expression of group velocity for each mode given in equations (1.43); all three expressions are in the form:

$$W = w_a p_a + w_r p_r \quad ,$$

where p_a and p_r are the axial and radial vector components of the slowness p , that is:

$$p = p_a + p_r \quad p_r \cdot a = 0 \quad ,$$

where a is the anisotropy axis which, according to our assumption and the strike axis being x_2 , may be written as:

$$a = (a_1, 0, a_3) \quad .$$

Alternatively, group velocity can be decomposed as:

$$W = W_{1,3} + W_2 \quad ,$$

where $W_{1,3}$ and W_2 are respectively the *in-plane* and *out-of-plane* vector components of group velocity:

$$W_2 = w_r p_2 x_2 \quad W_{1,3} = W - W_2 \quad . \quad (3.7)$$

Now consider shooting a ray from the source with an in-plane slowness (i.e $p_2 = 0$); according to Snell's law and the cylindrical nature of the model, the slowness must remain in-plane because p_2 is continuous across reflectors, that is:

$$p_2 = 0 \quad \text{along the ray} \quad .$$

Therefore, according to (3.7), we have:

$$W_2 = 0 \quad \text{along the ray} \quad ,$$

which means that rays that start in-plane remain in-plane.

III-2.2 Forward Problem

As we just showed, the kinematics of a shot-profile across the strike are confined to the dip plane. On the other hand, a proper handling of amplitudes in the forward problem requires to evaluate scattering at interfaces as well as geometric spreading. Interface scattering may be treated as described in Chapter I, but there is an additional simplification owing to the complete decoupling of the *SP* mode on one hand, and the

QP and QS modes on the other hand, in the case of in-plane propagation. To be more specific, there is no conversion of energy between SP and QP / QS modes at interfaces; the SP displacement is polarized exclusively in the strike direction, and in that sense is an SH mode, while QP and QS waves are polarized in the dip plane. In that situation, scattering breaks into two simpler parts: scalar scattering for the SP wave, and 2-D in-plane vector scattering for QP / QS waves.

There remains to compute the geometric spreading along rays. Here again, the problem can be decomposed into in-plane and out-of-plane spreading; the in-plane part may be computed as usual from neighboring in-plane rays and, fortunately, the out-of-plane part can be explicitly expressed from in-plane kinematic parameters, as we show below.

Let us recall the expression of the ray Jacobian:

$$J(\tau, \gamma_1, \gamma_2) = W \cdot \left[\frac{\partial \mathbf{x}}{\partial \gamma_1} \times \frac{\partial \mathbf{x}}{\partial \gamma_2} \right] .$$

For convenience, we take $\gamma_2 = p_2$ as the out-of-plane ray parameter, so that $\partial \mathbf{x} / \partial \gamma_1$ and $\partial \mathbf{x} / \partial \gamma_2$ are orthogonal, and J can be rewritten as:

$$J(\tau, \gamma_1, p_2) = J(\tau, \gamma_1, 0) \left| \frac{\partial \mathbf{x}_2}{\partial p_2} \right| ,$$

where $J(\tau, \gamma_1, 0)$ is the 2-D in-plane Jacobian:

$$J(\tau, \gamma_1, 0) = \left| W(\tau, \gamma_1, 0) \times \frac{\partial \mathbf{x}}{\partial \gamma_1} \right| ,$$

which is computed from in-plane kinematic parameters only. On the other hand, the out-of-plane coordinate of a ray after passing through the i^{th} layer is:

$$(x_2)_{i+1} = (x_2)_i + (W_2)_{i+1} (\tau_{i+1} - \tau_i) , \quad (3.8)$$

where $(\tau_{i+1} - \tau_i)$ is the traveltimes in the i^{th} layer and $(x_2)_i$ the out-of-plane coordinate of the ray upon entering that layer.

Now we introduce the out-of-plane component of slowness for the ray, p_2 , which according to Snell's law is identical in all layers, and rewrite (3.8) as follows:

$$(x_2)_{i+1} = (x_2)_i + (w_r)_{i+1} p_2 (\tau_{i+1} - \tau_i) \quad i = 0, \dots, n$$

By adding all these identities together, we obtain:

$$(x_2)_n - (x_2)_0 = p_2 \sum_i (w_r)_{i+1} (\tau_{i+1} - \tau_i) \quad .$$

Taking the limit of vanishing p_2 , we get a closed form expression for the out-of-plane spreading at the n^{th} interface:

$$\left(\frac{\partial x_2}{\partial p_2} \right)_n = \lim_{p_2 \rightarrow 0} \frac{(x_2)_n - (x_2)_0}{p_2} = \sum_i (w_r)_{i+1} (\tau_{i+1} - \tau_i) \quad , \quad (3.9)$$

where τ and w_r are now evaluated in the dip plane, that is, (3.9) provides the means of evaluating a full three-dimensional spreading from in-plane ray parameters only.

III-2.3 Inverse Problem

The inverse problem is also subject to significant simplifications in 2.5-D fractured media. First of all, the stationary points in the inversion formula are all located in the dip plane $x'_2 = 0$, so that we need only compute the output β_2^{NQ} on a two-dimensional grid. The image so obtained is a cross-section of the cylindrical reflector on which the processing is targeted.

The next simplification occurs in the determinant $|D_{NQ}|$ of (3.6); in effect, the geometry of the propagation and to the common shot configuration allow us to write the following identities:

$$\begin{aligned} \frac{\partial P^{NQ}}{\partial \xi_1} \cdot t_1 &= 0 \quad , \quad \left(\nabla_z P^{NQ} \cdot t_2 \right) \cdot t_2 = 0 \quad , \\ \left(\nabla_z P^{NQ} \cdot t_2 \right) \cdot t_2 &= \frac{\partial P_2^{NQ}}{\partial x_2} \quad \text{and} \quad \frac{\partial P^{NQ}}{\partial \xi_1} = \frac{\partial p^Q}{\partial \xi_1} \quad , \end{aligned}$$

so that $|D_{NQ}|$ simply reduces to:

$$|D_{NQ}| = \left| \frac{\partial p^Q}{\partial \xi_1} \cdot t_1 \right|^2 \left| \frac{\partial P_2^{NQ}}{\partial x_2} \right| \quad .$$

The first factor only involves in-plane parameters; we show next that the second one can be computed without out-of-plane ray tracing as well. For this, we recall that P_2 is just a sum of slownesses at the output point:

III-3.2 Imaging Curved Reflectors

Although our computer implementation allows for stratified backgrounds only, this does not exclude inverting for a curved reflector insofar as it is overlaid by a tabular sequence. To prove our point, we consider such a model and generate nine shot profiles using an acoustic ray-tracing program. The model comprises two flat reflectors on top of a curved reflector which constitutes the target to be imaged. The velocities increase from 3000m/s in the upper layer, to 6000m/s in the lower layer. The depth of the first and second reflectors are 500m and 1500m respectively, and the average depth to the curved reflector is 2500m. Each shot profile includes 41 split-spread receivers spaced 20m. The move-up between shots is 500m. Figure (3.8) shows the geometry of the model as well as the ray diagram for all nine shots (only 40% of the rays are plotted for clarity). Figure (3.9) shows all nine shot records from left to right; for the purpose of display, only one out of four traces is plotted.

To invert this data, we use isotropic elastic layers with shear velocities matching those of the acoustic model. We then simulate acoustic waves using *SH* waves, which are also scalar waves in 2.5D media. All shot records are inverted separately, and then stacked together to produce the final image (Figure (3.10)). Comparing Figures (3.8) and (3.10), which are plotted to the same scale, we conclude that the reflector has been accurately imaged everywhere but in the two regions not illuminated by any shot profile. In order to image these areas as well, one would need to extend the survey to the sides of the model.

III-3.3 Imaging Weak Reflectors

So far we have discussed examples where the input data is generated from a single reflector with a single wavetype. These are not necessarily realistic conditions, and we now examine a rather pathological model, where the signal of the target reflector is weak and superposed to that of other, stronger reflectors. Figure (3.11) describes the model in question. A vertically polarized source is placed at the surface, and all 64 primary reflections are traced to a set of 100 split-spread receivers. Figure (3.12) shows the corresponding shot records for the horizontal (in-line) and vertical components of displacement. The three events that dominate those records are all generated by the first reflector; from fastest to slowest, these events are $P-P$, $P-SV$, and $SV-SV$. After Automatic Gain Control (*AGC*) is applied (Figure (3.13)), other events become visible. In particular, the $P-P-QP-QP-P-P$ event from the target reflector is visible on the vertical component at about 1.5s zero offset arrival time.

Figure (3.14) shows a direct inversion of the data using the correct background velocities. Although the reflector is imaged at the correct depth of 2000m, there is an unacceptable level of artifacts in the image. Those spurious effects are due to the interference of strong events during the inversion. Actually, the "noise" at large offsets comes from the $SV-SV$ event. In effect, for an output point on the boundary of the survey, the sum of traveltimes to the source and to the farthest receiver becomes

comparable to the actual $SV-SV$ traveltimes at that receiver. Although the receiver integration tends to cancel such contributions, the spatial aliasing of the $SV-SV$ event and its relative strength with respect to the target event result in large artifacts. The "smile" above the reflector is, on the other hand, typical of an "overmigrated" event. The event in question is the strong $P-SV$ converted arrival clearly visible on the horizontal component around 1.5s zero-offset traveltimes. Although that event does not fit the polarization of the inversion operator, its strength relative to the target event results, once again, in a significant amount of artifacts.

To illustrate those points, we present two "quick and dirty" remedies to these problems. To minimize the interference of the $SV-SV$ event, we first truncate the data to keep only the 40% nearest offsets. Figure (3.15) shows that the $SV-SV$ arrival does not dominate the section anymore. In particular, the target event is now visible without any gain on the vertical component, around 1.5s zero-offset time. Inverting this data, we obtain the image in Figure (3.16); most of the noise at large offsets has disappeared, but we are still left with the overmigrated $P-SV$ arrival. In truncating the input data, we have also considerably limited the illuminated portion of the reflector so that the image only survives between offsets of -600m and 600m. To eliminate the smile artifact, we reprocess the data without the horizontal component, and obtain the image in Figure (3.17). The reflector image is now strong, and the only artifact left is actually an overmigrated $SV-SV$ still present on the vertical component. To get rid of the last artifact, we truncate the vertical component to traveltimes below 1.8s, and finally obtain a decent, though restricted, image of the reflector (Figure (3.18)).

There are other alternatives to enhancing image quality while keeping the complete angular aperture provided by the survey. The first one that we present here is based once again on the elimination of the undesirable $SV-SV$ and $P-SV$ events, but this time by means of $\tau-p$ filtering. Without entering into the details of this technique, let us simply say that it allows to separate events according to their velocity and zero-offset traveltimes, and thus makes it easy to select or reject particular events. Figure (3.19) shows the shot records after $\tau-p$ filtering: the $SV-SV$ and $P-SV$ events have been totally removed, and the target $P-P-QP-QP-P-P$ event can be guessed on the vertical component. Figure (3.20) presents the image obtained by inverting that data; the reflector is correctly mapped within the illuminated region, although the amplitudes are somewhat altered.

The second alternative we present for improving the inversion output consists in imposing limits on the reflector dip within the inversion algorithm. In effect, at an output point located on a reflector, the sum of slownesses from source and receiver defines the direction of the normal to the reflector. A priori information can therefore be included in the inversion process to retain only those reflector dips that fall in the expected range. That procedure has the advantage of not requiring any additional processing, and its success lies in an adequate restriction on the range of the receiver integration. Figures (3.21) and (3.22) show results of this technique when applied to the raw data with dip limits of 25° and 10° respectively. With the 10° dip limit, the image is virtually noise-free, and the full aperture of the survey has been used.

ACKNOWLEDGMENT

The author gratefully acknowledges the support of the Consortium Project on Seismic Inverse Methods for Complex Structures at the Center for Wave Phenomena, Colorado School of Mines. Consortium members are: Amerada Hess Corporation; Amoco Production Company; ARCO Oil and Gas Company; Conoco, Inc.; Geophysical Exploration Company of Norway A/S; Marathon Oil Company; Mobil Research and Development Corp.; Phillips Petroleum Company; Shell Development Company; Statoil; Sun Exploration and Production Company; Texaco USA; Union Oil Company of California; and Western Geophysical.

The seismic data processing in this paper was facilitated by the use of the SU (Seismic UNIX) processing line. This software, originated by the Stanford Exploration Project, has been further developed at the Center for Wave Phenomena.

REFERENCES

- Aki, K. and Richards, P.G., 1980, "Quantitative Seismology Vol.1", W. H. Freeman & Co. 185-188.
- Bleistein, N. and Handelsman, R.A., 1975, "Asymptotic Expansion of Integrals", Dover Publ. Inc..
- Bleistein, N., 1985, "Mathematical Methods for Wave Phenomena", Academic Press Inc..
- Bleistein, N., 1989, Fourier Integrals and Inversion, to appear in Wave Motion.
- Cerveny, J.T., Psencik, I. and Molotkov, I.A., 1977, "Ray Method in Seismology" Prague.
- Crampin, S., 1981, A review of wave motion in anisotropic and cracked elastic-media: **Wave Motion** **3**, 343-391.
- Crampin, S. and Radovich, B.J., 1982, Interpretation of synthetic common-depth-point gathers for a single anisotropic layer: **Geophysics** **Vol.47 no.3**, 323-335.
- Crampin, S., 1985, Evaluation of anisotropy by shear-wave splitting: **Geophysics** **Vol.50 no.1**, 142-152.
- Docherty, P., 1987, "Ray Theoretical Modeling, Migration, and Inversion" Ph.D. Dissertation, Colorado School of Mines.
- Friedlander, F.G., "Introduction to the Theory of Distributions" Cambridge University Press.
- Gajewski, D. and Psencik, I., 1987, Computation of high frequency seismic wavefields in 3-D laterally inhomogeneous anisotropic media: **Geophys. Jour. Roy. Astr. Soc.** **Vol.91**: 383-411.
- Gurch, M.L., 1989, "Four-Component Rotation of 3-D Shear Wave Data, Silo Field, Wyoming" M.Sc. Thesis T-3716, Colorado School of Mines.

- Henneke, E.G., 1971, Reflection-refraction of a stress wave at a plane boundary between anisotropic media: *J. Acoust. Soc. Am.* Vol.51 no.1: 210-217.
- Lanczos, C., 1961, "Linear Differential Operators", London, Van Nostrand.
- Lewis, C., 1989, "Three-Dimensional Multicomponent Imaging of Reservoir Heterogeneity, Silo Field, Wyoming" Ph.D. Dissertation T3700, Colorado School of Mines.
- Love, A.E.H., 1944, "A treatise on the Mathematical Theory of Elasticity", Dover Publ. Inc..
- Lu, Ming-Tar, 1988, "Offset Amplitude Analysis of Compressional Seismic Data for Fractured Reservoirs Exploration, Silo Field, Wyoming" Ph.D. Dissertation T-3405, Colorado School of Mines.
- Martin, M.A., 1987, "Three-Component Seismic Investigation of a Fractured Reservoir, Silo Field, Wyoming" Ph.D. Dissertation T-3339, Colorado School of Mines.
- Martin, M.A. and Davis, T.L., 1987, Shear-wave birefringence: A new tool for evaluating fractured reservoirs: *The Leading Edge*, 22-28.
- Morse, P.M., and Feshbach, H., 1953, "Methods of Theoretical Physics", Mc Graw Hill.
- Schipperijn, P.A., "One-Dimensional Forward and Inverse Modeling and Rotation Analysis of Azimuthally Anisotropic Shear Wave Data, Silo Field, Wyoming" M.Sc. Thesis T-3745, Colorado School of Mines.
- Stoneley, R., 1949, The seismological implications of aeolotropy in continental structures: *Geophys. Jour. Roy. Astr. Soc. Suppl.*5, 343-353.
- Sumner, B., 1988, "Asymptotic Solutions to Forward and Inverse Problems in Elastic Isotropic Media", Doctoral Dissertation, Colorado School of Mines.
- Thomsen, L., 1986, Weak elastic anisotropy: *Geophysics* Vol51 no.10: 1954-1966.
- Thomsen, L., 1986, Elastic Anisotropy Due to Aligned Cracks SEG 55th annual meeting Workshop 2.4.

- Van der Hijden, J.H.M.T., 1987, Radiation from an impulsive line source: **Geophys. Jour. Roy. Astr. Soc. Vol.91 no.2: 355-372.**
- Vlaar, N.J., 1968, Ray theory for an anisotropic inhomogeneous elastic medium: **Bull., Seis. Soc. Am. Vol.58 no.6, 2053-2072.**
- White, J.E. and Angona, F.A., 1955, Elastic wave velocities in laminated media: **J. Acoust. Soc. Am. Vol.27: 310-317.**
- White, J.E., 1983, "Underground Sound", Elsevier Science Publ. Co., Inc.: 208-210.
- Yeatts, R.F., 1983, Elastic radiation from a point force in an anisotropic medium: **Physical Review Vol.29 no.4, 1674-1684.**

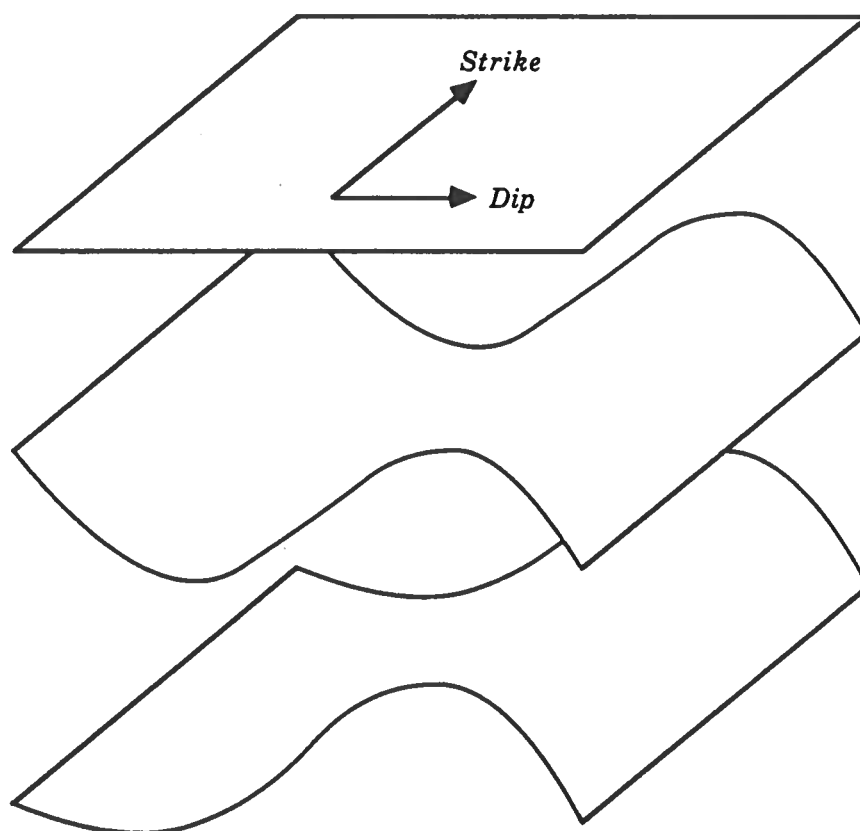


Figure (3.1): A typical cylindrical model: the geometry is invariant in the strike direction.



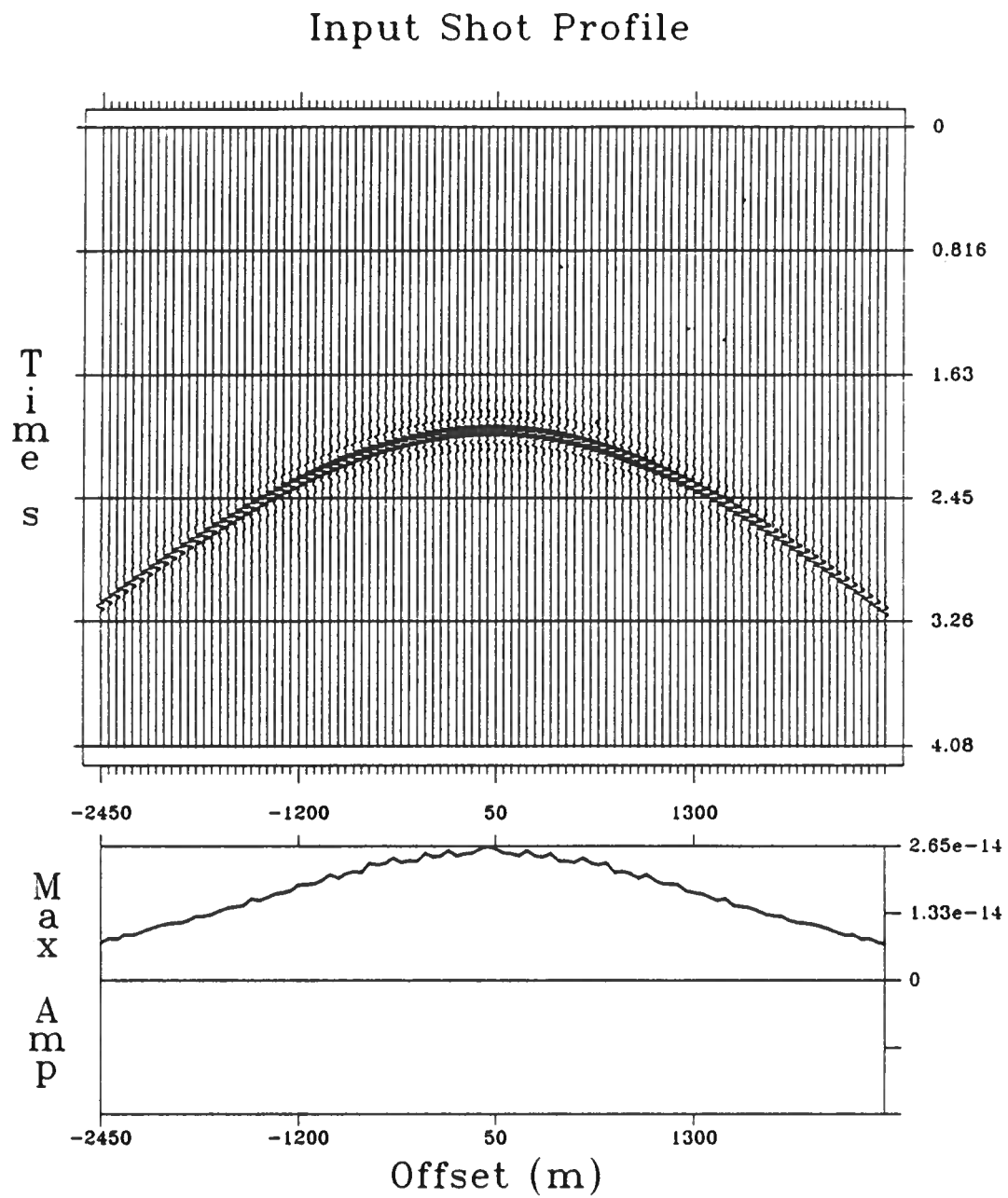


Figure (3.2): Shot record and amplitude plot for the test case discussed in section III-3.1.



Single Shot Inversion

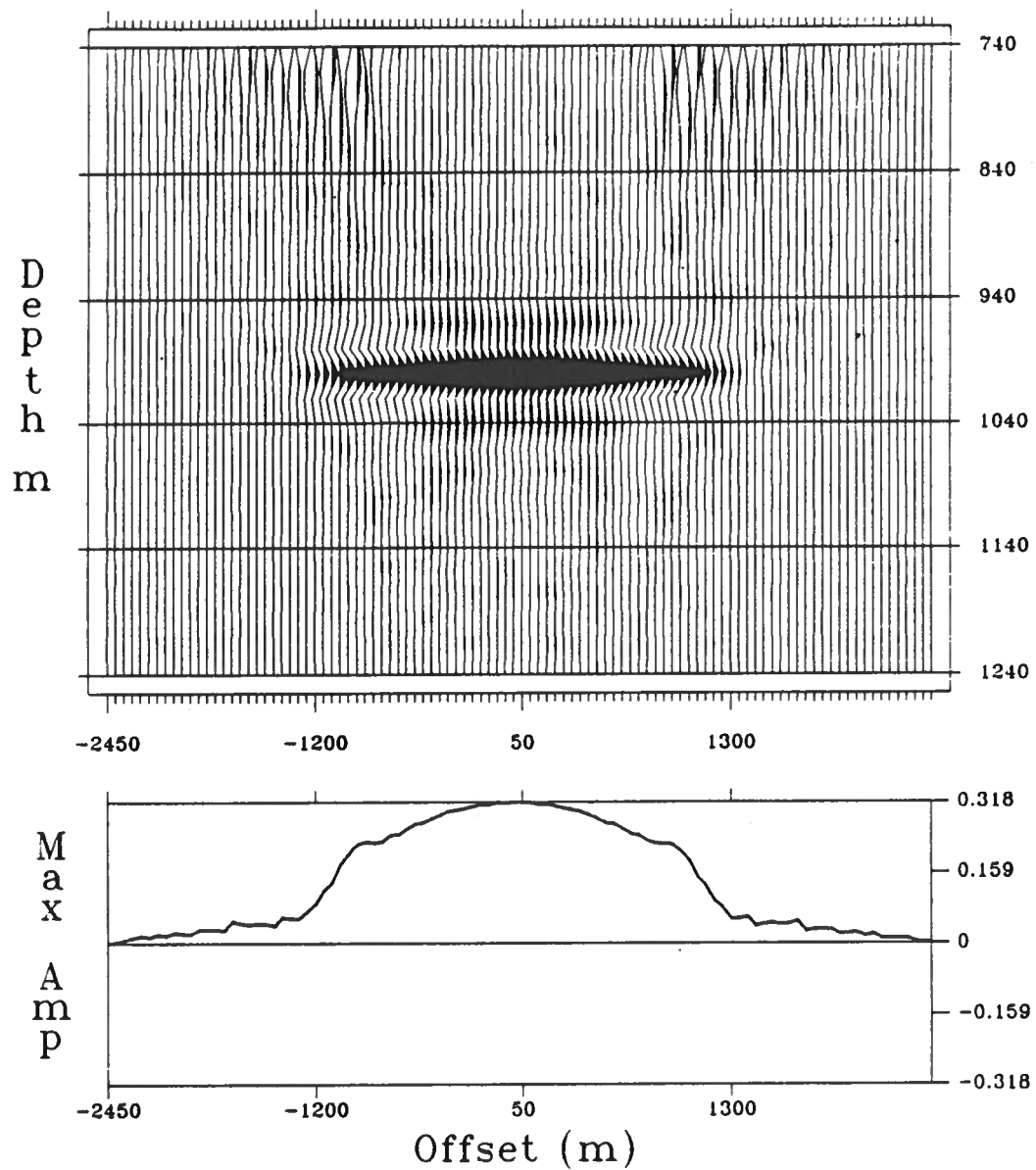


Figure (3.3): Inversion result for the example discussed in section III-3.1. Note that the reflector location and reflectivity are correctly recovered within the illuminated area.



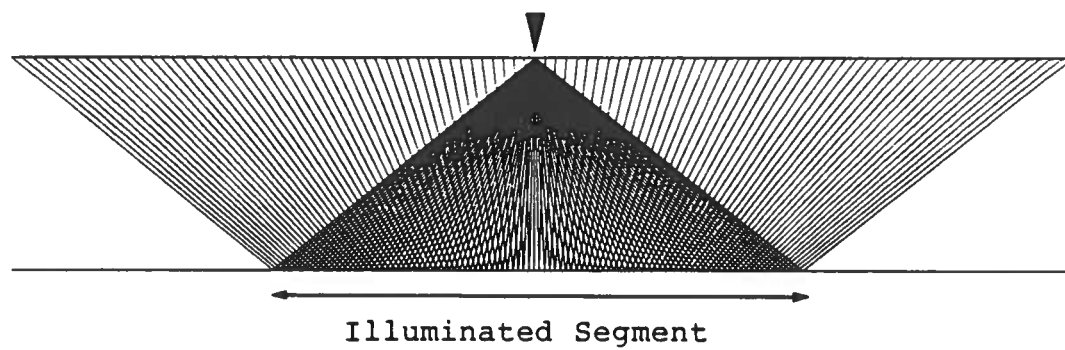


Figure (3.4): Ray diagram for the example of section III-3.1 showing the portion of reflector actually illuminated by the survey.



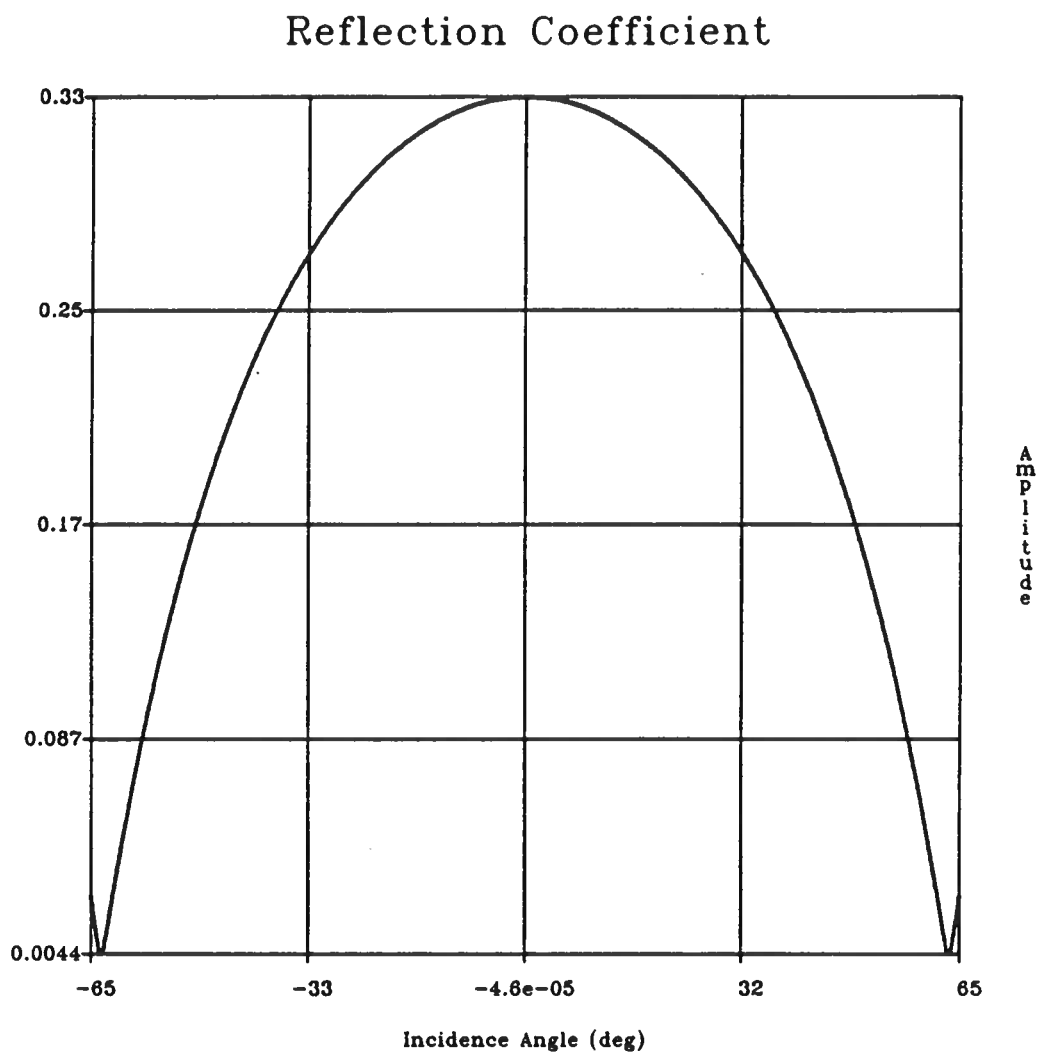


Figure (3.5): Theoretical reflection coefficient to be compared to the amplitude plot in Figure (3.3) (horizontal variables are different).



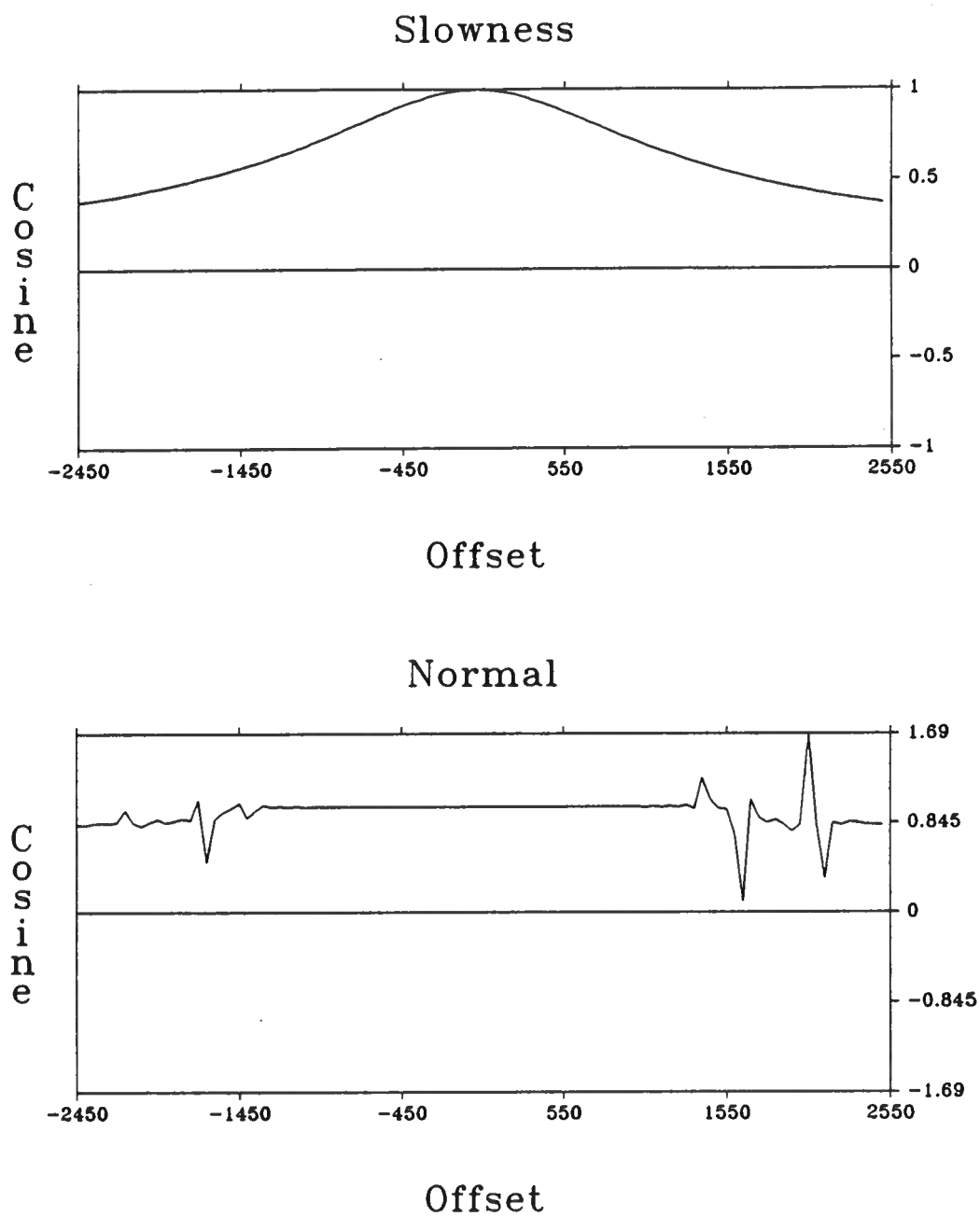


Figure (3.6): Direction cosines for the incident slowness and the reflector normal as retrieved by the inversion at the reflector depth. Values are relevant only within the illuminated zone (-1250m to 1250m).



Stack of 10 Shot Inversions

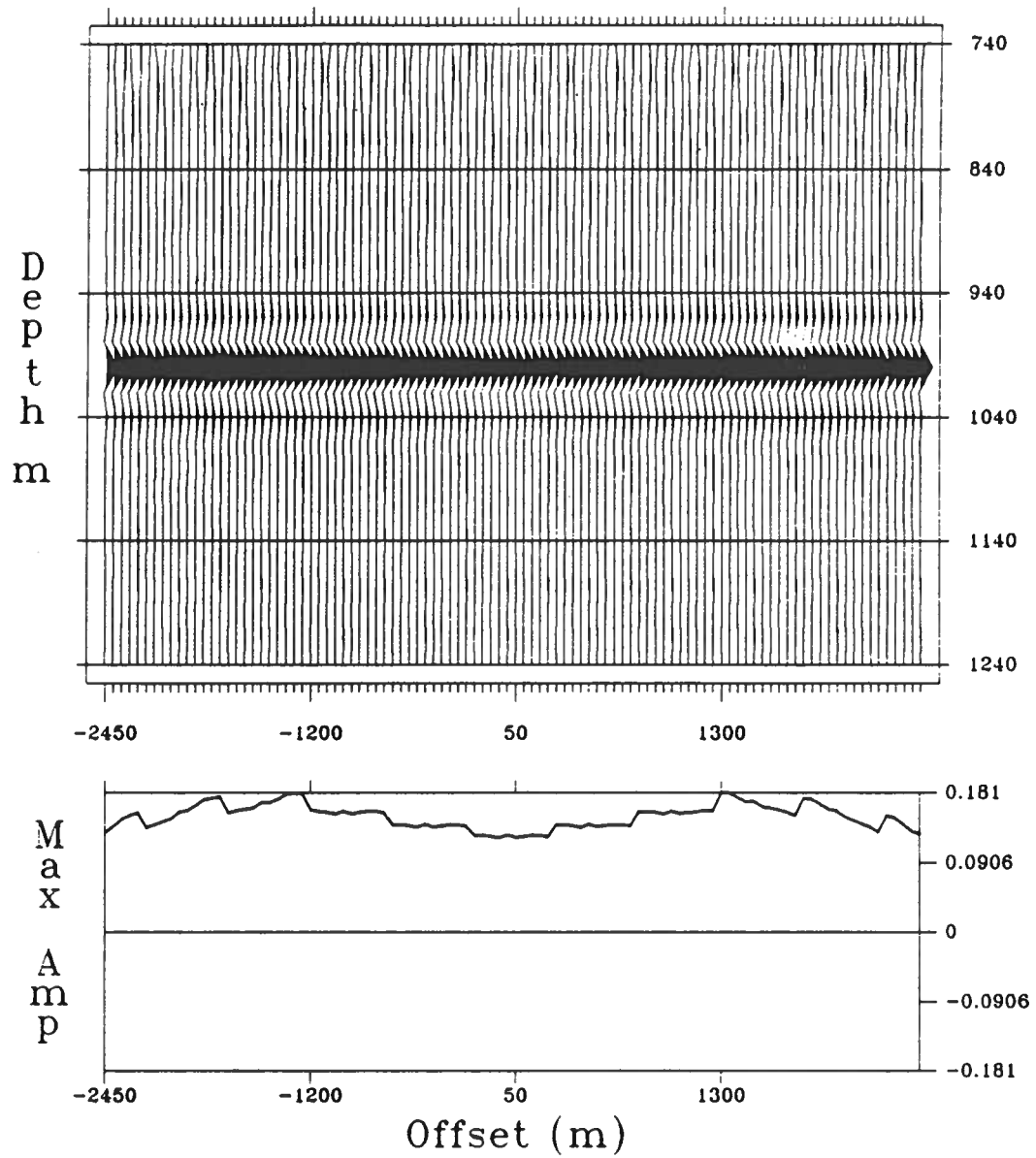


Figure (3.7): Stack of 10 shot inversions. Although the reflectivity information is lost, the image shows no edge effects.



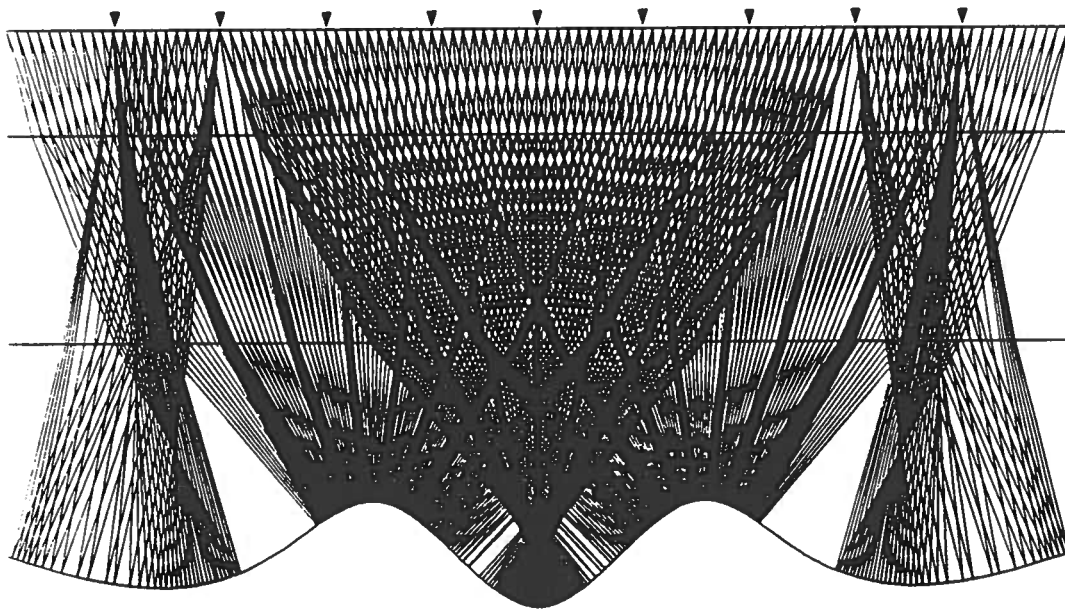


Figure (3.8): Model and ray diagram discussed in section III-3.2. Note that some portions of the curved reflector are not illuminated by the survey.



Shot Records

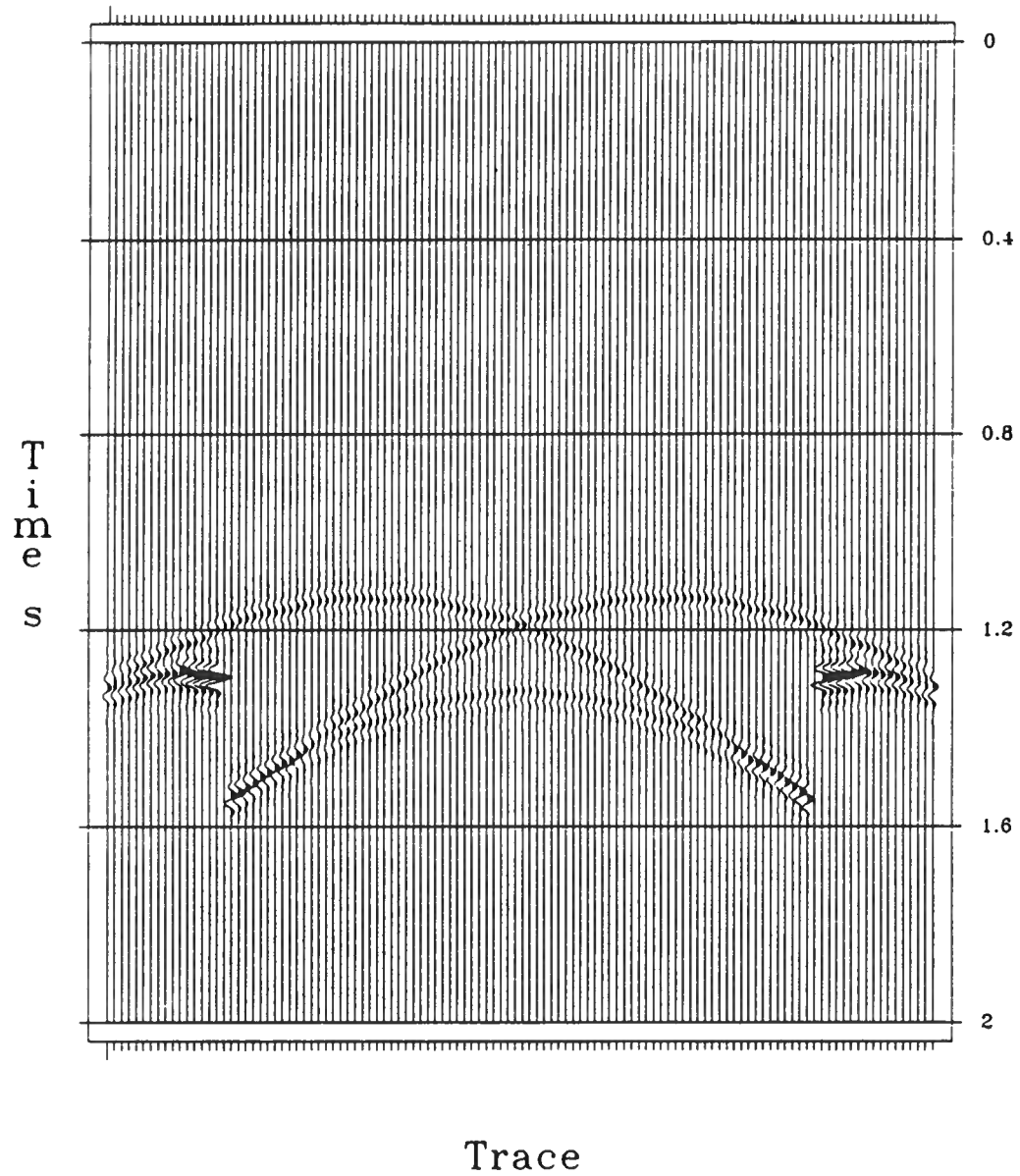


Figure (3.9): Nine shot records corresponding to the survey discussed in section III-3.2. One out of four traces shown.



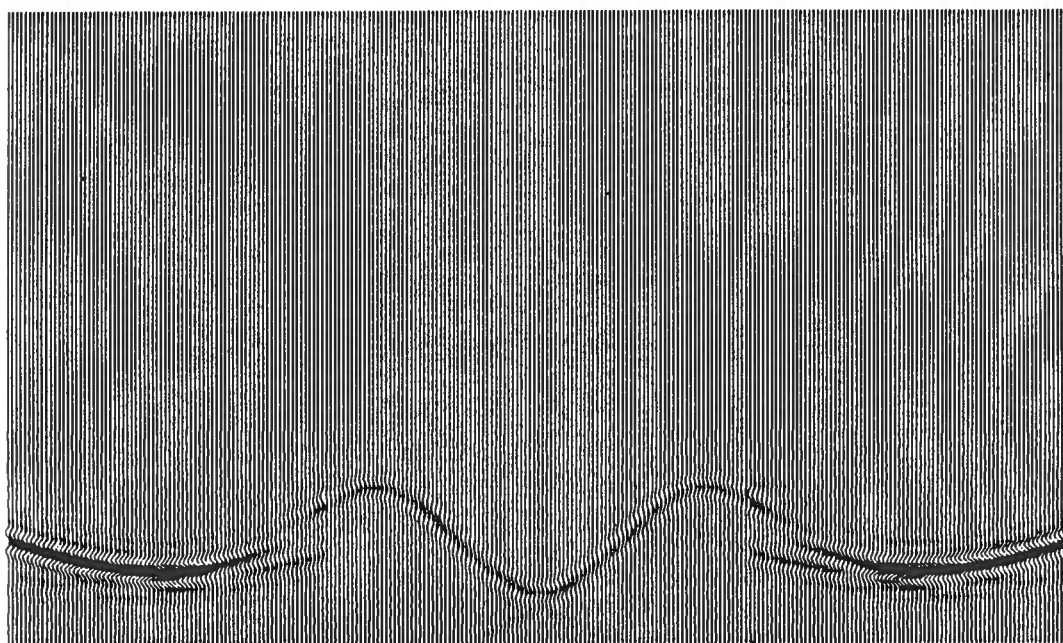


Figure (3.10): Inversion of the shot records shown in Figure (3.9). The curved reflector is accurately imaged except in the areas not illuminated by the survey.

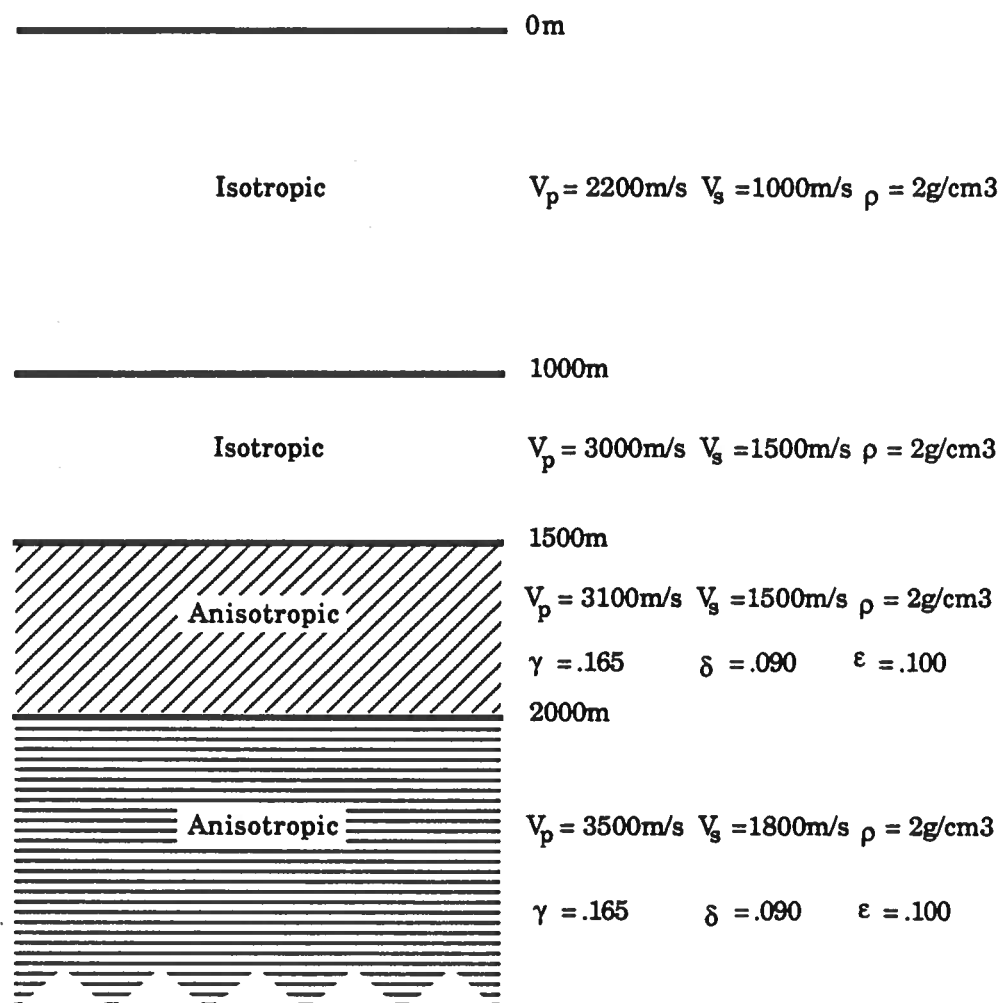


Figure (3.11): Four layer model discussed in section III-3.3.



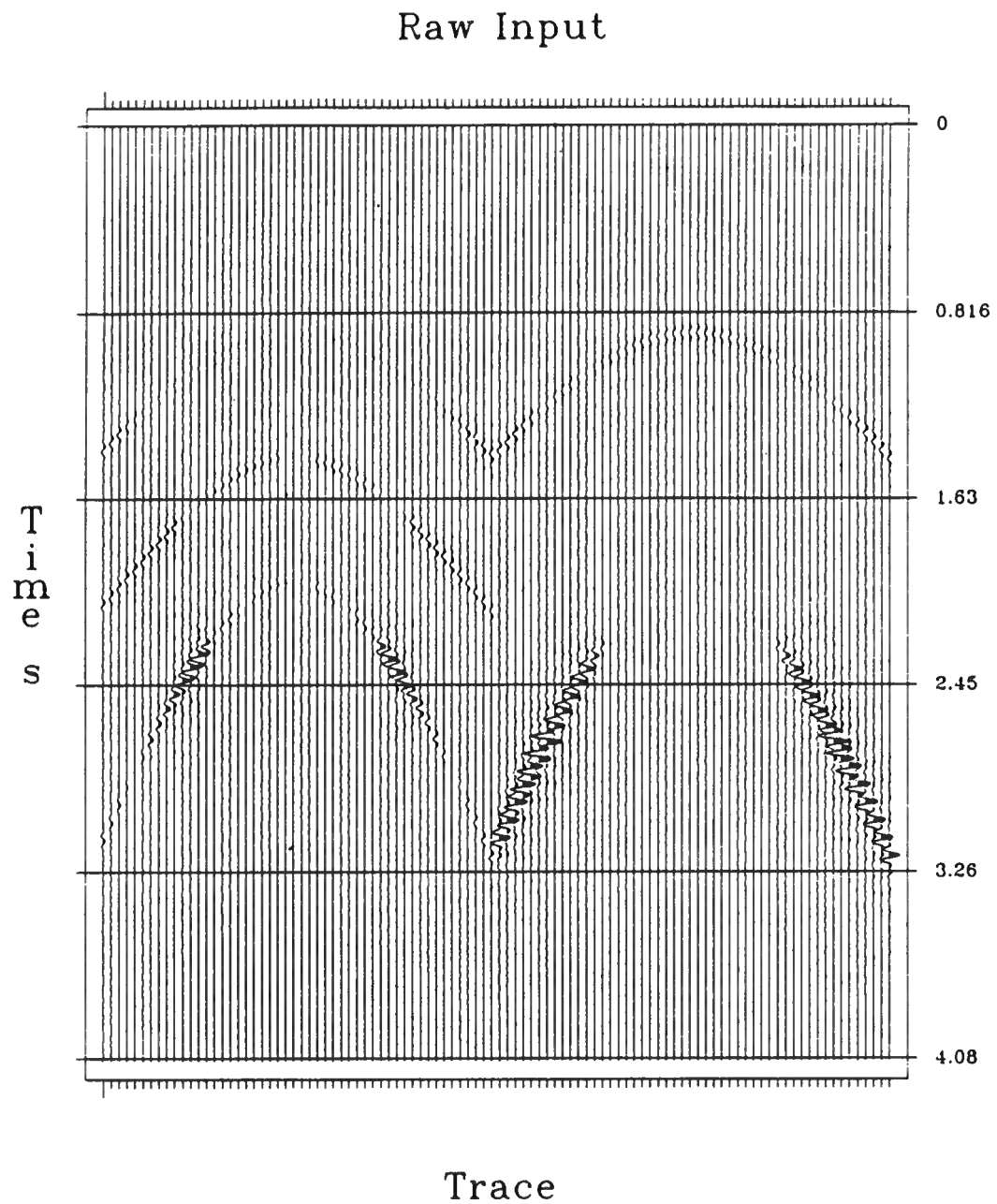


Figure (3.12): Ungained shot records for the horizontal (left) and vertical (right) components of displacement for the example discussed in section III-3.3.



Gained Input (AGC)

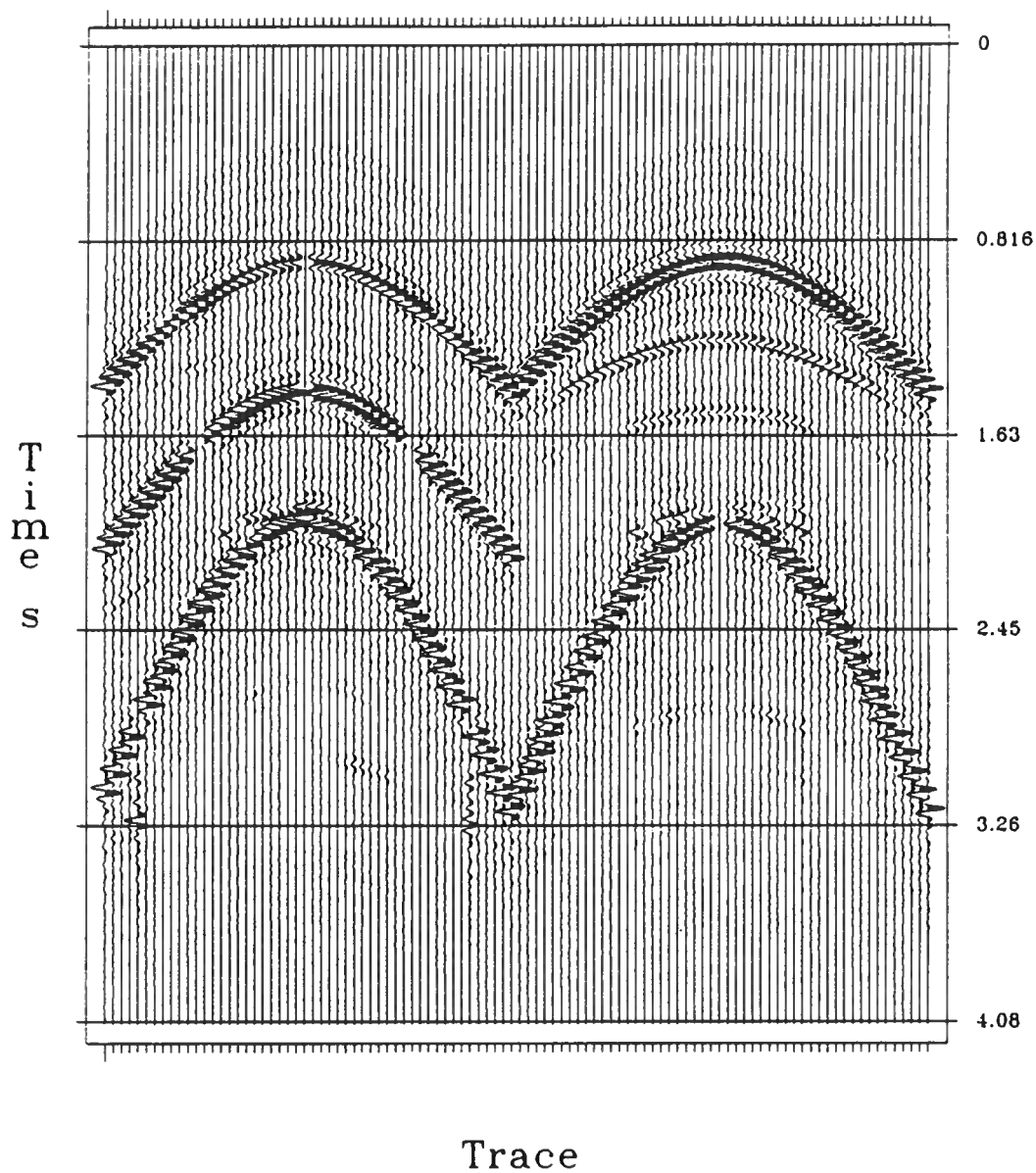


Figure (3.13): Gained shot records. Note the target event on the vertical component (right) at about 1.5s zero-offset time.



Brute Force Inversion

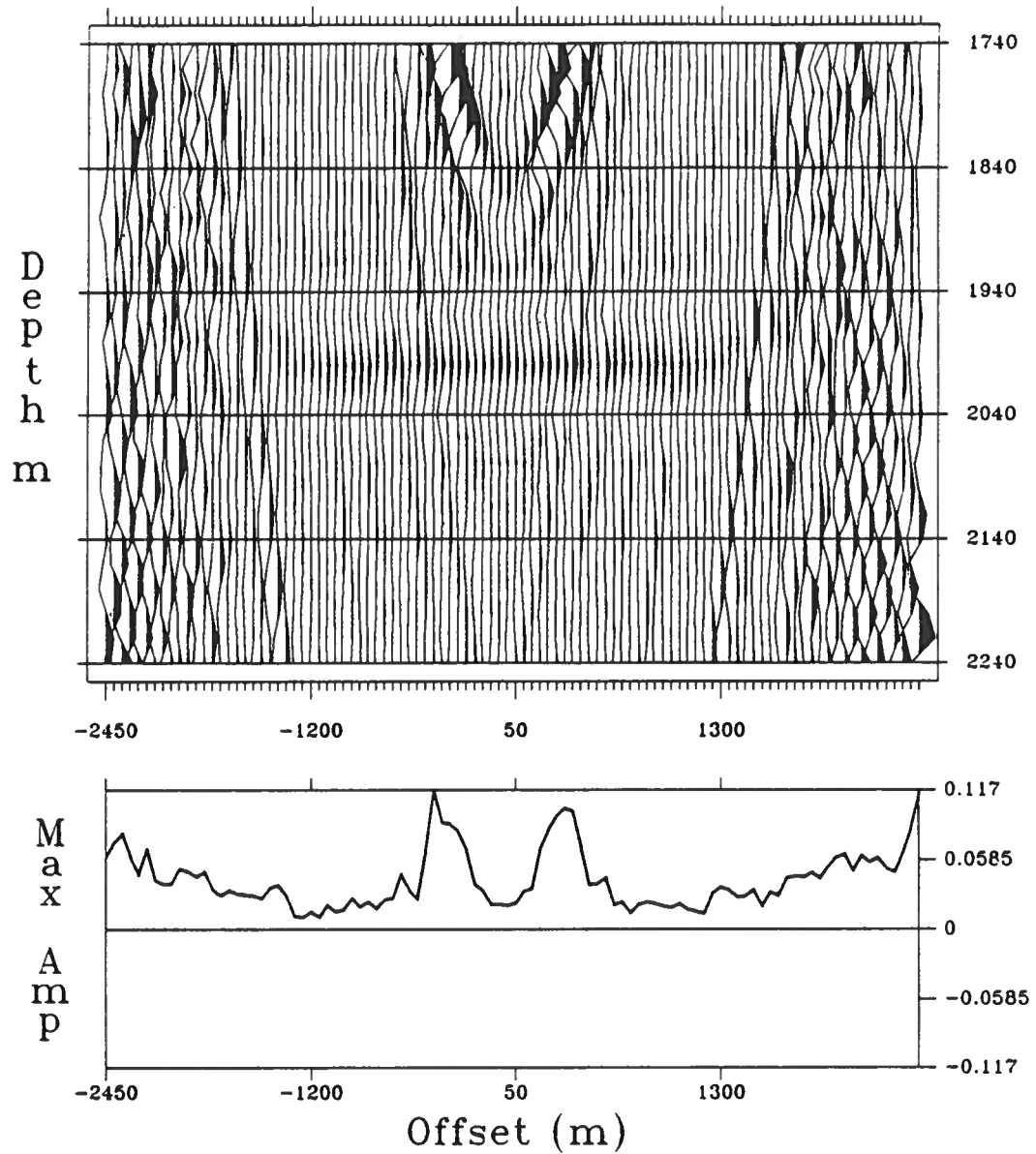


Figure (3.14): Direct inversion of the input of Figure (3.12). The reflector is correctly positioned at a depth of 2000m, but the image is dominated by some "noise" at wide offsets, and a "smile" above the reflector.



Truncated Input Data

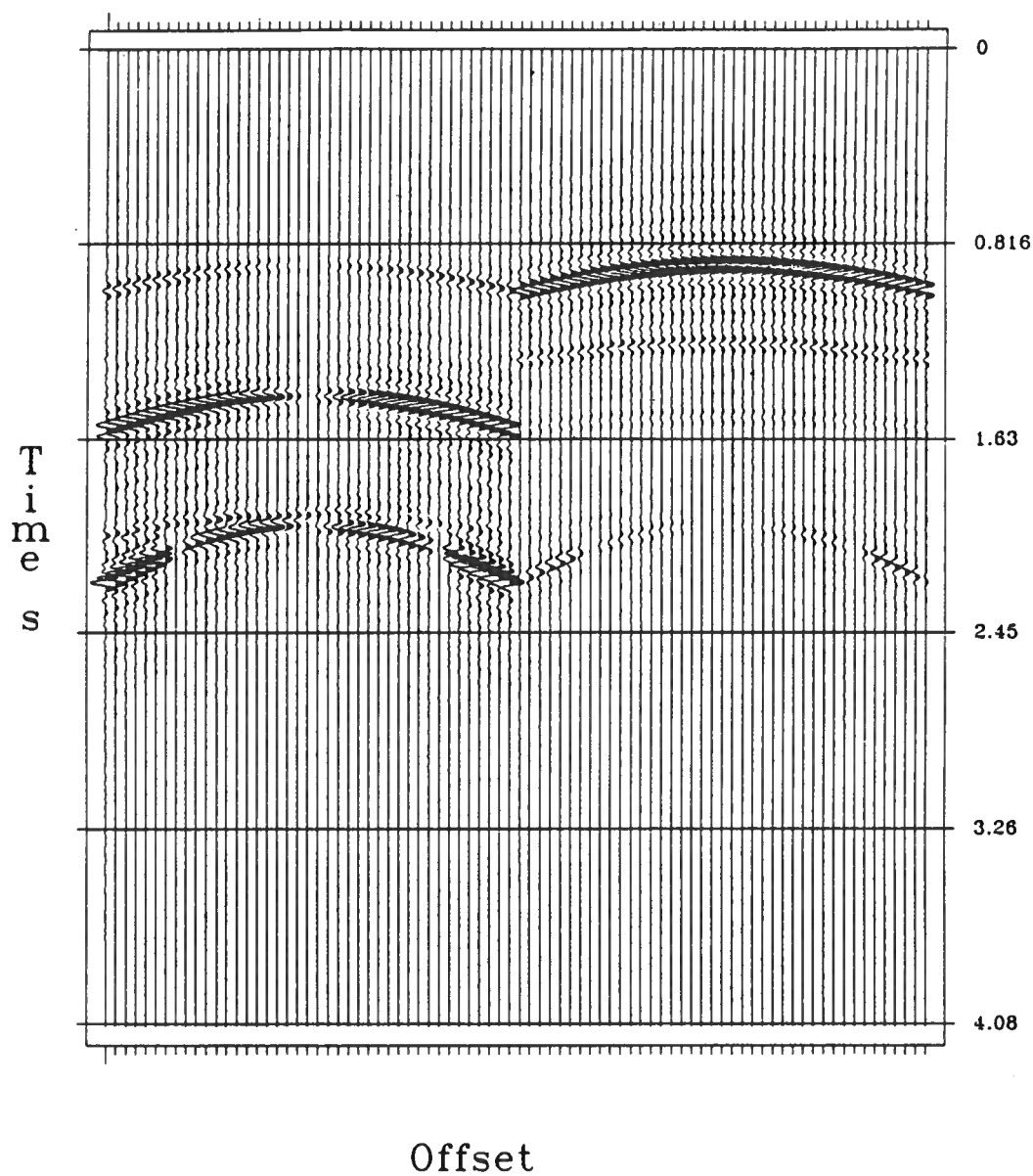


Figure (3.15): Raw shot records truncated to the 40% nearest offsets. The target event can be seen as the weak event at 1.5s zero-offset time on the vertical component (right).

Inversion of Near Offsets

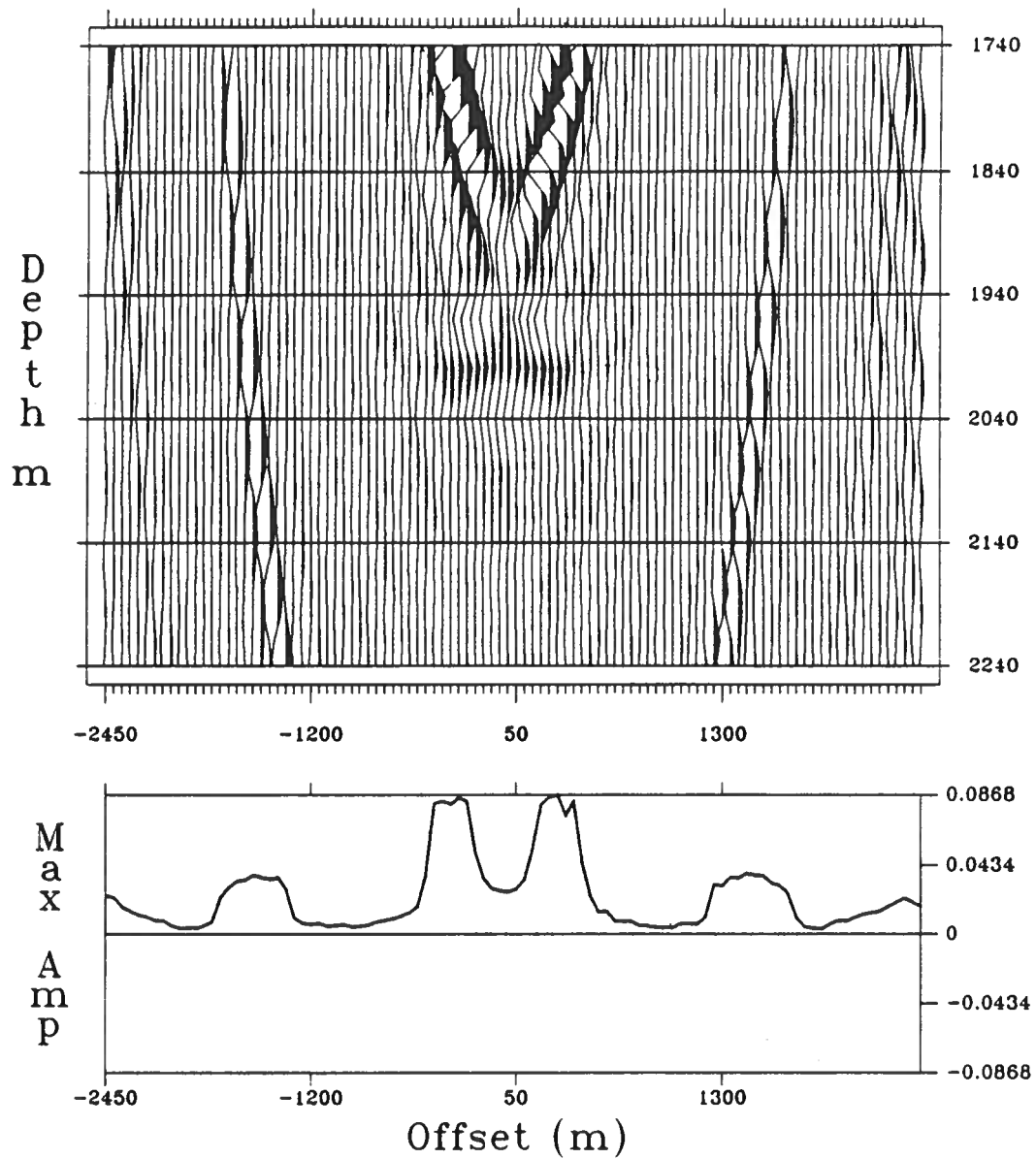


Figure (3.16): Inversion output for the data of Figure (3.15). The reflector image is confined to near offsets, but the "noise" at wide offsets is practically gone.



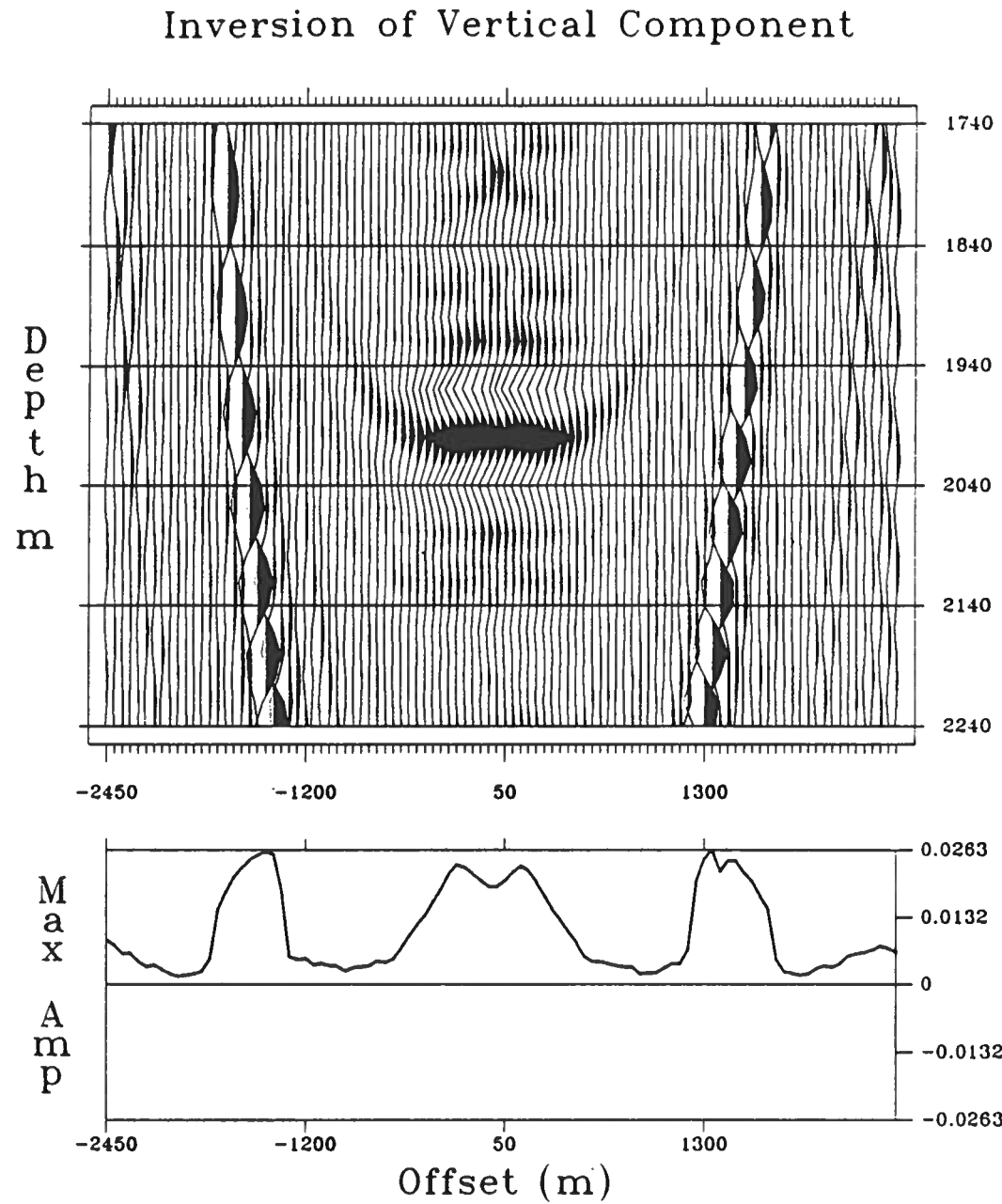


Figure (3.17): Inversion output for the data of Figure (3.15), but using the vertical component only. The "smile" associated with the $P-SV$ event is eliminated.

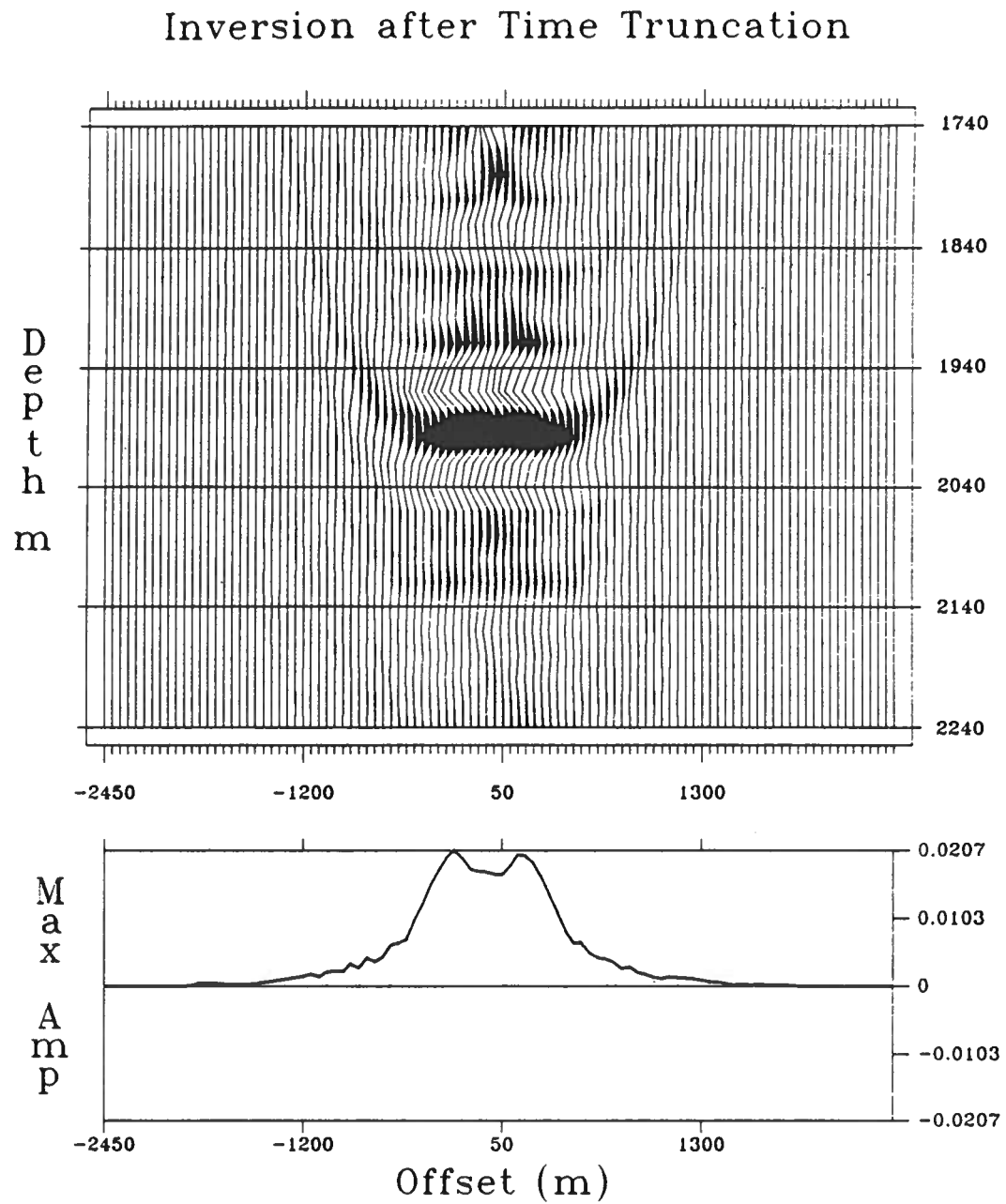


Figure (3.18): Inversion output when considering only the first 1.8 seconds of the near offset traces of the vertical component. All undesirable events being removed from the data, the image is good although limited to a small portion of the reflector.

Tau-P Filtered Input

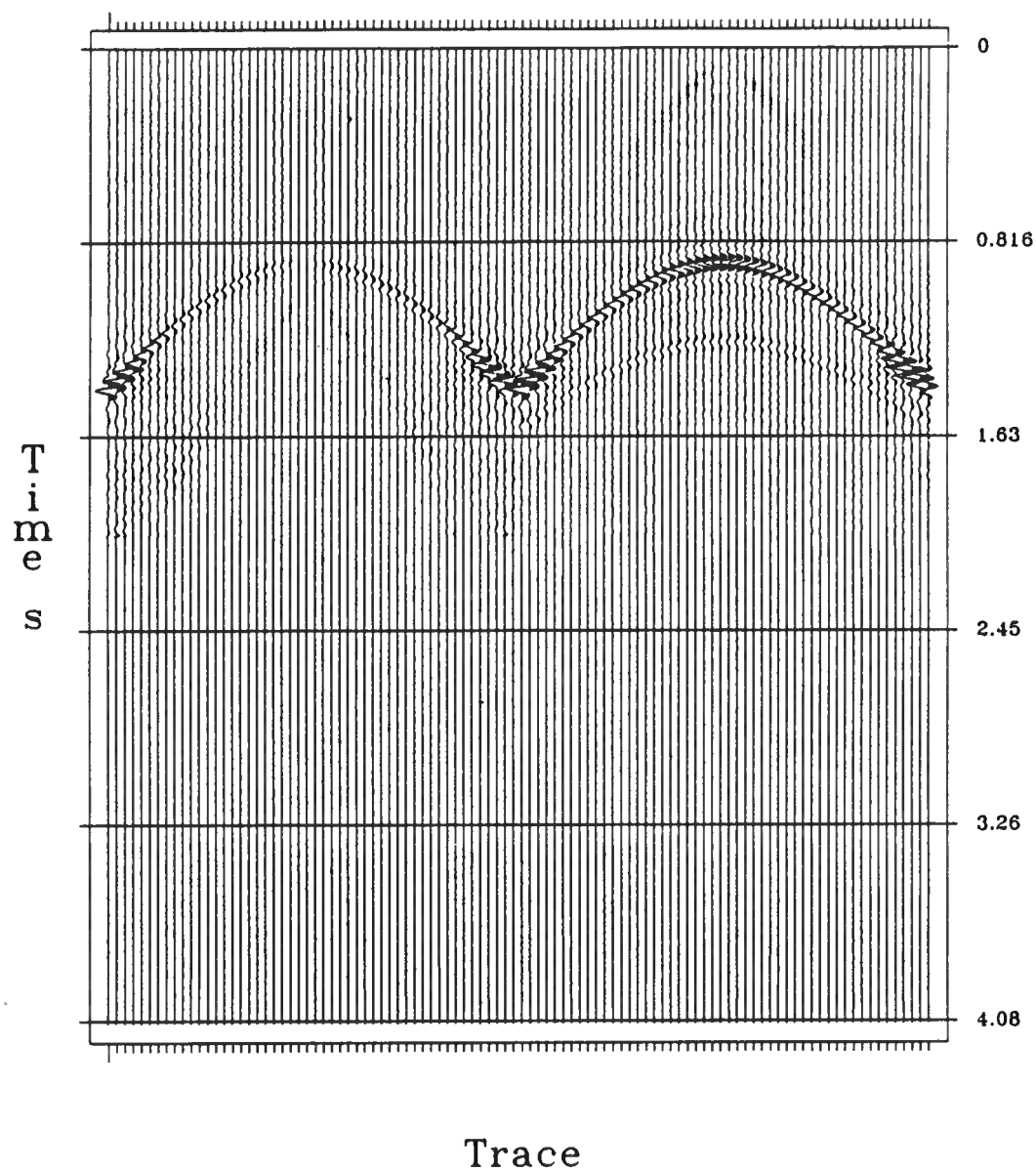


Figure (3.19): Shot records after τ - p filtering of the undesirable events. The target event can (barely) be guessed on the vertical component.

Inversion of Tau-P Filtered Input

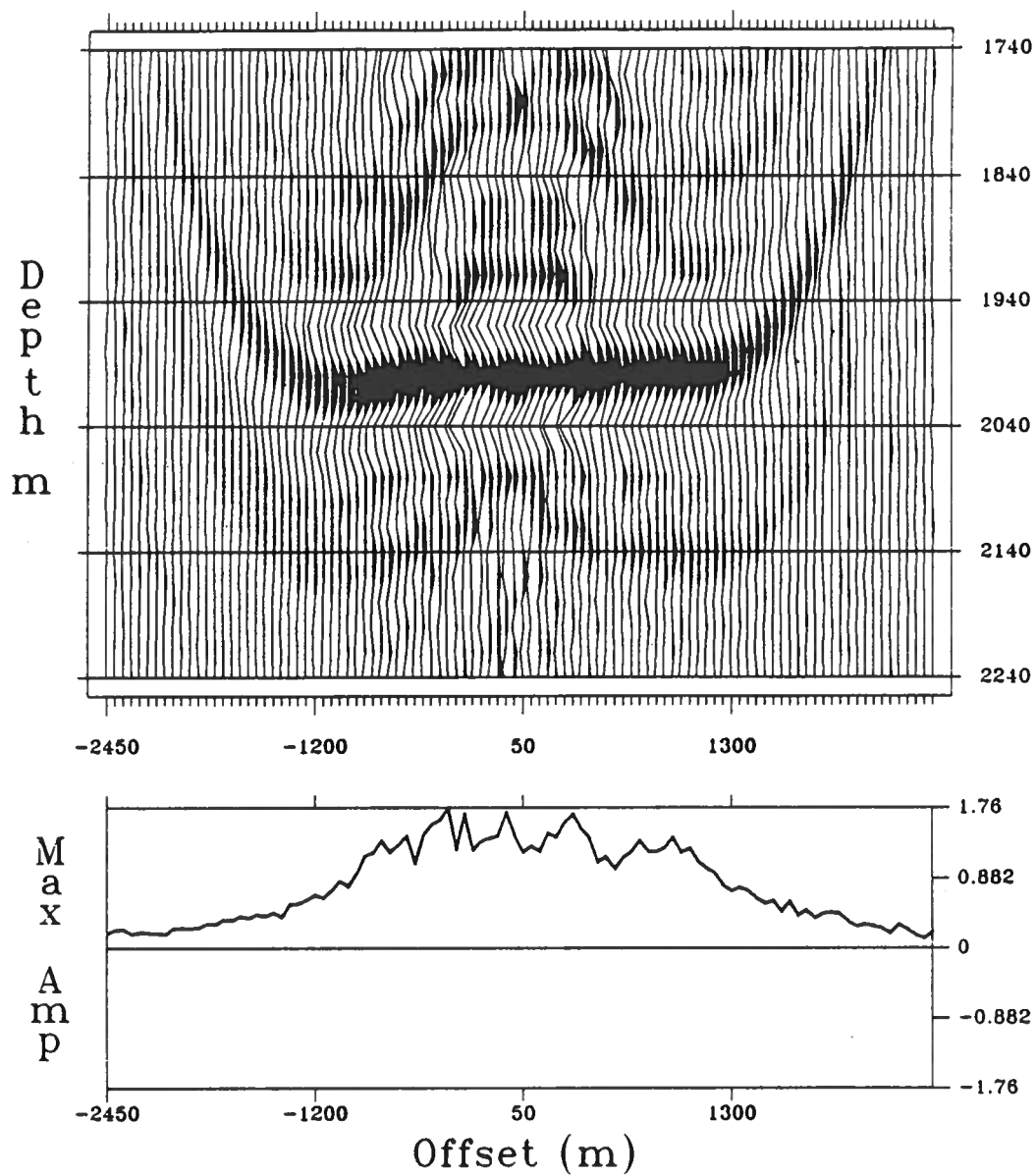


Figure (3.20): Inversion of the τ - p filtered input of Figure (3.19). The image quality is good despite of altered amplitudes.

Inversion with 25 deg. Dip Constraint

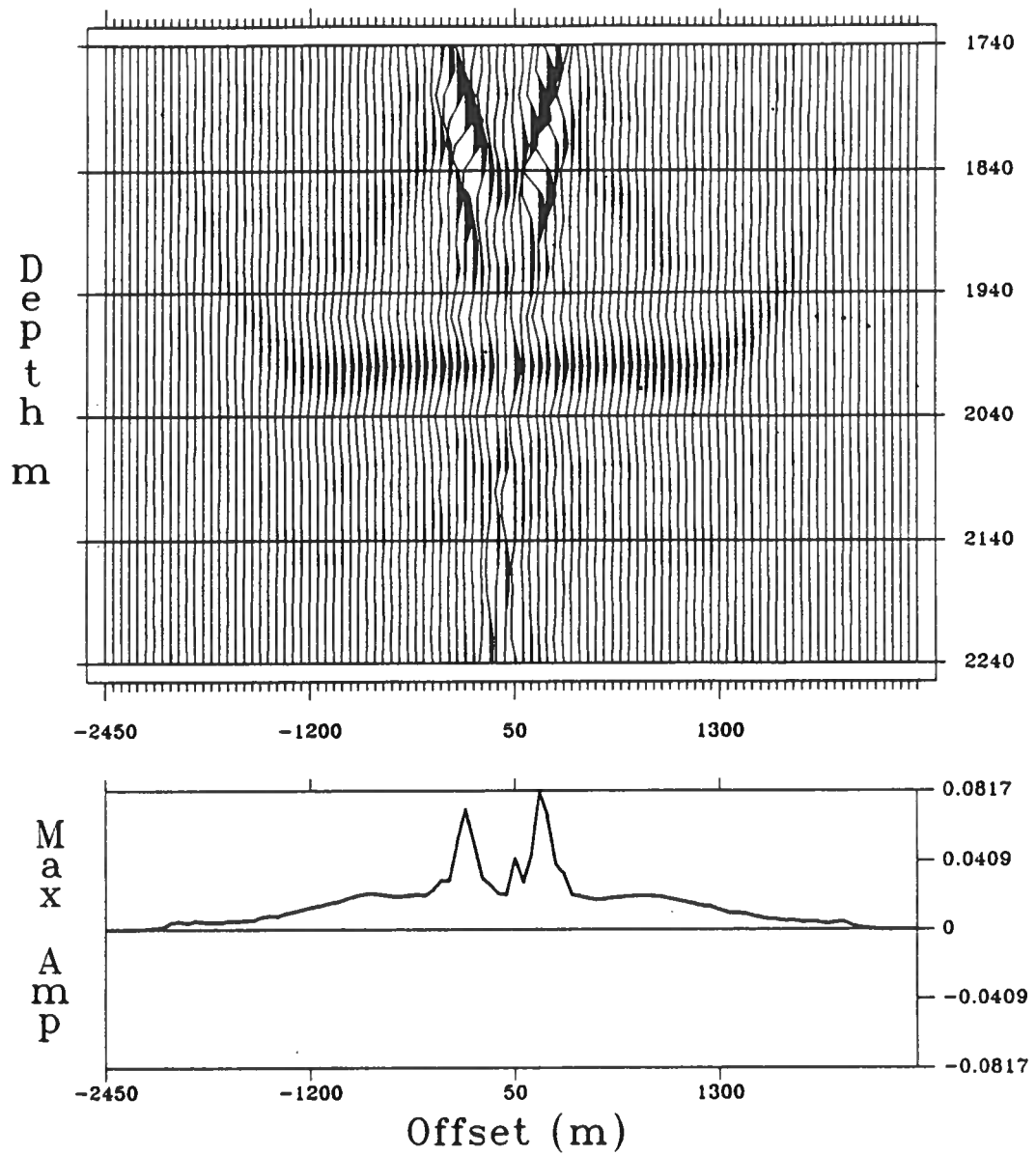


Figure (3.21): Inversion of the raw input of Figure (3.12) with a 25° dip limit. Only the $P-SV$ "smile" is still partly visible.



Inversion with 10 deg. Dip Constraint

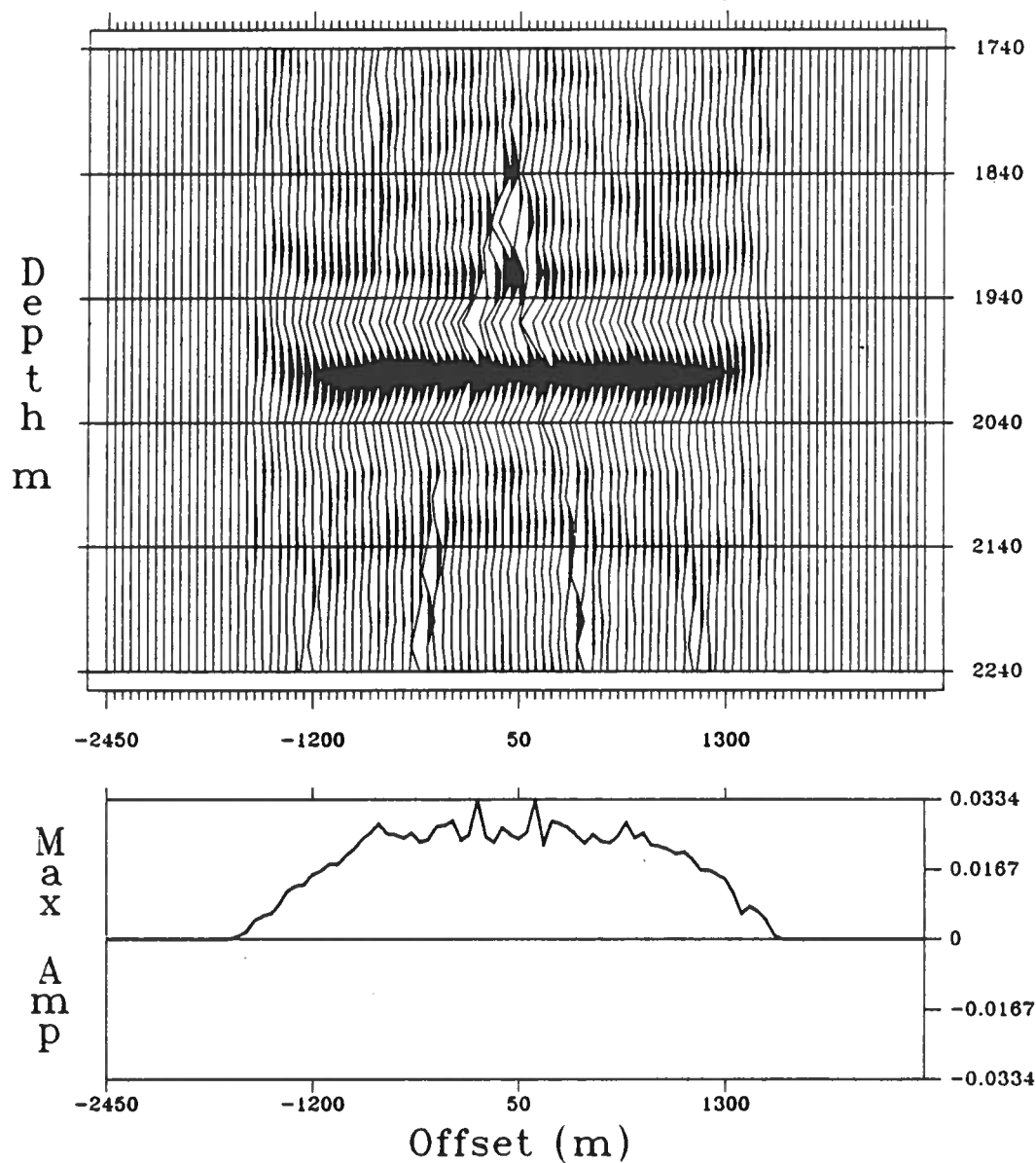


Figure (3.22): Inversion of the raw input of Figure (3.12) with a 10° dip limit. The image is virtually artifact-free and the amplitudes as well as the full aperture provided by the data are preserved.



Excerpts from
**Common Shot, Prestack Inversion
of Physical Model Seismic Data**

by

Jeff Emanuel

**Partially supported by the Consortium Project
on Seismic Inverse Methods for Complex Structures
at the Center for Wave Phenomena**

**Center for Wave Phenomena
Department of Mathematics
Colorado School of Mines
Golden, Colorado 80401
Phone (303) 273-3557**

ABSTRACT

Imaging physical model data provides a good test for an inversion algorithm. The physical model data include all wave effects and the parameters of the model are known beforehand. A physical model data set is inverted twice using different parameters. In both cases, the background velocity field is nearly identical to the actual model. The two inversions image different portions of the data better. Both inversions are superior to two available migrations of the data. A method to determine the model parameters from the inversion is described.



1. INTRODUCTION

Physical model data is useful for testing and comparing seismic data imaging techniques (migration or inversion). The physical model data are actual recorded wavefields and contain all wave effects including lateral waves, near field effects, mode conversions, and diffractions. Seismic data modeling and imaging methods are based on theory which incorporates simplifying assumptions about the wavefield. If an imaging procedure is based on the same theory as the modeling procedure, the imaging procedure is merely the inverse of the modeling procedure. The imaging will work perfectly on synthetic data from the modeling, but it may not work well on field data. Physical model data do not introduce this problem; the data are real wavefields as is field data. Since the models are simpler than the real earth and the physical parameters are known, physical model data can be used to verify imaging techniques.

This research was prompted by Marathon Oil Company. Marathon sends physical model data to contractors to evaluate their imaging (migration) technique. Since the result is known beforehand, this can be input as the migration background velocity function. The migration techniques can be compared independent of the velocity analysis. Marathon donated a physical model data set to the Center for Wave Phenomena so that we might try our inversion on the data. The model is structurally complicated enough to warrant prestack inversion. Wenjie Dong (1989) developed a common shot, $c(x,z)$, prestack inversion algorithm. This paper concerns the application of Dong's inversion routine to the physical model data.

2. DESCRIPTION OF THE PHYSICAL MODEL DATA

The data were collected at the Seismic Acoustics Laboratory at the University of Houston for Marathon Oil Company. I will refer to these data as the Marathon data. The data were collected in a water tank over a block model. Figure 2.1 is a cross-section of the model. The model varies only slightly in the y -direction so that the 2.5-D assumption used for deriving the inversion operator is correct for these data. The top layer was water. The subsequent layers were various epoxy resins. The dimensions in Figure 2.1 are labeled with feet instead of scale feet. For brevity, I will use feet and seconds instead of scale feet and scale seconds throughout this paper.

The data consist of 290 shot records. There were 48 receivers in an end-on spread. The receivers were to the left of the shot. The near receiver offset was 800 feet and the receiver spacing was 80 feet. The far receiver offset was, therefore, 4560 feet. The shot spacing was also 80 feet. The first shot was located at $x=0$ feet and the last was at $x=23200$ feet. The shots and receivers were at depth $z=0$ feet shown in Figure 2.1. This is not the water surface though. The shots and receivers were submerged sufficiently so that no reflections from the water surface were recorded. For each shot, two seconds of data were recorded for each shot sampled at 4 ms.

Figure 2.2 is a sample shot record from the Marathon data. AGC has been applied to this record so that more events are visible. The shot location is $x=2000$ feet and the receiver spread extends from $x=2800$ to $x=6560$ feet. The earliest event is the direct wave. The first curved event is the water bottom reflection. The next two events are reflections from the second and third interfaces. The strong event at about 1.45 seconds is a reflection from the model bottom. The reflection from the sawtooth interface does not produce an easily identifiable event on this record.

3. INVERSION OF MODEL DATA

This section describes the inversion of the Marathon data using the common shot, $c(x,z)$, prestack inversion algorithm of Dong (1989). The data have been inverted twice with different parameters. The parameters used to invert the data and the results of the inversions will be discussed. The inversion will be compared to migrations of the same data. Directions for future research concerning parameter estimation from the Marathon inversion will be discussed.

3.1. First Marathon Inversion

As with migration, inversion requires a reference velocity field. Figure 3.1 shows the interfaces bounding the velocity layers for the reference velocity field. The velocities used are the exact velocities shown in Figure 2.1. The interfaces in Figure 3.1 are located nearly in the same positions as the interfaces in Figure 2.1. Differences occur where the cubic spline fit to the control points causes unwanted bumps on the interfaces. The most severe of these occurs on the down thrown side of the fault cutting the third interface.

For each shot record, the inversion routine produced 48 output depth traces. The first output trace is located at the shot position. The trace separation is 160 feet. Each trace has 301 samples. The depth sampling rate is 40 feet. For each shot record, the inversion produced an image of the subsurface in the rectangular region from 0 to 12000 feet deep and from the shot location to 7520 feet right of the shot location.

The traveltime and amplitude functions required by the inversion formula are computed by ray tracing from the output point to the source and to the receivers. Rays were not, however, traced to every output point and every receiver. Instead, rays were traced from each depth point on every fifth output trace and to every fifth receiver. The traveltime and amplitude functions were interpolated from the values obtained by the ray tracing.

Figure 3.2 is the inversion of the shot record shown in Figure 2.2. (Note that Figure 2.2 shows the shot record after AGC. The inversion is applied to the ungained record.) The inversion is a partial image of the subsurface. Shallower than 1000 feet is

noise from the direct arrival. The events at 3000 feet, 4500 feet, and 6300 feet are images of the first three interfaces. The event at 11200 feet corresponds to the model bottom. The fourth reflector, the sawtooth, is faint and located at a depth of 9000 feet and distance of 6000 feet.

An inversion similar to Figure 3.2 is obtained for all 290 shot records. Each yields a different partial image of the subsurface. The inversions are sorted on the output trace location and stacked to form a full image of the subsurface. Figure 3.3 is a stack of all the individual shot inversions. Since the amplitudes are only significant in the individual shot inversions and not the stacked section, AGC has been applied so that all reflections are visible. All reflectors are located correctly including all teeth of the fourth reflector. There are some short comings in the inversion.

The first problem is that the steep flanks of the dome are not imaged well. To understand why, consider an experiment in a constant velocity medium with a single reflector and a single source and receiver. The envelope of all reflectors having the same reflection time is the familiar reflection ellipse with the source and receiver at the foci (Figure 3.4). If the reflector has zero dip, the specular point lies below the midpoint of the source and receiver. As the reflector dip increases, the specular point moves farther up dip and laterally away from the midpoint. Consequently imaging in a region near the source and receiver, as with this particular example inversion, discriminates against steep dips.

Another problem with the inversion is a phase reversal on the down thrown side of the fault cutting the third interface. There is also a streak of noise extending below this phase reversal. The phase reversal and the noise beneath it are due to the bump on the input model mentioned earlier. The second inversion of the data was performed to try to remedy these shortcomings.

3.2. Second Inversion

For the second example inversion of the Marathon data, several parameters were changed. The inversion output for each shot consisted of 300 traces spaced at 80 feet. This covers the entire model rather than the limited portion of the first inversion. Recorded energy from all dips should be imageable. The background velocity model was also changed; the velocities were the same but the interfaces have been changed. Figure 3.5 is the new background model. The interfaces do not have the extraneous bumps that the previous model (Figure 3.1) had. This should solve the phase shift problem observed in the first inversion. The remaining parameter changes concerned the traveltimes and amplitude function interpolation. Rays were traced from each depth point on every other output trace to every other receiver. This was done to achieve as accurate amplitude as possible. The second inversion of all shot records took 3.5 times as much CPU time as the first inversion.

Figure 3.6 is the inversion of the shot record in Figure 2.2. The inversion covers the whole model although the image is limited to a small zone. The result is similar to

Figure 3.2. The output outside the zone where the reflectors are imaged consists of *migration smile* noise. The noise is of lower order so that it is not as visible.

Inversions from all 290 shot records were stacked to form a complete image of the model. The image is shown in Figure 3.7. Compared to Figure 3.3, there are some improvements and also some disappointments. As expected, the steep flanks of the dome are better imaged. The phase reversal in the third interface was also removed. There also appears to be a fault plane reflection on the third interface. Ray tracing has shown, however, that no specular reflections could be recorded from the fault plane. The apparent fault plane reflection may be mispositioned energy due to slight deviations of the background velocity model from the actual model. Verifying this will be the subject of future research.

The main disappointment from this inversion is the large degree of *migration smile* noise. Migration smiles occupy more area in the shot inversions than the reflector images do. This results in many more noise traces being stacked than signal traces. Although the reflector images (signal) are higher order than the noise, the large quantity of noise traces being stacked can bring the noise to the same level as the signal. The noise has nearly obliterated the fifth tooth in the fourth (sawtooth) interface. Selective windowing of the shot inversions before stacking can reduce the noise level in the final image.

3.3. Migrations of the Marathon Data

Figure 3.8 is a finite difference, time migration of the Marathon data by the University of Houston. This should be compared to the inversions shown in Figures 3.7 and 3.3. The Houston migration shows significant pull up of the model bottom reflection. The inversions correctly show the model bottom as flat. The fourth and fifth teeth of the sawtooth interface are invisible in the Houston migration. In both inversions, the fourth sawtooth is imaged while the fifth is imaged in Figure 3.3. The third interface in Figure 3.8 is distorted in the center of the model due to pull up. Finally, there are two crossing events at the peak of the dome. Figure 2.1 shows that there should be only one event. Both inversions show only one event at the peak of the dome. The inversions image the model better than the Houston migration.

Figure 3.9 is a pre-stack migration supplied by Marathon. This migration images the data better than the Houston migration (Figure 3.8). In Figure 3.9, both the model bottom and the third interface are imaged correctly without pull up. The fourth sawtooth is imaged better than in Figure 3.8, but the fifth is still absent. Figure 3.9 should also be compared to Figures 3.3 and 3.7. The migration contains more noise than the inversions. Also, the migration images the steep flanks of the dome poorer than even the first inversion (Figure 3.3). Both inversions image the fourth sawtooth well, the migration images it poorly. In the migration, the fifth sawtooth is completely absent. The first inversion (Figure 3.3) images it well. In the second inversion (Figure 3.7), it is obscured by noise but still present. Again, the inversions imaged the model

better than the migration.

3.4. Future Research: Parameter Determination

Up to this point, only the kinematics of the inversion have been discussed. The main advantage of inversion is that it *corrects* the reflection amplitudes. The output of the inversion operator applied to the data is what Bleistein et al. (1987) call β . Inversion theory states that

$$\beta(x, z) \sim R(x, \theta) \gamma(x) .$$

γ is the singular function of the reflector and $R(x, \theta)$ is the angularly dependent reflection coefficient of the reflector. The peak value of γ (ie. on the reflector) is given by

$$\gamma(x)_{peak} = \frac{\cos \theta}{c(x)} \int F(\omega) d\omega .$$

$F(\omega)$ is the product of the amplitude spectra of all filters applied to the data. The reflection weight, therefore, is proportional to the reflection coefficient.

For parameter determination, the specular incidence angle, θ , must be determined. With minor modifications, the inversion routine can be altered to calculate an additional inversion operator, β_1 , simultaneously with β .

$$\beta_1(x, z) \sim R(x, \theta) \frac{\gamma(x)}{\cos \theta} .$$

The angle θ may be easily determined from the ratio of the peak values of β and β_1 . The physical parameters of the layer below the reflector may then be computed from the reflection coefficient. This technique is performed on the unstacked individual inversions. Stacking destroys the amplitude information. My future research will be geared toward verifying the model parameters by this method.

4. CONCLUSIONS

Common shot, $c(x, z)$, prestack inversion images the reflectors of the Marathon physical model data set well. The inversion parameters may be chosen to image the steep flanks of the shallow dome or the deeper sawteeth better. Both, however, may be optimized if care is taken to minimize stacking of noise. The kinematics of the inversion compare favorably to other migrations of the data. Inversion theory provides a means for computing the medium parameters from the value on the reflector.

ACKNOWLEDGMENT

The author gratefully acknowledges the support of the Office of Naval Research and the Consortium Project on Seismic Inverse Methods for Complex Structures at the Center for Wave Phenomena, Colorado School of Mines. Consortium members are: Amerada Hess Corporation; Amoco Production Company; ARCO Oil and Gas Company; Conoco, Inc.; GECO; Marathon Oil Company; Mobil Research and Development Corp.; Phillips Petroleum Company; Shell Development Company; Statoil; Sun Exploration and Production Company; Texaco USA; Union Oil Company of California; and Western Geophysical.

The seismic data processing in this paper was facilitated by use of the SU (Seismic UNIX) processing line. This software, originated by the Stanford Exploration Project, has been further developed at the Center for Wave Phenomena.

REFERENCES

- Bleistein, N., Cohen, J. K., and Hagin, F. G., 1987, Two and one-half dimensional Born inversion with an arbitrary reference: *Geophysics*, 52, 26-36.
- Dong, W., 1989, Finite Difference Ray Tracing and Common Shot Inversion: Center for Wave Phenomena Research Report number CWP-084 (Excerpts in this volume).

Marathon Data Model

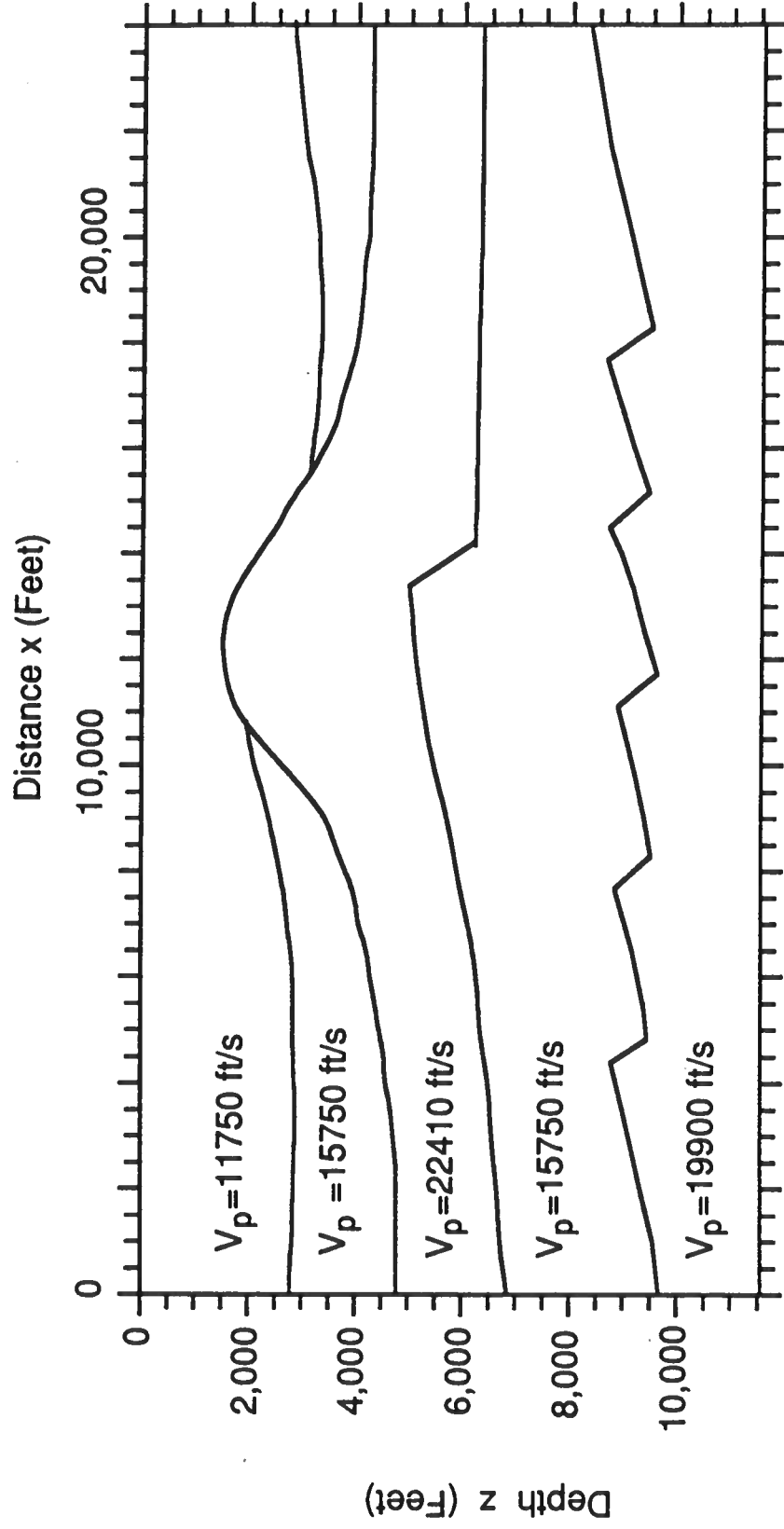


Figure 2.1: Cross-section of block model for the Marathon data. The top layer is water. The lower layers are various epoxy resins. The shots and receivers were at depth $z = 0$ feet.



Shot 2000 (agc)

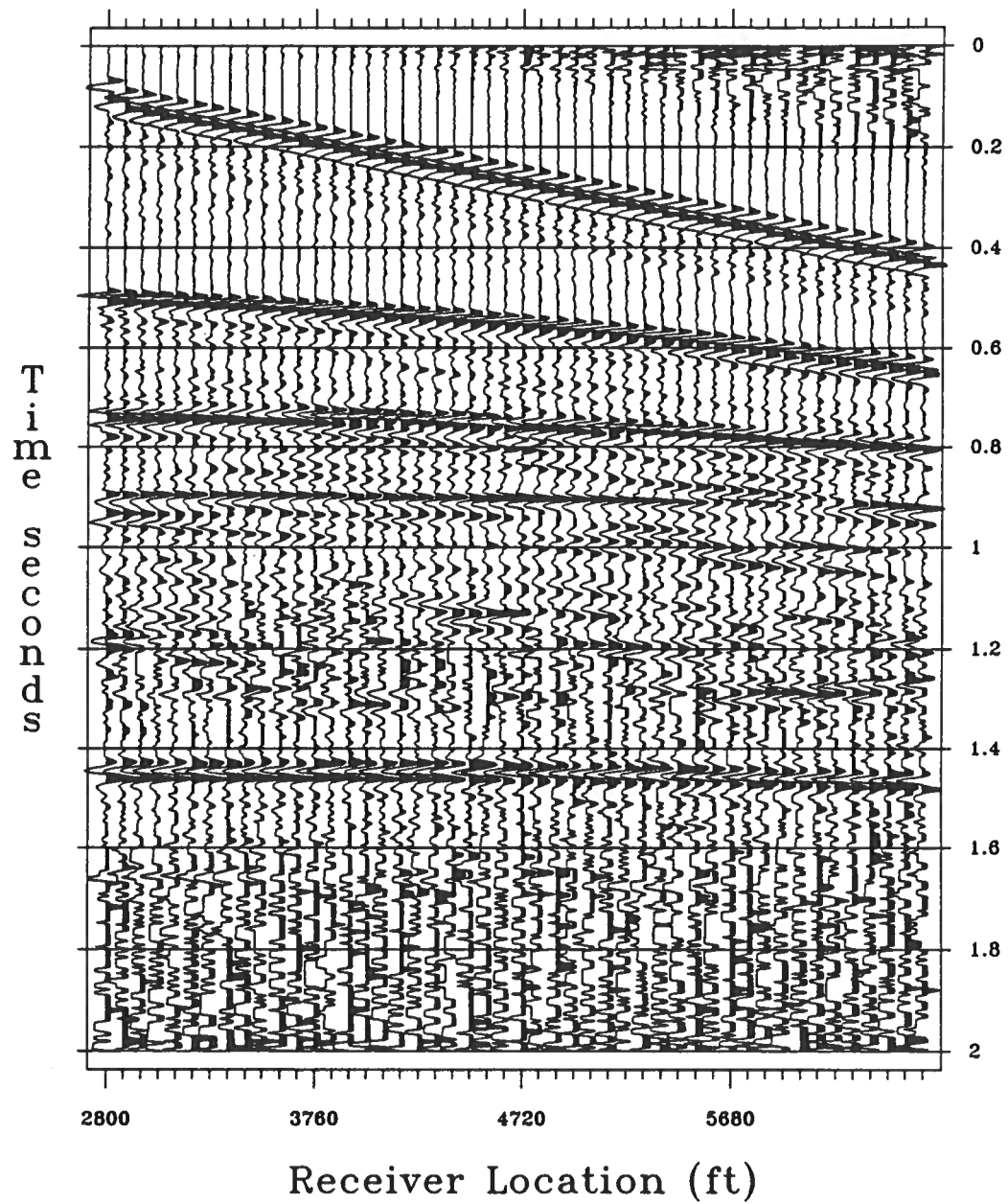


Figure 2.2: Sample shot record from the Marathon data. The shot location is $x = 2000$ feet. The receivers extend from $x = 2800$ feet to $x = 6560$ feet. AGC has been applied for display.

First Background Model

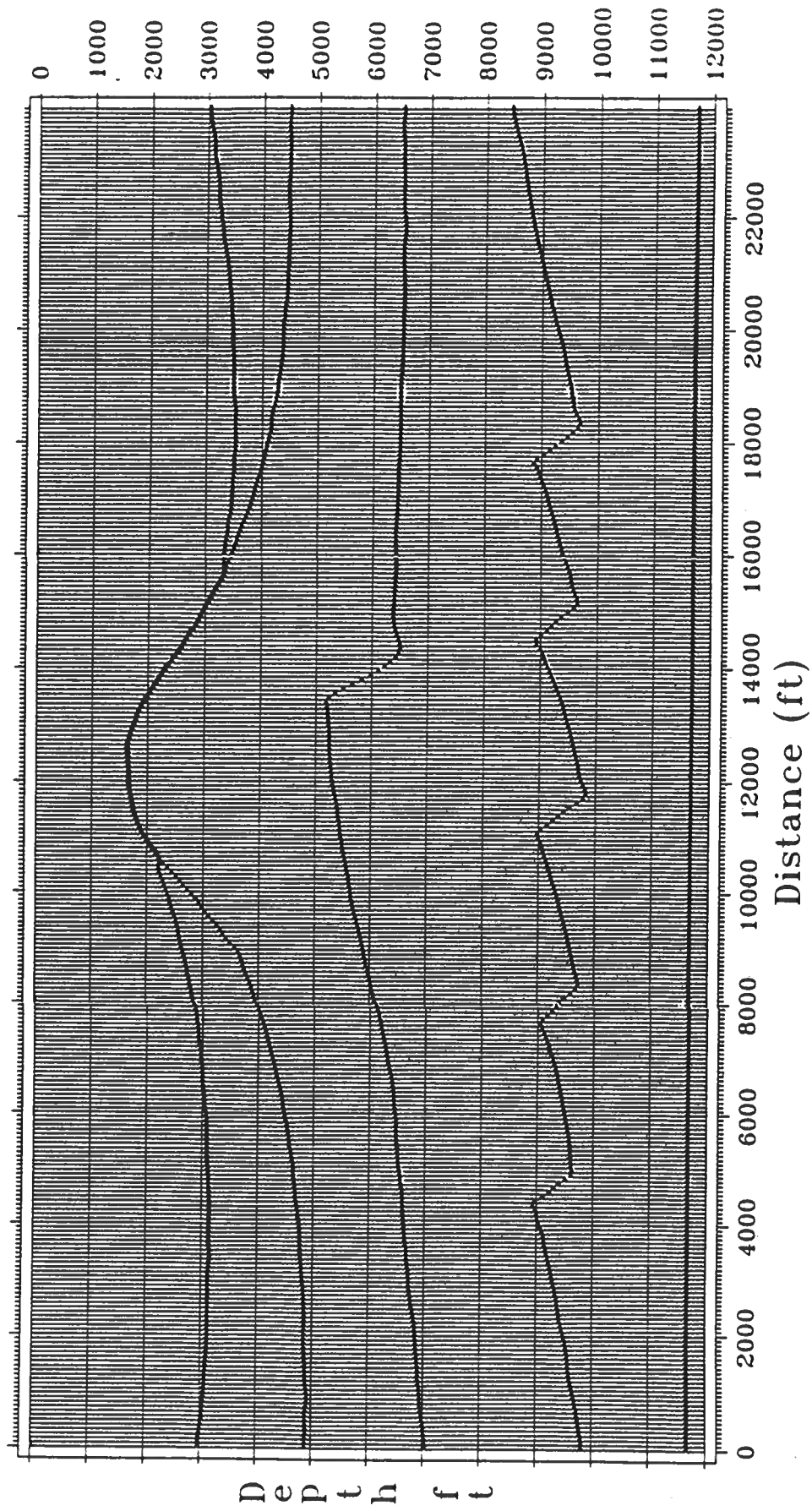


Figure 3.1: Input velocity model for first inversion. The velocities used were those shown in Figure 2.1.

Inversion of Shot 20000

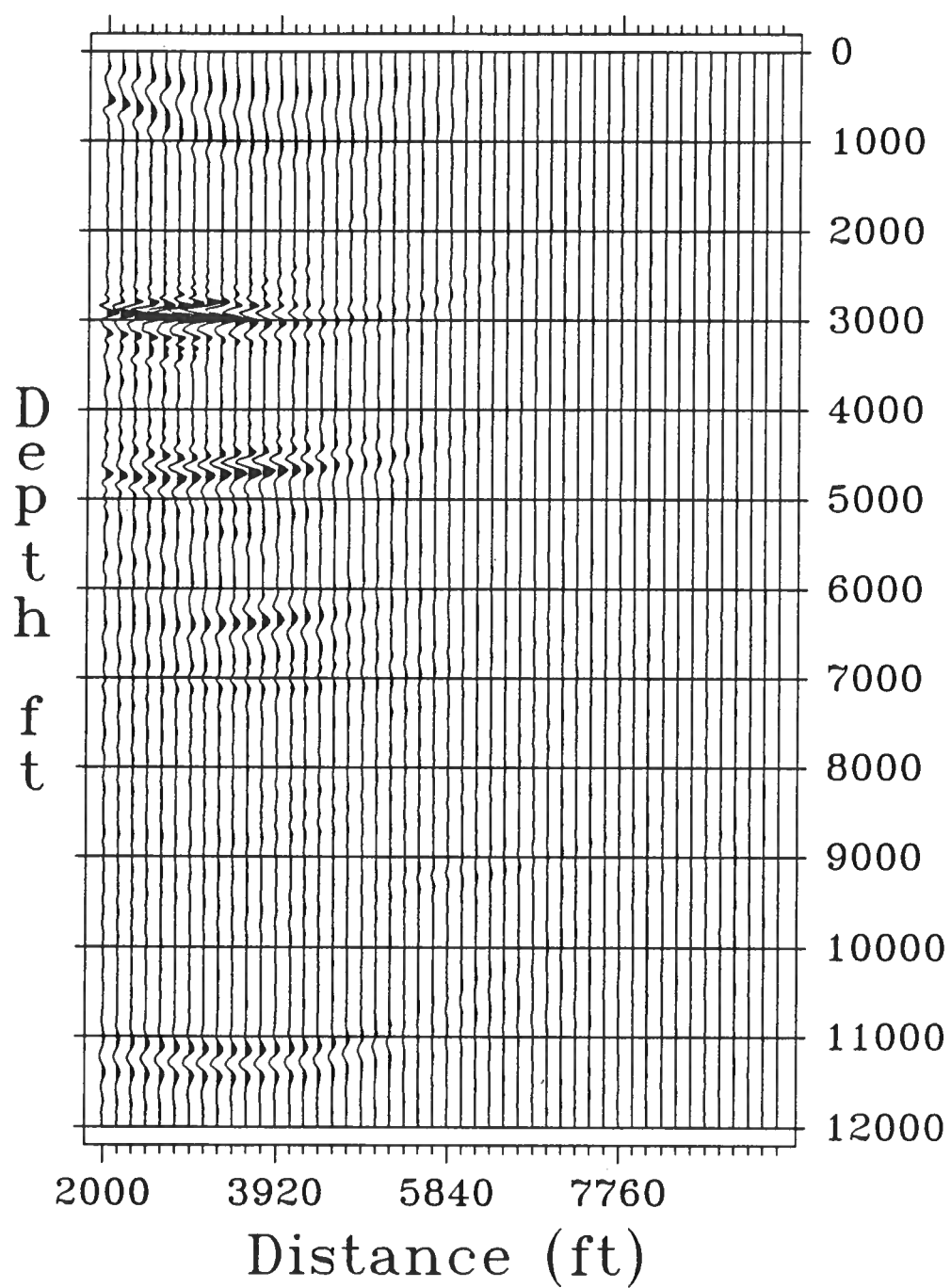


Figure 3.2: Shot inversion of shot record shown in Figure 2.2. Reflectors are partially imaged.



Second Background Model

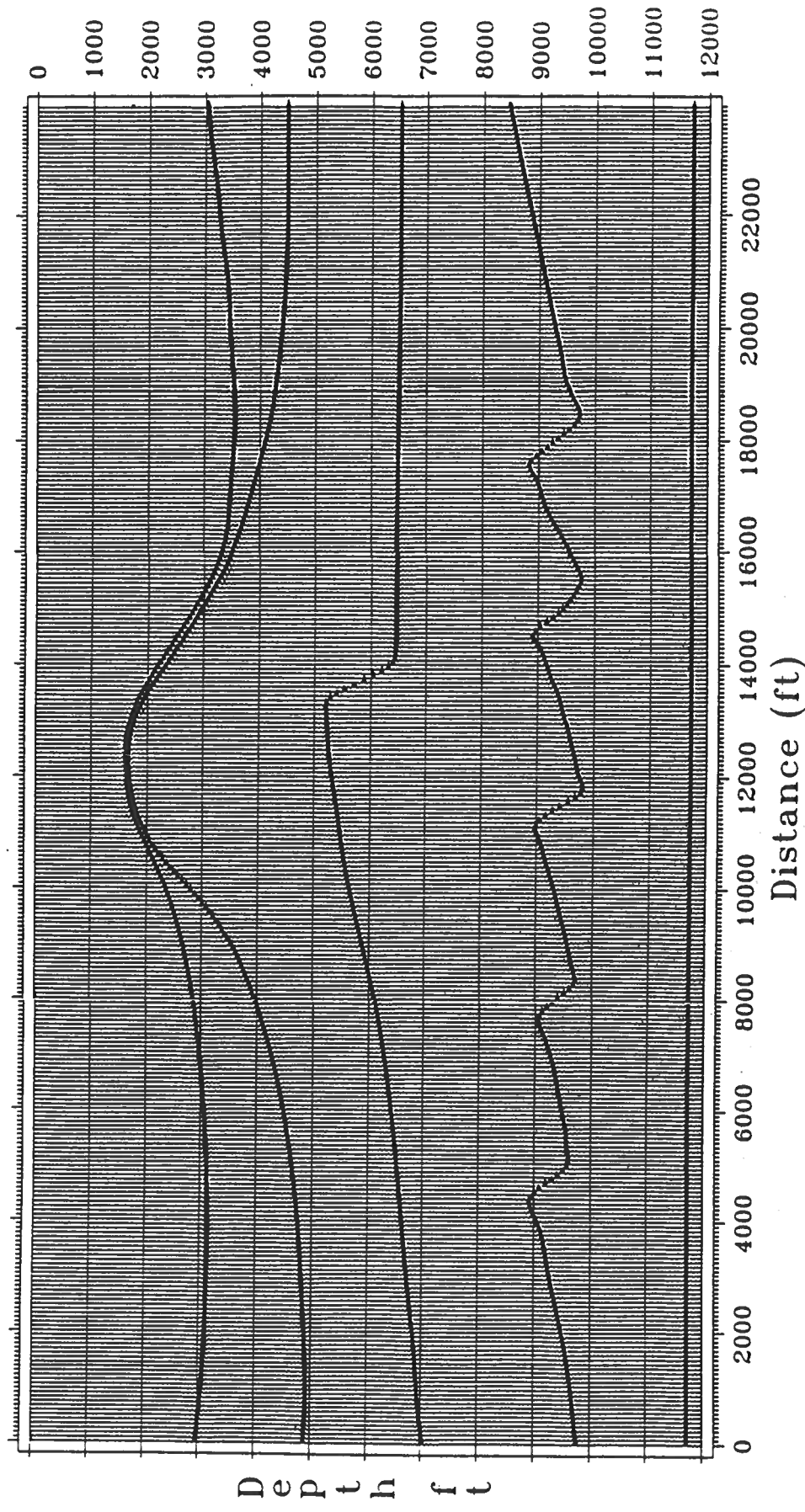


Figure 3.5: Input velocity model for second inversion. The velocities used were those shown in Figure 2.1. The interfaces here are smoother than in Figure 3.1

Inversion of Shot Record

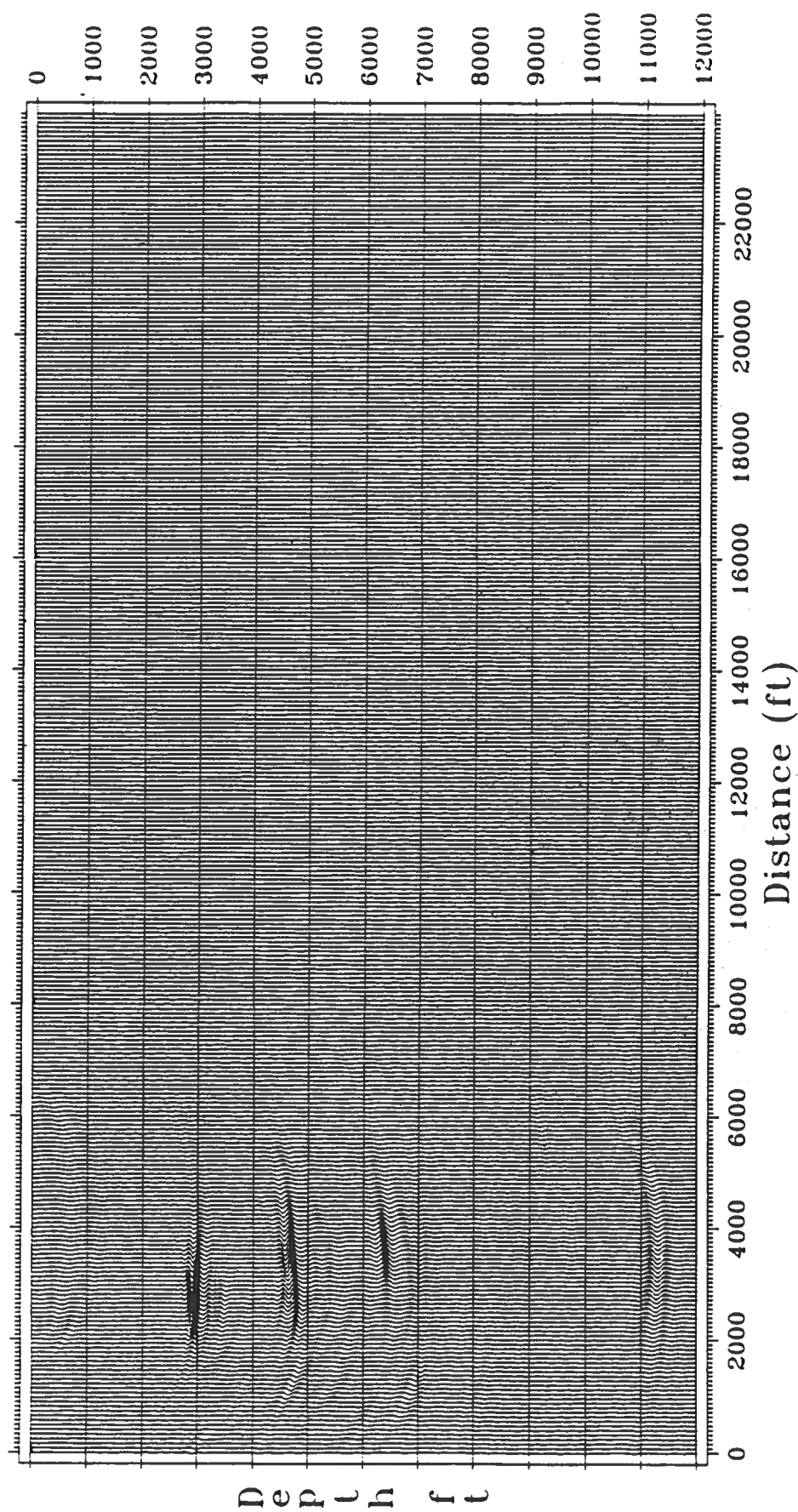


Figure 3.6: Second shot inversion of shot record shown in Figure 2.2. The second inversion output over a greater range than in the first inversion.

Stack of All Shot Inversions (gained)

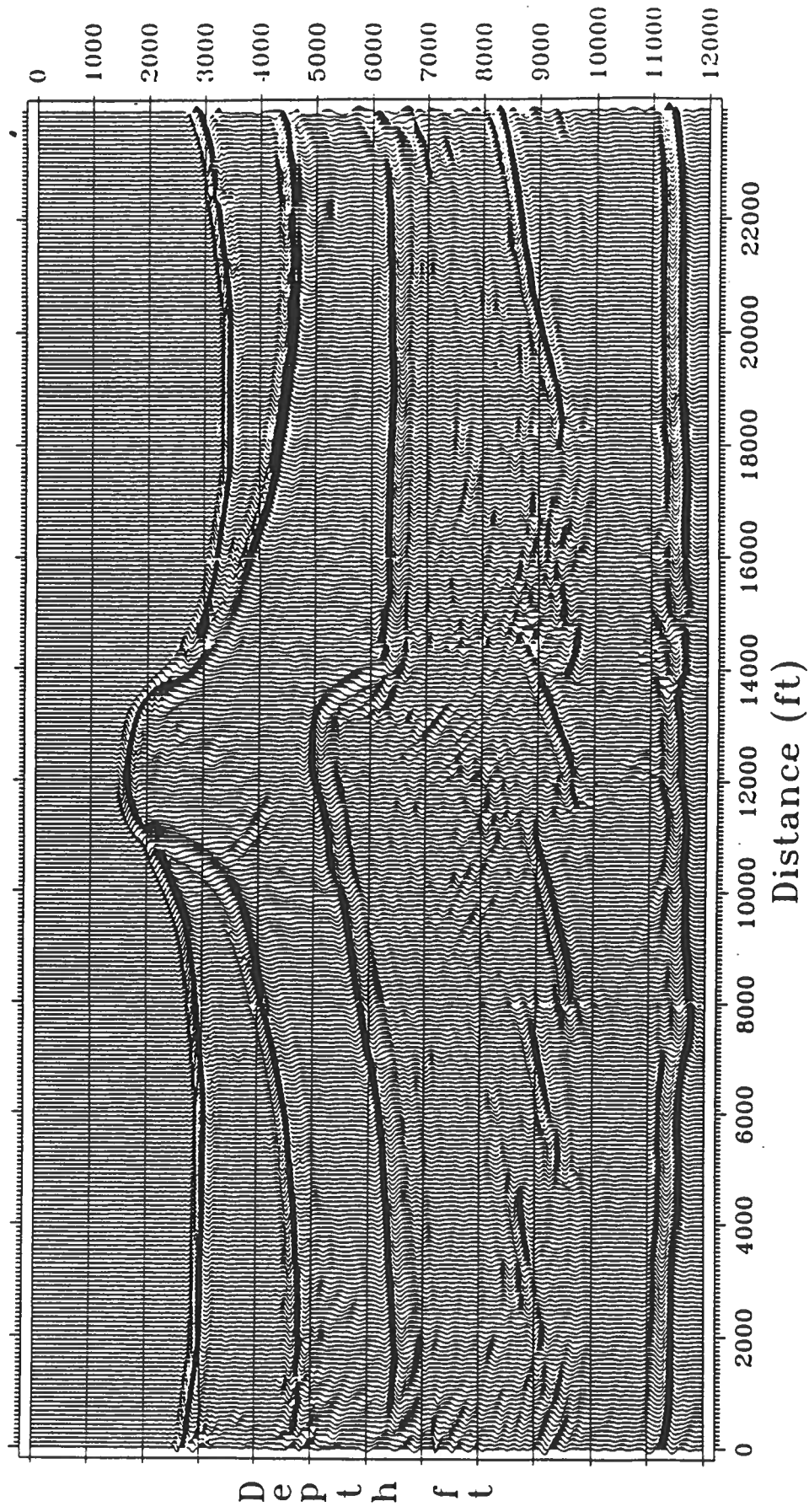
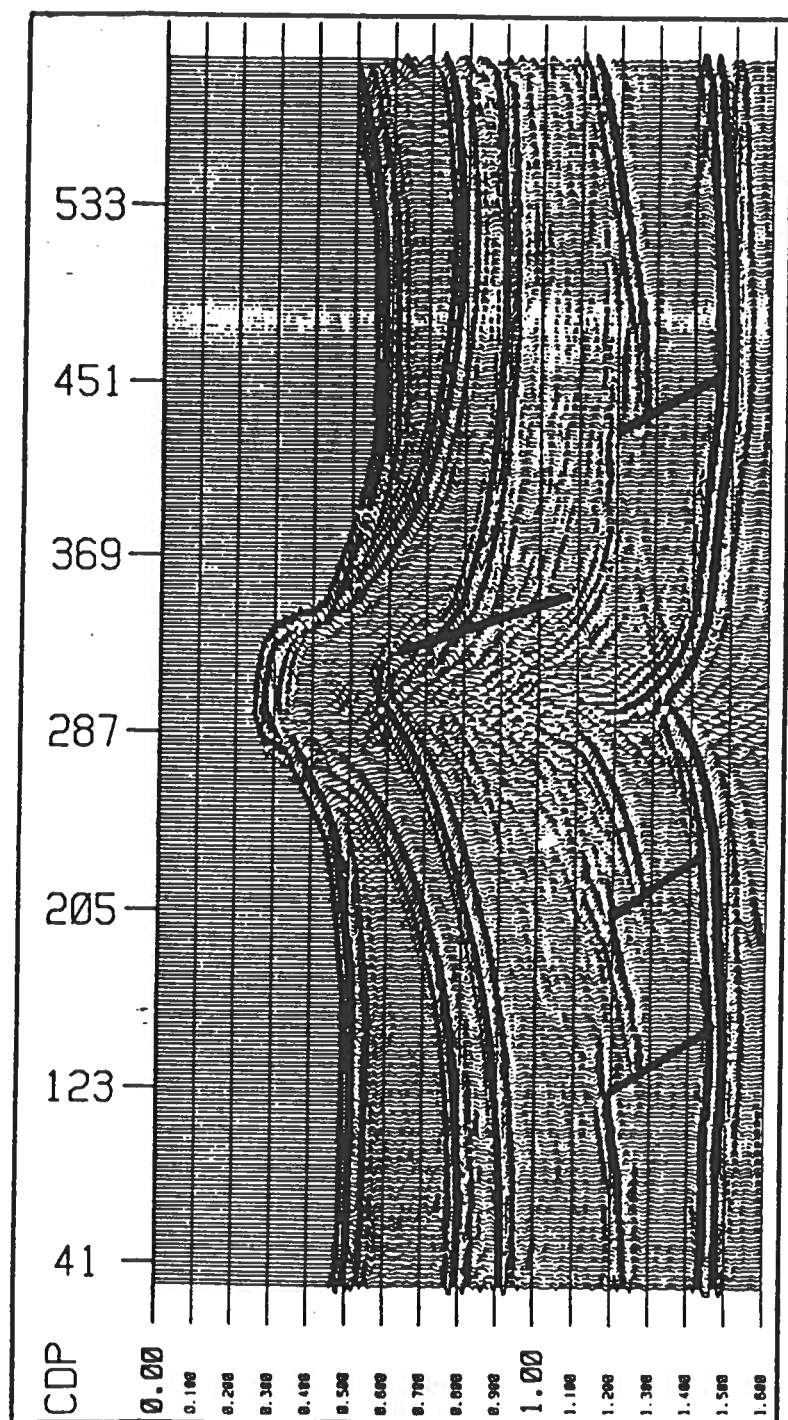


Figure 3.7: Stack of second inversions of all shot records. Migration noise is greater than in Figure 3.3 but steeper dips are imaged better. AGC has been applied after stack.



TIME MIGRATION
(FINITE DIFFERENCE METHOD)

Figure 3.8: University of Houston migration of Marathon data. Image is poorer than both Figure 3.3 and Figure 3.7.

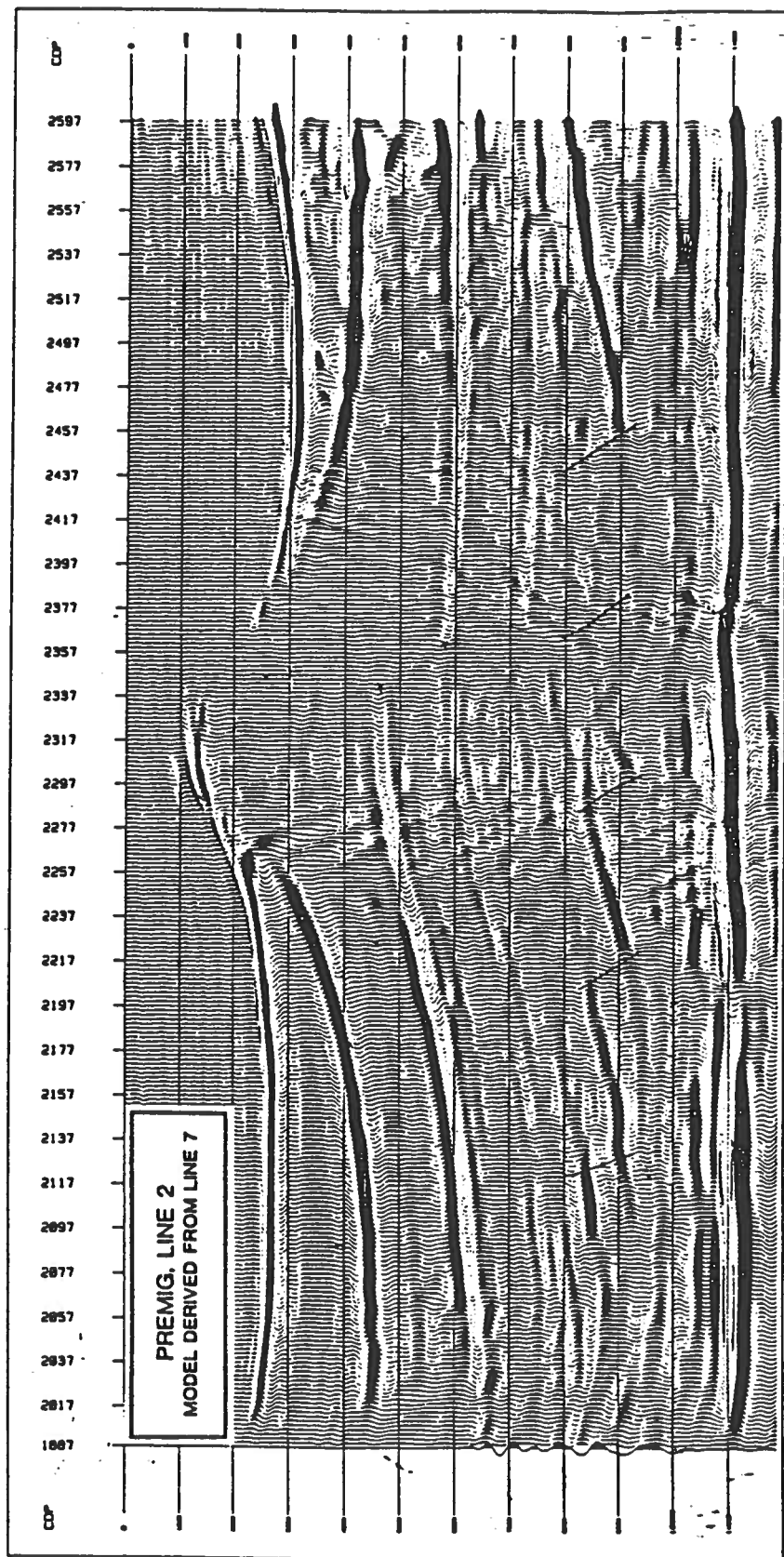


Figure 3.9: Prestack migration provided by Marathon. Result is better than Figure 3.8 but is still inferior to Figures 3.3 and 3.7.





Excerpts from

**Finite Difference Ray Tracing
and Common Shot Inversion**

by

Wenjie Dong

**Partially supported by the Consortium Project
on Seismic Inverse Methods for Complex Structures
at the Center for Wave Phenomena**

**Center for Wave Phenomena
Department of Mathematics
Colorado School of Mines
Golden, Colorado 80401
Phone (303) 273-3557**

3. 2.5D INVERSION OF COMMON-SHOT DATA

3.1 Introduction

The origins of this approach to seismic inversion can be found in the works of Cohen and Bleistein (1979). Beylkin (1985) proposed a method of operator inversion. The extended theory on that was developed in the papers of Cohen, Bleistein and Hagin (1986); and Bleistein, Cohen and Hagin (1987). The inversion operator presented in these papers is based on the Born approximation of the scattered field from a reflector. An alternative approach, an inversion operator based on the Kirchhoff representation of the scattered field from a single reflector, is presented in Sullivan and Cohen (1987). Docherty (1987) extended this approach to a medium comprised of many layers and implemented the theory for zero-offset data. This thesis, following the work of Docherty (1987), derives the explicit inversion formula for common-shot data. Also, the computer implementation was developed using Docherty's zero-offset inversion code as a point of departure.

Seismic inversion is similar to seismic migration in the sense of imaging. Therefore, migration can be viewed as partial inversion. In this chapter we begin a review of Kirchhoff migration, which is only concerned with traveltimes in this setting. Some insights are obtained to help us to understand the inversion process. Then, in an intuitive way, we introduce the idea of inversion. Based on the work of Bleistein, Cohen and Hagin (1987) and Docherty (1987), the inversion operator for common-shot data is derived. The operator takes into account the transmission effects through interfaces and out-of-plane as well as in-plane spreading factors. The output of the inversion is a reflectors map delineated by many singular functions scaled by angularly dependent reflection coefficients. The computer implementation of the formula is discussed. Finally, inversion results from three synthetic data examples and a real data example are presented.

3.2 Some Insights From Kirchhoff Migration

In migration, we seek to image or position reflectors in their true locations in the earth. The traveltimes within the medium play a crucial role in this imaging process. If the traveltimes can be calculated accurately, then, with no further information, it is possible to obtain a true image. The problem of migration is thus reduced to the problem of finding the traveltimes. For a post-stack (zero-offset) migration algorithm, the traveltimes argument is very simple.

We begin by considering the response of a point diffractor in a 2.5D medium. If a zero-offset survey was carried out along the in-plane direction vertically above the reflector, the two-way traveltimes between the observation surface and a diffractor

would define some curve, which is called a *diffraction curve*. For a constant velocity medium, the curve is a hyperbola. In general, however, it has other shapes depending on the location of the diffractor and the velocity structure in the medium above the point. It is important to note that the scattered energy from the point scatterer lies along this diffraction curve. On the time section shown in Figure 3.1, the hyperbola for the constant velocity case is presented.

Given the zero-offset time section, it is possible to locate the point scatterer by means of the following procedure. At an output point $x = (x, z)$ in the subsurface, compute the diffraction curve by tracing a ray to each receiver and then calculating the two-way traveltime. Then, lay the diffraction curve on top of the time section and when it cuts each trace, read the value of the data. Finally, sum these data values together and output the result at the point x . Repeating this operation at every point in the subsurface, we can obtain the migrated depth section.

Only when the output point x is at the location of the point scatterer will there be any significant output value from the above procedure. Thus, we expect to obtain an image of the point scatterer. If we treat a reflector as the ensemble of many point scatterers, this would produce a smooth reflector. This procedure leads to the formula

$$u(x) = \int d\xi [u_s(\xi, t)]_{t=2\tau(x, \xi)} \quad , \quad (3.2.1)$$

where $u(x)$ is the output at depth point x , $u_s(\xi, t)$ is the zero offset data at receiver location ξ and time t , and $\tau(x, \xi)$ is the one way traveltime between x and ξ found by ray tracing or by directly solving the eikonal equation.

For common shot gathers, it is not Kirchhoff migration as in Schneider (1978). It is more like a *diffraction migration* and the formula becomes

$$u(x, x_s) = \int d\xi_r [u_s(\xi_r, x_s, t)]_{t=\tau(x, \xi_r) + \tau(x_s, \xi_r)} \quad . \quad (3.2.2)$$

To implement (3.2.1) or (3.2.2), it is necessary to find many rays, since rays must be traced from each output point x to the receivers and source on the upper surface. This will be costly when the number of traces and output points increases.

Let us examine the imaging property of the function $u(x)$ in (3.2.1). We first consider the simplest case of constant velocity layer and flat reflector, for which the analysis is fairly straightforward.

The zero-offset time data collected above a flat reflector at depth h can be expressed as

$$u_s(\xi, t) = \frac{R}{8\pi h} \delta_B(t - 2h/c) \quad , \quad (3.2.3)$$

where R is the normal incident reflection coefficient, c is the velocity and $1/8\pi h$ is the two-way ($2h$) spreading factor. We use δ_B to denote the band-limited delta function in acknowledgement of the restricted range of frequencies in the data. In frequency domain, (3.2.3) becomes

$$U_s(\xi, \omega) = \frac{R}{8\pi h} F(\omega) e^{2i\omega h/c} \quad . \quad (3.2.4)$$

Here $F(\omega)$ is a high frequency bandpass filter. Then, we can rewrite (3.2.1) as

$$u(x) = \frac{1}{2\pi} \int d\xi \int d\omega U_s(\xi, \omega) e^{-2i\omega \tau(x, \xi)} \quad . \quad (3.2.5)$$

In a 2.5D constant velocity medium, τ , between an output point and a receiver location ξ , is

$$\tau(x, \xi) = \frac{\sqrt{(x - \xi)^2 + z^2}}{c} = \frac{r(x, \xi)}{c} \quad . \quad (3.2.6)$$

Substituting (3.2.4) and (3.2.6) into (3.2.5) and interchanging the order of integration, we have

$$u(x) = \frac{R}{16\pi^2 h} \int d\omega F(\omega) e^{2i\omega h/c} \int d\xi e^{-2i\omega r(x, \xi)/c} \quad . \quad (3.2.7)$$

We propose to analyze (3.2.7) by first applying the method of stationary phase (Bleistein, 1984) to the ξ integration. Treat $2\omega/c$ as *large* and consider the phase function

$$\phi = r(x, \xi) \quad . \quad (3.2.8)$$

According to the stationary phase method, the significant contribution to this

integration comes from the point(s) at which $\partial\phi/\partial\xi=0$. For this example, this is the point, $x=\xi$. This states that the major contribution comes from the receiver directly above the output point (not surprising). Calculating the second derivative of phase function at the stationary point, we get

$$\frac{\partial^2\phi}{\partial\xi^2} = \frac{-1}{z} \quad , \quad x=\xi \quad . \quad (3.2.9)$$

Using these results in the stationary phase formula (Bleistein, 1984), we find

$$u(x) = \frac{R\sqrt{cz}}{16\pi^{3/2}h} \int d\omega \frac{F(\omega)}{\sqrt{i\omega}} e^{-2i\omega(z-h)/c} \quad . \quad (3.2.10)$$

The result of the second integral is

$$u(x) = \frac{Rc}{8\pi h} \sqrt{z/2|h-z|} H_B(h-z) \quad . \quad (3.2.11)$$

H_B is a band-limited step function.

If there were no band-limiting present, then we would have a function that increased monotonically to a peak on the reflector and was zero everywhere below the reflector. This is illustrated by Figure 3.2. There are only two intersecting points between curve 1 and the data. The data values at these points are lower order comparing the value at the one point A of curve 2. Therefore, the summation near point A outputs the maximum value. There is no intersection between curve 3 and the data, therefore, the output is zero when $z > h$.

In equation (3.2.10),

$$\sqrt{i\omega} = \sqrt{|w|} e^{i\frac{\pi}{4}\text{sgn}(\omega)} \quad .$$

If this factor were not present above, the ω -integration would produce a band-limited delta function that peaked on the reflector, that is

$$\delta_B(z-h) = \frac{1}{\pi c} \int d\omega F(\omega) e^{-2i\omega(z-h)/c} \quad . \quad (3.2.12)$$

Therefore, multiplication of $U_s(\xi, \omega)$ in (3.2.4) by $\sqrt{i\omega}$ before migration would produce

an output of this form. Otherwise, the wavelet would be phase distorted and its peak would not be at the reflector. As a comparison, in Figure 3.3, 5 traces computed without including $\sqrt{i\omega}$ are plotted at the left, and another 5 traces computed by including that factor are at the right (from Docherty, 1987).

3.3 The Methodology Of Inversion Operator Derivation

As indicated in the first chapter, our inversion operator W , when applied to the data, should output a reflector map delineated by singular functions and angularly dependent reflection coefficients as a scale factor. In this section, starting from the analysis of migration, we develop this inversion operator.

Our analysis in Section 3.1 indicates that the image from the migration formula (3.2.1) is not a delta function. However, it is clear from that analysis that multiplication by $\sqrt{i\omega}$ leads to a delta function peaked at the reflector for a flat interface. We expect that the same is true for a curved reflector. Then the output will be a delta function with a slowly varying scale factor $h(x)$. That is

$$h(x)\gamma_B(x) = \int d\xi \int d\omega \sqrt{i\omega} e^{-i\omega[\tau(z,z_s) + \tau(z,z_r)]} U_s(\xi, \omega) \quad (3.3.1)$$

Then, what is left is to find a scaling factor for the operator that will transform $h(x)$ to $R(x, \theta)$.

In order that the height of the singular function on the reflector be $R(x, \theta)$, we insert into the above equation an unknown scaling function $b(x, \xi)$. This gives the final form of inversion operator W :

$$W[U_s(\xi, \omega)] = R(x, \theta)\gamma(x) = \int d\xi b(x, \xi) \int d\omega \sqrt{i\omega} e^{-i\omega[\tau(z,z_s) + \tau(z,z_r)]} U_s(\xi, \omega) \quad (3.3.2)$$

The remaining problem is to find a function $b(x, \xi)$, such that the above equation is satisfied.

This scaling function $b(x, \xi)$ is determined by our inversion theory (Bleistein, etc. 1987). That inversion theory is based on the assumption that seismic data is high-frequency data for which asymptotic methods are justified. The way that $b(x, \xi)$ is determined is by substituting a known representation of scattered $U_s(\xi, \omega)$ in 2.5 dimensions into equation (3.3.2). There are two spatial integrals involved in that formula. The integration along the recording surface (imaging procedure) and the integration along the reflector (diffraction from a interface) are performed by the

method of stationary phase in two dimensions (Bleistein, 1984). By doing all the above analysis, Bleistein, Cohen and Hagin (1987) find that for Kirchhoff data $b(\mathbf{x}, \xi)$ has to be chosen as

$$b(\mathbf{x}, \xi) = \frac{\sqrt{1/\sigma_s + 1/\sigma_r} |I_s \partial\beta(\mathbf{x}_s)/\partial\xi + I_r \partial\beta(\mathbf{x}_r)/\partial\xi|}{2(2\pi)^{3/2} A_f A(\mathbf{x}, \mathbf{x}_s) A(\mathbf{x}, \mathbf{x}_r)} \quad (3.3.3)$$

Where σ_s and σ_r are the running parameters for rays from source and receiver point to output point. A_f is the area under the bandpass filter $F(\omega)$. β is the takeoff angle of a ray at source or receiver, and its derivative with respect to ξ is the in-plane spreading factor. I_s and I_r are parameters determined by recording geometry. $A(\mathbf{x}, \mathbf{x}_s)$ and $A(\mathbf{x}, \mathbf{x}_r)$ are the leading order amplitudes recorded at output point \mathbf{x} due to source and receivers at positions \mathbf{x}_s and \mathbf{x}_r , respectively. Then, our inversion operator for Kirchhoff data is

$$W[U_s(\omega, \xi)] = \frac{1}{2(2\pi)^{3/2} A_f} \int d\xi \frac{\sqrt{1/\sigma_s + 1/\sigma_r} |I_s \partial\beta(\mathbf{x}_s)/\partial\xi + I_r \partial\beta(\mathbf{x}_r)/\partial\xi|}{A(\mathbf{x}, \mathbf{x}_s) A(\mathbf{x}, \mathbf{x}_r)} \int d\omega \sqrt{i\omega} e^{-i\omega[\tau(\mathbf{x}, \mathbf{x}_s) + \tau(\mathbf{x}, \mathbf{x}_r)]} U_s(\omega, \xi) \quad (3.3.4)$$

This formula tells us that the amplitude and traveltimes of wave propagating from source to output point is needed, so is the amplitude from receiver to the output point. This means we have to shoot new rays for every receiver without using the ray information of the previous ray. This will slow down the ray computation. A faster way to do this is to shoot rays from the output point to receiver, so we can utilize the information of the previous ray. This will bring the problem of reciprocity of the amplitudes and traveltimes. In the next section we discuss the reciprocity problem.

3.4 The Reciprocity Problem

Formula (3.3.4) tells us that the traveltimes and amplitudes are obtained by recording waves propagating from source and receiver to the output point. This requirement can be satisfied using our second method of solving the eikonal equation and the transport equation. Now, consider the reciprocity. It is clear that traveltimes has the property of reciprocity, that is

$$\tau(\mathbf{x}, \mathbf{x}_s) = \tau(\mathbf{x}_s, \mathbf{x}) ; \quad \tau(\mathbf{x}, \mathbf{x}_r) = \tau(\mathbf{x}_r, \mathbf{x}) \quad (3.4.1)$$

Next, let us consider the reciprocity of amplitude. Suppose we have a flat interface with wave incident on it at an angle of θ_i . The transmitted ray is at the angle of θ_t .

Suppose also there is a point source at x_s . The amplitude of the wave at the incident point is A_1 such that

$$A_1 = A_0 \frac{r_0}{r_1} , \quad (3.4.2)$$

where, A_0 is the magnitude of the source, r_0 for the radius of the initial sphere, and r_1 for the radius of the sphere intersecting with the interface.

The amplitude of the wave in the lower medium A_2 is determined by the formula

$$A_2 = A_1 \frac{\sqrt{\cos\theta_t}}{\sqrt{\cos\theta_i}} T , \quad (3.4.3)$$

where the ratio of the square root cosines is due to the ray tube expansion or contraction. It is computed from the ratio of the areas. T is the transmission coefficient and

$$T = \frac{2c_2 \cos\theta_i}{c_2 \cos\theta_i + c_1 \cos\theta_t} . \quad (3.4.4)$$

The amplitude at point x is

$$A_3 = A_2 \frac{r_1}{r_1 + r_2} . \quad (3.4.5)$$

Substituting (3.4.2) and (3.4.3) to (3.4.5), we have

$$A(x, x_s) = A_3 = \frac{2tc_1 c_2 \sqrt{\cos\theta_i} \sqrt{\cos\theta_t}}{(r_1 + r_2)(c_2 \cos\theta_i + c_1 \cos\theta_t)} . \quad (3.4.6)$$

Here, we have written $r_0 = c_1 t$. If we place our source at the point x , and do the same calculation, we find that the same result is obtained. The effect of the transmission coefficient difference is compensated for by the expansion or contraction factor and the fact that the initial amplitude depends on the local velocity. Here we write down the corresponding equations.

$$A_2 = A_0 c_2 t / r_2 \quad , \quad A_1 = A_2 T^* \frac{\sqrt{\cos\theta_i}}{\cos\theta_t} \quad . \quad (3.4.7)$$

$$T^* = \frac{2c_1 \cos\theta_t}{c_1 \cos\theta_t + c_2 \cos\theta_i} \quad , \quad A(x_s, x) = A_1 \frac{r_2}{r_2 + r_1} \quad . \quad (3.4.8)$$

Then,

$$A(x_s, x) = A_3 = \frac{2tc_1 c_2 \sqrt{\cos\theta_i} \sqrt{\cos\theta_t}}{(r_1 + r_2)(c_2 \cos\theta_i + c_1 \cos\theta_t)} \quad . \quad (3.4.9)$$

We have proved the reciprocity of amplitudes between the source and output point; the same is true between receiver and output point. That is

$$A(x, x_s) = A(x_s, x) \quad ; \quad A(x, x_r) = A(x_r, x) \quad . \quad (3.4.10)$$

Thus, the amplitudes recorded at the output point x due to the source at x_s or x_r are equivalent to the amplitudes recorded at x_s or x_r due to the source at the output point x . The running ray parameters also satisfy reciprocity.

3.5 Inversion Operator For Common-Shot Data

Based on the reciprocity of amplitudes, traveltimes and running parameters, the inversion operator in (3.3.4) can be rewritten as

$$W[U_s(\omega, \xi)] = \frac{1}{2(2\pi)^{3/2} A_f} \int d\xi \frac{\sqrt{1/\sigma_s + 1/\sigma_r} |I_s \partial\beta(x_s)/\partial\xi + I_r \partial\beta(x_r)/\partial\xi|}{A(x_s, x) A(x_r, x)} \int d\omega \sqrt{i\omega} e^{-i\omega[\tau(x_s, x) + \tau(x_r, x)]} U_s(\omega, \xi) \quad . \quad (3.5.1)$$

Therefore, in order to implement (3.5.1), it is necessary to trace rays from each output point, x , to source and receivers on the upper surface. This is true regardless of the recording geometry and is by far the most difficult operation in the inversion procedure. Because of the cost of ray tracing, we proposed in Chapter 1 the method of directly solving the eikonal equation by finite difference. Because it was terrible around caustics, we will at the moment use equation (3.4.3) to derive the inversion

operator for common shot data.

Specializing to the case of layered media with constant velocity in each layer, we can use the results in Section 2.3, equation (2.3.11) for the amplitude of the Green's function. For a flat observation surface, the differential surface element is 1, and $n_0 \cdot p(x_s, r, x) = \cos \beta(x_s, r)$. We write the transmission loss factor as

$$T(x_s, r, x) = \prod_{j=1}^N K_j [\cos \theta_{j'} / \cos \theta_j]^{1/2} . \quad (3.5.2)$$

Here, K_j is the transmission coefficient of the upcoming wave at j -th interface; $\theta_{j'}$ and θ_j are the incident and transmitted angle for the upcoming wave. The amplitude expression for the ray from x to x_s becomes

$$A(x_s, x) = \frac{1}{4\pi} [c(x) \cos \beta(x_s) / \sigma_s]^{1/2} |\partial \beta(x) / \partial x_s|^{1/2} T(x_s, x) . \quad (3.5.3)$$

Here $\beta(x_s)$ is the emerging angle of the ray at x_s measured from the vertical. The expression for $A(x_r, x)$ is analogous to (3.4.5). Substituting $A(x_s, x)$ and $A(x_r, x)$ into 3.5.1, we have

$$W[U_s(\omega, \xi)] = \frac{2\sqrt{2\pi}}{c(x)A_f} \int d\xi \frac{\sqrt{\sigma_s + \sigma_r} \sqrt{\cos \beta(x_s) \cos \beta(x_r)}}{\sqrt{\partial \beta(x) / \partial x_s \partial \beta(x) / \partial x_r}} \\ \frac{|I_s \partial \beta(x_s) / \partial \xi + I_r \partial \beta(x_r) / \partial \xi|}{T(x_s, x) T(x_r, x)} \int d\omega \sqrt{i\omega} e^{-i\omega[\tau(x_s, x) + \tau(x_r, x)]} U_s(\omega, \xi) . \quad (3.5.4)$$

For the special case of a common-shot gather in 2.5D, $I_s = 0$ and $I_r = 1$, see Bleistein, Cohen and Hagin (1987). Applying these conditions to (3.7.3) we have the final result of the inversion operator for common shot data as

$$W[U_s(\omega, \xi)] = \frac{2\sqrt{2\pi}}{c(x)} \int d\xi \frac{\sqrt{\sigma_s + \sigma_r} \sqrt{\cos \beta(x_s) \cos \beta(\xi)} \sqrt{\partial \beta(\xi) / \partial \xi}}{T(x_s, x) T(\xi, x) \sqrt{\partial \beta(x_s) / \partial \xi}} \\ \frac{1}{A_f} \int d\omega \sqrt{i\omega} e^{-i\omega[\tau(x_s, x) + \tau(\xi, x)]} U_s(\omega, \xi) . \quad (3.5.5)$$

3.6 Computer Implementation

For the common shot inversion formula in equation (3.5.5), the computer processing proceeds as follows.

1. Preprocessing the data

The function $U_s(\omega, \xi)$ represents the Fourier transform of seismic data in a trace, with the source and receiver points given by ξ and x_s . The ω integration represents a filtering and inverse transform of the trace, and because this is independent of the ξ integration, the computation can be done as a preprocessing step. This is equivalent to establishing an inverse Fourier transform table with time as index.

2. Computing traveltime and amplitude for each ray

Given an output point $x = (x, z)$ and a ξ value, we determine the ray paths from x to x_s and ξ , and calculate $\tau(x_s, x)$, $\tau(\xi, x)$, and the transmission and spreading factors.

3. Interpolation and sum over receivers

After calculating traveltime, the program obtains the corresponding value in the inverse Fourier transform table by checking the time index. Multiplying this value with amplitude and other factors, we get the inversion contribution from that particular receiver. Finally, summing these contributions over all the possible receivers, we obtain the angularly dependent reflection coefficient at that particular output point. The summation corresponds to the ξ integration.

In the inversion code, I actually divided the integrand of the ξ integration into three parts as

$$amp1 = \frac{\sqrt{\cos\beta(x_s)}}{\sqrt{c(x)} T(x_s, x) \sqrt{\partial\beta(x_s)/\partial x_s}}, \quad (3.6.1)$$

$$amp2 = \frac{\sqrt{\cos\beta(\xi)} \sqrt{\partial\beta(\xi)/\partial \xi}}{\sqrt{c(x)} T(\xi, x)}, \quad (3.6.2)$$

$$amp3 = \sqrt{\sigma_s + \sigma_r}. \quad (3.6.3)$$

Then, the amplitude subroutine computes T and the emergence angle. Therefore, the same subroutine can be used for calculating $amp1$ and $amp2$. The derivative terms (spreading factor) and $amp3$ are calculated in the main program right after ray tracing.

There are other considerations in the code that are worth mentioning here. The first is the antialiasing filter. Spatial aliasing of seismic data is caused by insufficient sampling. Receiver spacing and temporal bandwidth determine the maximum dip that the inversion can recover. The energy coming from steeper reflectors becomes the aliased energy and, as in the frequency domain, this energy will appear as a lower wave number event. Therefore, in the inversion code we have to remove the aliased energy before we perform inversion. In Appendix A, we derive the antialiasing criterion for common shot data. It turns out that for rays emerging into the surface at angles less than θ_a , the energy is not aliased energy. Here θ_a is defined as

$$\theta_a \leq \sin^{-1} \left(\frac{c}{2f_{\max} \Delta \xi} \right) . \quad (3.6.4)$$

Where, f_{\max} is the maximum frequency in the data, c is the near surface layer velocity, and $\Delta \xi$ is the receiver spacing. For rays whose emerging angle is greater than θ_a , we set the amplitude contribution of these rays to zero.

The second consideration is the sampling rate of output depth. We know that our band-limited singular function is approximately a sinc function. We require that the sampling rate in depth be such that there are four sample points in the interval of the main lobe. Therefore, if Δz is the sample interval, from the analysis in Appendix B, we have

$$\Delta z = \frac{c}{8(f_{\max} + f_{\min})} , \quad (3.6.5)$$

because the identification of a reflector is due to the main lobe of the sinc function. We remark also that the first zero of sinc function away from its maximum belongs to the upper medium. That is, the output point within a range lower than the reflector will be treated as an output point in upper medium. This range is

$$z = \frac{c}{2(f_{\max} + f_{\min})} . \quad (3.6.6)$$

Another concern in the code is to reduce the CPU time for calculation of traveltime and amplitude. What was done in the code is to shoot sparse rays and then interpolate in three dimensions. That is, interpolation between receivers, between

output traces, and between output points. In this way the computation time will be significantly reduced.

3.7 Test Cases Of the Inversion

To test our inversion operator for common shot data, in this section we present three synthetic examples and a real data example in this section.

Example 1:

This example is designed to test mainly whether or not the inversion result is a reflector map with angularly dependent reflection coefficient as its scalar. For this reason we choose a very simple geological model with one flat interface at 2000 units depth. The upper medium velocity is 5000 units, and the lower medium is 10000 units. The shot position at 5000. units, and 200 receivers starting from 2000. to 8000. with the receiver spacing 30. The data is generated using our common shot modeling program. Figure 3.4 shows the ray paths and Figure 3.5 the data. The inversion result is shown in Figure 3.6. We can see that the inversion operator outputs the interface exactly at 2000 units depth. To compare the inversion result to the exact reflection coefficient on the reflector, we plotted them in Figure 3.7. We find that the exact reflection coefficient for normal incidence is 0.333., while our inversion result at normal incidence position outputs the reflection coefficient as 0.347. The relative error here is 4 percent. In fact, the inversion output in the transverse range, 4250 to 5750, has an error within 4 percent.

Given the lower and upper medium velocities, one can easily compute that the critical points are at 3842.3 and 6154.7. At these points, the errors increase to 22 percent. This is not surprising because our inversion theory breaks down at the critical reflection. Beyond the critical point, the error in our inversion output will decrease. The theory predicts that the output will be twice the real part of the reflection coefficient.

Therefore, we remark that our common shot inversion is very accurate for small velocity contrast and small dip reflectors and for larger contrast away from critical. Certainly, if the upper medium has higher velocity than the lower medium, there will be no problem with a critical angle.

Example 2 and 3:

These two examples are designed to test the inversion on two typical geological models of seismic interest. One is a syncline consisting of four interfaces, and the other one is a salt dome of five layers. For the syncline case, the shot is located at the middle of the receiver array. Sample ray paths and the shot record are displayed in Figure 3.8

and Figure 3.9. We can see the bow-tie-like reflection from the lowest interface, respectively. The inversion result is shown in Figure 3.10. We can see that for portions that rays have illuminated, the inversion result is close to the original model. All the tails on the inversion section are due to the arbitrary truncation of the data and the impulse response of the inversion operator. Also, we note that for the portion not illuminated by rays, the inversion result is weak. Therefore, we can not expect to determine the reflection coefficient in this part of the output.

For the testcase on a salt dome, the results are similar. The ray paths, shot record and inversion result are shown in Figures 3.11, 3.12 and 3.13.

Example 4:

This is a testcase on real common shot data. The data was generated by Marathon Oil Company in a physical laboratory. There are four layers made of epoxy immersed in water. The experiment is equivalent, after scaling to a transverse range of -800 to 23200. The model of this experiment is shown on Figure 3.14. There are 301 shot records generated over this range. For each shot there are 48 receivers with receiver spacing 80. The offset (distance from shot to first receiver) is 800. The shot move-up between experiments is 80. Therefore the data is 24 fold (if the reflector is flat). In Figure 3.15 we show four shot records over the shot range from 8000 to 8240. For detail we also show on Figure 3.16 a single shot gather. From these gathers we can see the very strong direct wave (as first break). Also, we can see the first primary event which is very strong and is recognized as the water bottom reflection. All other primary events are identified by their skewed hyperbolic shapes, which indicate the reflectors dip down toward the left. The tank bottom reflection can be easily identified by its strong energy character.

The inversion results are shown in Figures 3.17 and 3.18, respectively. We can easily see that three dipping interfaces and the tank bottom are clearly located. The first event in the inversion plot is due to the direct arrivals in the shot gathers. The strong character of the second event in the plot indicates the strong reflection coefficients at the water bottom. Also, we can not see noise events on the plot. This indicates that there is little or no P-S converted energy in the shot gathers. This was verified by J. Emanuel using several other methods.

After carrying out the inversion on 296 gathers, we stacked them together to obtain the post-inversion stacked result, which is shown in Figure 3.19. We can see from this figure that the water bottom and the second interface are clearly delineated. The fault on the third interface is identified correctly. In this plot we can not tell many details about the fourth interface. Therefore, we apply automatic gain in a window of 200 samples to the inversion output. Figure 3.20 shows the result of this gain process. We can see that the fourth interface with clear faulting position is

identified. The tank bottom can also be clearly located. Comparing the model to this figure, we remark that all the interfaces are located correctly, as are the faulting positions.

REFERENCES

- Beylkin, G., 1985, Imaging of Discontinuities in the Inverse Scattering Problem by Inversion of a Causal Generalized Radon Transform: *J. Math. Phys.*, **26**, 99-108.
- Bleistein, N., 1984, *Mathematical Methods for Wave Phenomena*: Academic Press, New York.
- Bleistein, N., 1986, Two-And-One-Half Dimensional In-plane Wave Propagation: *Geophys. Prosp.*, **34**, 686-703.
- Bleistein, N., Cohen, J. K., and Hagin, F. G., 1985, Computational and asymptotic aspects of velocity inversion: *Geophysics*, **50**, 1253-1265.
- Bleistein, N., and Gray, S. H., 1985, An extension of the Born inversion method to depth dependent reference profile: *Geophysical Prospecting*, **33**, 999-1022.
- Cohen, J. K., and Bleistein, N., 1979a, Velocity inversion procedure for acoustic waves, *Geophysics*, **44**, 1077-1085.
- Cohen, J., Hagin, F., Bleistein, N., 1986, Three-Dimensional Born Inversion With An Arbitrary Reference: *Geophysics*, **51**, 1552-1558.
- Docherty, P. C., 1987, Ray theoretical modeling, migration and inversion in two-and-one-half-dimensional layered acoustic media: Center for Wave Phenomena Research Report, CWP-051.
- Gray, S. H., 1986, Efficient traveltimes calculations for Kirchhoff migration: *Geophysics*, **51**, 1685-1688.
- Allen, R., Pruess, S., Shampine, L., 1987, *Fundamentals of numerical computing: Lecture Notes*.
- Schneider, W. A., 1978, Integral formulation for migration in two and three dimensions: *Geophysics*, **43**, 49-76.
- Sullivan, M. F. and Cohen, J. K., 1987, Prestack Kirchhoff inversion of common-offset data: *Geophysics*, **52**, 745-754.



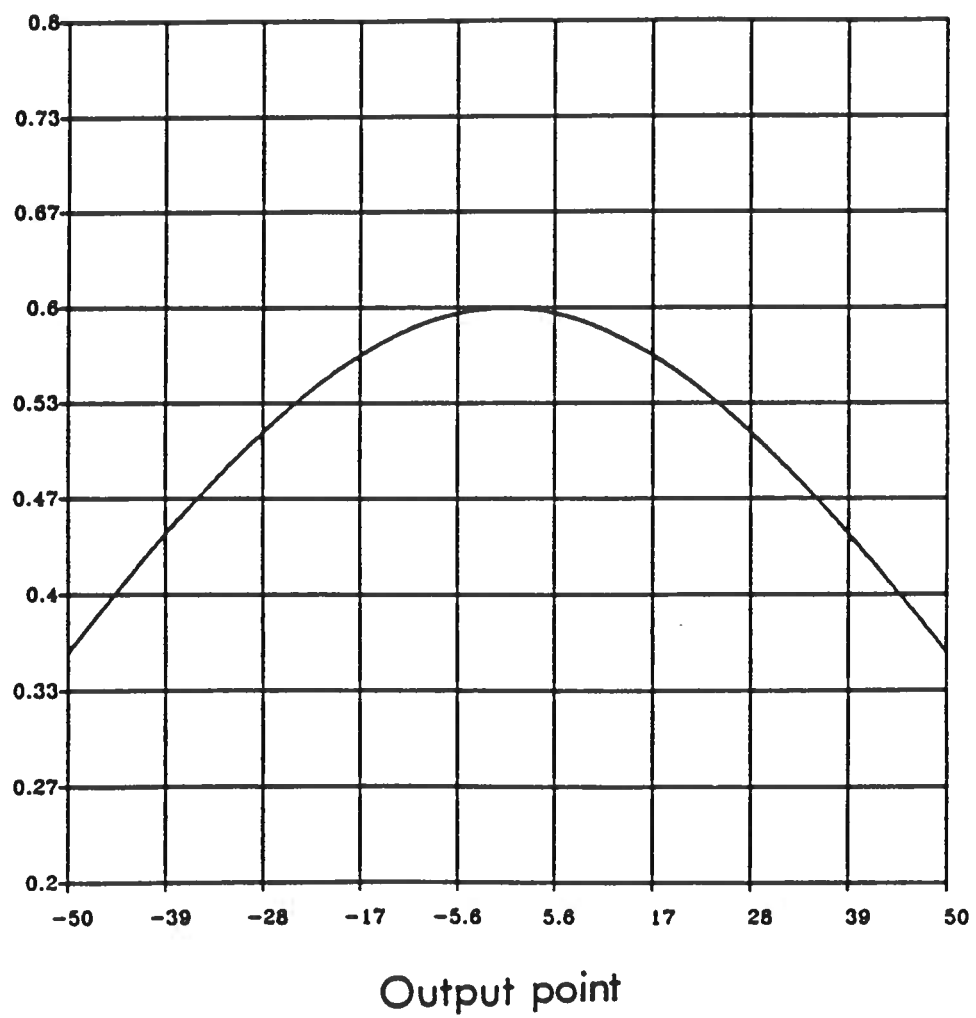


Figure 3.1 – Diffraction curve in constant speed medium.

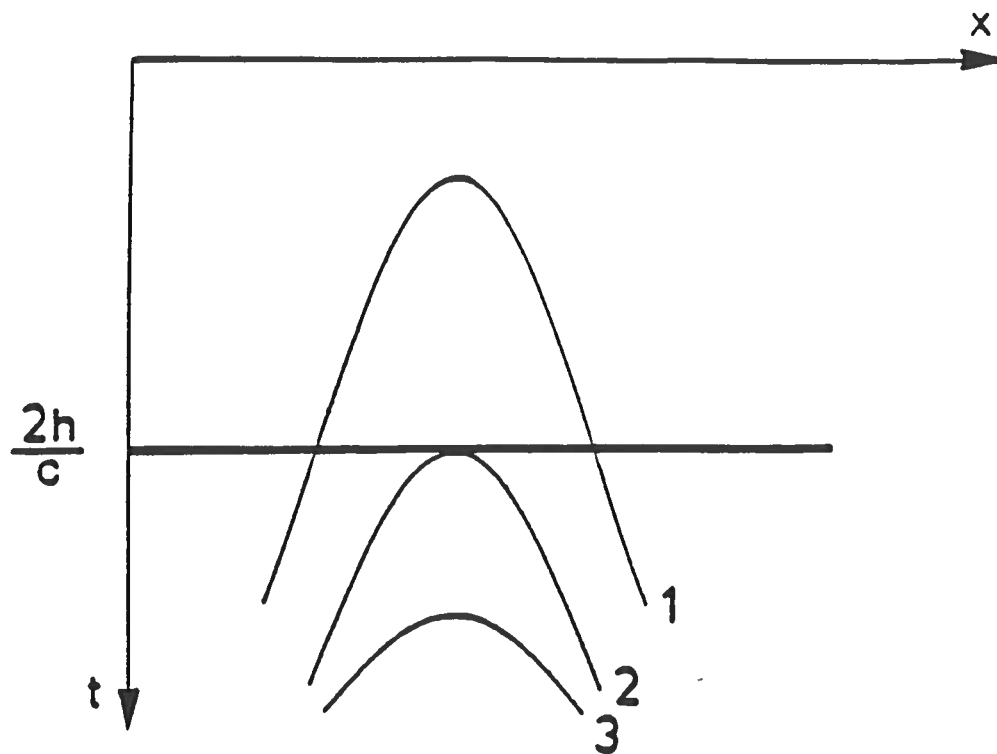


Figure 3.2 – Diffraction curves calculated at three depths in a model consisting of a single horizontal reflector. Curve 1 is for an output point above the reflector. Curve 2 corresponds to an output point at the depth of the reflector and curve 3 for an output point below the reflector (From Docherty, 1987).

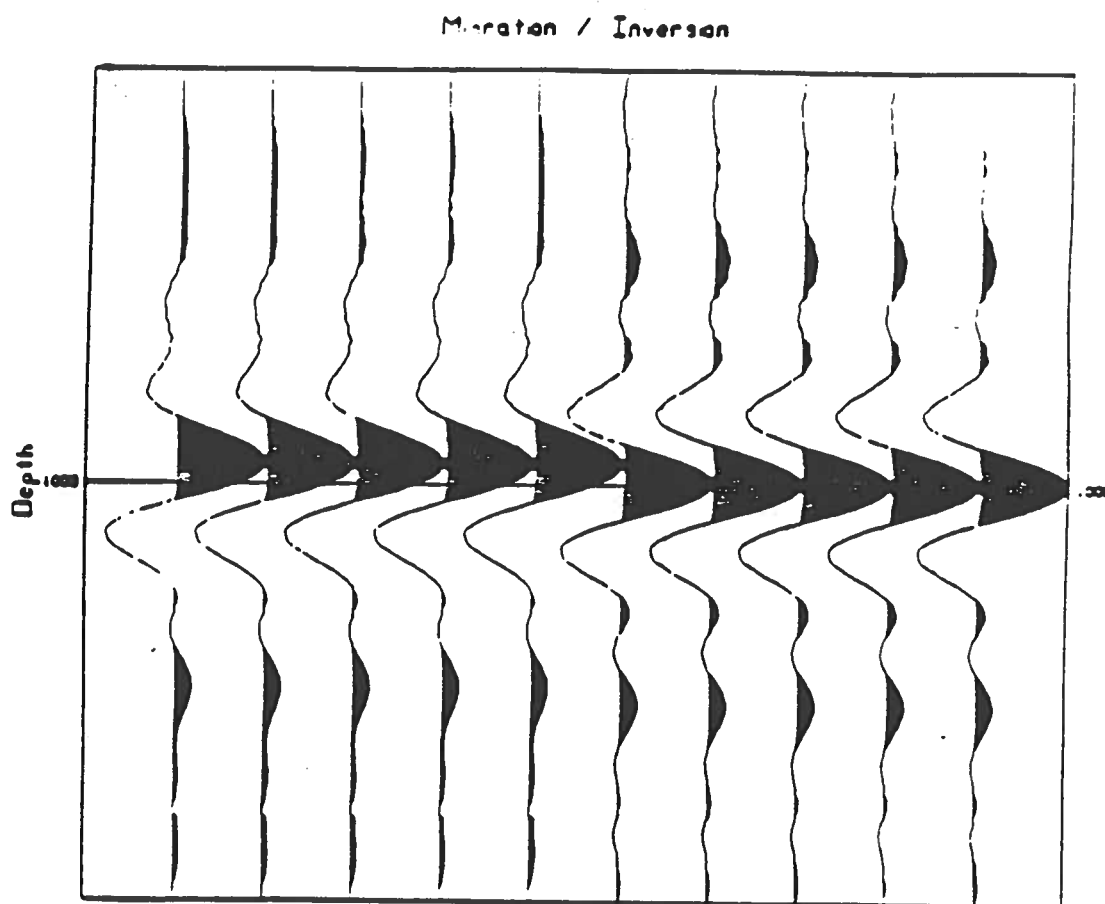


Figure 3.3 – The five traces on the left are the output of the migration algorithm when the time data was from a horizontal at depth 1000 ft. The five traces on the right illustrates the effect of multiplying the time data by $\sqrt{i\omega}$ before migration. Note the correct positioning of the amplitude in the five traces on the right. (From Docherty, 1987).



Model and Rays

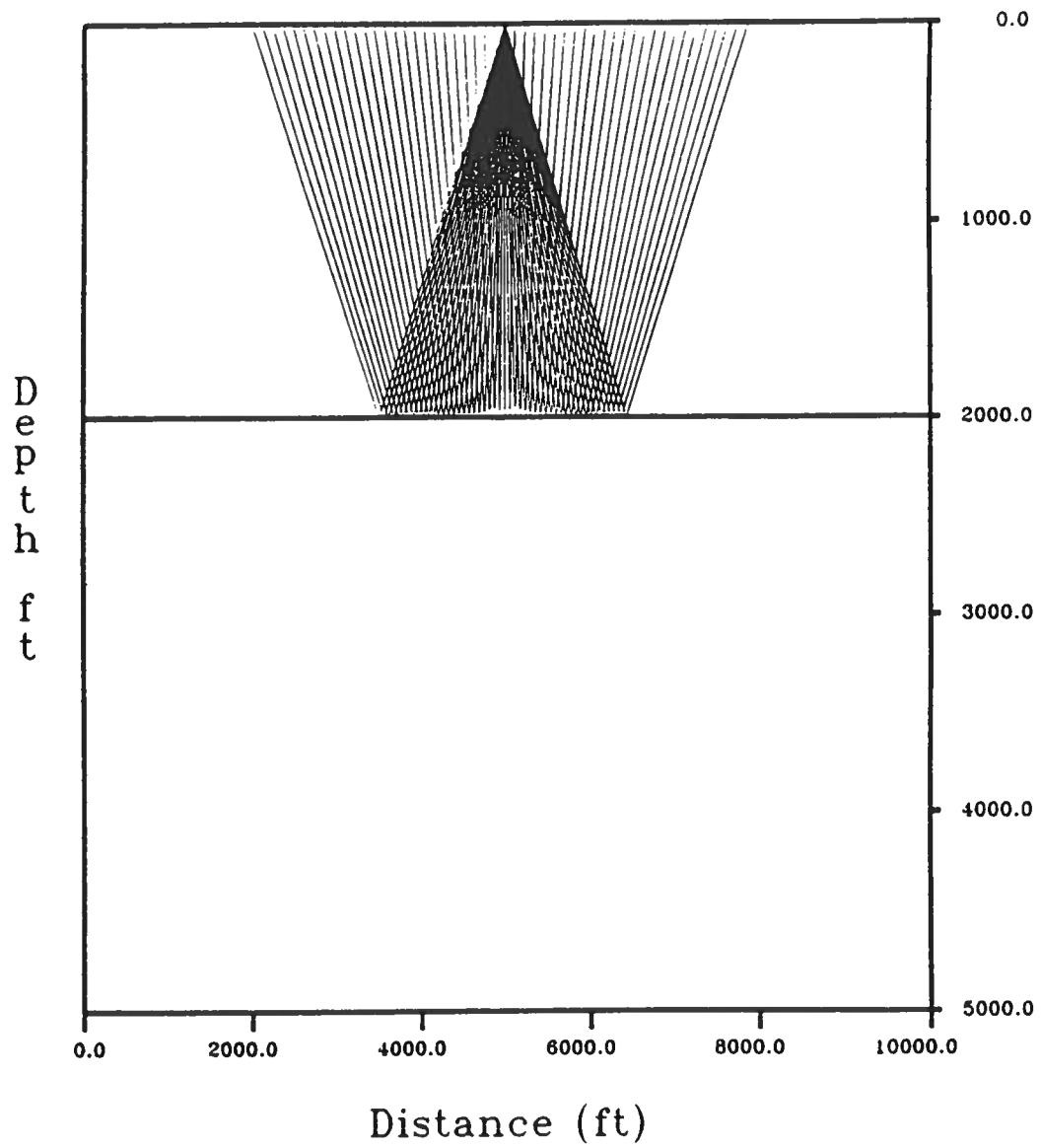


Figure 3.4 — The model used and ray path in amplitude test case. Velocity profile is 5000, 10000 *ft/sec*

Amplitude Test Data

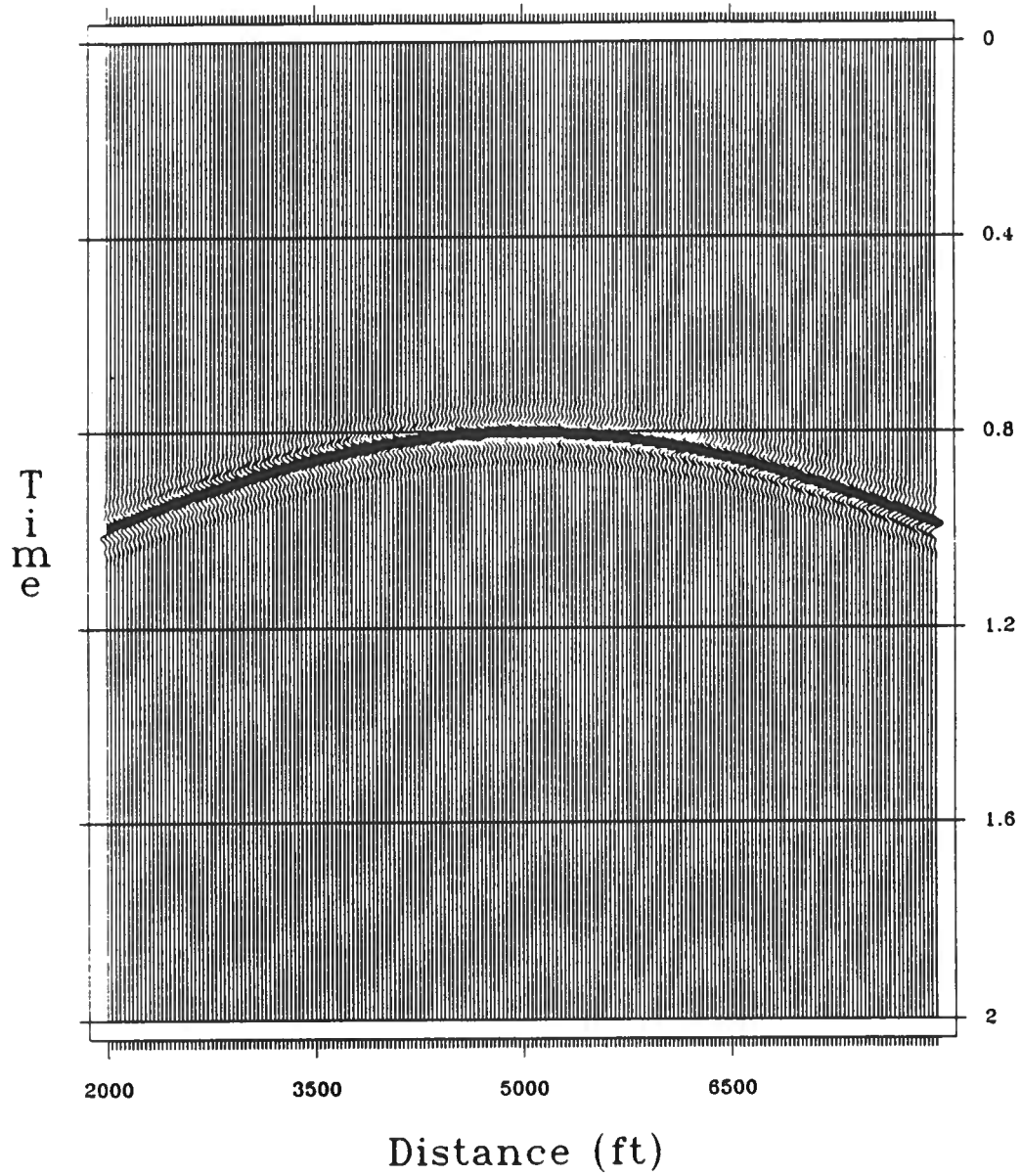


Figure 3.5 — Ray theoretical common shot time section for the model in Figure 3.4.

Amplitude Test

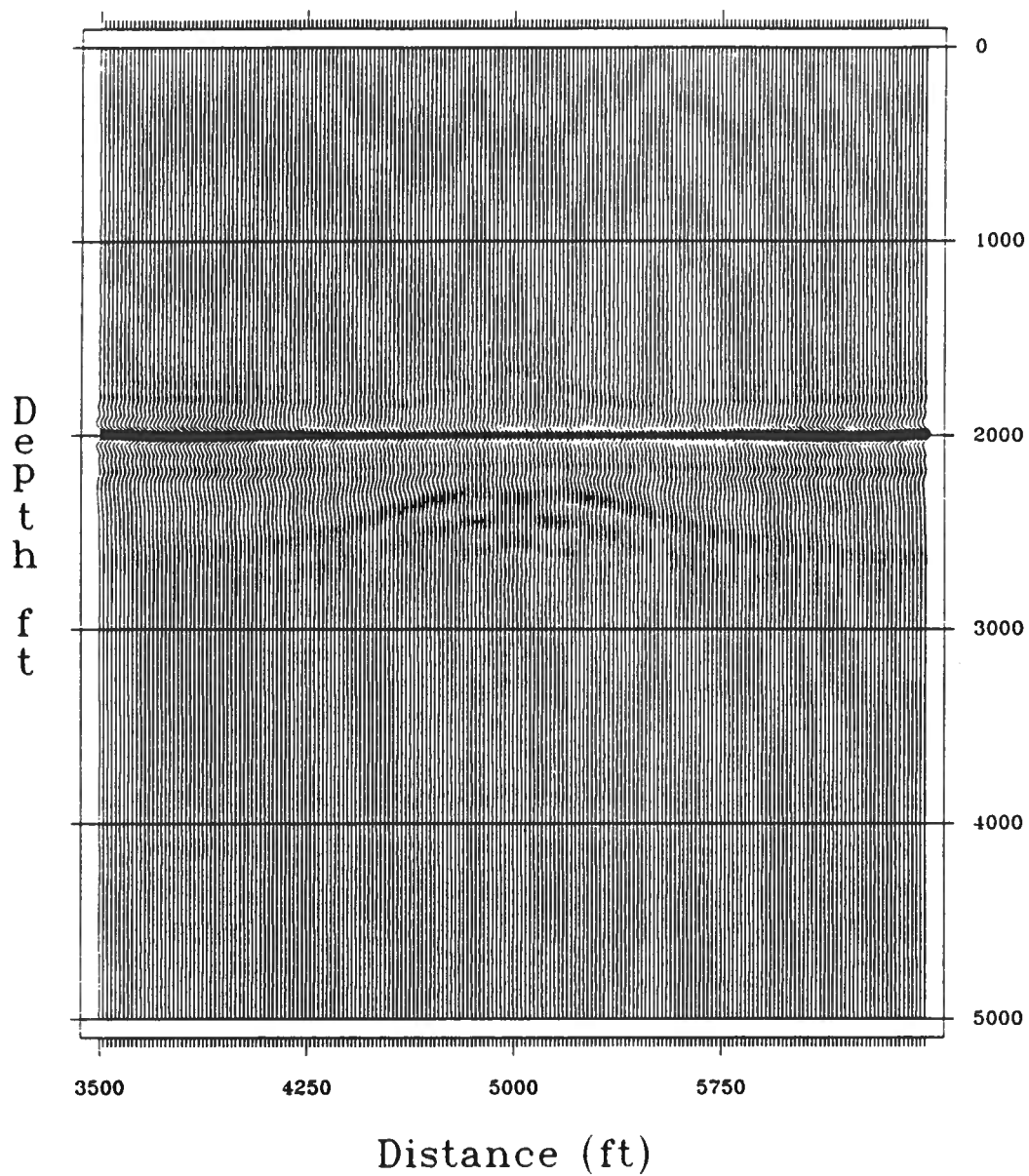


Figure 3.6 – The inversion result of the common shot data in Figure 3.5.

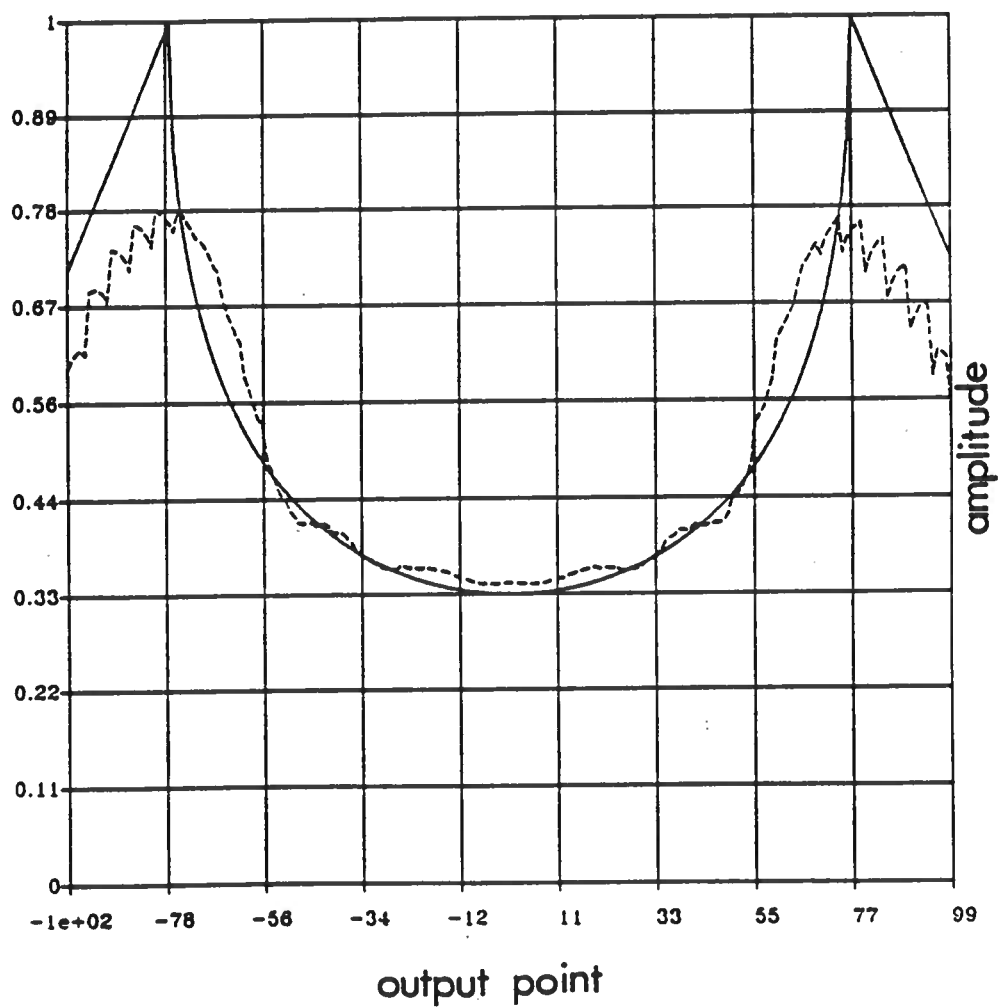


Figure 3.7 — Comparison of theoretical angularly dependent reflection coefficients with the inversion output. Trace numbers corresponds to their correct position on the reflector.



Marathon Model

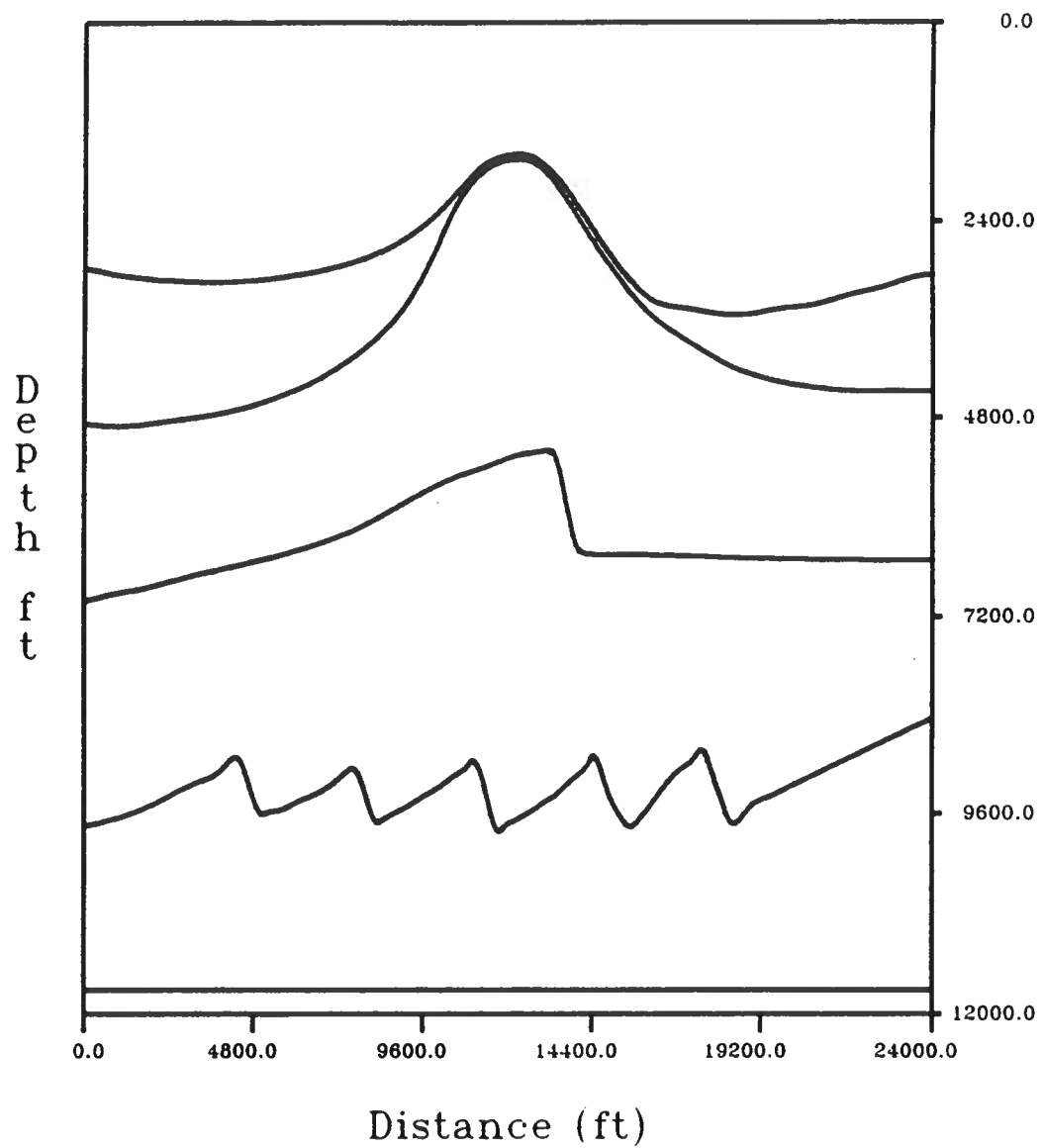


Figure 3.14 – The model used by Marathon to generate common shot data in water tank. Velocity profile is 11750, 15750, 22410, 15750, 19900 *ft/sec*. Depth and distance do not have same scale.



Four Shot Gathers

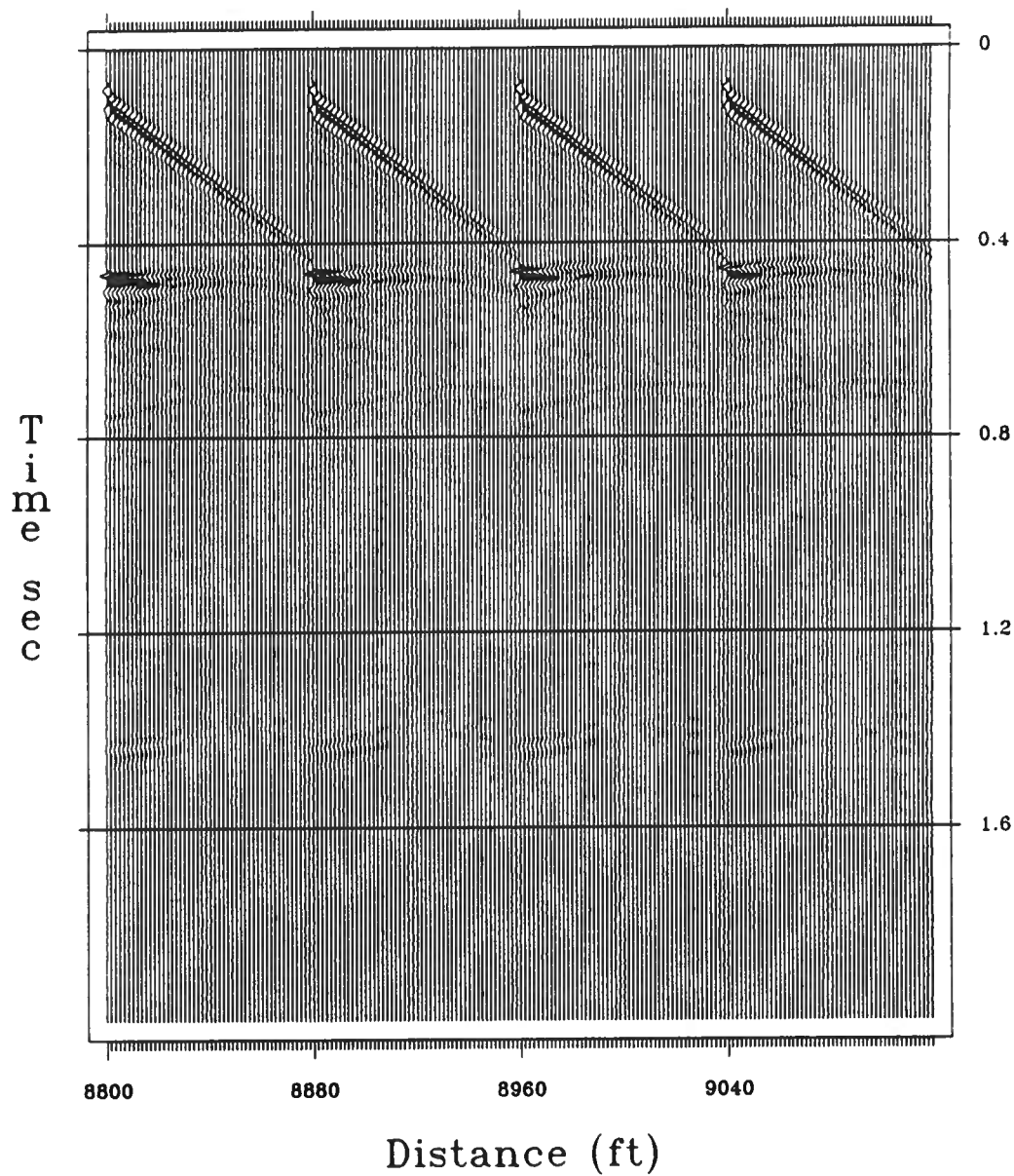


Figure 3.15 – Four sample common shot gathers from Marathon data set. The labels of distance indicate the first receiver position in each record. A whole gather is squeezed into a small portion.



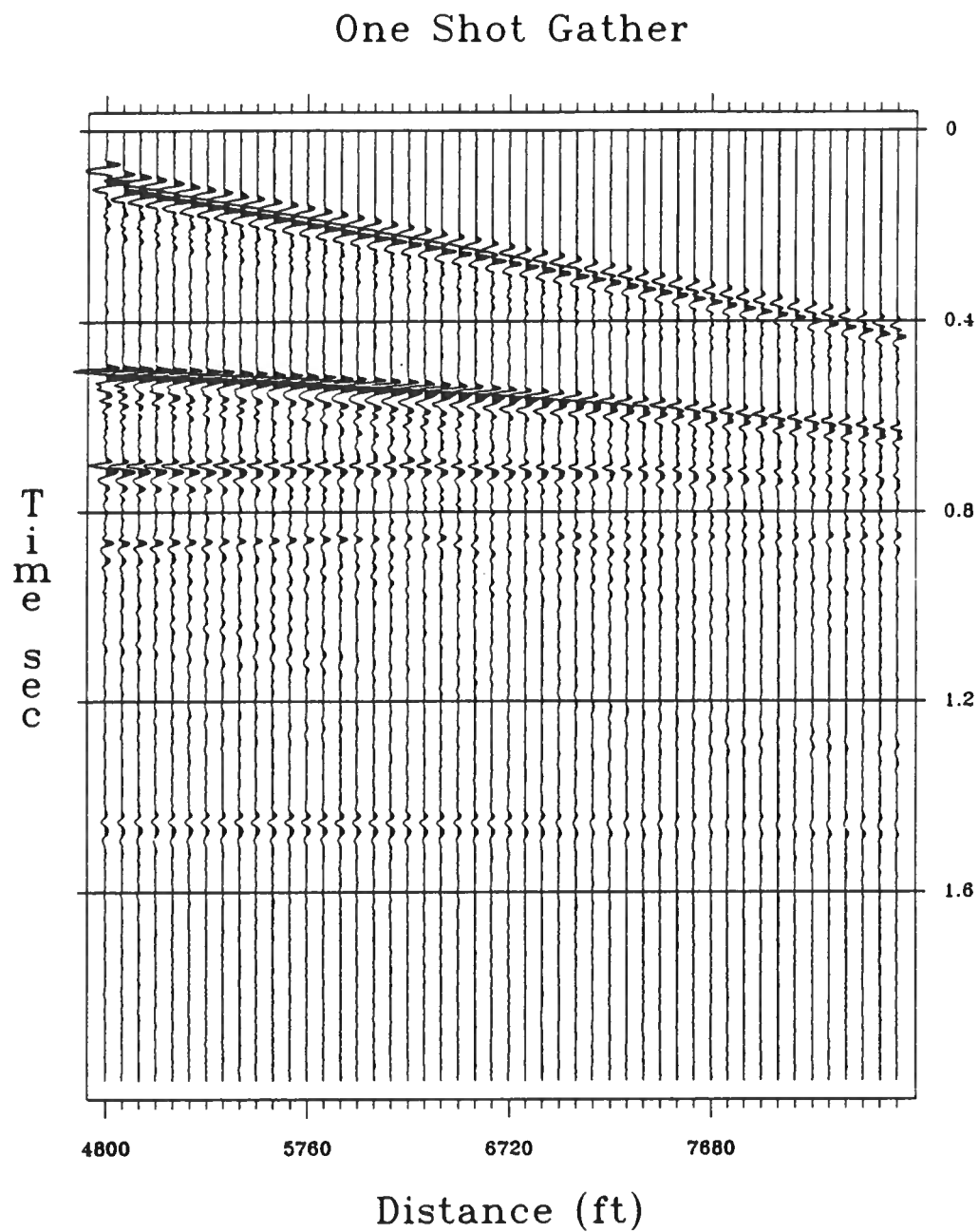


Figure 3.16 – Single shot gather from the Marathon data.



Inversion of the Four

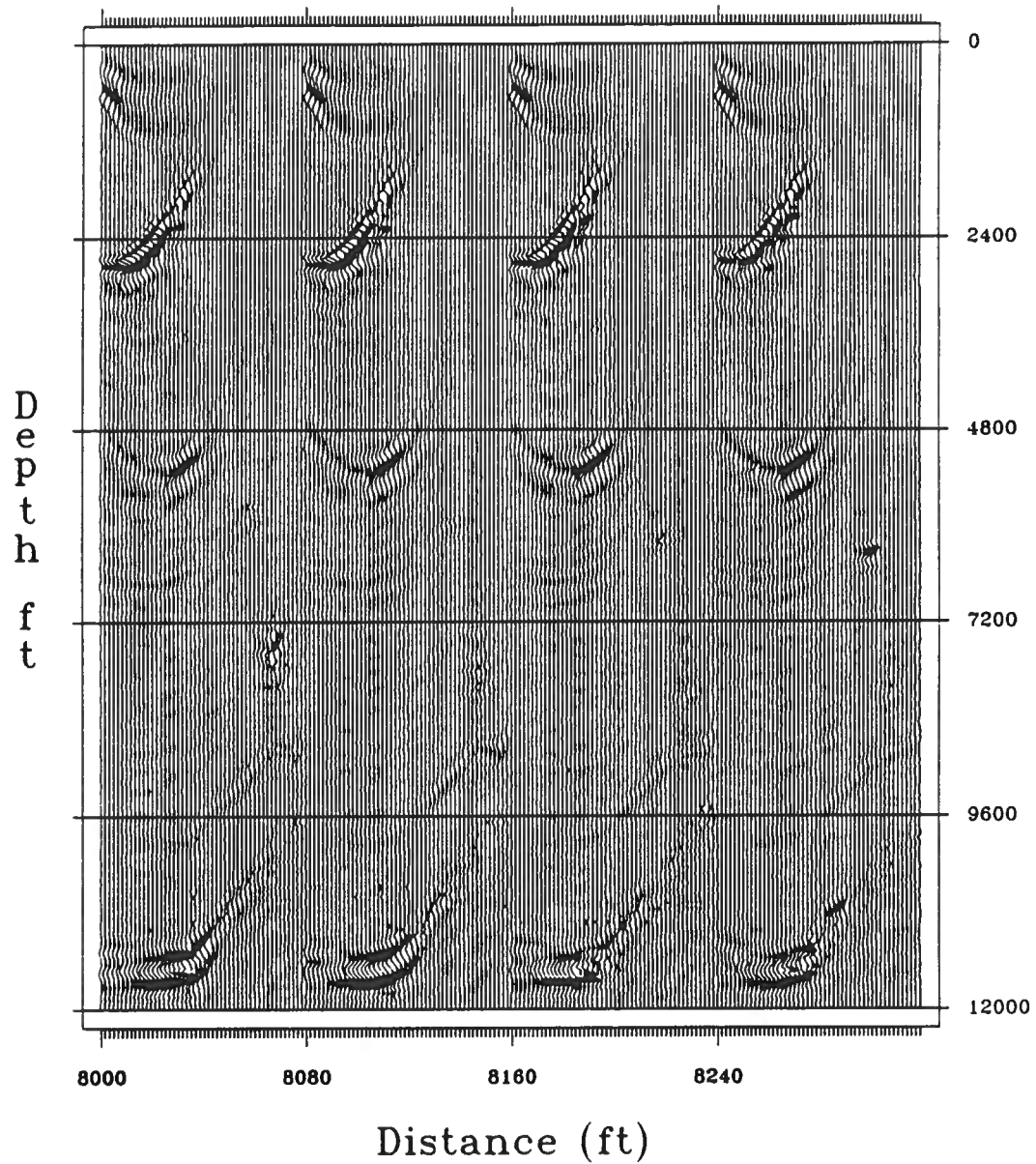


Figure 3.17 — The inversion result of the data in Figure 3.15. The labels of distance indicate the first output trace position in each inversion. Individual inverted section is squeezed into a small portion.

One Gather Inversion

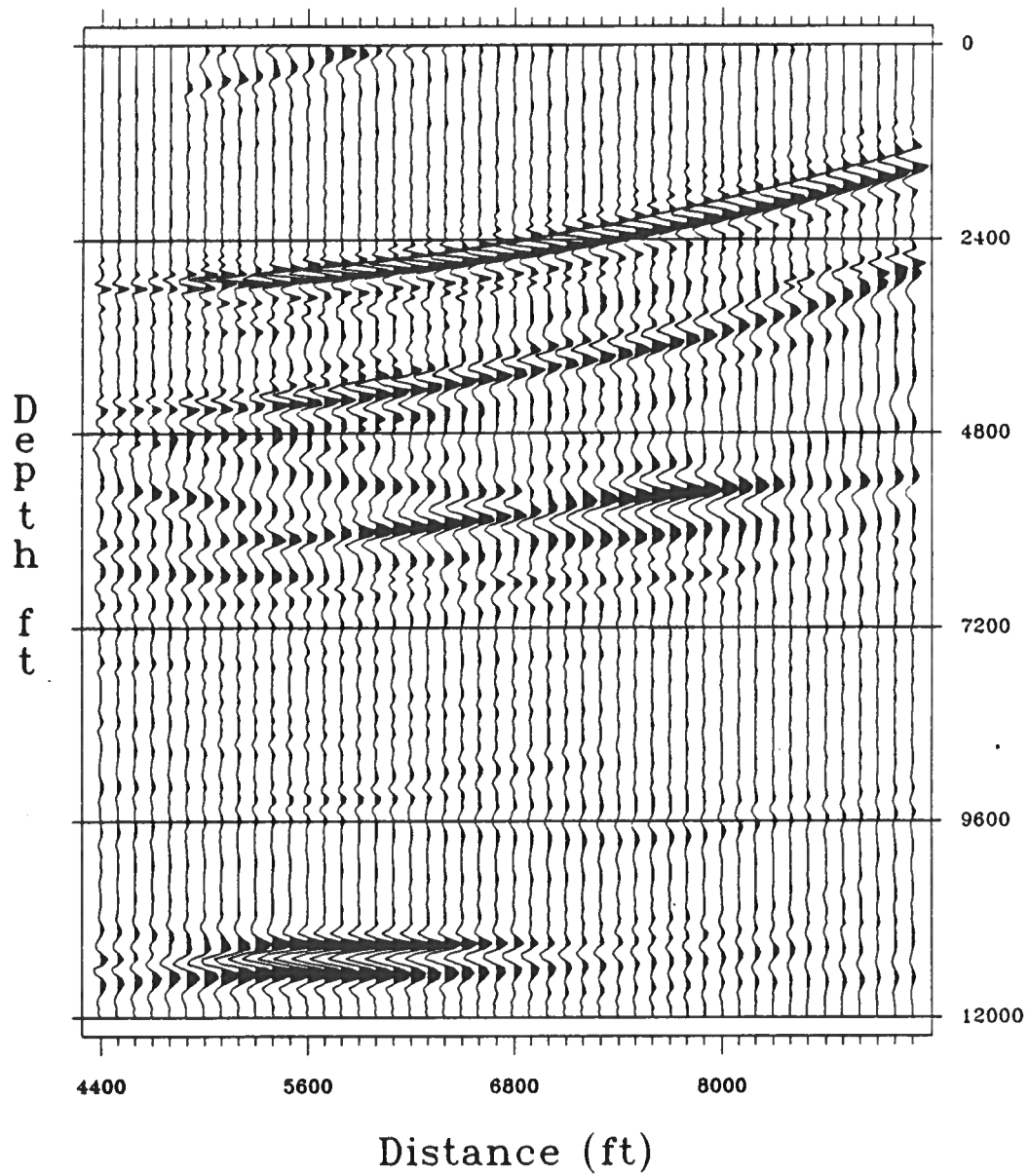


Figure 3.18 – The inversion result of the data in Figure 3.16.

Stack of Inversions

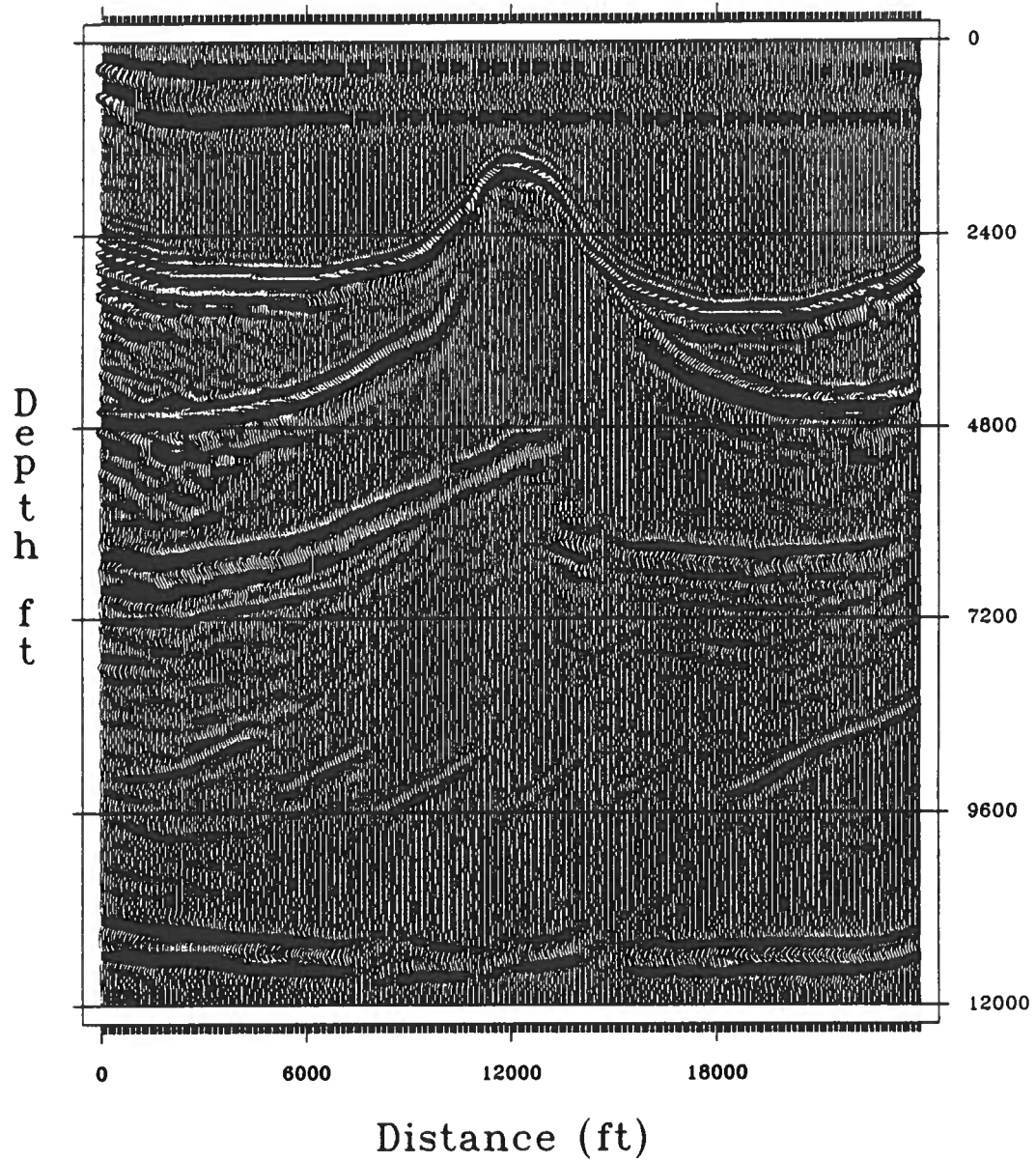


Figure 3.19 — The inversion result of the whole Marathon data sets. This is the stacked result after invert each shot record.



Marathon Inversion (AGC)

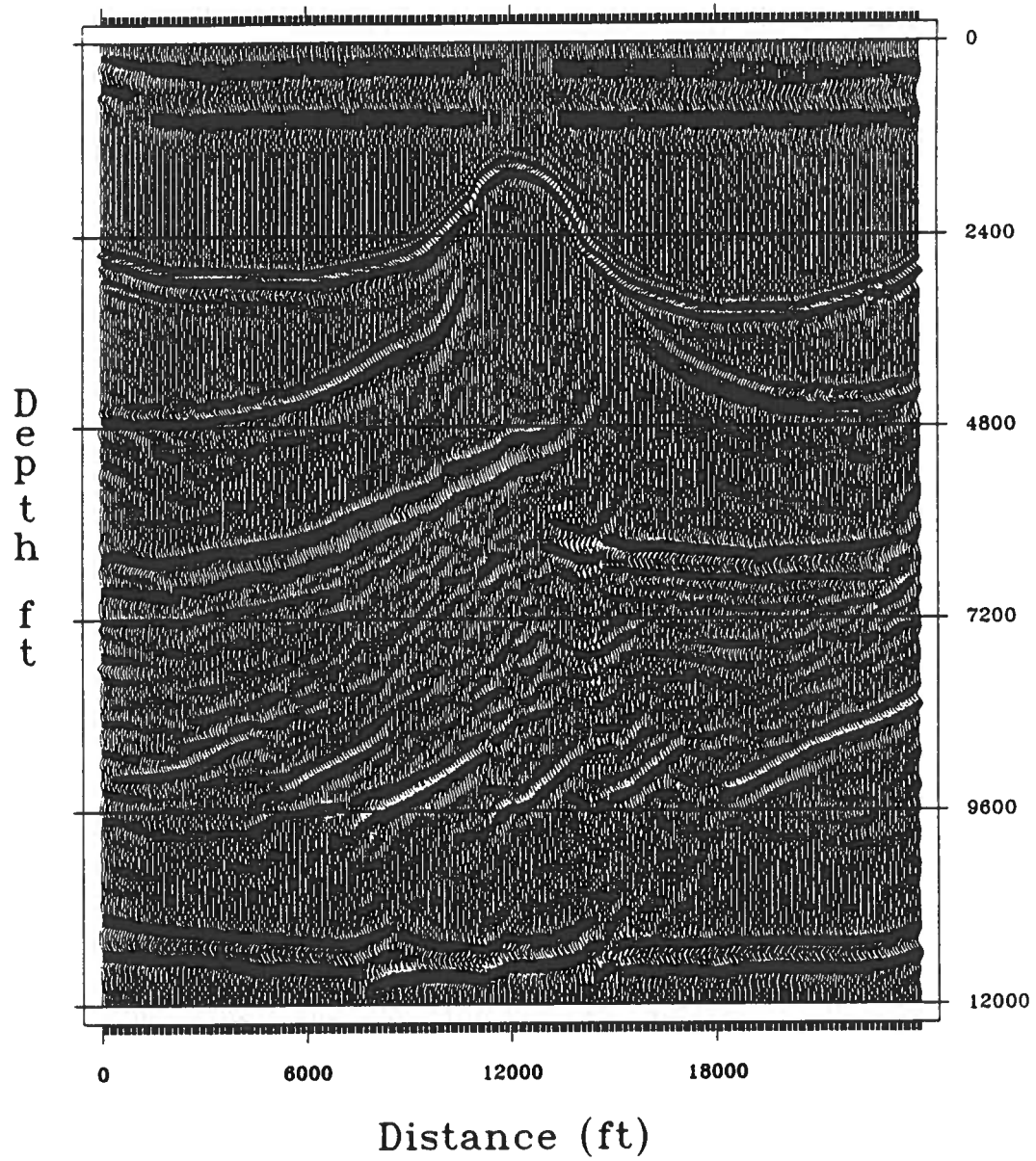


Figure 3.20 – AGC result of Figure 3.19.





**Diffraction Tomography and
Inversion Aperture
Preliminary Report**

by

Norman Bleistein and Jack K. Cohen

**Partially supported by the Consortium Project
on Seismic Inverse Methods for Complex Structures
at the Center for Wave Phenomena**

**Center for Wave Phenomena
Department of Mathematics
Colorado School of Mines
Golden, Colorado 80401
Phone (303) 273-3557**



TABLE OF CONTENTS

ABSTRACT	ii
INTRODUCTION	1
INVERSION FORMULAS FOR CONSTANT BACKGROUND	2
COMPUTER SIMULATION	5
APERTURE AND RESOLUTION	6
k-domain Display	6
Forward Scattering	8
Imaging of a Line Scatterer	8
Limited Aperture Imaging of a Delta Function	9
CONCLUSIONS	10
BIBLIOGRAPHY	10



ABSTRACT

This is an "in progress" report on applying common shot inversion to a well-to-well configuration, commonly called "diffraction tomography." In the context of that problem, the idea of k-domain aperture for finite bandwidth and finite source/receiver configuration is introduced. Display of the domain and two approaches to showing the effects of finite aperture are described. The first approach is to apply the 2.5D inversion to an out-of-plane line scatterer, where the objective is to reproduce the image of the delta function scatterer in the (x,z) plane. In the second approach, the Fourier transform of a delta function is directly inverted on the k-domain of coverage prescribed by the source/receiver configuration and finite bandwidth of the model experiment. The latter provides a theoretical limit of accuracy of the former, while not including the inversion amplitudes of the former, which are based on various assumptions of relative sizes of parameter variations and ratios of magnitudes of field components.



INTRODUCTION

This is a preliminary report on some recent investigations into the process known as "diffraction tomography." This work was motivated, in part, by the recent paper, Pratt and Worthington [1988]; and, in part, by an inquiry from one of our sponsors about the relevance of our methods to diffraction tomography. (They are, indeed, relevant.)

These preliminary investigations have suggested closer examination of the more fundamental issues of "aperture" and "resolution." In particular, we find that the Fourier domain aperture available in actual diffraction tomography experiments is much less than the theoretical apertures based on infinite spatial ranges shown in papers such as Pratt and Worthington [1988], Wu and Toksöz [1987], and Devaney [1984].

In describing the application of diffraction tomography to cross-hole seismic data, Pratt and Worthington [1988] state that

Diffraction tomography will not fulfill its potential as an inversion scheme until the extension to the 2½-D problem is achieved.

We believe that we have a reasonable approach to the 2.5D problem. The experiment described by Pratt and Worthington [1988] is really a common shot inversion in a constant background medium. Thus, our 2.5D common shot inversion, adapted to well-to-well experiments should suffice to deal with this problem. In this regard, we view the name, diffraction tomography, as a misnomer. "Tomography" was originally reserved for problems that were modeled by line integrals along the propagation path. The line integral might represent elapsed travel time or attenuation along the trajectory. Scattering problems are modeled by integrals over the scattering region (line, curve, area, volume). The former have the interpretation of a Radon transform in homogeneous media, or generalized Radon transform in inhomogeneous media. The latter do not, although Beylkin [1985], suggests the interpretation of inversion operators for the latter as generalized Radon transforms over equal travel time curves or surfaces. Note, however, that the Radon transform variable of the latter is, in some sense, *orthogonal* to the Radon transform variable of the former. Further, the Radon transform interpretation of the latter rests with the inversion operator, while the Radon transform of the former is in the forward modeling operator.

On the other hand, the name, diffraction tomography, might seem appropriate when applied to the experiment being carried out. That is, the common shot experiment and the tomographic experiment are the same, but the measured quantities are different.

A 2.5D common shot inversion formula for a surface survey was proposed by us in Bleistein, Cohen and Hagin [1987]. That formula has been successfully used in the cases of constant background soundspeed and depth dependent background soundspeed, for which explicit formulas were given in that paper. A computer code for the homogeneous background medium was written by M. F. Sullivan [1987]. For the case of a background medium depending on two variables, a computer code has just

been completed by Dong [1989]. Explicit formulas for these cases are given in the above mentioned paper, along with a general formula for arbitrary location of the sources and receivers. That general formula can be specialized to the diffraction tomography problem of interest here.

The above cited references depict k-domain coverage for well-to-well experiments (as well as for surface and VSP surveys) under the assumption that at least one of the source and receiver arrays is infinite in extent. We examine the k-domain coverage for source and receiver arrays of finite extent — more specifically for the range of source and receivers of the model experiments being studied. In some cases, that coverage is extremely small. Furthermore, study of coverage maps provides a means of deciding on the adequacy or redundancy of a particular source/receiver array.

To study the effects of k-domain coverage, we apply our inversion theory to inversion of data from an out-of-plane line scatterer. This is the appropriate 2D “point scatterer” for a 2.5D theory. The spread of the delta function image on output provides a means of measuring the accuracy of the inversion for the prescribed source/receiver configuration. The poor quality of diffraction tomography in the forward scattering direction is apparent from this study.

As a second check, we consider the Fourier inversion of a 2D Dirac delta function on the limited aperture of the source/receiver configuration. This inversion will contain only the effects of the limited aperture and not the effects of the amplitude compensations of the seismic inversion operator. Although we again see degradation in the forward scattering direction, it is not nearly as bad as it was for the inverse scattering result.

At this point, we consider both the development of diffraction tomography operators for variable background media and the study of k-domain apertures to be fruitful areas for further investigation.

INVERSION FORMULAS FOR CONSTANT BACKGROUND

Our approach to the 2.5D problem is based on the following *thought experiment*. Suppose that there were two planes of wells, each orthogonal to the plane containing the two wells in which the actual experiment is carried out. Suppose that exactly the same experiment is carried out in each pair of wells parallel to the given pair of the actual experiment. On the one hand, this is now a three dimensional diffraction tomography configuration. On the other hand, under the assumption of 2D variation in the earth, the data obtained from each separate well-to-well experiment is *identical*.

Proceed as follows.

- (1) Assume *point sources* and derive a 3D inversion operator for the configuration of the thought experiment. This operator takes the form of a Kirchhoff migration operator, but with variable background medium and spatial filtering as dictated by the inversion theory [Bleistein, 1987a,b].

- (2) Apply the operator under the assumption that the data is *independent of the out-of-plane variable*.
- (3) Under this assumption, note that only the known operator kernel depends on the out-of-plane variable. Hence, use the method of stationary phase to analytically evaluate the out-of-plane contribution.

This yields a Kirchhoff inversion integral over geophones, differing from Pratt and Worthington's integral in the spatial and Fourier amplitudes, but not in the phase. That is, the spatial part of the inversion operator is an integral over the (preprocessed) data of the original diffraction tomography experiment. The preprocessing consists of taking a fractional derivative, achieved via Fourier transform, at which time appropriate frequency domain filtering for smoothing is carried out as well.

Our output is related to the work of the above cited authors as follows. They invert for a quantity denoted by $O(\mathbf{x})$, called the "object function." This is just the quantity that we call $\alpha(\mathbf{x})/c(\mathbf{x})$, with $c(\mathbf{x})$ the background sound speed. We will provide our answer in terms of $\alpha(\mathbf{x})$ and the related quantities, $\beta(\mathbf{x})$ and $\beta_1(\mathbf{x})$. The latter two are "reflectivity functions." That is, the output of either of them provides a reflectivity map of the subsurface, similar to a migration output. The peak values of either output are in known proportion to the angularly dependent reflection coefficient, $R(\mathbf{x}, \theta)$ at some distinguished value of the incidence angle, θ . The asymptotic ratio of the two peak values is $\cos\theta$, thus reducing by one the number of unknowns in $R(\mathbf{x}, \theta)$.

All of the quantities, $O(\mathbf{x})$, $\alpha(\mathbf{x})$, $\beta(\mathbf{x})$, $\beta_1(\mathbf{x})$, assume a constant density acoustic medium. The extensions of our approach to a variable density acoustic medium, isotropic elastic medium, anisotropic elastic medium would follow along the lines of the work in Bleistein [1987b], Sumner [1988], Sumner and Bleistein [1988], Geoltrain and Bleistein [1988], Geoltrain [1989]. In this preliminary report, we only mean to "test the waters" of diffraction tomography and therefore consider only the simplest case of straight vertical wells in a homogeneous background.

The quantity α is defined in terms of the reference or background sound speed, $c(\mathbf{x})$ and the true sound speed $v(\mathbf{x})$ by

$$\frac{1}{c^2(\mathbf{x})} = \frac{1}{v^2(\mathbf{x})} [1 + \alpha(\mathbf{x})] . \quad (1)$$

The specialization of our inversion theory for well-to-well common shot processing — diffraction tomography — yields the following formula for α :

$$\alpha(x) = \frac{|x-h| \sqrt{2r_s}}{\sqrt{\pi c}} \int d\zeta \frac{\sqrt{r_s+r_g}}{r_g^{3/2}} \cdot \int \frac{d\omega}{\sqrt{|\omega|}} D(\omega, \zeta) \exp \left\{ -i\omega [r_s+r_g]/c - (\pi i/4) \operatorname{sgn} \omega \right\}. \quad (2)$$

In this equation, the well containing the sources is located at $x = -h$; the well containing the geophones is at $x = +h$; the depth of the receiver is at $z = \zeta$, with the (Fourier transformed) observed data given by $D(\omega, \zeta)$. The quantities, r_s and r_g denote the distances from the output point, $x = (x, z)$, to the source and geophones, $(-h, z_s)$ and (h, ζ) , respectively,

$$r_s = \sqrt{(x+h)^2 + (z-z_s)^2}, \quad r_g = \sqrt{(x-h)^2 + (z-\zeta)^2}. \quad (3)$$

The corresponding formulas for β is

$$\beta(x) = \frac{2|x-h| \sqrt{r_s}}{\sqrt{\pi} c^{3/2}} \int d\zeta \frac{\sqrt{r_s+r_g}}{r_g^{3/2}} \sqrt{1 + \hat{r}_s \cdot \hat{r}_g} \cdot \int d\omega \sqrt{|\omega|} D(\omega, \zeta) \exp \left\{ -i\omega [r_s+r_g]/c + (\pi i/4) \operatorname{sgn} \omega \right\}. \quad (4)$$

In this equation, we introduce the unit vectors,

$$\hat{r}_s = (x+h, z-z_s)/r_s, \quad \hat{r}_g = (x-h, z-\zeta)/r_g. \quad (5)$$

The square root involving the dot product of these two vectors is the quantity that makes $\beta(x)$ proportional to $\cos\theta$ at the distinguished θ value. Thus, for $\beta_1(x)$, we use

$$\beta_1(x) = \frac{2 |x-h| \sqrt{2r_s}}{\sqrt{\pi} c^{3/2}} \int d\zeta \frac{\sqrt{r_s + r_g}}{r_g^{3/2}} \cdot \int d\omega \sqrt{|\omega|} D(\omega, \zeta) \exp \left\{ -i\omega [r_s + r_g]/c + (\pi i/4) \operatorname{sgn} \omega \right\}. \quad (6)$$

Equations (2,4,6) are our inversion formulas. As noted above, (2) corresponds most closely to the processing carried out in the above cited diffraction tomography references. The formulas, (4) and (6), are the reflectivity functions of the type we standardly process for a reflectivity map of the earth's interior. The ratio, β_1/β , evaluated at the peak of a reflector image, yields an estimate of $\cos\theta$ for the distinguished θ of the reflection coefficient, $R(x, \theta)$. Other than this difference of scale of $\cos\theta$ the remaining factors in the peak output of either of them are $R(x, \theta)$ and the area under the filtered source signature in the frequency domain. We forego the details of the discussion of amplitude here, because it is available in the above cited references.

COMPUTER SIMULATION

We consider a model in which the wells are 250 meters apart. We place sources in one well at 100 meter intervals, from 0 to 400 meters and receivers in the other well at 1.5 meter intervals from 200 to 440 meters. See Figure 1. We used a signal of bandwidth 40-240 Hz, for which a maximum receiver spacing of 3 meters was required to avoid spatial aliasing at all incidence angles at propagation speed of 1500 m/s. The denser 1.5 meter spacing yields four point per wave length sampling at the maximum frequency and vetical propagation.

As a simple example, we consider a single plane at 500 meters. we use CSHOT, Paul Docherty's [1987] modeling code to generate synthetic data for this model. Figures 2 and 3 show the output of the inversion code for $\beta(x)$, the first for the shot at $z=0$, the second for the shot at $z=400$ meters. Both outputs give a partial image of the reflector, with diffraction smiles beyond the range of speculars. In Figure 4, we show a stack of all five inversion outputs. Here we see a fairly complete image of the reflector; it is, indeed, located at 500 meters depth. (A slight assymetry of the output suggests that the peak is actually slightly lower, on a sample density of 2 meters used for the output.) Furthermore, the limiting range of speculars on the plane at 500 meters depth is $-62.5 \leq x \leq 98.2$. While the stacked result does remain flat in that range, the amplitude near the extremes is significantly smaller than the amplitude in the interior of the range. This is because these extreme values appear as speculars only on the last and first inversions, respectively. The former extreme appears in the output of Figure 3, while the latter appears in the output of Figure 2. On those outputs the amplitude at the respective extremes is not nearly so small relative to the maxima in

the two figures. Longer source and receiver arrays (not exceeding the depth, 500 meters) would image more of the plane.

Once we know the location of the reflector, it is reasonable to go back to the separate outputs to measure $\cos\theta$, as the ratio of the outputs, $\beta_1(x)$ and $\beta(x)$ at the peaks of the reflector. For example, from the shot at $z=0$, we can compare the estimated and theoretical values of $\cos\theta$ on the traces at $x=55, 65$ and 75 meters. The theoretical values and the values computed at 500 meters are as follows:

$\cos\theta$		
x	estimate	true value
55	.9340	.9409
65	.9293	.9348
75	.9203	.9285
85	.9246	.9220

The computed outputs are within 1% of the theoretical values. As a further check, the computed reflection coefficient at $x=75$ meters is .1830, while the theoretical value is .1797. The error here is 1.8%. We believe that these values of $\cos\theta$ and $R(x,\theta)$ demonstrate the validity of our approach to the 2.5D problem for diffraction tomography.

APERTURE AND RESOLUTION

We noted that the output of the individual inversions exhibited strong flat diffraction smiles when compared to our experience with surface surveys. We decided that this was related to the limited k-domain aperture of the observed data. We turn our attention to the problem of k-domain aperture and to generating various displays to demonstrate the impact of limited aperture on the resolution of the output.

k-domain Display

As a first approach to this problem, we decided to plot the actual k-domain for each shot. This is in the tradition of the authors cited in the introduction. However, in their plots, at least one of the arrays — source or receiver — is infinite in extent. For finite arrays, the coverage is dramatically different. We compute the coverage by using for k the formula,

$$k = \omega[\hat{r}_s + \hat{r}_g]/c . \quad (7)$$

In this formula, \hat{r}_s and \hat{r}_g are given by (5). For (x,z) we will use the value, $(x_0, z_0) = (55, 500)$, which is a point on the reflector.

As an expository example of this analysis, we consider a shot at $z=0$ in one well, and a set of receivers between 0 and 500 meters in the other well. In Figure 5, we plot the k -vectors for two frequencies, two octaves apart. As in the spatial domain, we plot k_z positive *downward*. However, we plot the k vectors for both positive and negative frequencies.

It is straightforward to reproduce this figure by hand. We consider positive frequencies only for this discussion. The reflection through the origin of the vectors we construct will yield the vectors for negative frequency. The vector from the source — the first term in (7) — is fixed, with length ω/c . For the given source/receiver configuration, this vector makes an angle of 20.9° to the right of vertical. The vector from the receiver has the same length, but varying direction. We place the initial point of the second vector at the terminal point of the first and see that its endpoint traces out the arc of a circle, centered at the endpoint of the first vector and passing through the origin. The extent of the arc is determined by the range of receivers. For the minimum and maximum frequencies, we show the extreme receiver vectors, making angles of -20.9° and -90° with the vertical. If we were to extend the limit at depth to infinity, the former angle would approach 0° . Similarly, if we were to extend the receivers above the earth's surface to minus infinity, the latter limit would approach -180° . Together, these limits would produce a semicircle. The other half of this semicircle requires sources and receivers in the left well. However, this set of k -vectors is partially covered by moving the source down and using receivers in the left well. Note also, that the density of the points on the arc is not uniform, decreasing as the receiver depth approaches the output depth.

We have also drawn a reference circle in the figure at a constant value of ω . This circle will remain the same size in all of the plots following. The arc at the larger frequency of this diagram is 88% of the frequency of the reference circle. That is, a wave vector for zero-offset at the larger frequency would have length equal to .88 times the radius of this reference circle. The lengths of all other source/receiver vectors at this frequency would be reduced from that, with limiting length zero in the forward scattering direction.

Figure 6 shows the k -domain for the shot at $z=0$ which produced the inversion of Figure 2. We did not plot the output for all of the discrete frequencies, but for a sufficient density of frequencies so that the k -domain coverage is clear from the figure. In Figure 7, we show the coverage for the shot at $z=400$.

Our inversion theory predicts that a reflector will be imaged if its normal is one of the directions of the k -domain aperture. Furthermore, the output will be a band limited delta function whose aperture is the k -domain aperture in the normal direction.

For the model problem, the normal direction is the vertical. Comparison of Figures 6 and 7 shows greater bandwidth in the vertical in the former figure than in the latter. Thus, we should expect higher resolution — narrower main lobe, smaller side lobes — in the reflector image produced by the former than by the image produced by the latter. Comparison of Figures 2 and 3 confirms this.

In Figure 8, we show the coverage for all of the shots, superimposed. The last figure shows adequate coverage, with overlap, mostly arising from the higher shots. The multiple overlap of k-vectors in the vertical suggests a strong image of a flat reflector (within the range of speculars) and that is what we see in Figure 4.

Forward Scattering

The smaller aperture of Figure 7, as compared to Figure 6, is a consequence of the smaller range of scattering angles associated with the k-vectors defined by (7). That is, the aperture narrows as the scattering problem takes on more of the character of a transmission problem.

We can show this another way. Figure 9 is a display of the aperture when the receiver range is from $z=0$ to 1000 meters. Note that the aperture is not significantly larger than for the smaller receiver range of Figure 6. In fact, the range $z=500$ to 1000 meters adds very little at all to the total aperture. To see this, we plot the k-domain for this range in Figure 10, as well. The output confirms our claim.

Imaging of a Line Scatterer

Now we examine resolution in another way. Since we are doing 2.5D modeling and inversion, we consider a line scatterer in the out-of-plane direction and use the Born approximation to generate scattered data. Again, we use point sources and point receivers. In the volume integral representing the scattered field, the out-of-plane integration is carried out by the method of stationary phase, while the in-plane integrals are computed by using the fact that the scatterer is a two-dimensional delta function. The result is

$$D(\omega, \zeta) = \frac{1}{2(2\pi c)^{3/2} \sqrt{r_s r_g} \sqrt{r_s + r_g}} \quad (8)$$

$$\cdot \int F(\omega) |\omega|^{3/2} \exp \left\{ i\omega \left[r_s + r_g \right] / c + (3\pi i/4) \text{sgn} \omega \right\} d\omega .$$

Here, $F(\omega)$ is the frequency domain filter; the functions r_s and r_g are given by (3), but with (x, z) replaced by the location of the line scatterer, (x_0, z_0) .

We computed the scattered field for a scatterer at (55,500), the same location used for the discussion of k-domain coverage above. We then used the α -inversion defined by (2) to invert the data. The output should be a delta function located at (55,500). The results are shown in Figures 11-13.

Figure 11 is the inversion for the shot at $z=0$; Figure 12 is the inversion for the shot at $z=400$; Figure 13 is the sum of the outputs for the five shots at 100 meter intervals from 0 to 400 meters. Corresponding to the narrower aperture of Figure 7 as compared to Figure 6, we see greater transverse dispersion of the point scatterer in Figure 12 as compared to Figure 11. The direction of dispersion of the point scatterer is also consistent with the direction of least information in the k -domain. Furthermore, the sharper imaging in the vertical in Figure 11 as compared to Figure 12 is consistent with our earlier discussion of directional resolution.

The post inversion stack by simple sum in Figure 13 shows a result only slightly better than the single shot inversion of Figure 11.

As a further check on this approach to resolution, we modeled the line scatterer data for the source/receiver configuration of Figure 10 and then inverted the data. The result is shown in Figure 14. The scale here is the same as in the previous figures. It is clear that the scattering point is not imaged at all. The inversion theory has broken down and the output is dominated by the inverse transform of the aperture function. We consider this to be a strong demonstration that diffraction tomography is a poor imaging technique for forward scattering.

Limited Aperture Imaging of a Delta Function

Our next display technique provides a means of separating the limitation of diffraction tomography from the limitation totally due to aperture considerations. To do this, we consider the aperture-limited Fourier inversion of the Fourier transform of a delta function. This output should indicate a theoretical limit on diffraction tomography imposed by aperture constraints alone and not on limits imposed by approximations which are a part of the inversion theory.

We consider the following integral.

$$\delta_B(\mathbf{x} - \mathbf{x}_0) = \frac{1}{(2\pi)^2} \int_{D_k} F(c|\mathbf{k}|) \exp\left\{i\mathbf{k} \cdot [\mathbf{x} - \mathbf{x}_0]\right\} d^2k. \quad (9)$$

In this integral, D_k is the aperture in the k -domain and $F(c|\mathbf{k}|)$ is a filter function to be defined below.

We can transform this integral into an integral over the frequency/receiver domain by using the definition, (7), for \mathbf{k} . That is,

$$\delta_B(\mathbf{x} - \mathbf{x}_0) = \int \frac{\partial(\mathbf{k})}{\partial(\omega, \xi)} F(\omega) \exp\left\{i(\omega/c)[\hat{\mathbf{r}}_s + \hat{\mathbf{r}}_g] \cdot [\mathbf{x} - \mathbf{x}_0]\right\} d\omega d\xi. \quad (10)$$

The domain of integration is now seen to be the bandwidth in the ω -domain and the receiver array in the spatial domain. Furthermore, $F(\omega)$ is now seen to be the same

filter as in (8). The Jacobian of this transformation is given by

$$\frac{\partial(k)}{\partial(\omega, \xi)} = \frac{|\omega|}{c^2} \frac{|x-h|}{r_g^2} (1 + \hat{r}_s \cdot \hat{r}_g) . \quad (11)$$

Figures 15-17, generated with the Fourier inversion formula, (10), should be compared to Figures 11-13, generated with the diffraction tomography formula (2). Both produce images of a delta function at (55,500). The set, Figures 15-17, appear consistently sharper than the images in Figures 11-13. However, the loss of quality is not significant and we can conclude that the theory does reasonable well at these apertures.

On the other hand, Figure 18 is the output comparable to the inversion of Figure 14. While the narrow aperture does not yield a well-resolved delta function in Figure 18, the result is significantly better than the inversion output of Figure 14. We believe that the assumptions in the inversion theory underlying its application to diffraction tomography are breaking down for this configuration.

CONCLUSIONS

We have begun a study of the application of our 2.5D inversion theory to diffraction tomography. We have shown in this preliminary study that there is clear indication that the theory does, indeed, apply. Thus, we anticipate extension of our current formulas and computer codes for variable background media to this source/receiver configuration, as well.

In the context of this problem, we have also begun a study of aperture. We have introduced a technique for depicting k-domain aperture with attention to limitations on the source and receiver ranges, as well as bandwidth. We have also introduced two techniques for checking the effects of aperture on imaging. In one of these, we invert Born data for a line scatterer to check the aperture-limited 2.5D inversion for a point in two dimensions. In the other, we directly process Fourier data for a delta function over the aperture of the source/receiver configuration and bandwidth.

BIBLIOGRAPHY

- Bleistein, N., 1987a, On the imaging of reflectors in the earth: *Geophysics*, 52, 931-942.
 Bleistein, N., 1987b, Kirchhoff inversion for reflector imaging and sound speed and density variations: *Proc. of EAEG/SEG Workshop on Deconvolution and Inversion*, Rome, Italy, 1986, M. Worthington, Ed., Blackwell Scientific Publishers Ltd., Oxford.

- Bleistein, N., J. K. Cohen, and F. G. Hagin, 1987, Two-and-one-half dimensional Born inversion with an arbitrary reference: *Geophysics*, 52, no. 1, 26-36.
- Devaney, A. J., 1982, A filtered backpropagation algorithm for diffraction tomography: *Ultrasonic Imaging*, 4, 336-350.
- Docherty, P., 1987, Two-and-one-half dimensional common shot modeling: Center for Wave Phenomena Research Report, CWP-050.
- Dong, W., 1989, Finite difference ray tracing and common shot inversion, Center for Wave Phenomena Research Report, CWP-084.
- Pratt, R. G., and M. H. Worthington, 1988, The application of diffraction tomography to cross-hole seismic data: *Geophysics*, 53, no. 1, 1284-1294.
- Sullivan, M. F., 1987, Prestack Kirchhoff inversion and modeling in 2.5 dimensions: Doctoral thesis. Center for Wave Phenomena Research Report, CWP-054.
- Sumner, B., 1988, Asymptotic solutions to forward and inverse problems in isotropic elastic media: Doctoral thesis, Center for Wave Phenomena Research Report, CWP-075.
- Sumner, B., and N. Bleistein, 1988, Prestack elastic Kirchhoff migration and parameter estimation: Expanded abstracts, SEG 58th Annual Meeting, Anaheim, 963-965.
- Wu, R., and Toksöz, M. N., 1987, Diffraction tomography and multi-source holography applied to seismic imaging: *Geophysics*, 52, 11-25.



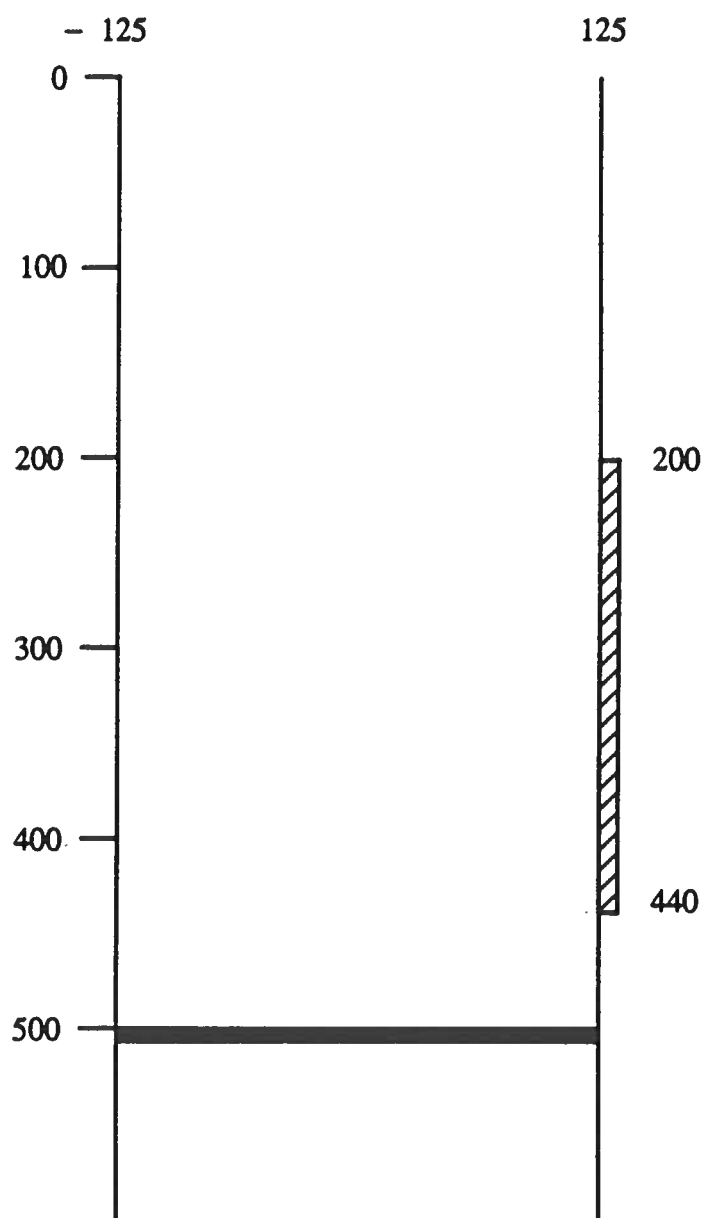


FIGURE 1



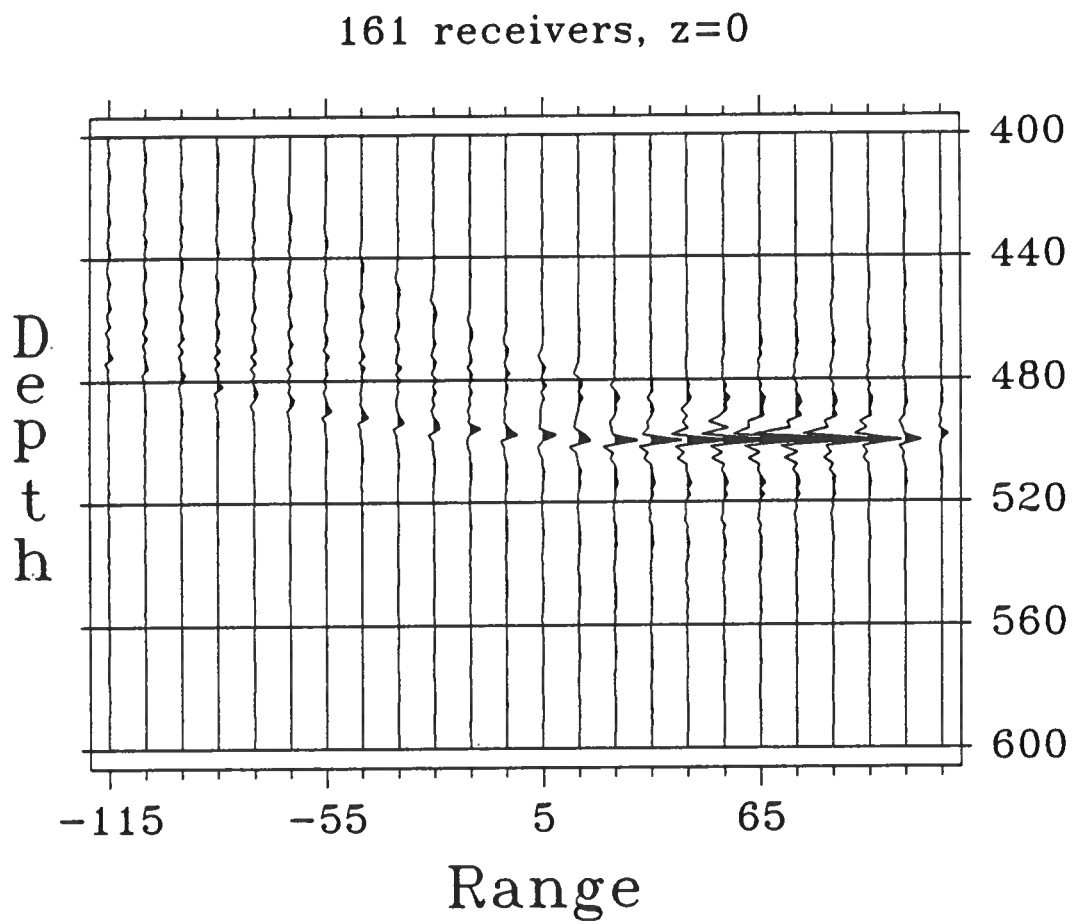


FIGURE 2



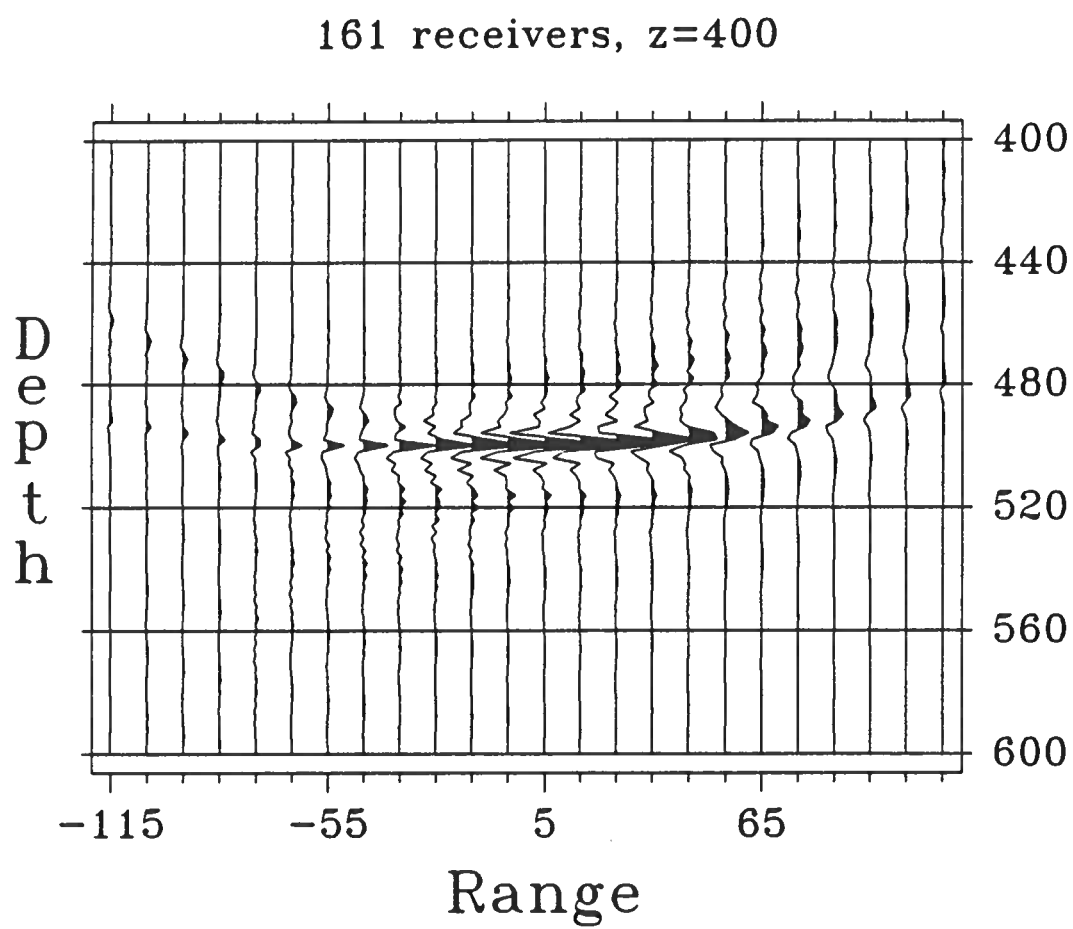


FIGURE 3



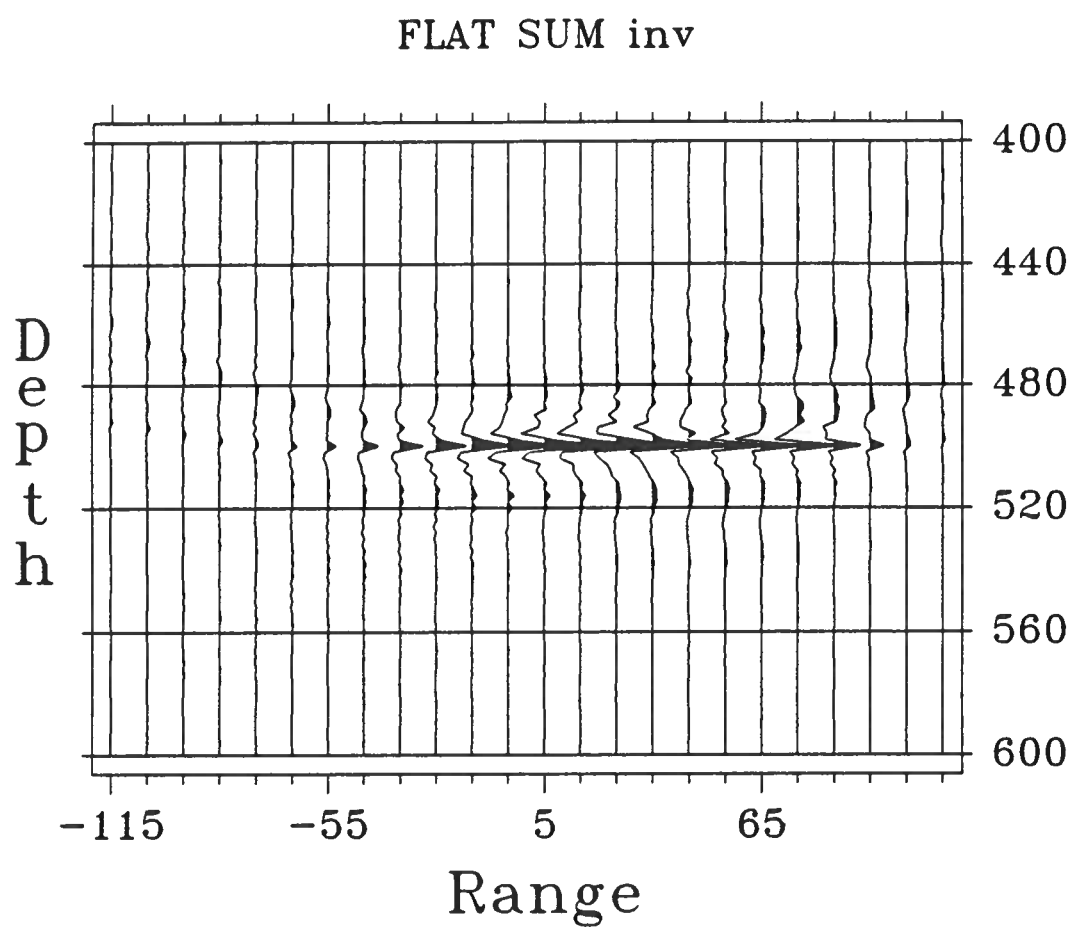
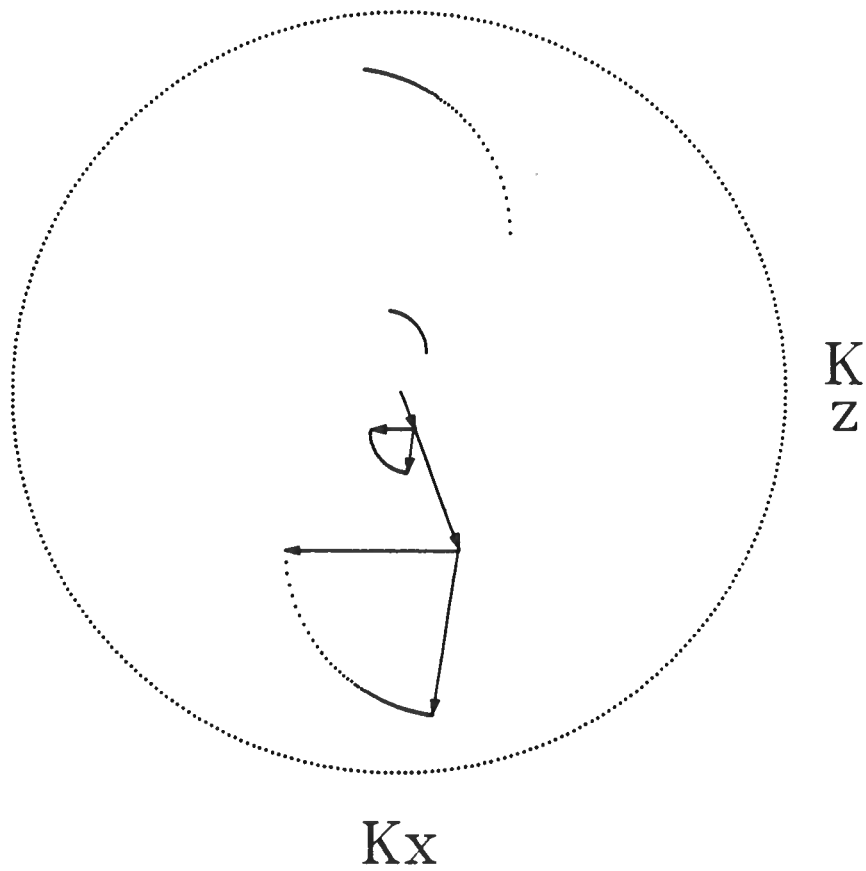


FIGURE 4



K Plot

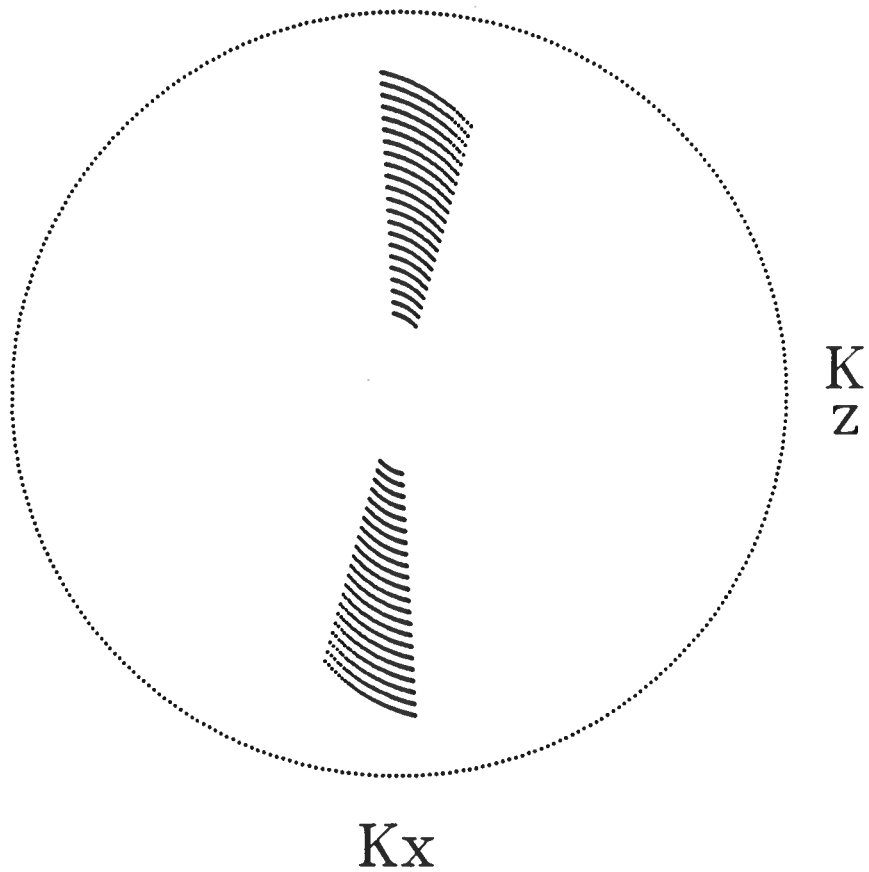


· $s_z = 0$ · $g_z: 0-500$
· $x_0 = 55$ · $z_0 = 500$

FIGURE 5



K Plot



$sz = 0$

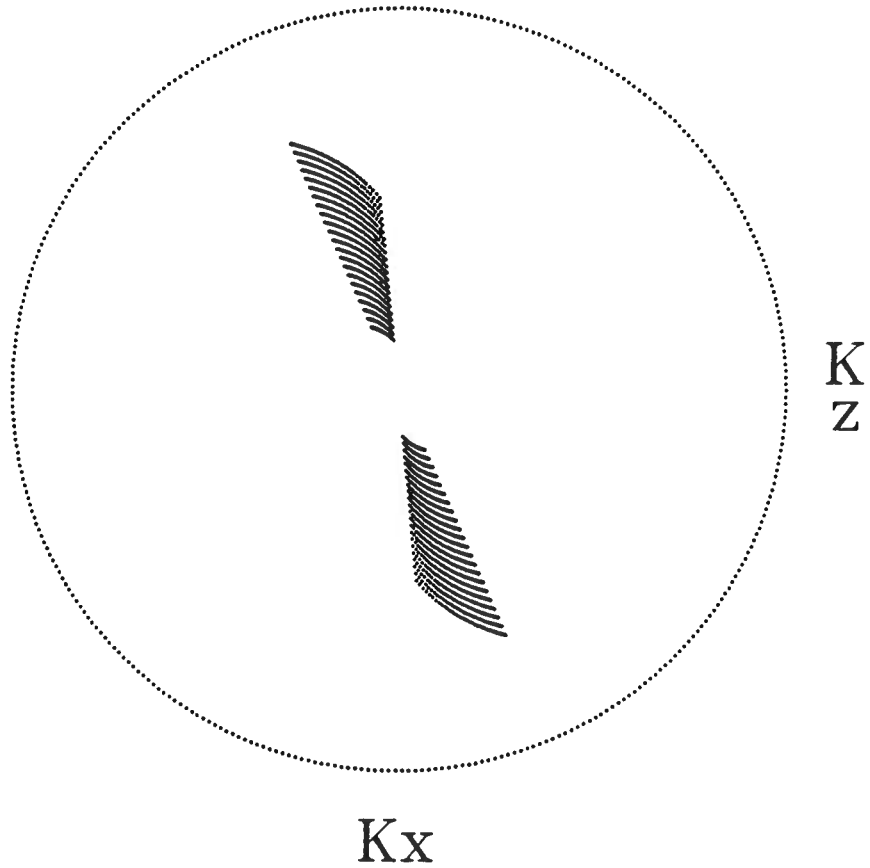
$gz: 200-440$

$x0 = 55$

$z0 = 500$

FIGURE 6

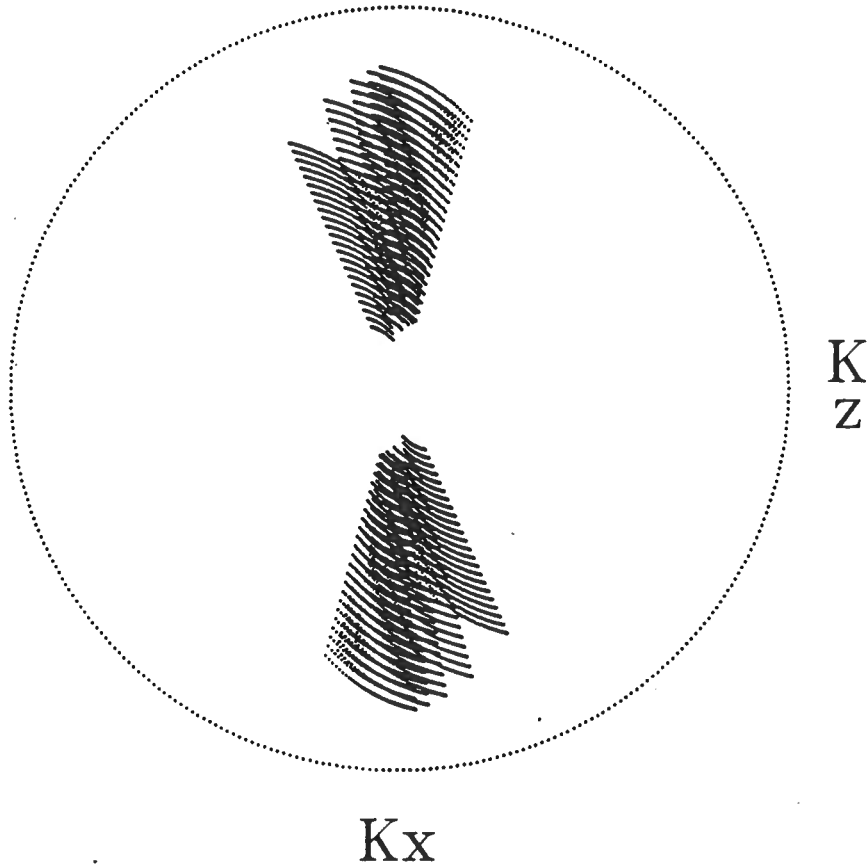
K Plot



sz = 400 gz: 200-440
x0 = 55 z0 = 500

FIGURE 7

K Plot

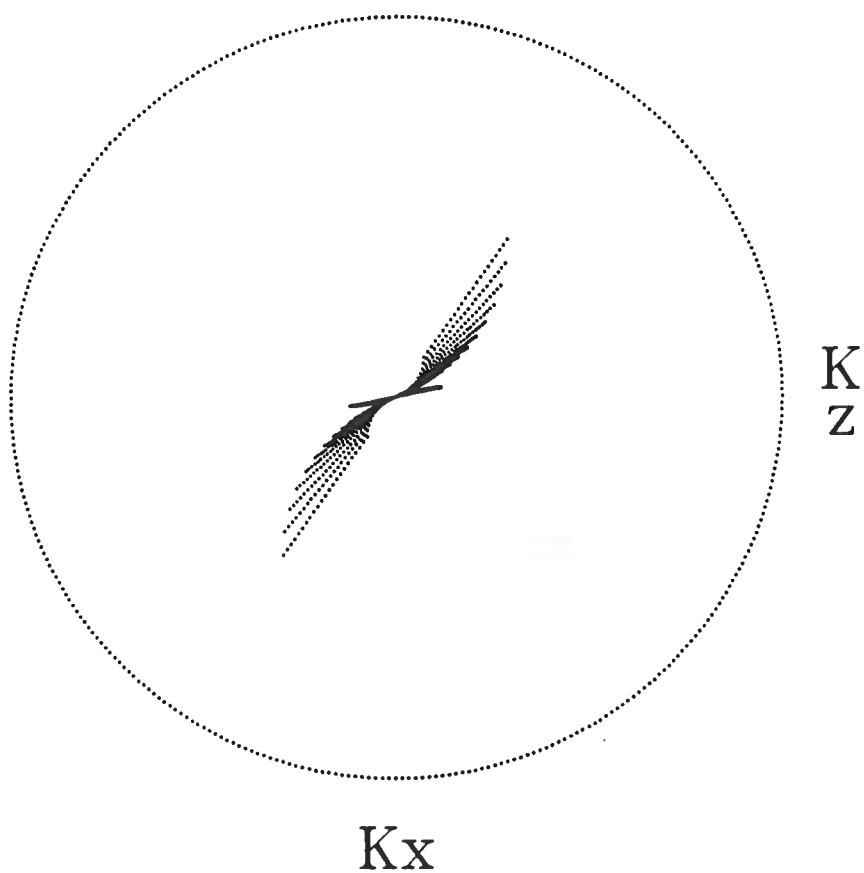


· sz = 0-400 · gz: 200-440
· x0 = 55 · z0 = 500

FIGURE 8

1
2
3
4
5
6
7
8
9
10
11
12
13
14
15
16
17
18
19
20
21
22
23
24
25
26
27
28
29
30
31
32
33
34
35
36
37
38
39
40
41
42
43
44
45
46
47
48
49
50
51
52
53
54
55
56
57
58
59
60
61
62
63
64
65
66
67
68
69
70
71
72
73
74
75
76
77
78
79
80
81
82
83
84
85
86
87
88
89
90
91
92
93
94
95
96
97
98
99
100

K Plot



$sz = 0$ $gz: 500-1000$
 $x0 = 55$ $z0 = 500$

FIGURE 10



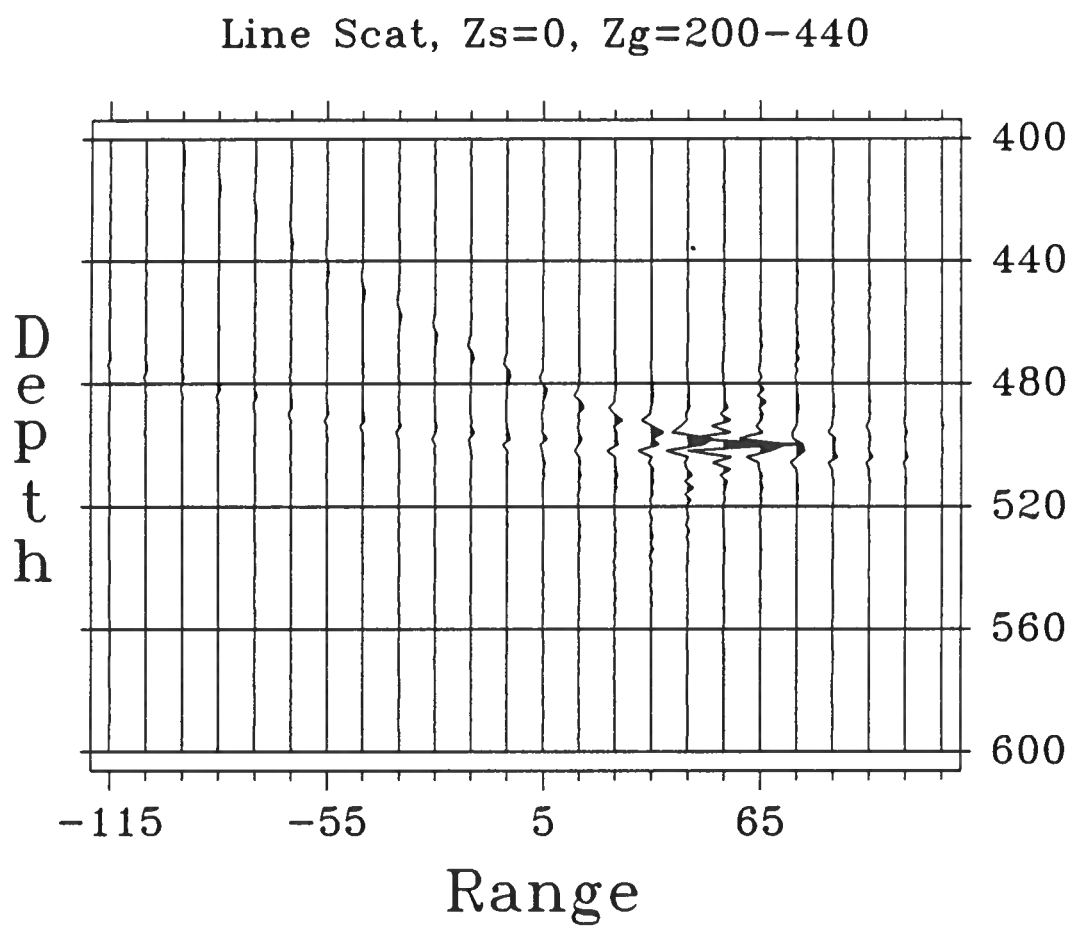


FIGURE 11



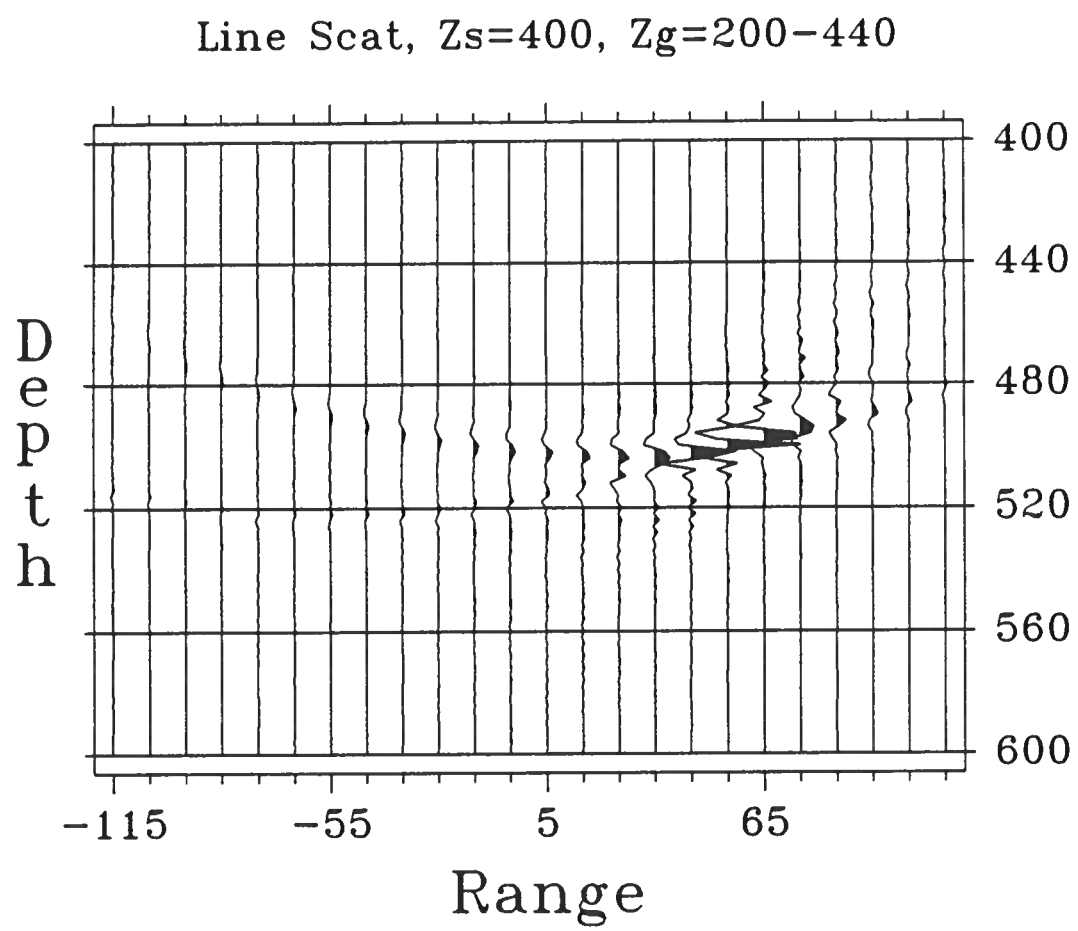


FIGURE 12

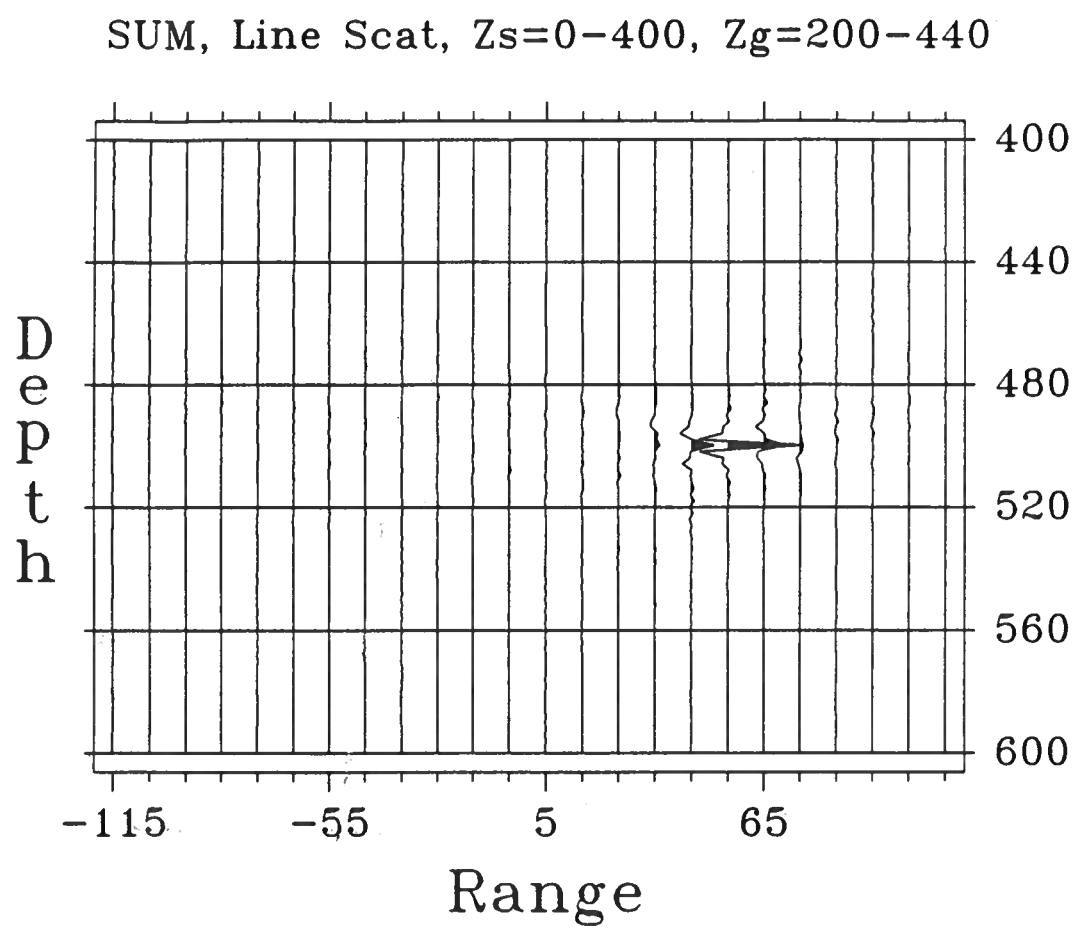


FIGURE 13



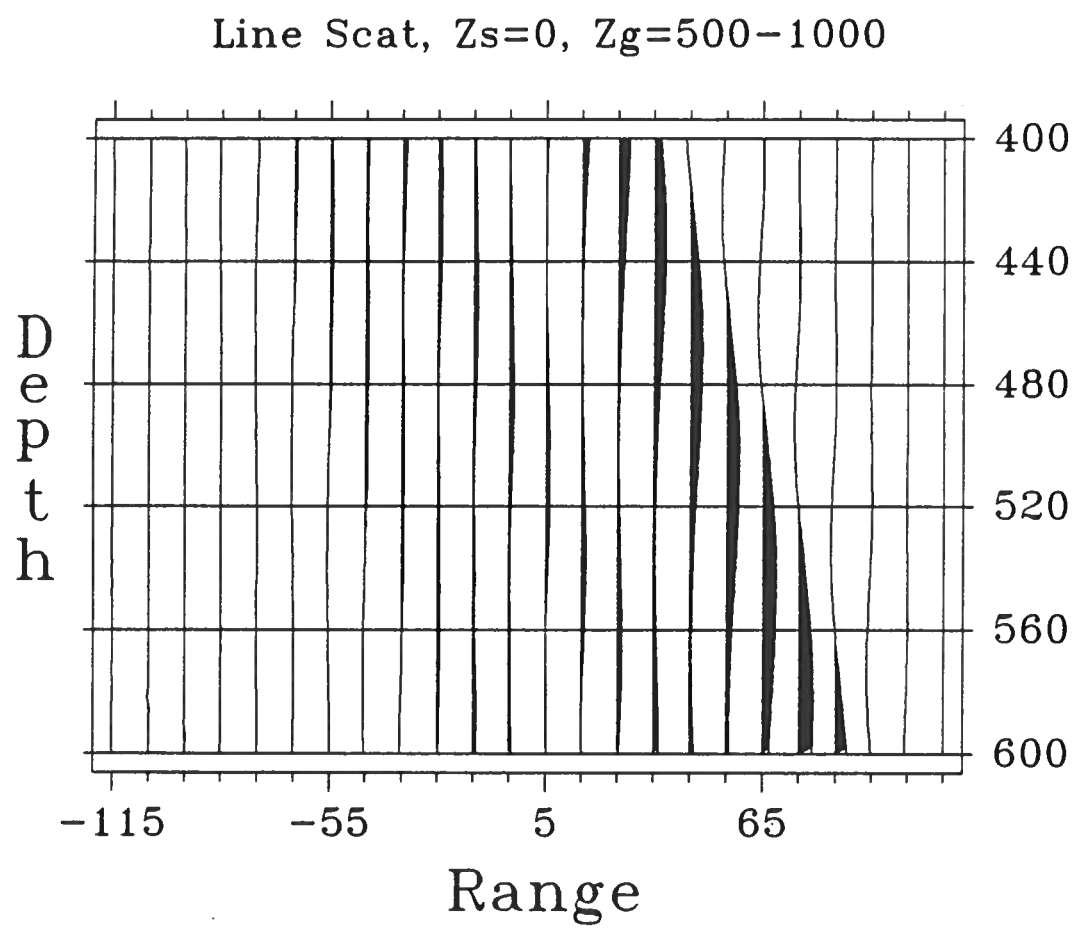


FIGURE 14



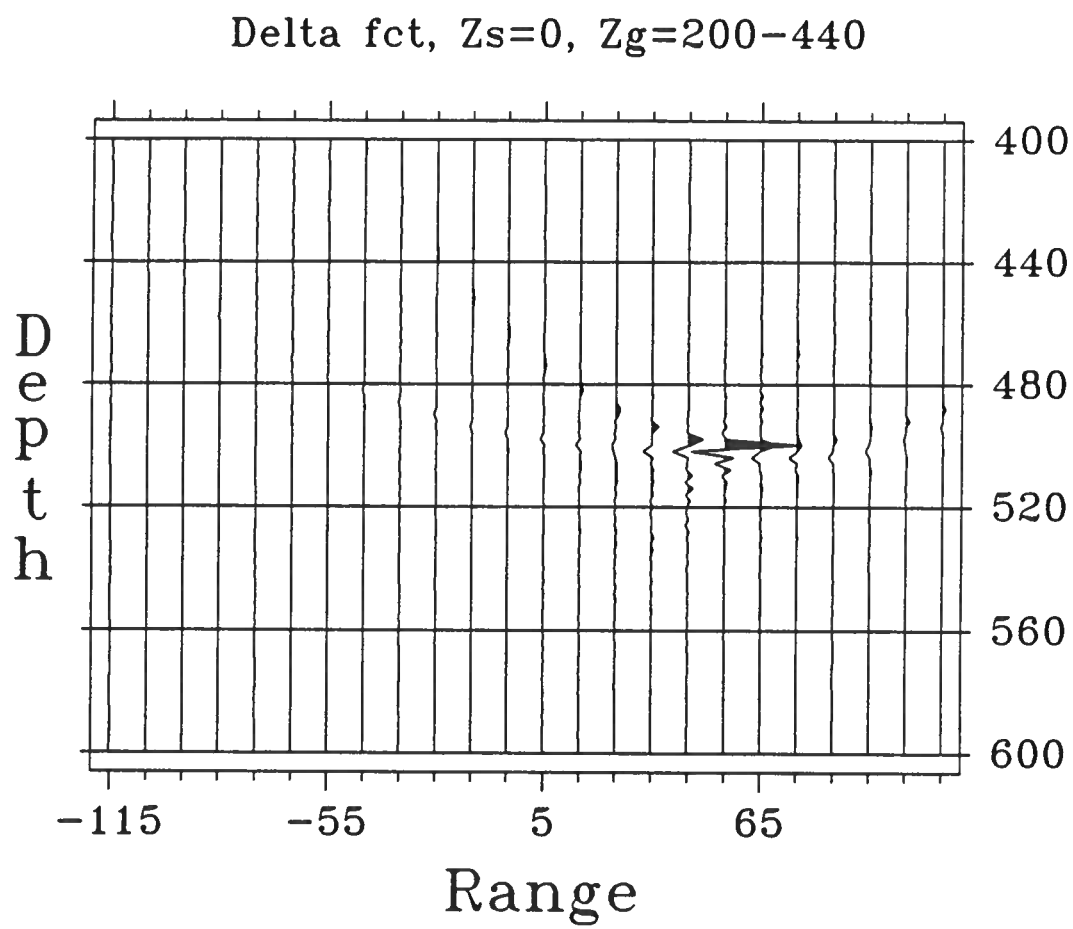


FIGURE 15



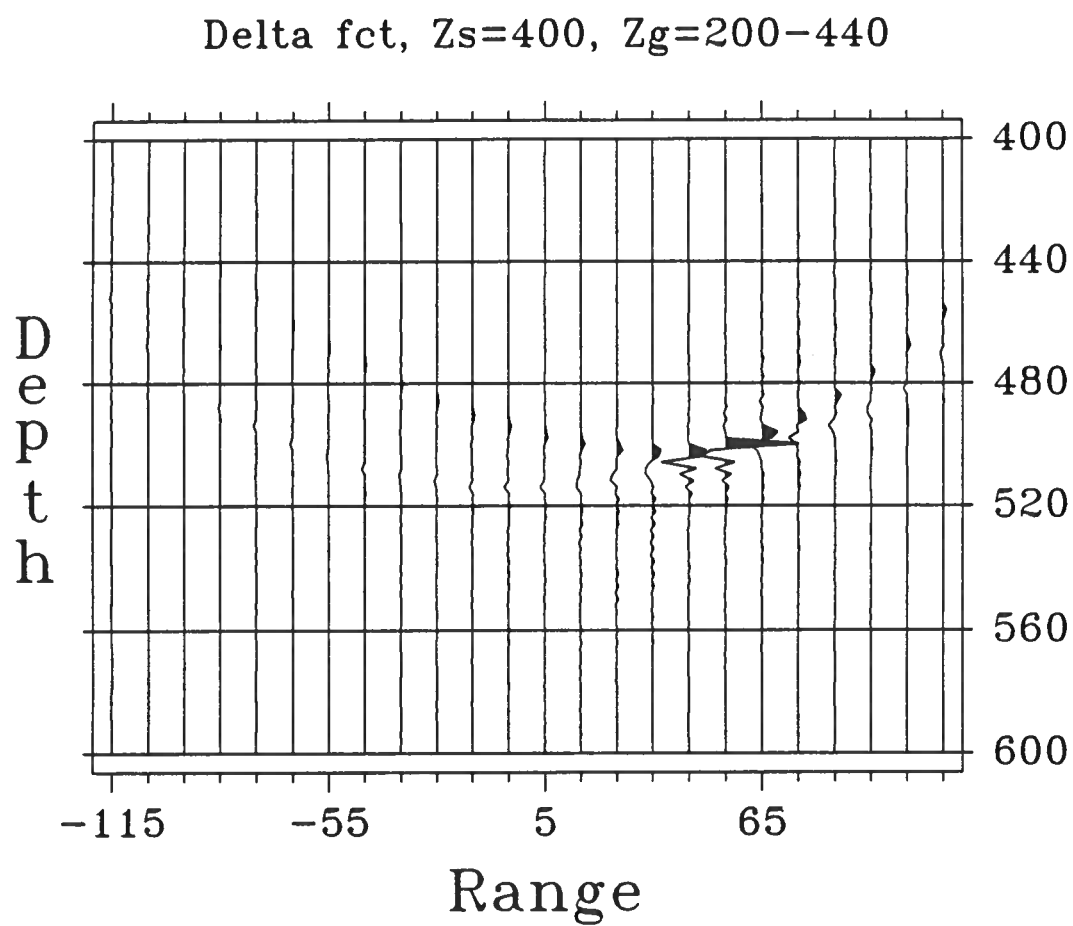


FIGURE 16



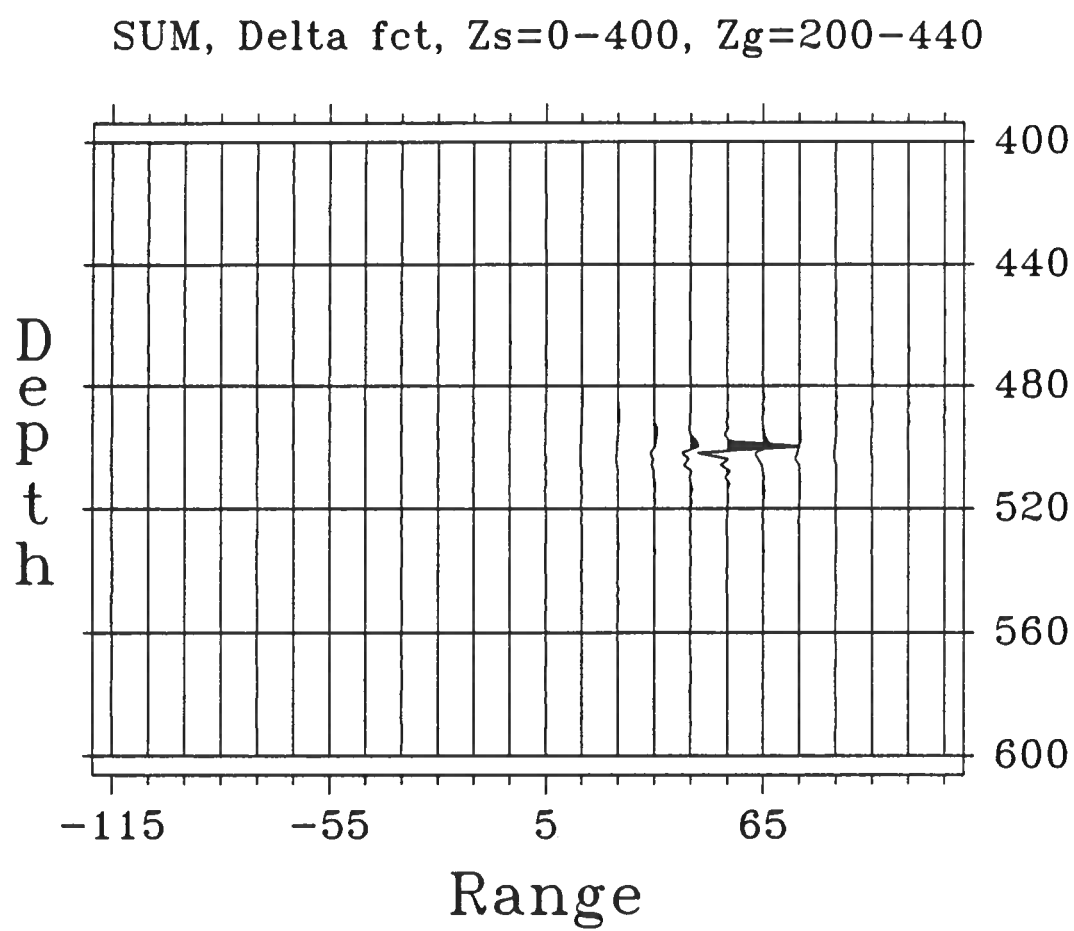


FIGURE 17

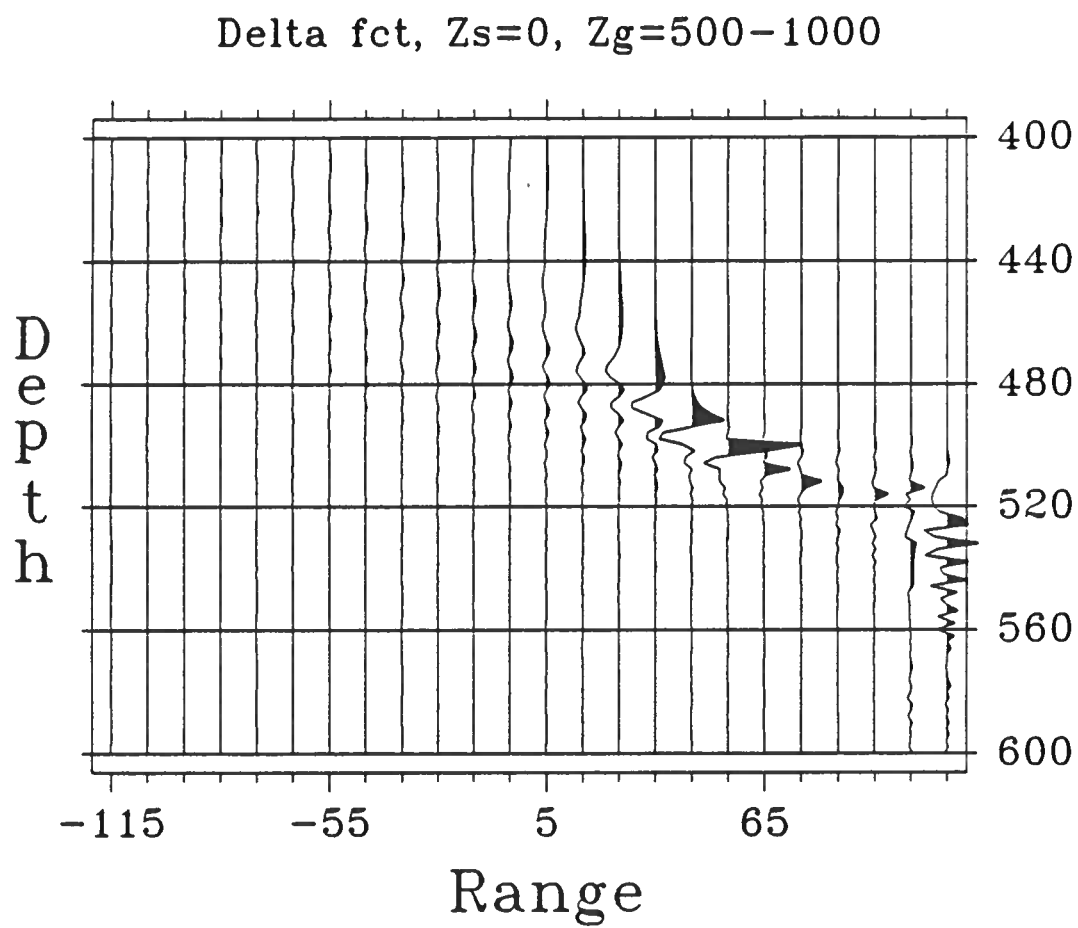


FIGURE 18

